Skyrmion dynamics in antiferromagnets

Dissertation
zur Erlangung des Grades
„Doktor
der Naturwissenschaften“
am Fachbereich Physik, Mathematik und Informatik
der Johannes Gutenberg-Universität
in Mainz

Hristo Velkov

geb. in Sofia, Bulgarien

Mainz, den 20. Dezember 2017

Tag der mündlichen Prüfung: 18. Mai 2018

Zusammenfassung

Die Forschungsfelder der magnetischen Skyrmionen und Antiferromagneten haben in den letzten Jahren, unabhängig voneinander, wesentliche Fortschritte erzielt. Skyrmionen sind kleine teilchenartige Objekte, die effizient mit elektrischen Strömen bewegt und dicht aneinander gepackt werden können, und Potential für neuartige Datenspeichergeräte, sowie Logikbausteine aufweisen. Antiferromagneten, magnetisch geordnete Materialien mit kompensierter Gesamtmagnetisierung, besitzen mehrere Vorteile gegenüber Ferromagneten, welche weit verbreitet in der Spintronik sind, wie z.B., schnellere Magnetisierungsdynamik, Unempfindlichkeit gegenüber externen magnetischen Störungen und Überfluss in der Natur.

In dieser Arbeit untersuchen wir die dynamischen Eigenschaften von Skyrmionen in Antiferromagneten mit zwei kollinearen Untergittern. Als erstes erweitern wir die phänomenologische Theorie, die die Wechselwirkung zwischen elektrischen Strömen und antiferromagnetischen Momente beschreibt, um Drehmomente die durch Spin-Bahn-Wechselwirkungseffekte induziert werden zu berücksichtigen (die so-genannten „spin-orbit torques“), und leiten eine Bewegungsgleichung für das antiferromagnetische Skyrmion her. Unsere analytischen Ergebnisse stimmen mit den ersten veröffentlichen numerischen Simulationen überein.

Als nächstes analysieren wir die intrinsische Dynamik von antiferromagnetischen Skyrmionen, die in dünnen Nanoscheiben eingesperrt sind. Wir entwickeln einen mikromagnetischen Code, der auf die Finite-Elemente-Methode basiert und sowohl Ferromagneten, als auch Antiferromagneten simulieren kann. Der Code beschreibt Proben mit gekrümmter Geometrie genau, findet den nächstliegenden Gleichgewichtszustand von dem vorgegebenen Modell und berechnet die intrinsischen Eigenmoden eines Gleichgewichtszustands. Wir finden skyrmionische Grundzustände ohne externe Magnetfelder, in Übereinstimmung mit theoretischen Voraussagen. Wir beobachten die gleiche Art von Anregungen in ferromagnetischen und antiferromagnetischen Skyrmionen: gyrotropische, „atmende“ und deformierte Moden und diskutieren ihre Unterschiede.

Theoretische Studien haben bereits die Existenz und Stabilität von antiferromagnetischen Skyrmionen prognostiziert; dennoch hat es bisher keine experimentellen Beobachtungen gegeben. Das Spektrum des eingesperrten antiferromagnetischen Skyrmion weist charakteristische Merkmale auf, die es von dem uniform-magnetisierten Zustand unterscheiden, und könnte wichtige Hinweise in der experimentellen Suche nach den antiferromagnetischen Skyrmion liefern.

Abstract

Research in the fields of magnetic skyrmions and antiferromagnets, independently from each other, has been gaining momentum in recent years. Skyrmions are small particle-like objects that can be moved efficiently with electric currents and packed densely together, and hold potential as candidates for novel information storage and logic devices. Antiferromagnets, magnetically ordered materials with compensating magnetization, possess a number of advantages over the widely used in the field of spintronics ferromagnets, such as faster magnetization dynamics, robustness to external magnetic perturbations and abundance in nature.

In this work, we investigate the dynamics of skyrmions in collinear two-sublattice antiferromagnets. First, we extend the phenomenological theory that describes the coupling of antiferromagnetic moments with electric currents to incorporate spin-orbit torques, and derive an equation of motion for the skyrmion within the collective-coordinate approach. Our analytical results are consistent with initial numerical simulations reported recently.

Next, we study the intrinsic dynamics of antiferromagnetic skyrmions confined in thin nanodisks. We develop a finite-element micromagnetic code that is able to simulate both ferromagnets and antiferromagnets. The code describes well curved geometries, finds the nearest equilibrium state of a given model and calculates the intrinsic eigenmodes of a specified equilibrium state. We find skyrmion ground-states at zero external field in both ferromagnets and antiferromagnets, consistent with theoretical predictions. Further, we observe the same types of excitations of both ferromagnetic and antiferromagnetic skyrmions – gyrotropic, breathing and deformed-code modes – and discuss their differences.

Theoretical studies have already predicted the existence and stability of antiferromagnetic skyrmions; however, there has not been an experimental observation yet. The spectrum of the confined antiferromagnetic skyrmion shows characteristic features that distinguish it from the spectrum of the uniformly magnetized state, which could provide important clues in the experimental pursuit of the antiferromagnetic skyrmion.

Contents

Chapter 1

Introduction

Magnetic materials, and especially ferromagnets, have become an indispensable part of modern technology. The orientation of magnetic moments[1] along a preferred direction is well suited for storing binary information in novel data storage media, whereas the manipulation of magnetic moments, e.g., by electric currents, provides a platform for data processing and the creation of logic devices. The implications of this interplay of the charge and spin degrees of freedom, together with the fundamental questions related to it, were the inception of the now well-established field of spintronics within the last few decades [1, 2].

Conventional technology relies heavily on the manipulation of semiconductors and magnetic materials with electric currents. The high and constantly increasing demand of processing power due to advancements in electronics and, especially, the role of the internet, has so far been met. This process has been described well by the observation known as Moore's law, stating that roughly every eighteen months the amount of transistors on an integrated circuit increases by a factor of two. However, this trend cannot be expected to continue indefinitely: as the transistors become smaller, eventually, the heat generated by the charge currents will impede the operation of the device [3, 4]. Spintronics offers a way to circumvent this problem by employing the spin degree of freedom, which features a lower power consumption [1, 4].

The current-induced manipulation of magnetic moments and textures has proved to be key for the rapid growth of the spintronics field. The discovery of magnetoresistive effects, such as the giant magnetoresistance that has found application in the hard-disk drive technology, gave the initial push in the field; it is now succeeded by the current-induced torque effects that can manipulate magnetic moments, e.g., based on the conservation of angular momentum [5, 6]. Next-generation devices using these effects, like the magnetic random access memory, have already been proposed [6, 7]. The latter employs the current-induced motion of domain walls in thin nanowires but, even though it possesses advantages over hard-disk drive technology, the need for high currents and sample-defects issues prevent its widespread application [8].

---

[1] Here, we use the terms magnetic moment and magnetization interchangeably. To be precise, the former is directly related to an individual electron spin, whereas the latter represents the average spin of large number of electrons.

A promising alternative to domain walls could be the recently discovered skyrmions, as their properties make them very appealing for novel spintronic devices [8]. Originally, skyrmions were predicted by the nuclear physicist Tony Skyrme as topologically stable particle-like solutions of nonlinear field models [9]. Since then, this concept has found applications in many diverse fields of physics, ranging from elementary particles to areas of condensed-matter, such as liquid crystals, quantum Hall systems and Bose-Einstein condensates [10].

In magnetic systems, skyrmions are stable chiral textures with a whirlpool-like winding of the magnetic moments[2], such that the unit sphere is covered entirely once. This is captured by the topological number, which takes the integer values $Q = \pm 1$. Here, the sign is related to the orientation of the magnetic moment at the center of the skyrmion.

Magnetic skyrmions were first predicted to appear as stable structures in chiral magnets theoretically [10, 11, 12, 13]. The breakthrough came with the first experimental observation of skyrmions in bulk systems [14, 15] and thin films [16] – where the skyrmions appeared in a lattice (henceforth called skyrmion lattices, or skyrmion crystals) – and, in particular, with the experimental evidence that skyrmion can be moved with much lower electric currents than domain walls [17]. Crucial for the stability of skyrmions in these systems is the bulk Dzyaloshinskii-Moriya interaction, which appears in noncentrosymmetric materials (where inversion symmetry is broken in the crystal structure) with high spin-orbit coupling [10, 18, 19, 20]. Importantly, in these experimental findings an external magnetic field applied in the out-of-plane direction was necessary for the skyrmion stabilization. As a consequence, the discovered skyrmions exist only in a narrow area of these materials' phase diagram [8, 14], which would limit their application in devices.

The skyrmion lattice phase was found to extend over a larger region in the phase diagram in thin films samples, compared to their bulk counterparts [10]. The first experimental observation of skyrmions at the interfaces of ultrathin magnetic films (less than one nm) with heavy metals showed further that the skyrmion phase is the groundstate of the system and an external field is not necessary for its stabilization [21]. The Dzyaloshinskii-Moriya interactions responsible for the stabilization of these skyrmions are due to the broken inversion symmetry at the interface, rather than in the crystal, and are therefore referred to as interfacial.

These two types of Dzyaloshinskii-Moriya interactions lead to skyrmions with different profiles. In all cases, the magnetic moments at the center and the outskirts of the skyrmions are aligned in opposite directions and rotate in the intermediate region only as a function of the radial coordinate. Bulk Dzyaloshinskii-Moriya interactions induce rotation of the spins in the plane perpendicular to the radial direction, whereas the interfacial type leads to rotation of the spin along the radius [8, 20]. The resulting skyrmions are labelled as Bloch and Néel, respectively, following the convention used for labelling domain walls (see figure 1.1).

Shortly after the experimental discovery, investigations have shown that magnetic skyrmions possess remarkable properties [10, 20], such as a very small size [21], the topological Hall effect [15], emergent electrodynamics [22], low threshold for the electric-current-induced motion and the presence of a Magnus force [17, 23]. These

---

[2] Here, the adjective chiral means that the winding of the spins occurs in a fixed direction.

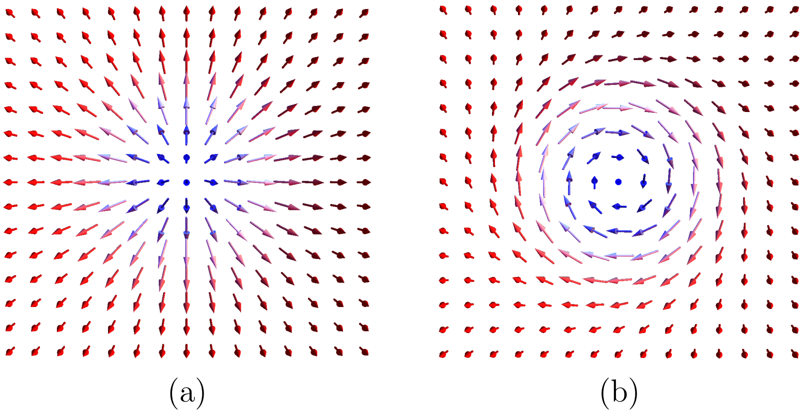
(a) (b)

Figure 1.1: *Schematic representation of the (a) Néel and (b) Bloch skyrmions.*

findings have revealed a high potential of skyrmions for low-energy, nonvolatile, ultradense memory and logic devices [8, 24].

Follow-up studies demonstrated the possibility to perform control operations, such as creation, manipulation and annihilation of isolated skyrmions stabilized by Dzyaloshinskii-Moriya interactions in perpendicularly magnetized thin magnetic films, which are essential for technological applications [20]. Theoretical predictions of the stability of such isolated skyrmions [24] were supported by numerical simulations, showing the creation [25], stability [25, 26], as well as manipulation by electric currents [25, 27] and, importantly, further supported by experimental demonstrations of the creation [28], manipulation [29] and annihilation [28] of isolated skyrmions.

Generally, thin films have the advantage that material parameters like the magnetic anisotropy, or Dzyaloshinskii-Moriya interactions can be adjusted experimentally [25, 29], which allows for tuning the skyrmion size. Numerical simulations showed potential for employing skyrmions in racetrack memories [25], as well as in skyrmion-based logic gates [30]. The experimental observation of stable skyrmions in thin films at room temperature and zero magnetic field [20, 29, 31], as well as the demonstration of current-induced motion of trains of skyrmions on a racetrack at high speeds – comparable to the ones in contemporary hard-disk drives – presented another important step towards bringing skyrmions closer to applications [29, 32].

Another important field of skyrmion research are excitations that involve the skyrmions' internal degrees of freedom. Generally, current-induced skyrmion motion can be treated by approximating the skyrmion as a rigid object. However, it was shown that the rigid assumption is not always justified and the skyrmion can deform as a result of the electric currents [27, 33]. This shows the importance of understanding how skyrmions can deform in response to external perturbations.

Numerical simulations have identified a number of different internal modes, such as the gyrotropic, uniform breathing and polygon-like distortion modes [34, 35, 36, 37], which have only partly been experimentally verified [38, 39, 40, 41]. As there is no consensus regarding the skyrmion excitation modes yet, they constitute an open field where research is being focused.

The internal skyrmion modes have been shown to produce distinct features in the power spectrum, which are different from features of the uniform state and can be used to identify skyrmion states in experiment [36]. Further, recent proposals employ such internal modes, e.g., for novel microwave detectors with high sensitivities [20, 42] or for spin-torque nano-oscillators driven by lower electric current densities [43], and show that the skyrmion excitations are an intriguing field of research also from the technological point of view.

Up until recently, the majority of the spintronics research with a focus on applications has been limited to ferromagnets. However, antiferromagnets – magnetically ordered materials with compensated magnetization – possess properties that make them appealing as potential alternatives of ferromagnets and as next generation data storage devices [6, 44]. Antiferromagnets are more robust against magnetic perturbations due to their insensitivity to external magnetic fields; densely arranged antiferromagnetic devices would not interfere with each other due to the lack of magnetic stray fields; they operate on faster timescales, which could enable ultrafast information processing; antiferromagnetic metals, alloys and semiconductors are not limited to combinations of only a few elements like Fe, Co, Ni and occur more frequently than their ferromagnetic counterparts [44, 45].

On the other hand, the insensitivity to external magnetic fields makes antiferromagnets also much harder to manipulate and control [44]. Recently, several breakthroughs were achieved in overcoming this obstacle. The anisotropic magnetoresistance effect was proposed [46] and utilized [47] to electrically detect antiferromagnetically ordered states. Another important step towards antiferromagnetic spintronics was the prediction [48] and subsequent observation [49] of Néel spin-orbit torques, in a certain class of antiferromagnets, that can electrically manipulate the antiferromagnetic Néel vector.

Following the developments in the field of ferromagnetic skyrmions and their potential, increasing attention has been given to the study of antiferromagnetic skyrmions. Theoretical predictions and arguments for the stability of antiferromagnetic skyrmions existed already before the experimental observation of their ferromagnetic counterparts [13, 50, 51]. Recently, numerical simulations have employed existing micromagnetic software for ferromagnets to solve the antiferromagnetic atomistic Heisenberg model [52, 53, 54]. These studies have focused on the thermal and current-induced motion of the antiferromagnetic skyrmion by implementing damping and current-induced torques in the same spirit as for ferromagnets. We have presented an analytical treatment of the current-induced skyrmion motion based on the phenomenological approach [55], which will be discussed in detail in the present work. Numerical Monte Carlo simulations of the Heisenberg model have further found stable isolated antiferromagnetic skyrmions even at higher temperatures in finite systems [56], as well as antiferromagnetic skyrmion crystals [57]. Ab-initio calculations were used to predict the existence of a topological spin-Hall effect in synthetic antiferromagnetic skyrmions [58] and crystals [57]. Even so, there has been no experimental observation of antiferromagnetic skyrmions up to date, possibly due to the challenges associated with detecting antiferromagnetic order in general, and chiral antiferromagnetic textures in particular [44, 58].

In this work, we focus our attention on gaining more insights on the dynamics of the elusive antiferromagnetic skyrmion. First, we apply the phenomenological approach – used in recent works to study the magnetization dynamics of antiferromagnets under the influence of electric currents [59, 60, 61, 62] – to the skyrmion state of a collinear two-sublattice antiferromagnet. Importantly, we take into account the effect of the inversion symmetry breaking, which induces the interfacial Dzyaloshinskii-Moriya interactions. Starting from general principles and symmetry considerations, we construct the equations describing the macroscopic antiferromagnetic magnetization dynamics in the presence of a DC current and an external magnetic field. In particular, we

(i) take into account the effect of the Dzyaloshinskii-Moriya interactions corresponding to a particular symmetry class of magnetic materials;

(ii) incorporate phenomenologically the spin-orbit torques of an antiferromagnetic system, and

(iii) study the role of the external magnetic field and its effect on the skyrmion motion.

We demonstrate that the latter has, in fact, no effect on the skyrmion motion. It does, however, affect its shape.

Our main result for the antiferromagnetic skyrmion under the influence of electric currents is an equation of motion for the position $\mathbf{R}$ of the skyrmion in the thin film given by

$$m_{\text{eff}}\ddot{\mathbf{R}} \;\; = -\Gamma\dot{\mathbf{R}} + \Delta\mathbf{j}. \tag{1.1}$$

Here, m_{eff} is the effective skyrmion mass, and Γ a friction constant. The external magnetic field does not appear in the equation. The dissipative spin-orbit and spin-transfer torques (described by Δ) lead to a longitudinal current-induced force on the skyrmion. In figure 1.2 we illustrate the resulting skyrmion motion. We emphasize that we included both homogeneous and inhomogeneous current-induced torques in our analysis, thus obtaining a more general form of the equation of motion than considered in references [52, 53].

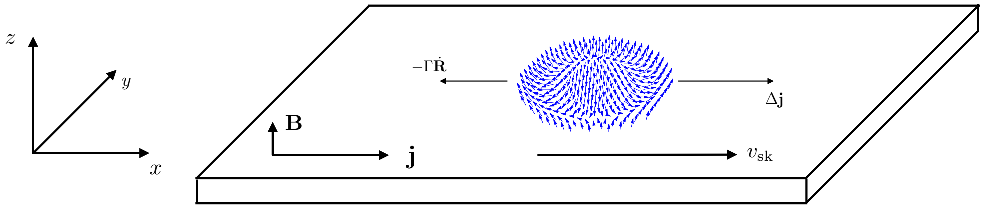

Figure 1.2: *Schematic representation of the skyrmion motion in an antiferromagnet driven by an electric current* $\mathbf{j} \parallel \hat{x}$ *and an external magnetic field* $\mathbf{B} \parallel \hat{z}$*, as described by equation (1.1). The friction force is denoted by* $\Gamma\dot{\mathbf{R}}$ *and the longitudinal current-induced force by* $\Delta\mathbf{j}$*. The combination of these forces leads to a skyrmion motion with the velocity* v_{sk}*. For simplicity, a static skyrmion shape is depicted, without taking into account the shape changes that the magnetic field and the electric current induce.*

Next, we perform numerical simulations to investigate the internal modes of an antiferromagnetic skyrmion confined in a thin film nanodisk. The resonance frequencies associated with these internal modes – similar to the distinct features of the ferromagnetic skyrmion [36] – could provide a gateway towards an experimental observation of antiferromagnetic skyrmions.

We develop a micromagnetic code that implements the phenomenological model described above in the absence of electric currents, for both ferromagnets and antiferromagnets[3]. It is based on the finite-element method, which has the advantage of describing samples of arbitrary geometry – such as circular nanodisks – accurately and reliably. The code consists of two parts: a relaxation solver that finds the nearest equilibrium state of the micromagnetic model, and an eigenspectrum solver, which calculates the frequencies and corresponding eigenvectors of a given equilibrium texture. In particular, we

(i) find an antiferromagnetic groundstate skyrmion at zero external field with a profile that is consistent with theoretical predictions [13];

(ii) calculate the eigenspectrum of both the ferromagnetic and antiferromagnetic skyrmion and observe gyrotropic, deformed-core and breathing modes. We find that the skyrmion modes in the antiferromagnet

    (a) have frequencies higher than the corresponding modes in the ferromagnet by at least an order of magnitude;
    (b) come in pairs, apart from the breathing mode, in the low-frequency spectrum;
    (c) represent rotation within the nanodisk of the skyrmion only at finite external fields.

The last point is illustrated schematically in figure 1.3. The differences of the antiferromagnetic skyrmion modes can be traced back to the (a) enhancement of antiferromagnetic magnetization dynamics due to the strong exchange interaction [44];

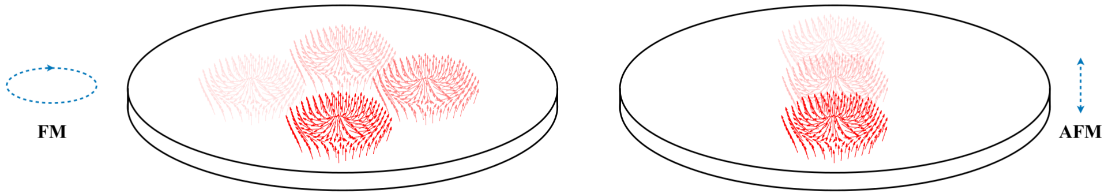

(a) Ferromagnet (b) Antiferromagnet

Figure 1.3: *Schematic representation of the lowest-frequency confined-skyrmion eigenmodes at zero external field. For simplicity, we show only one of the two antiferromagnetic modes; the other oscillates along a different direction in-plane. When the external field is turned on the antiferromagnetic modes begin rotating around the nanodisk center.*

---

[3] Up to date, there is no freely available micromagnetic software that can incorporate the magnetization dynamics of an antiferromagnet.

(b) doubling of degrees of freedom due to the presence of two magnetic sublattices; (c) absence of preferred direction of rotation in antiferromagnets at zero magnetic field.

This thesis is structured as follows. In chapter 2, we present the fundamentals and methods that we use throughout this work. We discuss first the type of skyrmions that we focus on in the context of other magnetic textures in section 2.1. We then present the basis of the phenomenological and collective-coordinate approaches in sections 2.2.1 and 2.2.2, respectively, and discuss the nature of the different current-induced torques in section 2.2.3. The numerical techniques are presented in section 2.3. We review the finite-element method in section 2.3.1 and discuss the basis of our code in section 2.3.2.

In chapter 3, we present the full phenomenological models for both ferromagnets and antiferromagnets, and study their equilibrium skyrmion solutions. We review well-known static properties of both the infinite-plane and confined ferromagnetic skyrmion in section 3.2.2. The antiferromagnetic skyrmion properties are presented in section 3.3.2, where – apart from reviewing the known antiferromagnetic skyrmion profile equation – we discuss the effect of the skyrmion motion, e.g., due to electric currents, on the skyrmion shape. Further, we investigate the confinement effects on the static properties of an antiferromagnetic skyrmion in the same section.

In chapter 4 we compare the current-induced motion (section 4.1) and the confined skyrmion eigenmodes (section 4.2) of both ferromagnets and antiferromagnets. In section 4.1.1, we review analytically the ferromagnetic skyrmion motion driven by electric currents via spin-transfer and spin-orbit torques. In section 4.1.2, we present the discussion of the antiferromagnetic skyrmion current-induced motion. In particular, we discuss the current-induced torques in antiferromagnets, derive a closed equation for the antiferromagnetic order parameter and reformulate the result into an equation for the position of the skyrmion. The latter results have been published in reference [55].

The confined-skyrmion dynamics are presented in section 4.2. First, we apply our micromagnetic code to a ferromagnetic skyrmion and review its eigenspectrum in section 4.2.2. The skyrmion excitation modes in ferromagnets have been studied on multiple occasions; however, there has not been a treatment of the same model and with the same methods as in this work. Therefore, our results draw a richer picture that complements studies in the existing literature. Next, we present the eigenmode dynamics of the antiferromagnetic skyrmion in section 4.2.3. The presentation of the results in both sections 4.2.2 and 4.2.3 is done in two steps: first, a numerical simulation is performed to find the skyrmion groundstate in both systems, and then the eigenspectrum of each is calculated. We discuss the lowest-frequency modes in the spectrum and study their behaviour as a function of the external field and sample size.

In chapter 5, we present a reference for the ferromagnetic and antiferromagnetic phenomenological models, the corresponding weak formulations relevant for the numerical simulations and the corresponding code scripts.

Finally, a summary and conclusions of the work are presented in chapter 6.

Chapter 2

Fundamentals

2.1 Magnetic textures and the advantages of skyrmions

In this work, we investigate the static and dynamic properties of magnetic skyrmions, stabilized by interfacial Dzyaloshinskii-Moriya interactions. Being topologically protected particle-like solutions of nonlinear field models, skyrmions fall under the general category of solitons, which have been studied extensively [10, 20]. Here, we discuss briefly the differences and advantages of skyrmions with respect to other solitons.

In magnetic systems, stable solutions of the Landau-Lifshitz-Gilbert equations (see section 2.2.1 below) are regarded as magnetic solitons [63]. Common examples are domain walls (one-dimensional solitons of the kink type), vortices, bubbles and skyrmions (two-dimensional solitons) [20].

Domain walls are topologically trivial magnetic textures and are, therefore, easier to remove out of a system than skyrmions. Both domain walls and skyrmions can be driven by spin-polarized currents and follow a similar equation of motion; however, domain walls are one-dimensional objects described by the wall position coordinate and tilting angle from the plane, whereas skyrmions are two-dimensional and are parametrized by in-plane position coordinates [10]. Importantly, the energy of a domain wall depends on the wall length and changes whenever a crossing (e.g., a bifurcation) is encountered. This leads to pinning sites for domain walls, which skyrmions can avoid. Finocchio *et al.* demonstrated the skyrmions can even move around corners in complex grid structures [20], thus highlighting their technological potential.

Vortices are easily distinguishable from skyrmions, as their magnetic moments curl in-plane around the core in a way that only half of the unit sphere is covered. On the other hand, magnetic bubbles have a similar appearance to skyrmions (of the Bloch type), with the magnetization vector rotating between two regions of oppositely aligned moments. Importantly, bubbles are stabilized by the long-ranged dipolar interactions; these are dominant in the stabilization even if weak Dzyaloshinskii-Moriya interactions are present. As a result, bubbles are generally larger with sizes of the order of 100 nm to 1 µm; skyrmions are smaller, of the order of $5 - 100$ nm [10]. Further differences are the topological number, which is non-trivial for skyrmions (some bubbles are topologically trivial, others non-trivial); skyrmions are chiral, whereas bubbles can be; bubbles are preferably driven by magnetic fields, whereas skyrmions, by electric currents.

We also note the existence of dynamical skyrmions (and solitons, in general [63]) that are stabilized, e.g., by current-induced effects that counteract the Gilbert losses in dissipative materials [20]; however, such objects fall outside of the scope of this work.

2.2 Analytical techniques

Here, we present the tools needed for the analytical analysis of magnetic skyrmions. In section 2.2.1, we introduce the phenomenological approach and discuss its advantages and disadvantages. We introduce the Landau-Lifshitz-Gilbert equation and the relevant contributions to the energy functional for the stabilization of skyrmions. In section 2.2.2, we present the collective-coordinate approach, which we use later to describe the current-induced skyrmion motion. Finally, we introduce phenomenologically the current-induced torques in section 2.2.3 and discuss the differences between spin-transfer and spin-orbit torques.

2.2.1 Phenomenology

The phenomenological approach is an effective method to describe magnetic systems that are deeply in the ordered phase. In ferromagnets the order is determined by the parameter $\mathbf{m}$ (magnetization vector) and in antiferromagnets, by $\mathbf{n}$ (Néel vector). Based on symmetries, the (Landau-Lifshitz-Gilbert) equation describing the magnetization dynamics is postulated, together with the energy functional defining the main interactions in a given system. The Landau-Lifshitz-Gilbert equation has proven to represent accurately the current-driven dynamics of magnetic textures, such as domain walls or skyrmions [10, 64, 65]. Importantly, the characteristic length of the magnetic texture ($\sim$ nm) has to be much smaller than the characteristic length over which it moves ($\sim$ µm) for the method to be valid. Further, the temperatures considered have to be lower than corresponding ordering temperature: Cure temperature for ferromagnets and Néel temperature for antiferromagnets. Also, for antiferromagnets the temperature has to be large enough, so that quantum effects can be ignored.

The approach relies on a “coarse-graining” of the magnetization structure, so that each magnetization site represents a large enough volume where the magnetic moment is established and varies only slowly within it [66, 67]. This defines the macroscopic character of the phenomenological approach. As a consequence, the system exhibits established thermodynamics and the predictions of the approach are robust.

Due to the macroscopic nature, the models considered within this method are generic: it covers a multitude of microscopically different systems that all obey the same symmetries. An immediate advantage is that physical phenomena can be described accurately without knowledge of the microscopic mechanisms. Further, the method establishes a clear connection to many experiments, where macroscopic quantities are measured.

On the other hand, the parameters determining the relative strength of the interactions within the model cannot be obtained from the phenomenological approach. These need to be taken as an input, e.g., from experiments or first-principle calculations (density functional theory [68], etc.). Further, the macroscopic nature of the approach leads to the smearing out of excitations with smaller lengthscales (generally, smaller than 1 nm), so that different methods need to be employed for studying such problems.

Landau-Lifshitz-Gilbert equation

A magnetic system is characterized by the magnetization vector $\mathbf{M}(\mathbf{r}) = M_\mathrm{s}\mathbf{m}(\mathbf{r})$, where $\mathbf{m}$ is a unit vector, and is treated in a continuum model. In both ferromagnets and antiferromagnets (in the ordered phase), the magnetization vector has a fixed length given by the saturation magnetization M_s. The dynamics of the magnetization structure is determined by the Landau-Lifshitz-Gilbert equation[1] [64, 65, 69]

$$\dot{\mathbf{M}}(\mathbf{r}) = \gamma\mathbf{M}(\mathbf{r}) \times \mathbf{B}_\mathrm{eff}(\mathbf{r}) + \alpha_G\mathbf{M}(\mathbf{r}) \times \dot{\mathbf{M}}(\mathbf{r}) + \tau_\mathrm{Torques}, \tag{2.1}$$

where γ is the electron gyromagnetic ratio and $\mathbf{B}_\mathrm{eff}$ the effective field. The latter is found by taking a functional derivative of the energy functional with respect to the magnetization vector

$$\mathbf{B}_\mathrm{eff}(\mathbf{r}) = -\frac{1}{M_\mathrm{s}}\frac{\delta f(\mathbf{r})}{\delta\mathbf{m}}, \tag{2.2}$$

where f is the energy density.

The first term on the right hand side of equation (2.1) represents the precession of the magnetization vector around the effective field. For the case of a single electron in an external magnetic field, this term describes the Larmor precession [68].

In realistic samples energy dissipates and the magnetization vector eventually relaxes towards the direction set by the effective field. This dissipation effect is captured phenomenologically by introducing the Gilbert damping term[2] [64, 67] proportional to α_G, which is the dimensionless Gilbert damping constant. Typical values of the damping constant are of the order of $10^{-2} - 10^{-3}$ [2, 68].

Similar to the damping term, any external perturbations to the system can be captured phenomenologically by adding a corresponding torque term. Such terms have been represented collectively by τ_external in equation (2.1). Common examples are current-induced or temperature effects. The benefit of the phenomenological approach is that no detailed knowledge of the microscopic mechanisms is needed; to construct such a term only the symmetries of the systems need to be respected (see section 2.2.3).

---

[1] If the magnetization vector length is not fixed (e.g., for high temperatures) the Landau-Lifshitz-Gilbert equation needs to modified.

[2] A different formulation was proposed initially by Landau and Lifshitz; however, for $\alpha_G \ll 1$ both formulations are equivalent [5, 64].

As the length of the magnetization vector is fixed, equation (2.1) can be conveniently reformulated in terms of the unit vector **m**

$$\dot{\mathbf{m}}(\mathbf{r}) = \gamma \mathbf{m}(\mathbf{r}) \times \mathbf{B}_{\text{eff}}(\mathbf{r}) + \alpha_G M_{\text{s}} \mathbf{m}(\mathbf{r}) \times \dot{\mathbf{m}}(\mathbf{r}) + \tau_{\text{Torques}}. \tag{2.3}$$

Equation (2.3) is the foundation of this work, as it contains all the information about a magnetic system within the phenomenological approach. In the following chapters, we investigate specific examples of ferromagnets and antiferromagnets, and discuss the static and dynamic properties of magnetic skyrmions based on the Landau-Lifshitz-Gilbert equation:

- **Static properties** In equilibrium, the magnetization texture has no dynamic component. As a result, the static part of equation (2.3) can be used to determine the equilibrium profile of the magnetization vector $\mathbf{m}(\mathbf{r})$[3]. This is explored further in chapter 3.

- **Dynamic properties** Due to the presence of the effective field, equation (2.3) is a coupled, nonlinear differential equation for the magnetization vector at every point in space in the system. This complexity makes it impossible to solve the equation analytically for magnetization textures such as skyrmions. A useful approach that we employ for an analytical analysis is the collective-coordinate method, discussed in section 2.2.2. For a more detailed treatment numerical techniques are necessary; we discuss these in section 4.2.

Energy functional

Information about the material of interest is encoded into the energy functional [65, 66]. The model is constructed based on the relevant interactions and the symmetries of the system. In this work the energy functional has the general form

$$F[\mathbf{m}] = \int d^3r \left[F_{\text{exch}} + F_{\text{ani}} + F_{\text{ext}} + F_{\text{DM}}\right], \tag{2.4}$$

where the individual contributions represent the exchange interactions, anisotropy energy, external magnetic field and the Dzyaloshinskii-Moriya interactions, respectively. Further contributions known to affect the magnetization texture, such as dipole-dipole interactions, magnetostrictive effects, etc., fall outside the scope of the present work. In ferromagnets, the dipolar interactions are a key ingredient in the stabilization magnetic bubbles [10] and are also important for certain skyrmionic systems [20]. Here, we investigate thin film samples, for which the effect of dipolar coupling can be incorporated into an effective anisotropy term [26]. In antiferromagnets, the contribution of dipolar interactions is negligible [44, 51].

In the following, we list the expressions of each term in equation (2.4) within the continuum model up to second order in the slowly varying magnetization vector and gradients thereof. The discussion here is based on ferromagnetic systems; the model for an antiferromagnet is developed in chapter 3.

---

[3] An alternative and equivalent approach is to minimize the energy functional with respect to **m**.

Exchange The isotropic exchange interactions originate from the electrostatic interactions between electrons and the Pauli exclusion principle [65]. These interactions align neighbouring spins collinearly and are independent of the orientation of the magnetic moments with respect to the crystal lattice. This isotropy is reflected in the energy functional

$$F_{\text{exch}} = \int d^3r \, A_{\text{ex}} \Big[\nabla \mathbf{m}(\mathbf{r})\Big]^2, \tag{2.5}$$

where the notation $(\nabla \mathbf{m})^2$ is to be understood as $\sum_{i=x,y,z} (\partial_i \mathbf{m}) \cdot (\partial_i \mathbf{m})$. In this work we do not consider variation of $\mathbf{m}$ in the out-of-plane $\hat{z}$-direction. For our purposes, it suffices to consider a scalar exchange stiffness constant A_{ex}; however, for a more detailed treatment it has to be generalized to a second-rank tensor. The energy of these interactions is minimized when the magnetization vectors are aligned parallel or antiparallel, and deviations from the collinear arrangement are penalized. The value of the exchange stiffness constant A_{ex} has to be taken from experiments or from first-principle calculations. Typical values are of the order of $A_{\text{ex}} = 10\,\text{pJ}\,\text{m}^{-1}$. The exchange stiffness constant is directly proportional to the Curie temperature [65].

Anisotropy Due to the weaker relativistic spin-orbit interactions between electrons and nuclei, any magnetic material exhibits preferred directions for its magnetic moments [65]. Being determined by the crystal symmetry, this energy contribution is called magnetocrystalline anisotropy. The most common types are uniaxial and cubic anisotropy. In the present work, we focus only on uniaxial anisotropy where the preferred direction (easy-axis) is along the $\hat{z}$-axis:

$$F_{\text{ani}} = \int d^3r \, K_u \Big[\mathbf{m}(\mathbf{r}) \cdot \hat{z}\Big]^2, \tag{2.6}$$

Higher order terms are generally small and are neglected here. Depending on the sign of the anisotropy constant K_u, one distinguishes generally between an easy axis ($K_u > 0$) and an easy plane ($K_u < 0$). Typical values are of the order of $K_u = 50 - 500\,\text{kJ}\,\text{m}^{-3}$ and can be calculated from first-principles or measured in experiment.

External field Magnetic moments interact with the external magnetic field through the Zeeman term

$$F_{\text{ext}} = \int d^3r \, B \Big[\mathbf{m}(\mathbf{r}) \cdot \hat{B}\Big]^2, \tag{2.7}$$

where $\hat{B}$ is the direction of the external magnetic field. This term aligns the magnetic moments in the direction of the external field. In this work, the magnetic field will be put in the $\hat{z}$-direction. Typical values used in experiments with ferromagnets of the order of mT; antiferromagnets are more robust to magnetic fields [44] and stronger fields (of the order of 10 T) need to be used to align the magnetic moments away from the easy-axis.

Dzyaloshinskii-Moriya interactions Magnetic materials that lack inversion symmetry (i.e., with non-centrosymmetric crystal structures) and exhibit strong spin-orbit interactions contain an additional important contribution to the energy functional [10, 11, 18, 19]. The Dzyaloshinskii-Moriya interactions cant neighboring moments away from each other and are an essential component in the stabilization of modulated magnetic textures such as spin-spirals and skyrmions.

The continuum description involves terms that are linear in the first derivatives of the order parameter with respect to the spatial coordinates - there are called Lifshitz invariants and have the general form [51, 69, 70]

$$L_{ij}^{k} = \mathbf{m}_i \left(\frac{\partial \mathbf{m}_j}{\partial x_k} \right) - \mathbf{m}_j \left(\frac{\partial \mathbf{m}_i}{\partial x_k} \right), \tag{2.8}$$

where x_k are the spatial coordinates and the indices $i, j, k = x, y, z$. The exact form of the Dzyaloshinskii-Moriya energy contribution depends on the symmetry of the crystal and may contains different combination of Lifshitz invariants.

Importantly for this work, in thin film systems where the inversion symmetry is broken in the $\hat{z}$-direction (structural inversion asymmetry), the Dzyaloshinskii-Moriya functional is

$$F_{\text{DM,interfacial}} = \int d^3r \, D \left[(\hat{z} \cdot \mathbf{m})(\nabla \cdot \mathbf{m}) - (\mathbf{m} \cdot \nabla)(\hat{z} \cdot \mathbf{m}) \right] \tag{2.9}$$

and can also be written as $\int d^3rD \left(L_{xz}^{x} + L_{yz}^{y} \right)$ [71]. This form of the Dzyaloshinskii-Moriya interactions applies also to magnetic materials belonging to the crystallographic symmetry group C_{nv} [4] [12].

The Dzyaloshinskii-Moriya interactions were first discovered as the origin of the phenomenon called "weak ferromagnetism" in antiferromagnets [66]; Dzyaloshinskii formulated the phenomenological theory [18] and Moriya proposed the spin-orbit interactions as an underlying microscopic mechanism [19]. Due to the induced canting of the magnetic moments, the perfect antiferromagnetic order is relinquished and a small magnetization component is formed even in the absence of an external magnetic field[5].

2.2.2 Collective coordinates

The Landau-Lifshitz-Gilbert equation (2.3) describes the magnetization dynamics of a given texture at every point in space; therefore, the complexity due to the large amount of degrees of freedom is, generally, analytically intractable. Many studies have shown that the dynamics of magnetic textures in ferromagnets and antiferromagnets can often be described by only a few variables [50, 61, 72]. In particular, Thiele [72] proposed a method to simplify the description of moving textures by integrating out the internal degrees of freedom. Specifically, this is equivalent to projection the Landau-Lifshitz-Gilbert equation on the translational

---

[4] The form of the bulk Dzyaloshinskii-Moriya interactions in materials like MnSi, where skyrmions were first experimentally discovered [14, 15] is not relevant for the present work and will not be discussed.

[5] This can be seen in equation (3.28) due to the Dzyaloshinskii-Moriya interactions term B_{d}.

mode of a given magnetic texture when electric currents are applied to the system [23, 73]. In the more recent literature, this method is referred to as the "collective-coordinate approach" [74, 75, 76]; in older literature, it is equivalent to finding integrals of motion, such as the total momentum of the magnetic texture [50, 63].

The collective-coordinate approach consists of identifying a finite set of collective coordinates $\xi_i(t)$. These coordinates are chosen to parametrize the type of excitation of the magnetic texture and define the time evolution of the order parameter – e.g., $\mathbf{m}(\mathbf{r},t) = \mathbf{m}(\mathbf{r},\{\xi_i(t)\})$ for the ferromagnet. For example, when considering the current-induced motion of a domain wall the collective coordinates are the position of the wall and the tilting angle from the easy plane. Two-dimensional objects, such as skyrmions, are parametrized by the in-plane position coordinates [10]. The method provides a simple description of the magnetization dynamics, which is valid as long as the driving forces are small [73, 75].

In ferromagnets, the time evolution of the magnetization vector $\mathbf{m}(\mathbf{r},\{\xi_i(t)\})$ in terms of the collective coordinates is given by

$$\dot{\mathbf{m}} = \sum_i \frac{\partial \mathbf{m}}{\partial \xi_i}\dot{\xi}_i. \tag{2.10}$$

This expression is plugged in the Landau-Lifshitz-Gilbert (2.3) and, subsequently, the equation is projected on the translation mode of the magnetic texture (see section 4.1 and Appendices B.2 for details).

The same approach can be applied also to collinear, two-sublattice antiferromagnets, where the time evolution of the Néel order parameter is specified in terms of a finite set of collective coordinates $\mathbf{n}(\mathbf{r},t) = \mathbf{n}(\mathbf{r},\{\xi_i(t)\})$ [61]. Details are discussed in section 4.1 and Appendix B.3.

2.2.3 Current-induced torques

The manipulation of magnetization by electric currents is a key topic within the spintronics field [1, 5, 6]. Here, we discuss briefly the relevant current-induced effects – spin-transfer torques and spin-orbit torques – from the point of view of phenomenology.

The non-relativistic spin-transfer torques originate from the conservation of angular momentum. They describe the effect, where a spin-polarized current can transfer angular momentum from the carriers to the magnetic moments of a ferromagnet and, thus, change their orientation [1]. We distinguish between two types of spin-transfer torques: homogeneous and inhomogeneous.

The homogeneous torques are found typically in nanostructures consisting of two magnetic layers separated by a spacer layer, where the current is flowing in the out-of-plane (OOP) direction of the layers. The electric current is polarized upon passing the first layer (called a polarizer) and exerts a torque on the magnetic moments of the second magnetic layer [2, 77]. Since the Landau-Lifshitz-Gilbert equation preserves the magnitude of the magnetization vectors, the current-induced torques need to be perpendicular to it

$$\begin{aligned} \tau_{\text{OOP,FL}} &= \alpha_{\text{OOP}}\mathbf{m}\times\mathbf{p}, \\ \tau_{\text{OOP,AD}} &= \beta_{\text{OOP}}\mathbf{m}\times\Big(\mathbf{m}\times\mathbf{p}\Big). \end{aligned} \tag{2.11}$$

Here, $\alpha_{\mathrm{OOP}}, \beta_{\mathrm{OOP}}$ are constants that need to be determined from microscopic calculations and $\mathbf{p}$ determines the polarization of the electric current. These terms are referred to as field-like and antidamping-like, respectively, due to the similarity of their expressions with the precession and damping terms in equation (2.3)[6].

The inhomogeneous torques appear when the electric current is applied in the in-plane (IP) direction of a magnetic layer, which contains an inhomogeneity such as a domain wall or a skyrmion. In that case, the spins of the conduction electrons change adiabatically according to the magnetization gradient and, at the same time, exert a torque on the magnetic moments of the magnetic layer due to the conservation of angular momentum [20]. These torques have the form

$$\begin{aligned} \tau_{\mathrm{IP,adiabatic}} &= \alpha_{\mathrm{IP}} \mathbf{m} \times (\mathbf{j} \cdot \nabla)\mathbf{m}, \\ \tau_{\mathrm{IP,non\text{-}adiabatic}} &= \beta_{\mathrm{IP}} (\mathbf{j} \cdot \nabla)\mathbf{m}, \end{aligned} \tag{2.12}$$

where $\mathbf{j}$ is the electric current. Here, the non-adiabatic term has been included phenomenologically to explain discrepancies with experimental findings [20, 79].

Recently, it was demonstrated that the spin-orbit coupling in a system can polarize electric currents even in the absence of inhomogeneities and magnetic polarizer layers [80]. The current-induced effects in systems with a strong spin-orbit coupling are called spin-orbit torques. An important difference to the spin-transfer torques is that the spin-orbit torque efficiency is not limited by the conservation of angular momentum (as for the spin-transfer torques). Here, there is the additional possibility to transfer linear momentum to spin angular momentum [44, 80].

A different setup, which also leads to the generation of spin-orbit torques, involves the spin-Hall effect in heavy-metal layers interfaced with magnetic layers [20]. Here, the spin-Hall effect generates a spin-polarized current that is injected vertically into the magnetic layer. The resulting spin-orbit torques are phenomenologically equivalent to the homogeneous spin-transfer torques in equation (2.11); however, the corresponding coefficients will be different due to the different microscopic mechanism.

By definition, the spin-orbit torques are homogeneous. In this work, we investigate thin films samples in which the inversion symmetry is broken in the out-of-plane direction. Therefore the spin-orbit torques have a similar form to the torques shown in equation (2.11):

$$\begin{aligned} \tau_{\mathrm{SOT,FL}} &= \alpha_{\mathrm{SOT}} \mathbf{m} \times (\mathbf{j} \times \hat{z}), \\ \tau_{\mathrm{SOT,AD}} &= \beta_{\mathrm{SOT}} \mathbf{m} \times \Big[\mathbf{m} \times (\mathbf{j} \times \hat{z}) \Big], \end{aligned} \tag{2.13}$$

where we have chosen the out-of-plane direction to be along the $\hat{z}$-axis. Importantly, the role of the spin-polarization $\mathbf{p}$ of the electric current is taken over by the cross product $\mathbf{j} \times \hat{z}$, which is fixed by the direction of inversion symmetry breaking [20].

---

[6] The antidamping-like torque is also referred to as Slonczewski torque [78].

2.3 Numerical techniques

Here, we present the method used to perform the numerical micromagnetic calculations. First, we list a few popular micromagnetic software packages and explain the differences to our approach. In section 2.3.1, we introduce the finite-element method: its principle, essential building blocks, solver methods, and relevant software packages used within this work. Finally, in section 2.3.2, we show the methods used to transform the Landau-Lifshitz-Gilbert equations into the form required by the finite-element method.

In this work, we use numerical simulations to investigate antiferromagnetic systems and compute the spectrum of excitations of antiferromagnetic skyrmions. Up to now, there is no software that is able to do either, in the way necessary for this work.

There are several established open-source codes in the micromagnetic community that focus on ferromagnetic systems. The most common are OOMMF [81], MicroMagnum [82] and mumax^3 [83], which are all based on the "standard" finite-difference method[7]. Advantages:

- OOMMF (C++): mature, reliable code with good documentation and extensibility;
- MicroMagnum (C++/Python): speed, efficiency and extensibility;
- mumax^3 (Go): fastest code, most efficient parallelization using graphics cards;

Disadvantages:

- OOMMF: slowest of the three in performance and to start using;
- MicroMagnum: not well documented;
- mumax^3: requires expensive hardware to harness its power.

None of these codes provide a direct solver that can compute the excitation spectrum for a given state.

In recent years, the finite-element method has been used to develop an extension of MicroMagnum, magnum.fe, for the numerical analysis of ferromagnetic structures [84, 85]. It relies on the same building blocks as our code for mesh generation (Gmsh) and the solution of the differential equations (FEniCS, see section 2.3.1).

2.3.1 Finite-element method

The finite-element method has been established as a universal method for the solution of partial differential equations. A defining strength of this method is its universality, as it makes it possible to solve a plethora of differential equations that reach from science to engineering and beyond. For the simulations in the present

---

[7] In the finite-difference method, differential equations are discretized on a regular grid and the derivatives are approximated by "finite differences".

work it offers a better description of three-dimensional thin-film samples. A good introduction into the subject can be found in references [86, 87]

We implement the finite-element method with the open-source platform FEniCS [86, 88]. Besides having a powerful finite-element engine, a key feature of FEniCS is its unified form language (UFL), which allows physical models to be implemented easily and in a notation similar to the mathematical one [89]. The software allows programs to be written in C++ and Python; the finite-element method is encoded in the software library DOLFIN [90].

Model

To demonstrate how the method works, we consider the Poisson equation, represented by the exchange term

$$\nabla^2 \mathbf{m} = \mathbf{B}_{\text{eff,FM}} \tag{2.14}$$

The equation is valid on a domain $V \subset \mathbb{R}^3$ and can be complemented by a set of Dirichlet (e.g. $\mathbf{m} = \mathbf{m}_0$ on $\Gamma_\text{D} \subset \partial V$) or Neumann ($-\partial_s \mathbf{m} = \mathbf{g}$ on $\Gamma_\text{N} = \partial V \backslash \Gamma_\text{D}$) boundary conditions for the solution $\mathbf{m}$ on the boundary ∂V of V.

To discretize the equation by the finite element method, we first multiply it by a test function $\mathbf{v}$ and integrate over the whole volume

$$-\int_V d^3r\, \nabla \mathbf{m} \cdot \nabla \mathbf{v} + \int_{\partial V} d^2r\ (\partial_s \mathbf{m}) \cdot \mathbf{v} = \int_V d^3r\, \mathbf{B}_{\text{eff,FM}} \cdot \mathbf{v}, \tag{2.15}$$

where ∂_s is the derivative in the direction normal to the surface ∂V, and we have performed integration by parts. Typically, the test function $\mathbf{v}$ is set to vanish on the boundary Γ_D.

Now, the original differential equation (2.14) has been transformed into a variational problem:

Find the trial function $\mathbf{u} \in T$, such that

$$\int_V d^3r\, \nabla \mathbf{u} \cdot \nabla \mathbf{v} = -\int_V d^3r\, \mathbf{B}_{\text{eff,FM}} \cdot \mathbf{v} - \int_{\partial V} d^2r\ (\partial_s \mathbf{u}) \cdot \mathbf{v}, \tag{2.16}$$

for $\forall \mathbf{v} \in \hat{T}$.

Here, the trial and test spaces are defined by

$$\begin{aligned} T &= \{v \in H^1(V) : v = u_0 \text{ on } \partial V\}, \\ \hat{T} &= \{v \in H^1(V) : v = 0 \text{ on } \partial V\}, \end{aligned} \tag{2.17}$$

respectively, and $H^1(V)$ is the Sobolev space containing functions v, for which v^2 and $|\nabla v|^2$ have finite integrals over V [86].

Next, we discretize the variational problem (2.16) onto a pair of discrete spaces. The goal is to find $\mathbf{u}_h \in T_h \subset T$, such that

$$\int_V d^3r\, \nabla \mathbf{u}_h \cdot \nabla \mathbf{v} = -\int_V d^3r\, \mathbf{B}_{\text{eff,FM}} \cdot \mathbf{v} - \int_{\Gamma_\text{N}} d^2r\ (\partial_s \mathbf{u}) \cdot \mathbf{v}, \tag{2.18}$$

for $\forall \mathbf{v} \in \hat{T}_h \subset \hat{T}$. The choice of the discrete spaces T_h and $\hat{T}_h$ is directly related to the type of finite elements chosen for the discretization.

Here, it is important to note that [86]

- the Dirichlet boundary condition enters directly into the definition of the trial space T_h (it is an "essential" boundary condition)
- the Neumann condition enters directly into the variational problem (it is a "natural" boundary condition).

We assume a basis $\{\phi_j\}_{j=1}^N$ for T_h and $\{\hat{\phi}_j\}_{j=1}^N$ for $\hat{T}_h$, were N denotes the dimension of each space. The discrete trial functions can be represented in the basis of the discrete trial space:

$$u_h^i(\mathbf{r}) = \sum_{j=1}^N U_j^i \phi_j^i(\mathbf{r}). \tag{2.19}$$

Here, i denotes the vector component index of $\mathbf{u}_h$ and $U \in \mathbb{R}^N$ is the vector containing the degrees of freedom. The finite-element method changes the target of finding the solution $\mathbf{m}$ of (2.14) to finding the vector U.

The discrete variational problem (2.18) can now be reformulated as

$$\sum_{j=1}^N U_j^i \int_V d^3r\, \nabla\phi_j^i \cdot \nabla\hat{\phi}_k^i = -\int_V d^3r\, B_{\text{eff,FM}}^i \hat{\phi}_k^i - \int_{\Gamma_\text{N}} d^2r\, g^i\, \phi_k^i, \tag{2.20}$$

for $k = 1, 2, \ldots, N$. Finally, the finite element solution u_h is obtained by solving the linear system

$$AU = b, \tag{2.21}$$

where

$$\begin{aligned} A_{kj} &= \int_V d^3r\, \nabla\phi_j \cdot \nabla\hat{\phi}_k, \\ b_k &= -\int_V d^3r\, B_{\text{eff,FM}}\hat{\phi}_k - \int_{\Gamma_\text{N}} d^2r\, g\, \phi_k. \end{aligned} \tag{2.22}$$

The whole procedure is summarized in Table 2.1.

General formulation

The variational problem (2.16) can be generalized to

$$a(\mathbf{u}, \mathbf{v}) = L(\mathbf{v}), \tag{2.23}$$

where the integrals are represented by a bilinear form a and a linear form (or, functional) L:

$$\begin{aligned} a &: T \times \hat{T} \to \mathbb{R}, \\ L &: \hat{T} \to \mathbb{R}. \end{aligned} \tag{2.24}$$

Step	Procedure	Function Space	Target
1	multiply by $\mathbf{v}$	$\mathbf{m} \in V \subset \mathbb{R}^3$ $\mathbf{v} \in \hat{T}$	$\mathbf{m}$
2	integrate over space; introduce $\mathbf{u} = \mathbf{m}$	$\mathbf{u} \in T$ $\mathbf{v} \in \hat{T}$	$\mathbf{u}$
3	discretize	$\mathbf{u}_h \in T_h \subset T$ $\mathbf{v} \in \hat{T}_h \subset \hat{T}$	$\mathbf{u}_h$
4	decompose in basis	$\{\phi_i\}_{i=1}^N$ $\{\hat{\phi}_i\}_{i=1}^N$	ϕ_i
5	solve linear system	$AU = b$	U

Table 2.1: *Procedure to use the finite-element method.*

The generalization of equation (2.20) becomes

$$\sum_{j=1}^{N} U_j a(\phi_j, \hat{\phi}_i) = L(\hat{\phi}_i), \tag{2.25}$$

and the target equation $AU = b$, is now defined by

$$\begin{aligned} A_{ij} &= a(\phi_j, \hat{\phi}_i), \\ b_i &= L(\hat{\phi}_i), \end{aligned} \tag{2.26}$$

for $i, j = 1, 2, \ldots, N$.

Function spaces and mesh

The finite-element method relies on finding discrete subspaces $T_h \subset T$ of infinite-dimensional function spaces.

To define the discrete space T_h, the domain V is divided into a finite set of cells $\mathcal{T}_h = \{C\}$ with disjoint interiors, such that $\cup_{C \in \mathcal{T}_h} C = V$. Typically, the cells are simple polygonal shapes like intervals, triangles, tetrahedra, etc. More information on different shapes can be found in reference [86]. Throughout this work, we focus on tetrahedra. All cells together form the mesh of the domain V.

The generation of a mesh and its discretization is done with Gmsh [8] [91].

What is a finite element?

The formal definition of a finite element necessitates introducing a local function space $\mathcal{V}$ on each cell C. A cell C, together with a local function space $\mathcal{V}$, and a set of rules for describing the functions in $\mathcal{V}$ is called a finite element [86]. Formally, a finite element is a triple $(C, \mathcal{V}, \mathcal{L})$, where:

---

[8] This software allows to create meshes using parametric input in Gmsh's own scripting language.

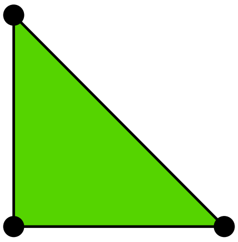

Figure 2.1: *Linear Lagrange triangle (finite element). The degrees of freedom are given by point evaluation at the three vertices of the triangle. Figure adapted from reference [86].*

- the domain C is a bounded, closed subset of $\mathbb{R}^d$ (for $d = 1, 2, 3, ...$) with nonempty interior and piecewise smooth boundary;
- the space $\mathcal{V} = \mathcal{V}(C)$ is a finite dimensional function space on C of dimension n;
- the set of degrees of freedom (nodes) $\mathcal{L} = \{l_1, l_2, \ldots, l_n\}$ is a basis for the space of bounded linear functionals on $\mathcal{V}$ (we call it $\mathcal{V}'$).

An example of the above definition is the standard linear Lagrange finite element[9] on the triangle in figure 2.1. The cell C is given by the triangle and the local function space $\mathcal{V}$ is the space of first degree polynomials on C (a space of dimension three). Point evaluation at the three vertices of C can be chosen as the basis for $\mathcal{V}'$.

Solvers

Having defined the finite elements and function spaces, the next step is to discretize the differential equations and solve the resulting algebraic system. This task can be difficult even for linear systems and solvers that can handle sparse and, possibly, ill-conditioned matrices have to be chosen.

Iterative Krylov methods are a common approach to solve linear equations of the type (2.21) [92]. Popular ones are the conjugate gradients (CG) and generalized minimal residual (GMRES) [93]. They generate a sequence of approximations converging to the solution of the linear system. These methods are based only on the matrix-vector product.

In this work we use the generalized conjugate residual method (GCR), which is equivalent to GMRES [93, 94], as well as the direct methods method called a lower-upper (LU) decomposition [86].

Each of the above mentioned methods can be made more efficient, by transforming the linear system

$$AU = b \tag{2.27}$$

into

$$P^{-1}AU = P^{-1}b, \tag{2.28}$$

---

[9] Within our code, the term "Continuous Galerkin" (CG, not to be confused with the Conjugate Gradient Krylov method) is used a synonym for the Lagrange finite element; see chapter 5.

which is known as preconditioning. To achieve good convergence the preconditioner P^{-1} should be a good approximation of A^{-1} [86].

All of the solvers mentioned here (together with a large number of preconditioners) are available in modern open-source numerical libraries. For the numerical simulations in this work, we use the "Portable, Extensible Toolkit for Scientific Computation" (PETSc) [95].

Finally, the visualization of magnetic structures and meshes in this work is done by using the open-source data analysis and visualization software Paraview [96]. The underlying data processing engine is the Visualization Toolkit (VTK) [97].

2.3.2 Relaxation and eigenspectrum solvers

Our code implements micromagnetic models for both a ferromagnet and an antiferromagnet to find an equilibrium state (relaxation solver) and the intrinsic dynamics of the latter (eigenspectrum solver). Here, we discuss both solvers in detail.

The relaxation solver employs an implicit projection method based on the Gauss-Seidel technique [98, 99, 100]. The main advantage is that the method is simple and unconditionally stable. It comes with the disadvantage of higher computational effort, which for our purposes is negligible. For more involved calculations, the higher computational cost is compensated by the increasing computing power of present-day computers and technologies like cloud computing.

The eigenspectrum solver calculates the frequencies and eigenstates of a slightly perturbed equilibrium state by considering the linearized dissipationless Landau-Lifshitz-Gilbert equation in frequency space [101]. The corresponding generalized eigenvalue problem is solved numerically by using the sparse eigenvalue problem solver (EPS) object within the "Scalable Library for Eigenvalue Problem Computations" (SLEPc) [102, 103, 104]. The possibility to integrate this approach with established numerical libraries, such as SLEPc, gives the advantage of fast calculation of the excitation modes of a given equilibrium state.

In the following, we describe the operation of both solvers on the example of the ferromagnet. For the antiferromagnet, the implementation is equivalent when the doubling of degrees of freedom is taken into account: we group the two sublattice-magnetization vectors of the antiferromagnet together in a single six-dimensional vector[10].

Projection method

We consider the general form of the Landau-Lifshitz-Gilbert equation with damping:

$$\dot{\mathbf{m}} = -\gamma \mathbf{m} \times \mathbf{B}_{\text{eff}} + \alpha_G \mathbf{m} \times \dot{\mathbf{m}} \tag{2.29}$$

where γ is the gyromagnetic ratio and α_G the Gilbert damping constant. Using the property $\mathbf{m}^2 = 1$, we can rewrite the equation as:

---

[10] Within our micromagnetic approach, both sublattice magnetization vectors of the two-sublattice antiferromagnet are assigned to a single point in the space (see section 3.3 for details).

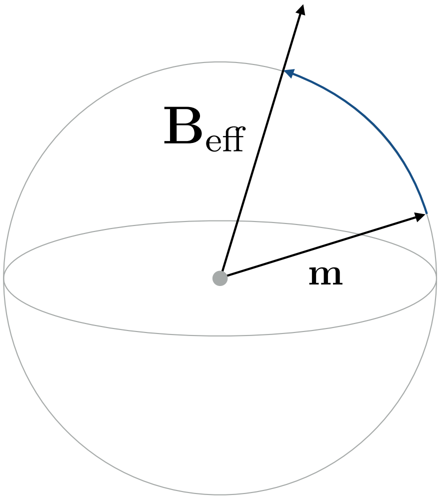

Figure 2.2: *Evolution of the magnetization vector* $\mathbf{m}$ *driven by the effective field* $\mathbf{B}_{\mathit{eff}}$*. The blue arrow represents the direct path on the unit sphere, which the magnetization vector follows within the projection method.*

$$\begin{aligned}
\dot{\mathbf{m}} &= -\gamma\mathbf{m}\times\mathbf{B}_{\text{eff}} + \alpha_G\mathbf{m}\times\Big[-\gamma\mathbf{m}\times\mathbf{B}_{\text{eff}} + \alpha_G\mathbf{m}\times\dot{\mathbf{m}}\Big] \\
&= -\gamma\mathbf{m}\times\mathbf{B}_{\text{eff}} - \gamma\alpha_G\Big[\mathbf{m}(\mathbf{m}\cdot\mathbf{B}_{\text{eff}}) - \mathbf{B}_{\text{eff}}\Big] - \alpha_G^2\dot{\mathbf{m}} \\
&= -\frac{\gamma}{1+\alpha_G^2}\mathbf{m}\times\mathbf{B}_{\text{eff}} - \frac{\gamma\alpha_G}{(1+\alpha_G^2)}\Big[\mathbf{m}(\mathbf{m}\cdot\mathbf{B}_{\text{eff}}) - \mathbf{B}_{\text{eff}}\Big] \qquad (2.30)
\end{aligned}$$

To simplify the notation, we introduce the rescaled gyromagnetic ratio $\gamma' = \gamma/(1+\alpha_G^2)$. A typical approach here is to study the overdamped regime ($\alpha_G \gg 1$), in which the precession term is neglected with respect to the damping term[11].

Within the projection method, we neglect both the precession term and the component of $\mathbf{B}_{\text{eff}}$ that is parallel to $\mathbf{m}$ – that is, the first two terms in equation (2.30). As a consequence, during each numerical step, the full effective field vector is added to the magnetization vector; this makes $\mathbf{m}$ relax straight to $\mathbf{B}_{\text{eff}}$ by taking the shortest route on the unit sphere, as shown in figure 2.2. The magnitude of $\mathbf{m}$ is fixed; therefore, to compensate for the neglected terms and fulfill the constraint $\mathbf{m}^2 = 1$, we normalize the magnetization vector $\mathbf{m}$ by hand during each step of the numerical calculation.

The equation that we are left with is

$$\begin{aligned}
\frac{1}{\alpha_G}\frac{d\mathbf{m}}{dt} &= \gamma'\mathbf{B}_{\text{eff}} \\
\frac{d\mathbf{m}}{dt'} &= \mathbf{B}_{\text{eff}}, \qquad (2.31)
\end{aligned}$$

where, we defined $t' = \gamma'\alpha_G\, t$.

---

[11] Formally, this is done by multiplying equation (2.30) by α_G, so that the second term on the right hand side remains finite after taking the limit $\alpha_G \to \infty$.

Next, we use an implicit first-order Runge-Kutta method to discretize the Landau-Lifshitz-Gilbert equation in time[12]

$$\frac{\mathbf{m}_{n+1} - \mathbf{m}_n}{\Delta t} = \gamma' \mathbf{B}_{\text{eff}}[\mathbf{m}_{n+1}], \tag{2.32}$$

where n and $n+1$ are the indices of the previous and current numerical step, respectively, and Δt is the time step. Reordering the terms brings us to

$$\mathbf{m}_{n+1} - \gamma' \Delta t \mathbf{B}_{\text{eff}}[\mathbf{m}_{n+1}] = \mathbf{m}_n. \tag{2.33}$$

We use a manual step-size control, where the step Δt is decreased once the observed error level $|\mathbf{m}_{n+1} - \mathbf{m}_n|$ is less than Δt^2. Convergence is reached when the error decreases below a specified value, which sets the precision of the algorithm. In that case the magnetization vector is aligned with the effective field (zero-torque condition), as can be seen in equation (2.31)

To proceed, we need to transform the partial differential equation (2.33) into a variational problem (see section 2.3.1). We do this by multiplying the whole equation by a test function $\mathbf{v}$, integrate over the volume V, and perform integration by parts on the term containing second-order derivatives. From here onwards, we denote the unknown function to be computed $\mathbf{m}_{n+1}$ by $\mathbf{u}$ and the previous-step magnetization vector $\mathbf{m}_n$ by $\mathbf{m}_0$. For simplicity, we cast equation (2.33) dimensionless by dividing it by the (reference) saturation field $B_\text{s} = \mu_0 M_\text{s}$

$$\frac{1}{B_\text{s}} \int_V d^3r \Big(\mathbf{u} \cdot \mathbf{v}\Big) - \frac{\gamma' \Delta t}{B_\text{s}} \int_V d^3r \Big(\mathbf{B}_{\text{eff}} \cdot \mathbf{v}\Big) = \frac{1}{B_\text{s}} \int_V d^3r \Big(\mathbf{m}_0 \cdot \mathbf{v}\Big). \tag{2.34}$$

Linearized Landau-Lifshitz-Gilbert equation

To obtain the eigenmodes of a magnetization texture described by $\mathbf{m}$, we consider small linear deviations $\delta\mathbf{m}$ from the equilibrium structure $\mathbf{m}_0$, defined by [101]

$$\mathbf{m}(t) = \mathbf{m}_0 + \delta\mathbf{m}(t), \tag{2.35}$$

with $|\delta\mathbf{m}| \ll 1$ and $\mathbf{m}_0 \cdot \delta\mathbf{m} = 0$. The latter condition ensures that the magnitude of the unit magnetization vector $\mathbf{m}$ does not change and all the excitations $\delta\mathbf{m}$ are transverse to it.

The intrinsic dynamics are given by the undamped Landau-Lifshitz-Gilbert equation (2.29)

$$\dot{\mathbf{m}} = -\gamma \mathbf{m} \times \mathbf{B}_{\text{eff}}, \tag{2.36}$$

which is defined within the volume V. Equation (2.36) is complemented by a boundary condition for $\partial\mathbf{m}/\partial S$[13] on the boundary ∂V (Γ_N, see section 2.3.1).

By definition, the equilibrium structure $\mathbf{m}_0$ does not have any dynamics

$$0 = \mathbf{m}_0 \times \mathbf{B}_{\text{eff}}[\mathbf{m}_0]. \tag{2.37}$$

---

[12] For simplicity, we denote the rescaled time again by t.

[13] If Dzyaloshinskii-Moriya interactions are present in the system, the boundary condition is non-trivial – see Appendix A.2 for details. If not, the condition is simply $\partial\mathbf{m}/\partial S = 0$.

The excitations $\delta\mathbf{m}$, on the other hand, do. Plugging the full magnetization vector (2.35) into the Landau-Lifshitz-Gilbert equation (2.36) and keeping terms up to first order in the deviations $\delta\mathbf{m}$ leads to

$$\begin{aligned}\delta\dot{\mathbf{m}} &\simeq -\gamma\mathbf{m}_0 \times \mathbf{B}_{\text{eff}}[\mathbf{m}_0 + \delta\mathbf{m}] - \gamma\delta\mathbf{m} \times \mathbf{B}_{\text{eff}}[\mathbf{m}_0] \\ &= -\gamma\mathbf{m}_0 \times \frac{\delta\mathbf{B}_{\text{eff}}[\mathbf{m}_0]}{\delta\mathbf{m}} - \gamma\delta\mathbf{m} \times \mathbf{B}_{\text{eff}}[\mathbf{m}_0], \end{aligned} \tag{2.38}$$

which is complemented by a boundary condition for the deviations vector $\partial\delta\mathbf{m}/\partial S$.

For the sake of simplicity, in the following we call $\mathbf{B}_{\text{eff}}[\delta\mathbf{m}] = \delta\mathbf{B}_{\text{eff}}[\mathbf{m}_0]/\delta\mathbf{m}$[14]. We perform a Fourier transform into frequency space, so that

$$i\omega\delta\mathbf{m} = -\gamma\mathbf{m}_0 \times \mathbf{B}_{\text{eff}}[\delta\mathbf{m}] - \gamma\delta\mathbf{m} \times \mathbf{B}_{\text{eff}}[\mathbf{m}_0] + \Lambda\left(\mathbf{m}_0 \cdot \delta\mathbf{m}\right)\mathbf{m}_0, \tag{2.39}$$

where

$$\delta\mathbf{m}(t) = \int_V d^3r\, e^{i\omega t}\delta\mathbf{m}(\omega), \tag{2.40}$$

and we have added the Lagrange multiplier Λ to ensure that only deviations that do no change the magnitude of $\mathbf{m}$ are considered (in other words, that the condition $\mathbf{m}_0 \cdot \delta\mathbf{m} = 0$ is not violated). It suffices to choose the value of Λ to be $10 - 100$ times the magnitude of the effective field $\mathbf{B}_{\text{eff}}$.

Next, we construct the weak formulation of the linearized Landau-Lifshitz-Gilbert equation (2.39). The resulting equation can be written in matrix form as (see Appendix A.1 for details)

$$-\frac{i\omega}{\gamma}\mathrm{M}\tilde{\mathbf{u}} = \mathrm{A}\tilde{\mathbf{u}}, \tag{2.41}$$

Equation (2.41) represents a generalized eigenvalue problem, which we solve numerically using the EPS object within SLEPc [102].

As can be seen directly from equation (2.41), to find the eigenfrequencies we need the imaginary components of the solver output. The eigenvectors $\tilde{\mathbf{u}}$ are also complex; however, the physical eigenmodes are real, so that we take

$$\begin{aligned}\delta\mathbf{m}(t) &= \mathrm{Re}\left\{\tilde{\mathbf{u}}e^{i\omega t}\right\} \\ &= \mathrm{Re}\left\{\Big(\mathrm{Re}\{\tilde{\mathbf{u}}\} + i\mathrm{Im}\{\tilde{\mathbf{u}}\}\Big)\Big(\cos(\omega t) + i\sin(\omega t)\Big)\right\} \\ &= \mathrm{Re}\left\{\mathrm{Re}\{\tilde{\mathbf{u}}\}\cos(\omega t) - \mathrm{Im}\{\tilde{\mathbf{u}}\}\sin(\omega t) + i\Big(\mathrm{Re}\{\tilde{\mathbf{u}}\}\sin(\omega t) + \mathrm{Im}\{\tilde{\mathbf{u}}\}\cos(\omega t)\Big)\right\} \\ &= \mathrm{Re}\{\tilde{\mathbf{u}}\}\cos(\omega t) - \mathrm{Im}\{\tilde{\mathbf{u}}\}\sin(\omega t). \end{aligned} \tag{2.42}$$

Due to the use of complex numbers for the representation of the deviations $\delta\mathbf{m}$ and their corresponding frequencies, the code gives as a result always a pair of eigenmodes with complex conjugated frequencies (that is, $i\omega$ and $-i\omega$). The real parts of the corresponding eigenvectors are the same.

---

[14] For effective fields that are linear in the magnetization vector $\mathbf{m}$ this relation is mathematically valid and not just a definition.

Chapter 3

Static skyrmion properties, confinement and shape effects in antiferromagnets

The magnetic skyrmions we consider in this work are stabilized due to the presence of Dzyaloshinskii-Moriya interactions in perpendicularly magnetized ultrathin films. The thickness of such films ranges typically from a few atomic layers to a few nm [21, 25, 36, 105]. Here, we focus on interfacial Dzyaloshinskii-Moriya interactions that are induced by a broken structural inversion symmetry in the out-of-plane direction. We do not consider bulk Dzyaloshinskii-Moriya interactions, which result from the interplay of broken crystal inversion symmetry and strong spin-orbit coupling is the system. Therefore, the skyrmions here are of Néel type (see figure 3.1) [20, 25].

For both ferromagnets and antiferromagnets we consider models that include exchange and interfacial Dzyaloshinskii-Moriya interactions, uniaxial anisotropy (in the out-of-plane direction) and an external magnetic field. We disregard the contributions of the demagnetization field – in ferromagnetic thin films it can be incorporated into an effective anisotropy term [26], and in antiferromagnets it is negligible due to the antiparallel alignment of the sublattice magnetizations [51][1].

The existence of skyrmions in such systems is an established fact theoretically – in ferromagnets the results of references [11, 12, 13, 24] and in antiferromagnets of reference [51] are all applicable to thin films. Experimentally, there is evidence in ferromagnets [21]. However, in antiferromagnets there has been no observation of skyrmions yet.

We consider an isolated skyrmion both in an infinite-plane setup and in a confined nanodisk, where the disk boundaries play an important role for the stability of the skyrmions. For the latter we follow the approach presented by Rohart *et al.* [26] for ferromagnets, and apply it to study the boundary effects on confined antiferromagnetic skyrmions.

This chapter is structured as follows. In section 3.1 we summarize the symmetry

---

[1] We refer to references [12, 73] for studies of the ferromagnetic skyrmion profile where the demagnetization field is taken into account. A model of a collinear antiferromagnet taking into account the demagnetization field is presented in reference [106], however, in the absence of Dzyaloshinskii-Moriya interactions.

of magnetic skyrmions and present the method to obtain analytically the skyrmion profile equation. Then, we present the phenomenological models, rederive the respective skyrmion profile equations and solve them numerically for both free and confined skyrmions – for ferromagnets in section 3.2 and antiferromagnets in section 3.3. We show the behaviour of the skyrmions as a function of the Dzyaloshinskii-Moriya constant and the external magnetic field, and discuss the differences between ferromagnets and antiferromagnets.

3.1 Introduction

Skyrmions are two-dimensional objects with a cylindrical symmetry – radially symmetric within the plane and translationally invariant in the out-of-the plane direction. For simplicity, we choose $\hat{z}$ as the out-of-plane direction. As a consequence, the skyrmion profile cannot have any dependence on the z coordinate. Magnetic textures with such a symmetry can be found primarily in noncentrosymmetric materials with Dzyaloshinskii-Moriya interactions [12, 51]. In the following, we consider equilibrium solutions of ferromagnetic and antiferromagnetic models of such materials by minimizing the corresponding energy functional.

To exploit the symmetry of skyrmions, it is convenient to parametrize the position vector in cylindrical coordinates

$$\mathbf{r} = \begin{pmatrix} \rho\cos\phi \\ \rho\sin\phi \\ z \end{pmatrix}, \tag{3.1}$$

and the magnetization vector (in the case of antiferromagnets, the Néel vector) in spherical coordinates

$$\mathbf{m}(\mathbf{r}) = \begin{pmatrix} \sin\theta(\rho)\cos\psi(\phi) \\ \sin\theta(\rho)\sin\psi(\phi) \\ \cos\theta(\rho) \end{pmatrix}. \tag{3.2}$$

Here, the angle ψ determines the type of skyrmion. Common examples are the Néel (also called hedgehog) skyrmion (see figures 3.1a and 3.1c)

$$\psi = \phi, \qquad \theta = \theta(\rho), \tag{3.3}$$

and the Bloch (also called vortex-like) skyrmion for which the azimuthal angle is shifted by $\Delta\psi = \pi/2$ (figures 3.1b and 3.1d)

$$\psi = \phi - \frac{\pi}{2}, \qquad \theta = \theta(\rho). \tag{3.4}$$

In the present work we are interested in the properties and dynamics of Néel skyrmions. Therefore, we do not discuss the vortex-like skyrmions in the following.

The main goal of this chapter is to obtain the skyrmion profile from both ferromagnetic and antiferromagnetic functionals of noncentrosymmetric materials.

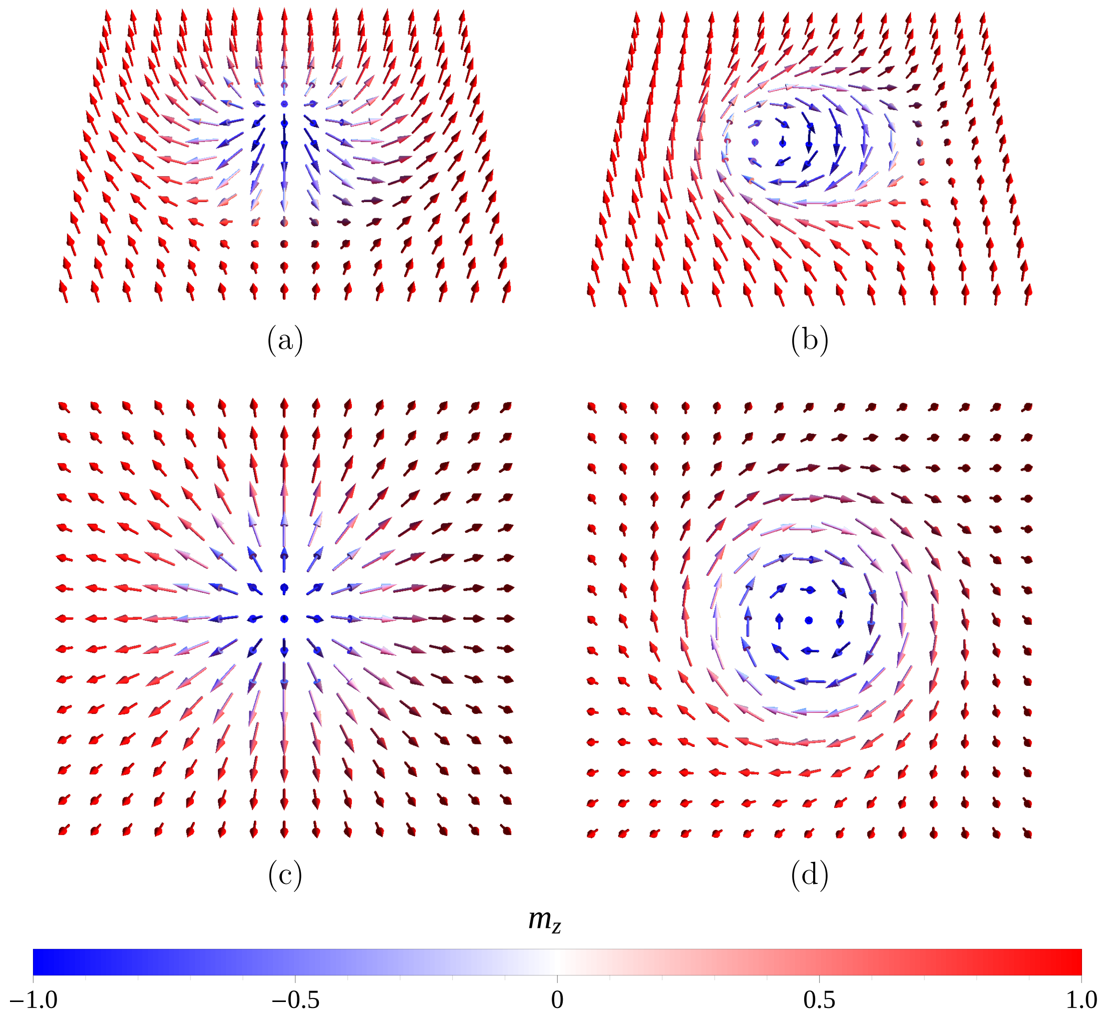
(a) (b)

(c) (d)

Figure 3.1: *Schematic representation of the Néel ("hedgehog") (a) side and (c) top view, and Bloch (vortex-like) skyrmions (b) and (d). In this work, we focus on skyrmions of the Néel type.*

We specify the energy functional of both systems and investigate its equilibrium skyrmion solutions by considering a steady state of the corresponding Landau-Lifshitz-Gilbert equation[2] This leads to a skyrmion profile equation, which determines the polar angle $\theta(\rho)$ of the magnetic texture (there is no dependence on the azimuthal angle $\psi(\phi)$ due to the rotational symmetry of the skyrmions around the $\hat{z}$-direction).

There is no analytical solution of the profile equation. Therefore, we solve it numerically by specifying the boundary conditions $\theta(\rho = 0) = \pi$ and $\theta(\rho \to \infty) = 0$. This corresponds to a skyrmion with negative polarity $p = -1$: the magnetization vector is pointing in the negative $\hat{z}$-direction in the skyrmion core and, in the positive $\hat{z}$-direction away from the skyrmion (see figure 3.1). The first condition is implemented as an initial condition of the differential profile equation. We use a

---

[2] Alternatively, this can be done by minimizing the energy functional with respect to the order parameter (magnetization vector $\mathbf{m}$ for ferromagnets and Néel vector $\mathbf{n}$ for antiferromagnets).

shooting method to find an initial value for $d\theta(\rho = 0)/d\rho$ that fixes the profile in a way that the second condition is fulfilled. In this chapter, we will investigate the skyrmion profile as a function of the Dzyaloshinskii-Moriya constant and the external magnetic field. Since the profile is sensitive to both parameters, the shooting method has to applied for each parameter set to find the value of $d\theta(\rho = 0)/d\rho$ that fulfills the condition $\theta(\rho \to \infty) = 0$.

The skyrmion is characterized by the topological charge

$$Q = \frac{1}{4\pi} \int dxdy\, \mathbf{m} \cdot \left(\frac{\partial \mathbf{m}}{\partial x} \times \frac{\partial \mathbf{m}}{\partial y} \right), \tag{3.5}$$

which can take values $Q = \pm 1$. For the boundary conditions chosen here the topological charge evaluates to $Q = -1$. In spherical coordinates equation (3.5) becomes (see Appendix B.2)

$$Q = \frac{1}{2} \int_0^\infty d\rho \left(\frac{d\theta}{d\rho} \right) \sin\theta. \tag{3.6}$$

Next, we introduce the phenomenological models for both ferromagnets and antiferromagnets, and discuss the static properties of the corresponding skyrmions.

3.2 Ferromagnets

Here, we discuss a generic ferromagnetic model, which contains exchange interactions, uniaxial anisotropy, external field and interfacial Dzyaloshinskii-Moriya interactions (consistent with the C_{nv} symmetry class). The demagnetization field (resulting from dipolar interactions) is disregarded in the following discussion. A more complete treatment can be found in reference [73] and the references therein.

3.2.1 Model

The energy functional of a ferromagnetic system that can host skyrmions in terms of the unit vector of the magnetization $\mathbf{m}(\mathbf{r})$ is [73]

$$\begin{aligned} F_{\mathrm{FM}} = \int d\mathbf{r} \Big\{ & A_{\mathrm{ex}} \left(\nabla \mathbf{m}\right)^2 + K_u M_{\mathrm{s}} \Big[1 - (\mathbf{m} \cdot \hat{z})^2\Big] - B M_{\mathrm{s}} \mathbf{m} \cdot \hat{z} \\ & - D \Big[(\hat{z} \cdot \mathbf{m})(\nabla \cdot \mathbf{m}) - (\mathbf{m} \cdot \nabla)(\hat{z} \cdot \mathbf{m})\Big] \Big\}, \end{aligned} \tag{3.7}$$

where A_{ex} is the exchange stiffness constant and represents the exchange interactions, K_u the magnetocrystalline anisotropy constant, D the Dzyaloshinskii-Moriya constant and we have set the external magnetic field B in the $\hat{z}$-direction. The corresponding effective field is found through equation (2.2) and reads

$$\mathbf{B}_{\mathrm{eff,FM}} = \frac{2A_{\mathrm{ex}}}{M_{\mathrm{s}}} \nabla^2 \mathbf{m} + 2K_u (\mathbf{m} \cdot \hat{z})\hat{z} + B\hat{z} + \frac{2D}{M_{\mathrm{s}}} \Big[\hat{z}(\nabla \cdot \mathbf{m}) - \nabla(\hat{z} \cdot \mathbf{m})\Big]. \tag{3.8}$$

The Landau-Lifshitz-Gilbert equation corresponding to this model is

$$\dot{\mathbf{m}} = -\gamma \mathbf{m} \times \mathbf{B}_{\text{eff,FM}} + \tau_{\text{Torques}}, \tag{3.9}$$

where τ_{Torques} are torques that any external perturbations might exert on the magnetization texture (see section 2.2.1).

3.2.2 Skyrmion profile

The energy functional in equation (3.7) allows for Néel skyrmions when the azimuthal angles of the magnetization vector and the radial vector match, $\psi = \phi$ (see section 3.1) [12, 73]. The skyrmion profile can be found by investigating the steady state of equation (3.9)

$$\mathbf{m}(\mathbf{r}) \times \mathbf{B}_{\text{eff,FM}}(\mathbf{r}) = 0. \tag{3.10}$$

Due to the cylindrical symmetry of the skyrmion, finding the profile is reduced to a one-dimensional problem given by the polar angle θ. We rewrite both the energy functional and effective field in spherical coordinates and plug in the parametrization of the magnetization vector (3.2) to find the profile equation. The energy functional becomes

$$\begin{aligned} F_{\text{FM}} = t \int_0^\infty d\rho\rho \int_0^{2\pi} d\phi \Bigg\{ A_{\text{ex}} \left[\left(\frac{d\theta}{d\rho} \right)^2 + \frac{\sin^2\theta}{\rho^2} \right] + K_u M_{\text{s}} \sin^2\theta \\ - B M_{\text{s}} \cos\theta - D \left[\frac{d\theta}{d\rho} + \frac{\sin\theta\cos\theta}{\rho} \right] \Bigg\}, \end{aligned} \tag{3.11}$$

and equation (3.10) transforms to

$$\frac{2A_{\text{ex}}}{M_{\text{s}}} \left[\frac{1}{\rho}\frac{d\theta}{d\rho} + \frac{d^2\theta}{d\rho^2} - \frac{\sin\theta\cos\theta}{\rho^2} \right] - 2K_u \sin\theta\cos\theta - B\sin\theta - \frac{2D}{M_{\text{s}}}\frac{\sin^2\theta}{\rho} = 0. \tag{3.12}$$

When discussing infinite films, it is useful to recast the model in dimensionless form. We introduce the characteristic lengthscale of the system x_0 (which can be interpreted as the domain wall width [12]) and the threshold value of the Dzyaloshinskii-Moriya constant[3]

$$\begin{aligned} x_0 &= \sqrt{\frac{A_{\text{ex}}}{K_u M_{\text{s}}}}, \\ D_0 &= \frac{4}{\pi}\sqrt{K_u M_{\text{s}} A_{\text{ex}}}, \end{aligned} \tag{3.13}$$

and rescale the radial coordinate to $\tilde{\rho} = \rho / x_0$. The rescaled profile equation becomes

$$\frac{d^2\theta}{d\tilde{\rho}^2} + \frac{1}{\tilde{\rho}}\frac{d\theta}{d\tilde{\rho}} - \frac{\sin\theta\cos\theta}{\tilde{\rho}^2} - \frac{4D}{\pi D_0}\frac{\sin^2\theta}{\tilde{\rho}} - \sin\theta\cos\theta - \eta\sin\theta = 0, \tag{3.14}$$

where $\eta = B/(2K_u)$. Details of the derivation of equation (3.14) can be found in Appendix B.1.

Parameter	Value	Unit
A_{ex}	15.0	$\mathrm{pJ\,m^{-1}}$
K_u	0.5	T
B	0.1	T
D	3.5	$\mathrm{mJ\,m^{-2}}$
M_{s}	1.0	$\mathrm{MA\,m^{-1}}$

Rescaled Parameter	Value	Unit
x_0	5.42	nm
η	0.10	–
D_0	3.52	$\mathrm{mJ\,m^{-2}}$
D/D_0	0.99	–
ξ_{FM}	8.60	nm

Table 3.1: *Typical parameters of perpendicularly magnetized ferromagnetic materials that can host skyrmions [26, 36] Listed are the constants that enter the energy functional in equation (3.7) directly, as well as the rescaled parameters that appear in the profile equations (3.14) and (3.15).*

Next, we solve the skyrmion profile equation (3.14) numerically by using the shooting method, as described in section 3.1. We choose a skyrmion with core polarity $p = -1$, that is, a texture with the boundary conditions $\theta(\tilde{\rho} = 0) = \pi$ and $\theta(\tilde{\rho} \to \infty) = 0$ and investigate the shape of the profile for different values of the parameters D/D_0 and η. Typical parameters of ferromagnetic materials, which host skyrmions and the corresponding effective parameters are listed in Table 3.1.

The zero-field skyrmion solution $\theta(\tilde{\rho})$ of equation (3.14) for $D/D_0 = 0.9$ is shown in figure 3.2. We show both the skyrmion profile as $m_z = \cos\theta(\tilde{\rho})$ and the entire magnetization vector $\mathbf{m}$, defined in equation (3.2), in a region of dimensions 5×5 around the infinite-plane skyrmion.

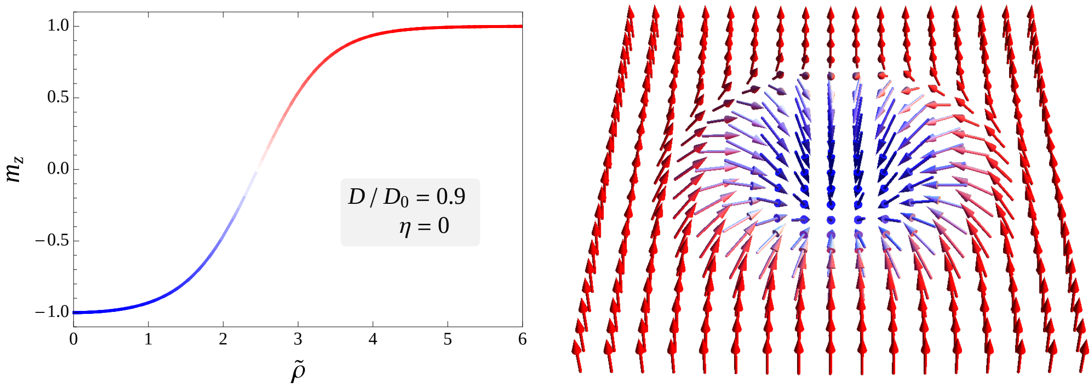

(a) (b)

Figure 3.2: *Isolated ferromagnetic skyrmion on an infinite plane. Shown is the numerical solution of equation (3.14) for $D/D_0 = 0.9$ and $\eta = 0$: (a) m_z and (b) full magnetization vector $\mathbf{m}$ on a 5×5 (in units of $\tilde{\rho}$) grid centered around the skyrmion. The color code represents the value of m_z, as defined in (a). The topological charge of the shown skyrmion evaluates to $Q = -1$.*

---

[3] The domain wall energy for a system with Dzyaloshinskii-Moriya interactions is given by $\sigma_{\mathrm{DW}} = 4\sqrt{A_{\mathrm{ex}} K_u M_{\mathrm{s}}} \mp \pi D$. Equation (3.13) defines the critical value of D, for which the domain wall energy goes to zero [12, 26].

The skyrmion profile depends strongly on the strength of the Dzyaloshinskii-Moriya interactions and the external magnetic field. In infinite planes, a skyrmion at zero magnetic field can be stabilized as long as $D < D_0$ [24, 26]. For typical ferromagnets this amounts to a critical Dzyaloshinskii-Moriya constant of $\sim 3.5\,\mathrm{mJ\,m^{-2}}$ (see Table 3.1).

We show both $\theta(\tilde{\rho})$ and $m_z(\tilde{\rho})$ for the skyrmion with negative polarity $p = -1$ as a function of D/D_0 in figure 3.3. The skyrmion grows with increasing D. For the chosen configuration, the magnetization vector makes a full π rotation from $\theta(0) = \pi$ to $\theta(\infty) = 2\pi$ as shown in figure 3.3a. The chirality of the skyrmion is fixed by the sign of D – in the analysis here we have a negative sign, as shown in equation (3.7). Choosing the opposite sign for D reverses the rotation from $\theta(0) = \pi$ to $\theta(\infty) = 0$, without a change to m_z in figure 3.3b[4].

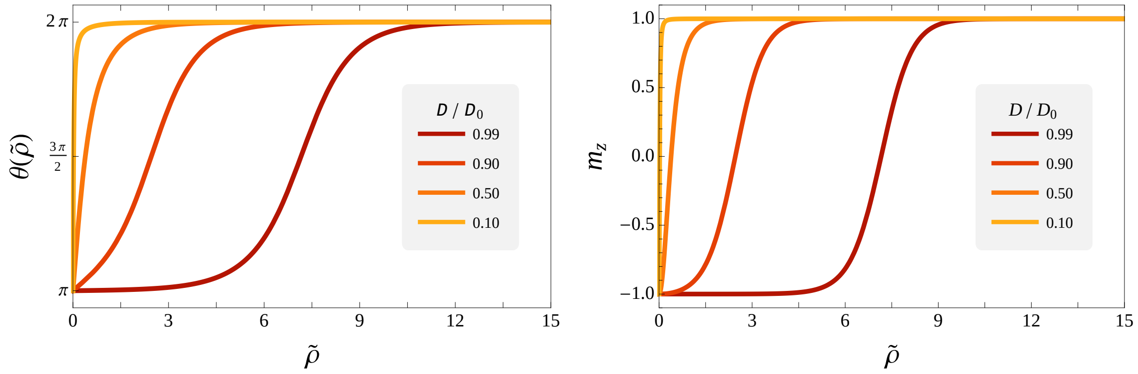

(a) (b)

Figure 3.3: *Profile of the ferromagnetic skyrmion for different values of the Dzyaloshinskii-Moriya constant and zero external field: (a) polar angle* $\theta(\tilde{\rho})$ *and (b)* m_z. *See Table 3.2 for a list of the corresponding values of* D.

$D(\mathrm{mJ\,m^{-2}})$	D/D_0	$\xi_{\mathrm{FM}}(\mathrm{nm})$
5.28	1.50	5.68
4.23	1.20	7.10
3.49	0.99	8.60
3.17	0.90	9.47
1.76	0.50	17.04
0.35	0.10	85.19

$D(\mathrm{mJ\,m^{-2}})$	D/D_0	$\xi_{\mathrm{AFM}}(\mathrm{nm})$
10.56	1.50	5.68
8.45	1.20	7.10
6.98	0.99	8.60
6.34	0.90	9.47
3.52	0.50	17.04
0.70	0.10	85.19

Table 3.2: *Different values of the Dzyaloshinskii-Moriya constant and the corresponding rescaled parameters for the ferromagnet in equations (3.14) and (3.15), and for the antiferromagnet in equations (3.32) and (3.34)**.

* The difference in D by a factor of two is an artefact of the definition of the energy functionals in equations (3.7) and (3.24).

---

[4] See figure 3.1 for a schematic representation of a Néel skyrmion with the opposite sign of D.

Next, we briefly sketch the effect of the external magnetic field on the ferromagnetic skyrmion. For visualization purposes, we fix $D/D_0 = 0.99$ to start with a larger skyrmion (see figure 3.3) and solve the profile equation for different values of η[5]. We show both $\theta(\tilde{\rho})$ and $m_z(\tilde{\rho})$ for the $p = -1$ skyrmion in figure 3.4. Due to the Zeeman coupling in the energy functional (3.11), the profile is sensitive to the direction of the external magnetic field. For positive B the preferred direction for the magnetization vector is along the $\hat{z}$-axis. Since $\mathbf{m}$ is antiparallel to $\hat{z}$ at the skyrmion core, with increasing external field the skyrmions shrinks. This effect is shown in figure 3.4. If B is chosen negative, then the effect is reversed and the skyrmion grows.

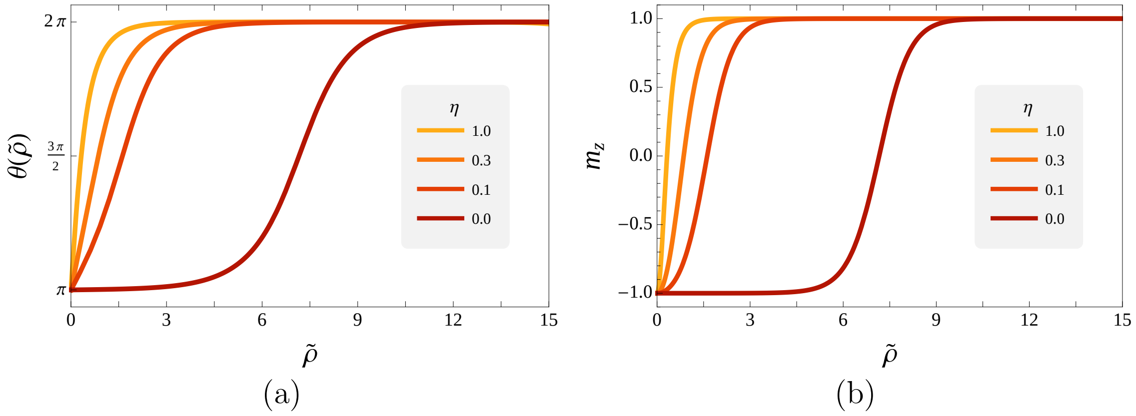

(a) (b)

Figure 3.4: *Ferromagnetic skyrmion profile for* $D/D_0 = 0.99$ *(see figure 3.3) and different values of the external magnetic field, where* $\eta = B/(2K_u)$. *The profile is obtained from the numerical integration of equation (3.14): (a) polar angle* $\theta(\tilde{\rho})$ *and (b) z-component of the skyrmion magnetization vector. See Table 3.3 for the corresponding values of* B.

B(T)	η	B^2/B_0^2
1.0	1.0	5.6×10^{-3}
0.3	0.3	5.0×10^{-4}
0.1	0.1	5.6×10^{-5}

B(T)	B^2/B_0^2	η
10	0.54	9.80
5	0.13	4.90
3	0.05	2.94
2	0.02	1.96
1	0.005	0.98

Table 3.3: *Different values of the external magnetic field and the corresponding rescaled parameters –* η *for the ferromagnet in equations (3.14) and (3.15), and* B^2/B_0^2 *for the antiferromagnet in equations (3.32) and (3.34). The values listed on the left are used for the ferromagnet in figures 3.4 and 3.7 and the ones one the right, for the antiferromagnet in figures 3.11 and 3.13.*

---

[5] The external field B is directly proportional to the dimensionless parameter η. For the present set of parameters (see Table 3.1) a value of $\eta = 1.0$ corresponds to $B = 1\,\mathrm{T}$.

Confined ferromagnetic skyrmions

Recently, Rohart *et al.* [26] showed that skyrmions confined in finite samples have different properties compared to skyrmions in infinite samples. The origin of this difference are the Dzyaloshinskii-Moriya interactions and the canting that they induce at the sample boundaries. Specifically, the volume energies of the model discussed in section 3.2 conspire to form a "natural" boundary condition that is clearly irrelevant in infinite samples. However, an important consequence of this boundary condition in nanostructures is that no uniform state is possible when Dzyaloshinskii-Moriya interactions are present.

To reproduce this effect, we rederive the steady-state Landau-Lifshitz-Gilbert equation (3.10) by applying a variational principle on the energy functional (3.7). Details are shown in Appendix A.2. The benefit of this approach is that, besides the volume terms already taken into account in equation (3.14), we obtain also the corresponding surface terms relevant for finite samples.

This procedure gives the exact same skyrmion profile equation as shown in equation (3.14). Since we are discussing nanostructures, it is beneficial not to rescale the equation and rewrite it in terms of the radial coordinate ρ (see also Appendix B.1)

$$\frac{d^2\theta}{d\rho^2} + \frac{1}{\rho}\frac{d\theta}{d\rho} - \sin\theta\cos\theta\left(\frac{1}{\rho^2} + \frac{1}{x_0^2}\right) - \frac{2}{\xi_{\mathrm{FM}}}\frac{\sin^2\theta}{\rho} - \frac{\eta}{x_0^2}\sin\theta = 0, \qquad (3.15)$$

where x_0 is the same characteristic domain wall width as before and $\xi_{\mathrm{FM}} = 2A_{\mathrm{ex}}/D$ is the characteristic length of the cycloid state [12, 26, 107]. The surface terms

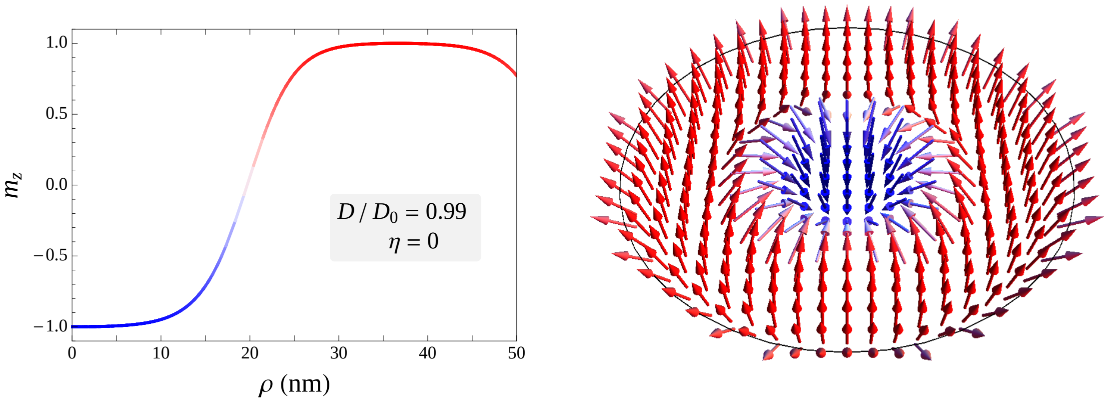

(a) (b)

Figure 3.5: *Ferromagnetic skyrmion confined in a nanodisk of* $R_{disk} = 50\,\mathrm{nm}$. *Shown is the numerical solution of equations (3.15-3.16) for parameters* $\eta = 0$, $x_0 = 5.42\,\mathrm{nm}$ *and* $\xi_{FM} = 8.60\,\mathrm{nm}$, *which correspond to for* $D/D_0 = 0.99$*: (a)* m_z *and (b) full magnetization vector* $\mathbf{m}$ *with the boundary of the nanodisk (black circle). The color code represents the value of* m_z*, as defined in (a). The topological charge of the shown confined skyrmion evaluates to* $Q = -0.89$*, as a result of the canting at the nanodisk boundaries.*

contribute the "natural" boundary condition (see Appendix A.2)

$$\left(\frac{d\theta}{d\rho}\right)_{\text{boundary}} = \frac{1}{\xi_{\text{FM}}}. \tag{3.16}$$

We solve equation (3.15) numerically on a finite nanodisk of radius $R_{\text{disk}} = 50\,\text{nm}$ by using a shooting method, as discussed earlier. The difference here is that we do not aim to fulfill the condition $\theta(\rho \to \infty) = 0$, but instead do so for the modified boundary condition $\theta'(\rho = R_{\text{disk}}) = 1/\xi_{\text{FM}}$.

We show the zero-field confined skyrmion in figure 3.5 for $x_0 = 5.42\,\text{nm}$ and $\xi_{\text{FM}} = 8.60\,\text{nm}$, which corresponds to $D/D_0 = 0.99$ for the infinite-plane skyrmion. The main difference here is the canting that occurs at the sample edges (compare to figure 3.2[6]). The chirality of the canting is again determined by the sign of the Dzyaloshinskii-Moriya constant – for negative D the canting at the edges is outwards and for positive D, inwards.

Another important difference is the improved stability of the confined skyrmion. Due to the confining potential at the edges, it is possible to stabilize skyrmions even for $D > D_0$, whereas in the same range isolated infinite-plane skyrmions transform to cycloids or skyrmion lattices [24, 26].

We show the zero-field confined skyrmion profile for different values of the Dzyaloshinskii-Moriya constant in figure 3.6, where profiles corresponding to $D < D_0$ are depicted in warm colors and the profiles with $D > D_0$, in cool colors. The larger skyrmions resemble magnetic bubbles in the sense that there are extended regions

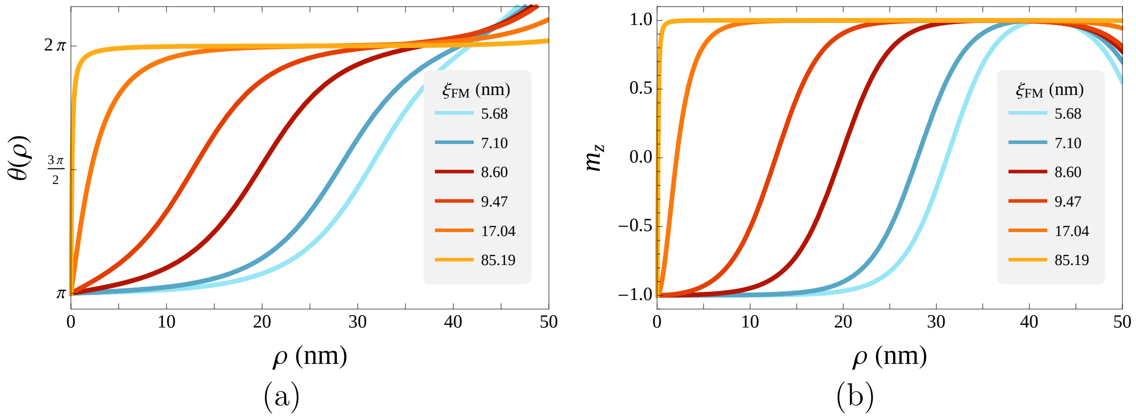

Figure 3.6: *Confined ferromagnetic skyrmion for different values of the Dzyaloshinskii-Moriya constant and zero external field: (a) polar angle* $\theta(\rho)$ *and (b) z-component of the skyrmion magnetization vector. Warm colors depict skyrmion profiles for which* $D < D_0$ *and cool colors,* $D > D_0$*. In both figures we use* $x_0 = 5.42\,\text{nm}$*. See also figure 3.5 for a visualization of the skyrmion with* $\xi_{FM} = 8.60\,\text{nm}$ *and Table 3.2 for a list of the corresponding values of* D*.*

---

[6] For visualization purposes, we show in figure 3.5 a confined skyrmion with parameters corresponding to $D/D_0 = 0.99$, whereas in figure 3.2 we showed an infinite-plane skyrmion for $D/D_0 = 0.9$. Here, we compare qualitatively the profiles of the confined and infinite-plane skyrmions, so that this difference in parameters is irrelevant.

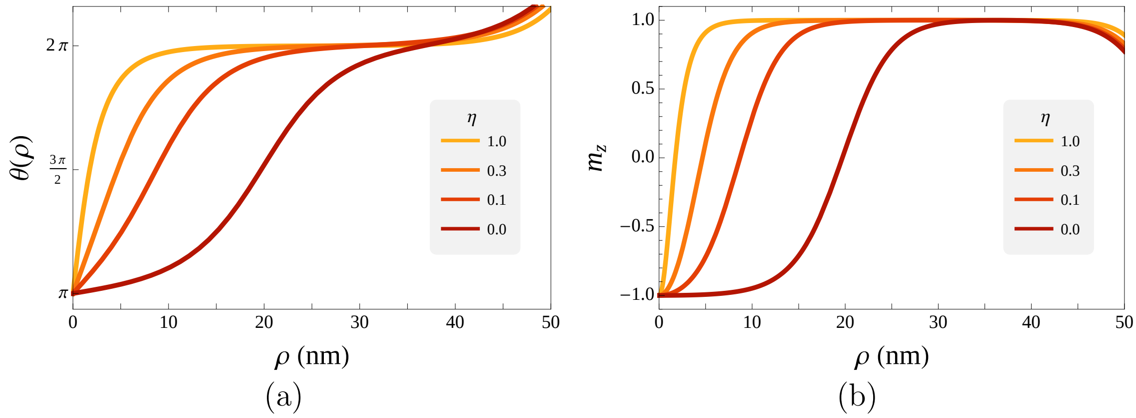

Figure 3.7: *Confined ferromagnetic skyrmion for* $\xi_{FM} = 8.60\,\mathrm{nm}$*,* $x_0 = 5.42\,\mathrm{nm}$ *and different values of the external magnetic field: (a) polar angle* $\theta(\rho)$ *and (b) z-component of the skyrmion magnetization vector. Shown is the numerical solution of equations (3.15-3.16). The choice of* ξ_{FM} *corresponds to* $D/D_0 = 0.99$ *(see figure 3.4). See also Table 3.3 for the corresponding values of the magnetic field.*

with $m_z = \pm 1$ separated by a continuous change of the magnetization vector. In the regime $D < D_0$ the skyrmion does not feel the confining potential of the edges and its radius is fixed by the value of D. In contrast, for $D > D_0$ the skyrmion size is determined entirely by the nanodisk radius, as long as the latter is not too large compared to the cycloid length $L_0 = 2\pi\xi_{\mathrm{FM}}$. If it is, then a single skyrmion cannot be stabilized and states with a larger rotation of the magnetization vector solve the profile equation [26].

The canting at the edges for the confined skyrmion is evident in figure 3.6 and increases with increasing D. Contrary to the infinite-plane skyrmion, the magnetization vector here makes a rotation larger than π (see figure 3.6a), which also leads to the fact that the topological charge defined in equations (3.5-3.6) does not equal one for confined skyrmions. For the skyrmion shown in figure 3.5 it amounts to $Q = -0.89$.

For comparison with the infinite-plane skyrmion (figure 3.4), we plot the profile of the confined skyrmion as a function of the external magnetic field in figure 3.7. Apart from the canting at the edges, the behaviour of both skyrmions is qualitatively similar as far as the present work is concerned.

3.3 Antiferromagnets

In this section, we consider a generic model for a collinear two-sublattice antiferromagnet. We investigate the interplay of the exchange interactions, uniaxial magnetocrystalline anisotropy, external magnetic field and interfacial Dzyaloshinskii-Moriya interactions. Stray field effects are neglected, as they are expected to be small due to the antiparallel alignment of the magnetization vectors. A detailed discussion of the demagnetization (stray field) effects in antiferromagnets can be found in reference [106].

3.3.1 Model

We consider a two-sublattice antiferromagnet within the exchange approximation with the sublattice magnetizations $\mathbf{M}_1 \simeq -\mathbf{M}_2$ and $|\mathbf{M}_1| = |\mathbf{M}_2| = M_\mathrm{s}$, where M_s is the saturation magnetization [51, 65]. We assume that the temperature is low enough, so that the magnitude of the magnetization vectors M_s does not change. This allows us to work with the unit vectors $\mathbf{m}_1 = \mathbf{M}_1/M_\mathrm{s}$ and $\mathbf{m}_2 = \mathbf{M}_2/M_\mathrm{s}$ in the following.

Our phenomenological approach is based on the exchange approximation [65], which requires rotational invariance of the magnetization vectors and invariance of the theory with respect to an exchange of the two sublattices. As a result, the energy functional has to be invariant under the transformations $\mathbf{M}_1 \to \mathbf{M}_2$ and $\mathbf{M}_2 \to \mathbf{M}_1$.

The sample of interest is a thin two-dimensional film with structural inversion asymmetry along the $\hat{z}$-direction, due to the presence of an interface. This structure is captured by the crystallographic class C_{nv} [7]

In terms of the two sublattices

Following reference [51], the model we consider is[8]

$$\begin{aligned} F_\mathrm{AFM} = \int d^3r \Bigg\{ & A\Big[(\nabla\mathbf{m}_1)^2 + (\nabla\mathbf{m}_2)^2\Big] + B_\mathrm{exch}M_\mathrm{s}\left(\mathbf{m}_1\cdot\mathbf{m}_2\right) \\ & - \frac{B_\mathrm{an}M_\mathrm{s}}{2}\Big[(\mathbf{m}_1\cdot\hat{z})^2 + (\mathbf{m}_2\cdot\hat{z})^2\Big] - BM_\mathrm{s}\Big[(\mathbf{m}_1\cdot\hat{z}) + (\mathbf{m}_2\cdot\hat{z})\Big] \\ & - B_\mathrm{d}M_\mathrm{s}\Big[\mathbf{m}_1\times\mathbf{m}_2\Big]\cdot\hat{z} + f_\mathrm{DM,surface}\Bigg\}. \end{aligned} \tag{3.17}$$

Here, the constant B_an describes the inhomogeneous exchange interaction and B_exch, the homogeneous exchange interaction. A uniaxial magnetocrystalline anisotropy is captured by the constant B_an and B denotes the external magnetic field. Both are set in the $\hat{z}$-direction. The Dzyaloshinskii-Moriya interactions are described by a homogeneous term B_d (which is the origin of weak ferromagnetism [51, 108]) and an inhomogeneous term[9]

$$f_\mathrm{DM} = -\frac{D}{4}\Bigg\{\Big[(\mathbf{m}_1-\mathbf{m}_2)\cdot\hat{z}\Big]\Big[\nabla\cdot(\mathbf{m}_1-\mathbf{m}_2)\Big] - (\mathbf{m}_1-\mathbf{m}_2)\cdot\nabla\Big[(\mathbf{m}_1-\mathbf{m}_2)\cdot\hat{z}\Big]\Bigg\}. \tag{3.18}$$

The latter part is the main ingredient needed to stabilize a skyrmion in this system and inhomogeneous textures in general [51]. Equation (3.18) is the antiferromagnetic generalization of the Dzyaloshinskii-Moriya functional in equation (3.7) [12, 51].

---

[7] This class describes also materials with non-centrosymmetric crystal lattices (an example of such an antiferromagnet is $K_2V_3O_8$ [51]).

[8] In the present work we disregard the exchange and anisotropy terms involving both sublattices, as they do not significantly affect the results. The full model can be found in reference [51].

[9] See also the discussion on Lifshitz invariants in section 2.2.1 and equations (2.8-2.9).

Due to the macroscopic nature of the phenomenological model, to every point $\mathbf{r}$ in space magnetization vectors of both sublattices $\mathbf{m}_1(\mathbf{r})$ and $\mathbf{m}_2(\mathbf{r})$ are assigned. This leads to the distinction between homogeneous terms (representing interaction between magnetization vectors at the same point in space) and inhomogeneous terms (interaction between magnetization vectors at different points in space) in the energy functional (see figure 3.8). Consequently, the inhomogeneous terms always contain gradients.

The Landau-Lifshitz-Gilbert equations for both magnetic sublattices are[10]

$$\begin{aligned} \dot{\mathbf{m}}_1 &= -\gamma \mathbf{m}_1 \times \mathbf{B}^{\mathrm{AFM}}_{\mathrm{eff},1}, \\ \dot{\mathbf{m}}_2 &= -\gamma \mathbf{m}_2 \times \mathbf{B}^{\mathrm{AFM}}_{\mathrm{eff},2}, \end{aligned} \tag{3.19}$$

which are coupled through the effective fields

$$\begin{aligned} \mathbf{B}^{\mathrm{AFM}}_{\mathrm{eff},1} &= \frac{2A}{M_{\mathrm{s}}}\nabla^2\mathbf{m}_1 - B_{\mathrm{exch}}\mathbf{m}_2 + B_{\mathrm{an}}(\mathbf{m}_1\cdot\hat{z})\hat{z} + B\hat{z} + B_{\mathrm{d}}(\mathbf{m}_2\times\hat{z}) + \mathbf{B}^{\mathrm{AFM}}_{\mathrm{DM}}, \\ \mathbf{B}^{\mathrm{AFM}}_{\mathrm{eff},2} &= \frac{2A}{M_{\mathrm{s}}}\nabla^2\mathbf{m}_2 - B_{\mathrm{exch}}\mathbf{m}_1 + B_{\mathrm{an}}(\mathbf{m}_2\cdot\hat{z})\hat{z} + B\hat{z} - B_{\mathrm{d}}(\mathbf{m}_1\times\hat{z}) - \mathbf{B}^{\mathrm{AFM}}_{\mathrm{DM}}, \end{aligned} \tag{3.20}$$

with the Dzyaloshinskii-Moriya field

$$\mathbf{B}^{\mathrm{AFM}}_{\mathrm{DM}} = \frac{D}{2M_{\mathrm{s}}}\left[\hat{z}\Big(\nabla\cdot(\mathbf{m}_1-\mathbf{m}_2)\Big) - \nabla\Big((\mathbf{m}_1-\mathbf{m}_2)\cdot\hat{z}\Big)\right]. \tag{3.21}$$

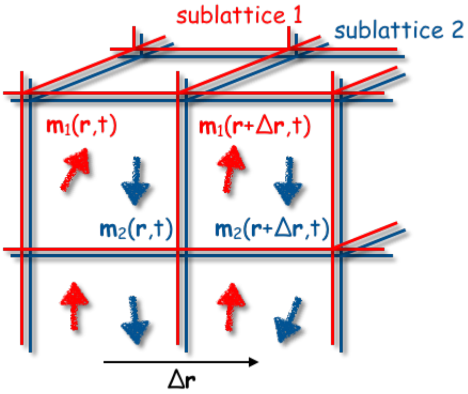

Figure 3.8: *Schematic representation of the coarse graining within the antiferromagnetic phenomenological model. The sublattice magnetizations* $\mathbf{m}_1$ *(depicted red) and* $\mathbf{m}_2$ *(blue) are macroscopic quantities and – due to the averaging over space – are both assigned to every point* $\mathbf{r}$ *in space. This leads to the appearance of homogeneous (*$\mathbf{m}_1, \mathbf{m}_2$ *at the same point in space) and inhomogeneous interaction terms (*$\mathbf{m}_1, \mathbf{m}_2$ *at different points in space, e.g.,* $\mathbf{r}$ *and* $\mathbf{r}+\Delta\mathbf{r}$*).*

---

[10] We disregard damping terms and current-induced torques for the present discussion regarding the static skyrmion profile.

In terms of the order parameter

For the analytical treatment, it is more convenient to formulate the theory in terms of the antiferromagnetic order parameter (also called the Néel vector)

$$\mathbf{n} = \frac{\mathbf{m}_1 - \mathbf{m}_2}{2}, \tag{3.22}$$

and the total magnetization

$$\mathbf{m} = \frac{\mathbf{m}_1 + \mathbf{m}_2}{2}. \tag{3.23}$$

See figure 3.9 for a schematic representation. In the following, we will refer to $\mathbf{n}$ and $\mathbf{m}$ as the antiferromagnetic vectors. Here, the invariance of the theory with respect to an exchange of the two sublattices translates to invariance under the transformations $\mathbf{n} \to -\mathbf{n}$ and $\mathbf{m} \to \mathbf{m}$.

The magnetic energy in terms of the antiferromagnetic vectors follows directly from equations (3.17) and (3.22-3.23)[11] [51, 65]

$$\begin{aligned} F_{\mathrm{AFM}} = \int d\mathbf{r} \Big\{ & 2A\,(\nabla \mathbf{n})^2 + 2B_{\mathrm{exch}} M_{\mathrm{s}} \mathbf{m}^2 - B_{\mathrm{an}} M_{\mathrm{s}} (\mathbf{n}\cdot\hat{z})^2 - 2BM_{\mathrm{s}}(\mathbf{m}\cdot\hat{z}) \\ & + 2B_{\mathrm{d}} M_{\mathrm{s}} (\mathbf{m}\times\mathbf{n})\cdot\hat{z} - D\Big[(\hat{z}\cdot\mathbf{n})(\nabla\cdot\mathbf{n}) - (\mathbf{n}\cdot\nabla)(\hat{z}\cdot\mathbf{n})\Big]\Big\}. \end{aligned} \tag{3.24}$$

The first and the second terms describe the inhomogeneous and homogenous exchange interaction with the constants A and B_{exch}, respectively. The uniaxial anisotropy is parameterized by the constant $B_{\mathrm{an}} > 0$ and the external magnetic field is denoted by B. The remaining terms describe the Dzyaloshinskii-Moriya interactions, where B_{d} and D represent the homogeneous (pointing in the $\hat{z}$-direction) and inhomogeneous parts, respectively.

The antiferromagnetic vectors obey the constraints $\mathbf{n}^2 = 1$ and $\mathbf{n}\cdot\mathbf{m} = 0$. Throughout this work we make the assumption that the homogeneous exchange interaction B_{exch} is the dominant energy scale, so that $B_{\mathrm{exch}} \gg B_{\mathrm{d}}, B_{\mathrm{an}}$. For typical values of the external magnetic field that do not destroy the antiferromagnetic order the exchange constants dominates the field too, $B_{\mathrm{exch}} \gg B$ [47].

Figure 3.9: *Schematic representation of the antiferromagnetic vectors: sublattice vectors* $\mathbf{m}_1$ *and* $\mathbf{m}_2$*, and Néel vector* $\mathbf{n}$ *and total magnetization* $\mathbf{m}$ *(not to scale).*

---

[11] The energy functional seems to satisfy the $C_{\infty v}$ symmetry group, however, the discrete symmetry origin of the antiferromagnetic vectors needs to be respected, which lowers the symmetry to C_{nv}.

To leading order in B_{exch} the corresponding Landau-Lifshitz-Gilbert equations take the form

$$\begin{aligned}\dot{\mathbf{n}} &= \gamma\Big[\mathbf{n}\times\mathbf{B}^{\text{AFM}}_{\text{eff},\mathbf{m}}\Big]+\tau_{\mathbf{n}},\\ \dot{\mathbf{m}} &= \gamma\Big[\mathbf{n}\times\mathbf{B}^{\text{AFM}}_{\text{eff},\mathbf{n}}+\mathbf{m}\times\mathbf{B}^{\text{AFM}}_{\text{eff},\mathbf{m}}\Big]+\tau_{\mathbf{m}},\end{aligned} \tag{3.25}$$

where $\tau_{\mathbf{n},\mathbf{m}}$ are possible torques from external perturbations (see section 2.2.3 for an example) and the effective fields here are defined as[12]

$$\begin{aligned}\mathbf{B}^{\text{AFM}}_{\text{eff},\mathbf{n}} &= -\frac{1}{2M_{\text{s}}}\frac{\delta f}{\delta\mathbf{n}},\\ \mathbf{B}^{\text{AFM}}_{\text{eff},\mathbf{m}} &= -\frac{1}{2M_{\text{s}}}\frac{\delta f}{\delta\mathbf{m}},\end{aligned} \tag{3.26}$$

and given by

$$\begin{aligned}\mathbf{B}^{\text{AFM}}_{\text{eff},\mathbf{n}} &= \frac{2A}{M_{\text{s}}}\nabla^2\mathbf{n}+B_{\text{an}}(\mathbf{n}\cdot\hat{z})\hat{z}+B_{\text{d}}(\mathbf{m}\times\hat{z})+\frac{D}{M_{\text{s}}}\Big[(\nabla\cdot\mathbf{n})\hat{z}-\nabla(\mathbf{n}\cdot\hat{z})\Big],\\ \mathbf{B}^{\text{AFM}}_{\text{eff},\mathbf{m}} &= -2B_{\text{exch}}\mathbf{m}+\mathbf{B}-B_{\text{d}}(\mathbf{n}\times\hat{z}).\end{aligned} \tag{3.27}$$

Static magnetization of the antiferromagnet

The static magnetization of this system without electric currents is found by minimizing the energy functional (3.24)[13]. This yields [50, 51]

$$\mathbf{m}_0 = -\frac{B}{2B_{\text{exch}}}\mathbf{n}\times(\mathbf{n}\times\hat{z})-\frac{B_{\text{d}}}{2B_{\text{exch}}}\mathbf{n}\times\hat{z}. \tag{3.28}$$

The presence of the homogeneous Dzyaloshinskii-Moriya term B_{d} shows that even in the absence of an external magnetic field the total magnetization is non-zero. This is the origin of the phenomenon called weak ferromagnetism (see section 2.2.1). In the present work, we are not interested in such effects. Further, this term does not contribute to the translational motion of an antiferromagnetic texture within the approximations we consider and we neglect it in the following[14].

Closed Landau-Lifshitz-Gilbert equation

The Landau-Lifshitz-Gilbert equations (3.25) can be brought in closed form by eliminating $\mathbf{m}$ by using the expression of $\mathbf{B}^{\text{AFM}}_{\text{eff},\mathbf{m}}$ in equations (3.27). We take $\mathbf{n}\times(\cdots)$ the first equation in (3.25), solve for $\mathbf{m}$ and plug the obtained expression in the equation for $\dot{\mathbf{m}}$ (3.25). In the absence of external torques this leads to the closed equation for the Néel vector

$$\mathbf{n}\times\ddot{\mathbf{n}} = 2B_{\text{exch}}\gamma^2\Big(\mathbf{n}\times\mathbf{B}^{\text{AFM}}_{\text{eff},\mathbf{n}}\Big)-\gamma^2\left(\mathbf{n}\times\mathbf{B}\right)\left(\mathbf{n}\cdot\mathbf{B}\right)+2\gamma\dot{\mathbf{n}}\left(\mathbf{n}\cdot\mathbf{B}\right). \tag{3.29}$$

---

[12] The factors of 1/2 come from the definition of the antiferromagnetic vectors in equations (3.22) and (3.23).

[13] Alternatively, the static magnetization can be obtained by taking the cross product of the first line of equations (3.25) with $\mathbf{n}$ and identifying the time-independent components under the constraints $\mathbf{n}^2 = 1$ and $\mathbf{n}\cdot\mathbf{m} = 0$.

[14] The main effect of B_{d} is that it renormalizes the effective anisotropy constant B_{an}. See reference [51] for more details.

Effects of external torques on the skyrmion profile

In section 4.1 we investigate the skyrmion motion induced by electric currents. Some of the current-induced torques that enter equation (3.25) in that case are field-like (see sections 2.2.3 and 4.1.2) and, therefore, represent potential forces. Such torques are equivalent to the terms appearing in equations (3.27), so that they have to be taken into account when investigating the static skyrmion properties. For this purpose, we introduce the external effective field $\mathbf{B}_{\text{ext,eff}}$ (see sections 3.3.2 and 4.1.2) that contains both the external magnetic field and the conservative current-induced fields

$$\mathbf{B}_{\text{ext,eff}} = \mathbf{B} - \frac{C_1}{2\gamma}\left(\hat{z} \times \mathbf{j}\right). \tag{3.30}$$

Here, C_1 is the coefficient of the field-like current-induced spin-orbit torque and $\mathbf{j}$ the electric current density (see section 2.2.3).

3.3.2 Skyrmion profile

The energy functional in equation (3.24) allows for skyrmion solutions as long as the external field is applied along the $\hat{z}$-direction or is zero [50, 51]. We assume the external magnetic field to be the dominant contribution towards $\mathbf{B}_{\text{ext,eff}}$ in equation (3.30), so that the current-induced field does not destroy the skyrmion ($B \gg C_1 j/2\gamma$). The skyrmion profile $\mathbf{n} = \mathbf{n}_{\text{sk}} + \delta\mathbf{n}$ is determined from the steady state of equation (3.29), which is valid in the absence of dissipative and damping terms

$$\mathbf{n} \times \mathbf{B}^{\text{AFM}}_{\text{eff},\mathbf{n}} - \frac{1}{2B_{\text{exch}}}\left(\mathbf{n} \times \mathbf{B}_{\text{ext,eff}}\right)\left(\mathbf{n} \cdot \mathbf{B}_{\text{ext,eff}}\right) = -\frac{1}{\gamma B_{\text{exch}}}\dot{\mathbf{n}}\left(\mathbf{n} \cdot \mathbf{B}_{\text{ext,eff}}\right). \tag{3.31}$$

In this chapter we are interested in the static skyrmion properties and focus our attention on the static component $\mathbf{n}_{\text{sk}}$ solves the equation with both $j, \dot{\mathbf{n}} = 0$.

The corrections $\delta\mathbf{n}$ originate from a non-zero dynamic term $\dot{\mathbf{n}}$ and the current-induced effective field $C_1/2\gamma(\hat{z}\times\mathbf{j})$ and are relevant for the current-induced skyrmion motion, which we investigate in section 4.1.2. Gomonay *et al.* [109] discussed that a deformation of an antiferromagnetic texture occurs at velocities close to the magnon velocity. In antiferromagnets the magnon velocity is of the order of $30\,\text{km}\,\text{s}^{-1}$, which is orders of magnitude higher than in ferromagnets. We are considering slow skyrmion dynamics in section 4.1.2 and, therefore, the corrections can be assumed small, $|\delta\mathbf{n}| \ll |\mathbf{n}_{\text{sk}}|$.

Following the procedure for the ferromagnetic skyrmion (section 3.2.2), we rewrite equation (3.31) into spherical coordinates (see Appendix B.1)

$$\frac{d^2\theta}{d\tilde{\rho}^2} + \frac{1}{\tilde{\rho}}\frac{d\theta}{d\tilde{\rho}} - \frac{\sin\theta\cos\theta}{\tilde{\rho}^2} - \frac{4D}{\pi D_0}\frac{\sin^2\theta}{\tilde{\rho}} - \left(1 - \frac{B^2}{B_0^2}\right)\sin\theta\cos\theta = 0. \tag{3.32}$$

Here, we presented the dimensionless form of the profile equation . The radial coordinate is rescaled according to $\tilde{\rho} = \rho/x_0$, where x_0 is the antiferromagnetic characteristic lengthscale (domain wall width), D_0 the threshold value of the inhomogeneous Dzyaloshinskii-Moriya interactions in antiferromagnets and B_0 the spin-flop field of the antiferromagnet

$$
\begin{aligned}
x_0 &= \sqrt{\frac{2A}{B_{\mathrm{an}} M_{\mathrm{s}}}}, \\
D_0 &= \frac{4}{\pi}\sqrt{2AB_{\mathrm{an}}M_{\mathrm{s}}}, \\
B_0 &= \sqrt{2B_{\mathrm{exch}}B_{\mathrm{an}}}.
\end{aligned} \tag{3.33}
$$

At this stage, we note that for zero magnetic field the profile equations for the ferromagnet (3.14) and the antiferromagnet (3.32) are identical. Therefore, we can readily take over the results for the zero-field ferromagnetic skyrmion after substituting the ferromagnetic magnetization $\mathbf{m}$ by the Néel vector $\mathbf{n}$[15] (see figures 3.2-3.3). On an infinite plane the profile equation has a skyrmion solution only when $D < D_0$, otherwise resulting structure is a cycloid. We plot the antiferromagnetic counterpart of figure 3.2 in figure 3.10, where we visualize the Néel vector with double-headed arrows.

When the magnetic field is turned on, the two ferromagnetic and antiferromagnetic skyrmion react differently. The main difference is that the antiferromagnet is not sensitive to the direction – parallel, or antiparallel – of the magnetic field, since only B^2 enters the profile equation (3.32). To show the antiferromagnetic skyrmion profile in the presence of magnetic field, we solve equation (3.32) numerically for the skyrmion with polarity $p = -1$ using the same technique as before and the material parameters listed in Table 3.4.

We plot the skyrmion profile for $D/D_0 = 0.99$ and different values of B are plotted in figure 3.11. As expected, the antiferromagnet is less sensitive than the

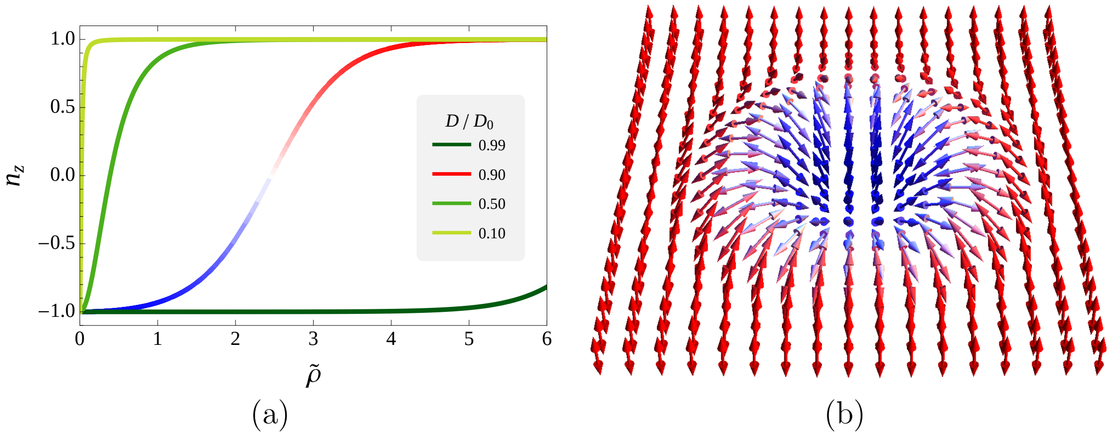

(a) (b)

Figure 3.10: *Isolated antiferromagnetic skyrmion on an infinite plane for zero external field. Shown is the numerical solution of equation (3.32): (a) n_z for different values of D; (b) Néel vector $\mathbf{n}$ for $D/D_0 = 0.9$ on a 5×5 (in units of $\tilde{\rho}$) grid centered around the skyrmion. The color code represents the value of n_z, as defined in (a). The exact same profile defines the ferromagnetic skyrmions, as shown in figures 3.2-3.3. See Table 3.2 for the corresponding values of D. The topological charge of the depicted skyrmion evaluates to $Q = -1$.*

---

[15] The same applies to the definition of the topological charge in equations (3.5-3.6).

Parameter	Value	Unit
B_{exch}	90.9	T
B	1.5	T
A	15.0	$\text{pJ}\,\text{m}^{-1}$
B_{an}	1.0	T
D	7.0	$\text{mJ}\,\text{m}^{-2}$
M_{s}	1.0	$\text{MA}\,\text{m}^{-1}$

Rescaled Parameter	Value	Unit
B_0	13.52	T
B^2/B_0^2	0.01	–
x_0	5.42	nm
D_0	7.04	$\text{mJ}\,\text{m}^{-2}$
D/D_0	0.99	–
ξ_{AFM}	8.60	nm

Table 3.4: *List of typical parameters for an antiferromagnetic material. The parameters here are chosen in such a way that the exchange field B_{exch} is the largest scale in the system and the same characteristic lengthscales as for the ferromagnet are reproduced (see Table 3.1). Shown are the constants that enter the energy functional in equation (3.24) directly and the corresponding rescaled parameters that appear in the profile equations (3.32) and (3.34).*

ferromagnet – a strong field of $B = 1\,\text{T}$ enlarges the antiferromagnetic skyrmion a little (figure 3.11b), whereas the effect on the ferromagnetic skyrmion is significantly stronger (figure 3.4b). This allows to apply even stronger fields without destroying the skyrmion. For fields larger than the spin-flop field $B > B_0$ the antiferromagnet enter the spin-flop phase, where the preferred direction of the Néel vector is in-plane. This phase is beyond the scope of the present work[16].

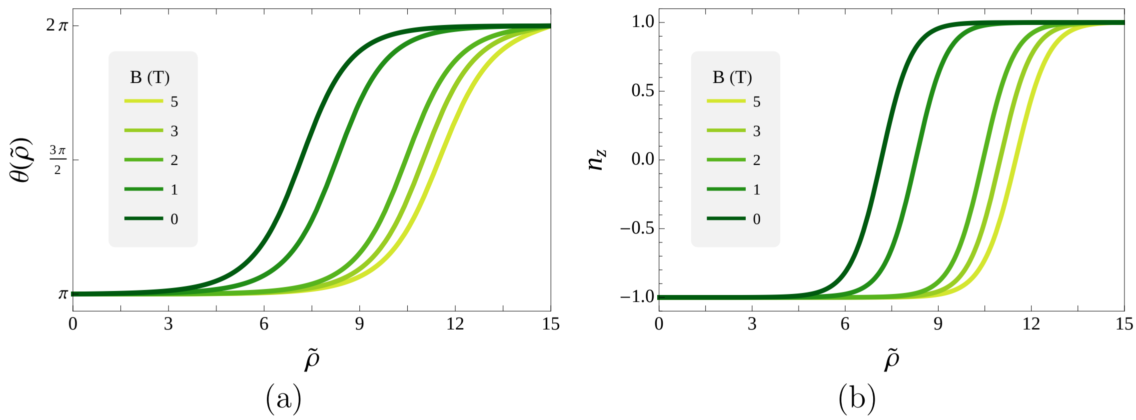

(a) (b)

Figure 3.11: *Antiferromagnetic skyrmion profile for $D/D_0 = 0.99$ (see figure 3.10) and different values of the external magnetic field. The profile is obtained from the numerical integration of equation (3.32): (a) polar angle $\theta(\tilde\rho)$ and (b) n_z. See also Table 3.3 for the corresponding values of the dimensionless parameter B^2/B_0^2.*

---

[16] See reference [51] for a discussion on the stability of states modulated by the Dzyaloshinskii-Moriya interactions within the spin-flop phase in antiferromagnets.

Confined antiferromagnetic skyrmions

Equivalent to ferromagnets, the Dzyaloshinskii-Moriya interactions in antiferromagnets will induce canting of the Néel vector at the edges of finite samples (see the corresponding discussion in section 3.2.2). Due to this effect, nanostructures with $D \neq 0$ cannot host uniform magnetic textures. Here, using the same variational approach on energy functional (3.17), we derive the boundary condition for the antiferromagnetic skyrmion profile equation (3.32). Details can be found in Appendix A.2.

For finite samples, it is beneficial not to rescale the equation and rewrite it in terms of the radial coordinate ρ (see also Appendix B.1)

$$\frac{d^2\theta}{d\rho^2} + \frac{1}{\rho}\frac{d\theta}{d\rho} - \sin\theta\cos\theta\left[\frac{1}{\rho^2} + \frac{1}{x_0^2}\left(1 - \frac{B^2}{2B_{\text{exch}}B_{\text{an}}}\right)\right] - 2\frac{\sin^2\theta}{\xi_{\text{AFM}}\rho} = 0, \tag{3.34}$$

where x_0 is the same antiferromagnetic domain wall width as before and $\xi_{\text{AFM}} = 4A/D$ is the characteristic length of the antiferromagnetic cycloid state [12, 26, 51, 107]. The surface terms contribute the “natural” boundary condition (see Appendix A.2)

$$\left(\frac{d\theta}{d\rho}\right)_{\text{boundary}} = \frac{1}{\xi_{\text{AFM}}}. \tag{3.35}$$

We solve equation (3.34) numerically on a finite nanodisk of radius $R_{\text{disk}} = 50\,\text{nm}$ and, as for the ferromagnet, with the initial condition $\theta(\rho = 0) = \pi$. The modified boundary condition $\theta'(\rho = R_{\text{disk}}) = 1/\xi_{\text{AFM}}$ is fulfilled by a shooting method.

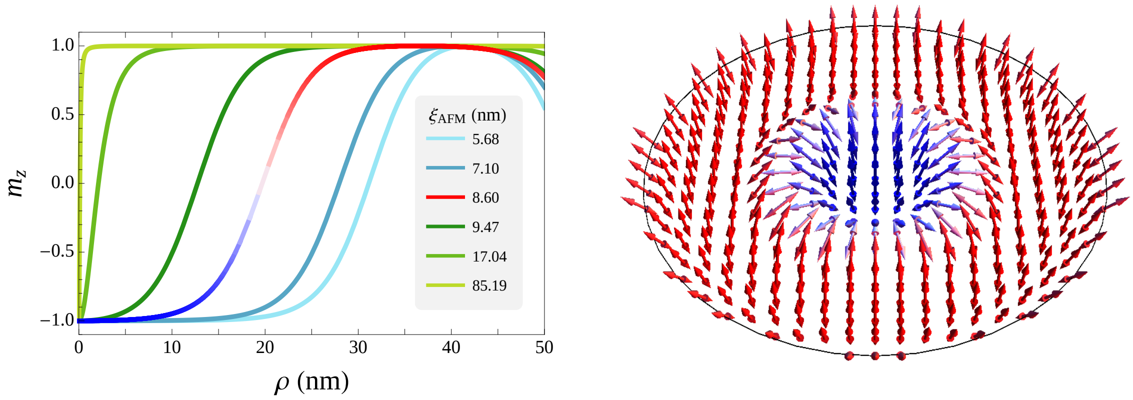

(a) (b)

Figure 3.12: *Antiferromagnetic skyrmion confined in a nanodisk of* $R_{disk} = 50\,\text{nm}$. *Shown is the numerical solution of equations (3.34-3.35) for parameters* $B = 0\,\text{T}$, $x_0 = 5.42\,\text{nm}$ *and* $\xi_{AFM} = 8.60\,\text{nm}$, *which correspond to for* $D/D_0 = 0.99$*: (a)* n_z *and (b) full Néel vector* $\mathbf{n}$ *with the nanodisk boundary (black circle). The color code represents the value of* n_z*, as defined in (a). The confined ferromagnetic counterpart is shown in figure 3.5. See also Table 3.2 for the corresponding values of* D*. The topological charge of the shown skyrmion evaluates to* $Q = -0.89$.

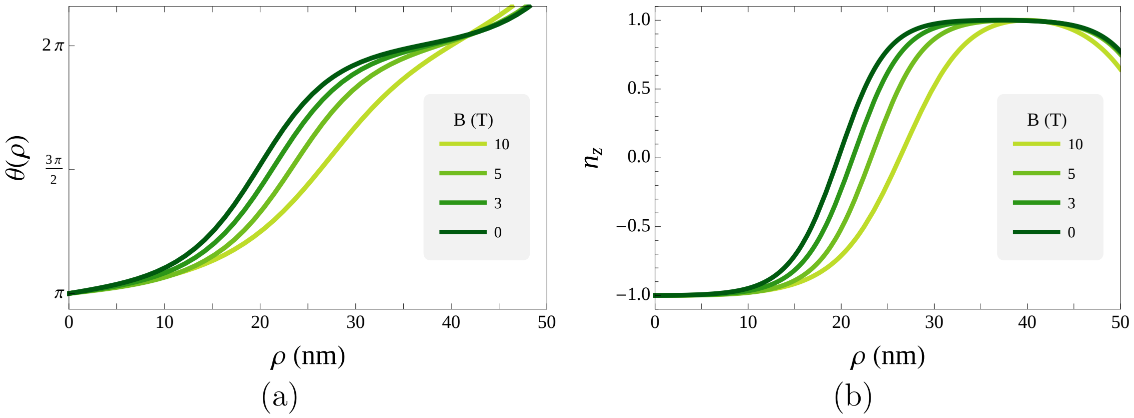

(a) (b)

Figure 3.13: *Profile of the confined antiferromagnetic skyrmion for* $\xi_{AFM} = 8.60\,\mathrm{nm}$*,* $x_0 = 5.42\,\mathrm{nm}$ *and different values of the external magnetic field: (a) polar angle* $\theta(\rho)$ *and (b) z-component of the Néel vector. Shown is the numerical solution of equations (3.34-3.35). The choice of* ξ_{AFM} *corresponds to* $D/D_0 = 0.99$ *(see figure 3.12). We note that the colors chosen here match the ones in figure 3.11 only for* $B = 0\,\mathrm{T}$*. The corresponding values of the dimensionless parameter* B^2/B_0^2 *are shown in Table 3.3.*

The conclusions drawn for the ferromagnetic skyrmion regarding the magnetization canting at the edges, its chirality, topological charge and the increased stability even for $D > D_0$ apply here as well. We show the antiferromagnetic confined skyrmion at zero field in figure 3.12 for $x_0 = 5.42\,\mathrm{nm}$ and $\xi_{\mathrm{AFM}} = 8.60\,\mathrm{nm}$, which corresponds to $D/D_0 = 0.99$ for the infinite-plane skyrmion. For completeness, we also show the profile for different values of D in figure 3.12a, where profiles for which $D < D_0$ are depicted in green colors and for $D > D_0$, in blue colors. In the latter case the skyrmion size is confined by the nanodisk boundaries, as long R_{disk} is not too large compared to the cycloid length $L_0 = 2\pi\xi_{\mathrm{AFM}}$. If it is, then a single skyrmion cannot be stabilized and states with a larger rotation of the magnetization vector solve the profile equation [26].

For comparison with the infinite-plane skyrmion (figure 3.11), we plot the profile of the confined skyrmion as a function of the external magnetic field in figure 3.13. In both cases the skyrmion grows when the magnetic field is increased. However, for the confined skyrmion, the growth is limited by the nanodisk boundaries, so that even at higher fields than for the infinite-plane skyrmion the size does not change much (compare figures 3.11b and 3.13b).

3.4 Summary

In this chapter, we presented the phenomenological models for ferromagnetic and antiferromagnetic thin films, and investigated the static properties of the corresponding skyrmion solutions. The models incorporate exchange interactions, uniaxial anisotropy, external magnetic field and interfacial Dzyaloshinskii-Moriya interactions. Dipolar interactions are negligible for the present setup and were not considered. Importantly, we reviewed two representations of the antiferromagnetic model – one in terms of the individual sublattices (which we later use in the numerical simulations), and the other in terms of the antiferromagnetic vectors (which we later use in the analytical calculations).

Based on these models, we reproduced analytically the profile equation for ferromagnetic and antiferromagnetic Néel skyrmions with negative polarity ($p = -1$) and reviewed known results regarding the dependence of the skyrmion profile on the Dzyaloshinskii-Moriya constant and the external field in infinite-plane films [12, 51]. We emphasize that

- at zero external field the profile equations in ferromagnets and antiferromagnets are identical – the former defines the ferromagnetic magnetization vector and the latter, the antiferromagnetic Néel vector [13];
- at finite magnetic fields, the ferromagnetic profile equation is linear in the field, whereas the antiferromagnetic equation is quadratic in it.

Due to the strong exchange interaction in antiferromagnets, the antiferromagnetic skyrmion is less sensitive to the external field than the ferromagnetic skyrmion and persists at higher fields.

Finally, we investigated the static properties of skyrmions confined in circular nanodisks. For ferromagnets, it was recently shown that the Dzyaloshinskii-Moriya interactions induce an additional canting of the magnetization vector at the sample boundaries [26]. This creates a confining potential, which stabilizes skyrmions for a larger range of the Dzyaloshinskii-Moriya constant compared to infinite-plane skyrmions. We reproduced these results through variational calculations and extended the analysis to antiferromagnetic confined skyrmions.

The derivation of the modified boundary conditions in finite antiferromagnetic thin films with Dzyaloshinskii-Moriya interactions is our main result in this chapter. At zero external field the findings are identical to the ferromagnetic case. At finite fields we find that the confining potential diminishes the effect of the magnetic field close to the boundaries and, as a result, the antiferromagnetic confined skyrmion persists at higher fields than the infinite-plane skyrmion (see figures 3.11 and 3.13).

With this, the stage is set to go beyond the static properties of ferromagnetic and antiferromagnetic skyrmions. In the next chapter, we apply the models introduced here to investigate the current-induced motion of infinite-plane skyrmions analytically, and the intrinsic dynamic modes of confined skyrmions numerically.

Chapter 4

Current-induced motion and confined intrinsic dynamics of skyrmions in antiferromagnets

4.1 Translational current-driven skyrmion motion

In this section, we focus on the current-driven motion of isolated skyrmions in perpendicularly magnetized (infinite) thin films. The inversion symmetry breaking at the interface of the magnetic thin film, which is assumed to exhibit a strong spin-orbit coupling, leads to the appearance of interfacial Dzyaloshinskii-Moriya interactions. When electric currents are applied to this systems, they become spin-polarized due to the spin-orbit coupling; this effect is captured by introducing spin-orbit torques into the model[1]*.*

The manipulation of magnetic textures with electric currents and the constant improvement of technological devices is a key area in spintronics. Magnetic skyrmions have gained a lot of attention as candidates for low-energy novel information storage and logic devices due to their unique characteristics, like the low threshold current needed to set them in motion [10, 25, 110].

In ferromagnets, the current-induced skyrmion motion has been studied extensively – both due to the effects of spin-transfer torques [23, 25, 110] and spin-orbit torques [73]. Here, we review the results of Knoester *et al.* [73], where both effects have been studied analytically.

In antiferromagnets there has been no experimental observation of antiferromagnetic skyrmions yet and the literature on current-induced motion is much more sparse. The first studies employed numerical simulations and highlighted the different dynamics of antiferromagnetic skyrmions driven by spin-transfer torques [52, 53]. The analysis presented in this chapter tackles the problem analytically – where the phenomenological model is extended to incorporate both spin-transfer and spin-orbit torques – and was published in reference [55].

---

[1] The same model is also applicable to setups in which spin-polarized currents are injected vertically into the magnetic thin film, for example, due to the spin-Hall effect in an adjacent heavy-metal layer with a large spin-orbit coupling [25].

For the analysis, we use the ferromagnetic and antiferromagnetic models discussed in the previous chapter and extend them to cover spin-transfer and spin-orbit torques. The models take into account spin-orbit coupling to lowest order [73] and, in addition, describe the antiferromagnetic dynamics to leading order in the exchange field [55]. We derive an equation of motion for a general magnetization texture analytically and apply the collective-coordinate method (see section 2.2.2) to project the full Landau-Lifshitz-Gilbert equations onto the skyrmion translational modes (parametrized by the center of mass coordinates R_x and R_y) for both systems. Within this approach, we use the equilibrium skyrmion profiles obtained in chapter 3. Finally, we estimate the resulting skyrmion drift velocities for both systems and compare the analytical results to existing numerical works.

As discussed previously, we disregard the effects of dipolar interactions in our models[2]. Further, we do not consider pinning effects or study the corresponding critical current density needed to move skyrmions. In ferromagnets these issues have been addressed numerically in the works of Iwasaki *et al.* [110] and experimentally in the work of Woo *et al.* [29]. The pinning of antiferromagnetic skyrmions has been numerically studied recently [54].

4.1.1 Ferromagnetic skyrmions

In this section, we review the results for the skyrmion motion driven by current-induced spin-transfer and spin-orbit torques. For the original works we refer to Knoester *et al.* and Sampaio *et al.* [25, 73].

Equation of motion

The full Landau-Lifshitz-Gilbert equation for a ferromagnet includes damping terms and external torques [73]

$$\dot{\mathbf{m}} = \gamma \mathbf{m} \times \mathbf{B}_{\text{eff,FM}} + \alpha_{\text{G,FM}} \mathbf{m} \times \dot{\mathbf{m}} + \tau_{\mathbf{j}}, \tag{4.1}$$

where γ is the gyromagnetic ratio, $\alpha_{\text{G,FM}}$ the phenomenological Gilbert damping coefficient and $\tau_{\mathbf{j}}$ represent the current-induced torques (see section 2.2.3). The effective field is given in equation (3.8) and reads

$$\mathbf{B}_{\text{eff,FM}} = \frac{2A_{\text{ex}}}{M_{\text{s}}} \nabla^2 \mathbf{m} + 2K_u (\mathbf{m} \cdot \hat{z}) \hat{z} + B\hat{z} + \frac{2D}{M_{\text{s}}} \Big[\hat{z}(\nabla \cdot \mathbf{m}) - \nabla(\hat{z} \cdot \mathbf{m}) \Big]. \tag{4.2}$$

The current-induced torques for the present system can be both homogeneous and inhomogeneous (see also the discussion in reference [73]). We write collectively $\tau_{\mathbf{j}} = \tau_{\text{FM,STT}} + \tau_{\text{FM,SOT}}$, where

$$\begin{aligned} \tau_{\text{FM,STT}} &= \alpha_{\text{FM}} \left(\mathbf{j} \cdot \nabla \right) \mathbf{m} + \beta_{\text{FM}} \mathbf{m} \times \left(\mathbf{j} \cdot \nabla \right) \mathbf{m}, \\ \tau_{\text{FM,SOT}} &= a_{\text{FM}} \mathbf{m} \times (\mathbf{j} \times \hat{z}) + b_{\text{FM}} \mathbf{m} \times \Big[\mathbf{m} \times (\mathbf{j} \times \hat{z}) \Big]. \end{aligned} \tag{4.3}$$

---

[2] We consider thin films where dipolar interactions are negligible [26]; further, there are studies showing that their inclusion does not have a sizeable influence [25].

Here, the terms proportional to α_{FM} and β_{FM} represent the conventional reactive and dissipative spin-transfer torques. In the second line of equation (4.3) a_{FM} describes the field-like and b_{FM}, the antidamping spin-orbit torque.

Bringing all terms together in equation (4.1) we obtain the time-evolution of the magnetization vector in the presence of electric currents

$$\begin{aligned}\dot{\mathbf{m}} = \gamma \mathbf{m} \times \mathbf{B}_{\mathrm{eff,FM}} + \alpha_{\mathrm{G,FM}} \mathbf{m} \times \dot{\mathbf{m}} + \alpha_{\mathrm{FM}} \left(\mathbf{j} \cdot \nabla\right) \mathbf{m} + a_{\mathrm{FM}} \mathbf{m} \times \left(\mathbf{j} \times \hat{z}\right) \\ + \beta_{\mathrm{FM}} \mathbf{m} \times \left(\mathbf{j} \cdot \nabla\right) \mathbf{m} + b_{\mathrm{FM}} \mathbf{m} \times \Big[\mathbf{m} \times \left(\mathbf{j} \times \hat{z}\right)\Big]. \qquad (4.4)\end{aligned}$$

This result has been obtained by Knoester *et al.* [73] and describes the dynamics of a general ferromagnetic texture driven by current-induced torques to first order in the spin-orbit coupling.

Current-driven skyrmion motion

Next, we apply the collective-coordinate approach to study the translational motion of a ferromagnetic skyrmion (see section 2.2.2). This is equivalent to the Thiele approach used in recent literature [25, 73, 79, 110, 111]. We assume that the skyrmion profile is composed of a static, cylindrical and rigid component (see section 3.2.2). For the time evolution we use the ansatz $\mathbf{m}(\mathbf{r}, t) = \mathbf{m}(\mathbf{r} - \mathbf{R}(t))$, where $\mathbf{m}$ is the equilibrium skyrmion texture obtained in section 3.2.2 and $\mathbf{R}(t)$ is the skyrmion position. As collective coordinates, we take $\{\xi_i\} = \{R_x, R_y\}$.

To obtain the equation of motion for the skyrmion, we project onto the translational mode by multiplying equation (4.4) by $\mathbf{m} \times \partial \mathbf{m}/\partial x_\beta$ for $\beta = x, y$ and subsequently integrating over space. We note that the equilibrium profile of the skyrmion is found from equation (3.10) so that, upon projection, the first term on the right hand side of equation (4.4) vanishes. The remaining terms determine the skyrmion equation of motion (see Appendix B.2 for details) [25, 43, 73, 79, 110, 111]

$$\mathbf{G} \times \dot{\mathbf{R}} = -\Gamma_{\mathrm{FM}} \dot{\mathbf{R}} + \Delta_{\|} \mathbf{j} + \Delta_{\perp} \Big(\hat{z} \times \mathbf{j}\Big), \qquad (4.5)$$

where

$$\begin{aligned}\mathbf{G} &= -\frac{M_{\mathrm{s}} x_0}{\gamma} Q \hat{z}, \\ \Gamma_{\mathrm{FM}} &= \frac{M_{\mathrm{s}} x_0}{\gamma} D \alpha_{\mathrm{G,FM}}, \\ \Delta_{\|} &= \frac{M_{\mathrm{s}} x_0}{\gamma} \left[\beta_{\mathrm{FM}} D + b_{\mathrm{FM}} x_0 I'\right], \\ \Delta_{\perp} &= \frac{M_{\mathrm{s}} x_0}{\gamma} \left[a_{\mathrm{FM}} x_0 I + \alpha_{\mathrm{FM}} Q\right]. \qquad (4.6)\end{aligned}$$

The first term in equation (4.5) describes the Magnus force and highlights the inherent gyrotropic dynamics of ferromagnets. It contains the gyrovector $\mathbf{G}$ [23, 72], which is directly proportional to the topological charge of the skyrmion (in the present case $Q = -1$). The electric current – applied in the xy-plane – produces two driving forces: a longitudinal dissipative force proportional to the coefficient $\Delta_{\parallel}$ and parallel to the direction of the current, and a transversal force proportional to $\Delta_{\perp}$ and perpendicular to the current. The Gilbert damping constant $\alpha_{\mathrm{G,FM}}$ is the origin of the friction force described by the coefficient Γ_{FM}.

We have schematically depicted the motion of the ferromagnetic skyrmion for an electric current applied in the $\hat{x}$-direction in figure 4.1.

Equation (4.5) contains the saturation magnetization M_{s}, the characteristic length-scale of the ferromagnet x_0 and the dimensionless constants D, I and I' which are integrals over the skyrmion profile and are listed in Appendix B.2.

Current-driven skyrmion velocity

The components of the velocity can be readily obtained from equation (4.5) [73, 110]

$$\begin{aligned} v_x &= \frac{D\alpha_{\mathrm{G,FM}}(D\beta_{\mathrm{FM}} + b_{\mathrm{FM}}x_0 I') + a_{\mathrm{FM}}x_0 I - \alpha_{\mathrm{FM}}}{1 + (D\alpha_{\mathrm{G,FM}})^2} j_x, \\ v_y &= \frac{D\beta_{\mathrm{FM}} + b_{\mathrm{FM}}x_0 I' + D\alpha_{\mathrm{G,FM}}(\alpha_{\mathrm{FM}} - a_{\mathrm{FM}}x_0 I)}{1 + (D\alpha_{\mathrm{G,FM}})^2} j_x, \end{aligned} \tag{4.7}$$

where we have limited our attention to electric currents applied in the $\hat{x}$-direction. In an infinite plane the skyrmion has both a longitudinal and a transversal velocity; however, if the skyrmion is confined in a narrow strip, it eventually feels the repulsive forces from the edges and resumes motion only in the longitudinal direction [25, 26, 27][3].

We list typical values of the torque coefficients for ferromagnets in Table 4.1. The expressions in equations (4.7) give an analytical estimate of the current-driven skyrmion velocity, which is in a very good agreement with the results from numerical simulations [27, 110]. Both results are summarized in 4.1.

We note that Iwasaki *et al.* [110] consider a scenario where only inhomogeneous torques are present (both the adiabatic and non-adiabatic spin-transfer torques), which drive the Néel skyrmion along the current in a narrow ferromagnetic strip. On the other hand, Tomasello *et al.* [27] consider the motion of a Néel skyrmion driven by homogeneous torques of the same form as in equation (4.3), but originating

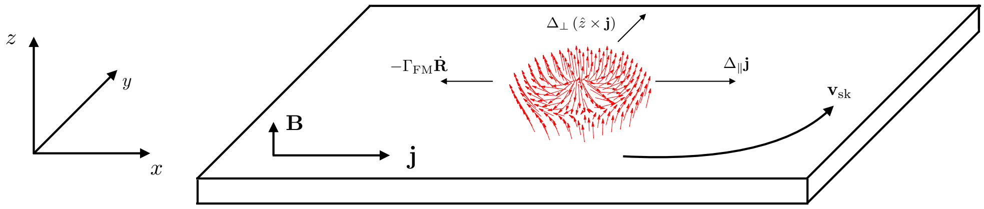

Figure 4.1: *Schematic representation of the skyrmion motion in a ferromagnet driven by an electric current* $\mathbf{j} \parallel \hat{x}$ *and an external magnetic field* $\mathbf{B} \parallel \hat{z}$*, as described by equation (4.5). The friction force is denoted by* $\Gamma_{FM}\dot{\mathbf{R}}$*, the longitudinal current-induced force by* $\Delta_{\parallel}\mathbf{j}$ *and the transversal current-induced force by* $\Delta_{\perp}\mathbf{j}$*. The combination of these forces leads to a skyrmion motion with the velocity* $\mathbf{v}_{\mathrm{sk}}$.

---

[3] This is a key component for the concept of skyrmion racetrack memory [25, 27].

Parameters	Units	Iwasaki *et al.* [110]*	Tomasello *et al.* [27]**
$\alpha_{\mathrm{G,FM}}$	–	0.5	0.3
α_{FM}	$\mathrm{m^3\,A^{-1}\,s^{-1}}$	7.8×10^{-11}	–
β_{FM}	$\mathrm{m^3\,A^{-1}\,s^{-1}}$	-3.9×10^{-11}	–
a_{FM}	$\mathrm{m^2\,A^{-1}\,s^{-1}}$	–	–
b_{FM}	$\mathrm{m^2\,A^{-1}\,s^{-1}}$	–	-0.019
x_0	nm	–	10^3
j	$\mathrm{A\,m^{-2}}$	10^{11}	10^{11}
Estimated			
$\lvert v_{x,\mathrm{sk}} \rvert$	$\mathrm{m\,s^{-1}}$	7.8	5.2
$\lvert v_{y,\mathrm{sk}} \rvert$	$\mathrm{m\,s^{-1}}$	0	17.4
Numerical results			
v_{sk}	$\mathrm{m\,s^{-1}}$	~ 8	~ 15

*The values of the current-induced torque coefficients α_{FM} and β_{FM} have been calculated from the expressions that the authors provide in [110] for their spin-transfer torque coefficients $\alpha_{\mathrm{FM}} = pa^3/(2e)$ and $\beta_{\mathrm{FM}} = -pa^3/(2e)\beta$, where $p = 0.2$ is the spin polarization of the electric current, e the electron charge and $a = 5\,\text{Å}$ is the lattice constant. We focus only on one set of values for $\alpha_{\mathrm{G,FM}}, \beta_{\mathrm{FM}}$ and v of the range provided in [110], namely $\alpha_{\mathrm{G,FM}} = \beta_{\mathrm{FM}} = 0.5$;

** Here, we focus only on the scenario of Néel skyrmions driven by spin-Hall effect torques. The corresponding torque coefficient is calculated according to $b_{\mathrm{FM}} = \gamma\hbar\theta_{SH}/(2eM_{\mathrm{s}}L)$, where γ is the gyromagnetic ratio, $\hbar$ the reduced Planck constant, $\theta_{SH} = -0.3$ the spin-Hall angle for the used setup, $M_{\mathrm{s}} = 1\,\mathrm{MA\,m^{-1}}$ the saturation magnetization and $L = 1\,\mathrm{nm}$ the ferromagnetic layer thickness. The rescaling factor that the authors use is not the characteristic width x_0, but rather the thin film length.

Table 4.1: *Estimated velocities of the ferromagnetic skyrmion using the parameters from references [27, 110] and the formulas for $v_{x,\mathrm{sk}}$ and $v_{y,\mathrm{sk}}$ presented in equations (4.7). The numerical results for v_{sk} are taken from the diagrams of the corresponding reference.*

from the spin-Hall effect of the electric current applied to an adjacent heavy metal layer[4]. Despite the different origin, the value of the homogeneous torque quoted in reference [27] is comparable to the estimated value of the homogeneous spin-orbit torque [73, 105]. Both scenarios are captured within the phenomenological model presented in this section.

In conclusion, homogeneous torques of the Slonczewski type (the term in equation (4.3) proportional to b_{FM}) are found to be more effective in driving Néel skyrmions and result in faster velocities [25, 27]. In this work the homogeneous torques are a direct result of the spin-orbit coupling in the ferromagnet, but they can also be due to the vertical injection of spin-polarized current from a multilayer structure into the ferromagnet [25], or due to the spin-Hall effect generated in a heavy metal layer adjacent to the ferromagnet [27].

---

[4] Due to the different nature of the torque in reference [27], the skyrmion is driven in a narrow ferromagnetic strip in a direction transverse to the electric current.

4.1.2 Antiferromagnetic skyrmions

In this section, we analyze the antiferromagnetic skyrmion motion driven by current-induced spin-transfer and spin-orbit torques. These results have been published in reference [55].

We start by discussing the current-induced torques in the antiferromagnet. We proceed with analyzing the magnetization dynamics of a uniaxial antiferromagnet in the presence of electric currents and a time-independent external magnetic field. Finally, we focus on the translational motion of a magnetic skyrmion, rewrite the equations of motion by using the collective-coordinate approach, and obtain an estimate for the skyrmion velocity as a result of the electric currents.

Spin-orbit torques in antiferromagnets

We follow a phenomenological approach to derive the current-induced torques. It is based on the Onsager reciprocity relations, which, in the case under consideration, relate the process of inducing charge currents by a time-varying magnetic texture to the effect that charge currents have on the magnetization dynamics.

Following Hals *et al.* [60], to lowest order in the spatial gradients and the magnetization $\mathbf{m}$, and zeroth order in spin-orbit coupling we find three contributions towards the magnetically pumped charge density $\mathbf{j}^{\text{pump}}/\sigma$ (where σ is the electrical conductivity) that obey the symmetries of the system (rotation and $\mathbf{n} \to -\mathbf{n}$): $\eta/\gamma\, \mathbf{n} \cdot (\dot{\mathbf{m}} \times \partial_i \mathbf{n})$, $\beta/\gamma\, \dot{\mathbf{n}} \cdot \partial_i \mathbf{n}$ and $\zeta/\gamma\, \mathbf{n} \cdot (\dot{\mathbf{n}} \times \partial_i \mathbf{m})$ [60]. After applying the Onsager relations these are transformed and result in the torques

$$\begin{aligned}
\tau_{\mathbf{n},\mathrm{STT}} &= \frac{\eta}{2}(\mathbf{j} \cdot \nabla)\mathbf{n} + \frac{\beta}{2}(\mathbf{j} \cdot \nabla)\mathbf{n} \times \mathbf{m} + \frac{\zeta}{2}\mathbf{m} \times \Big[(\mathbf{j} \cdot \nabla)\mathbf{m} \times \mathbf{n}\Big], \\
\tau_{\mathbf{m},\mathrm{STT}} &= \frac{\eta}{2}\mathbf{m} \times \Big[(\mathbf{j} \cdot \nabla)\mathbf{n} \times \mathbf{n}\Big] + \frac{\beta}{2}(\mathbf{j} \cdot \nabla)\mathbf{n} \times \mathbf{n} + \frac{\zeta}{2}\mathbf{n} \times \Big[(\mathbf{j} \cdot \nabla)\mathbf{m} \times \mathbf{n}\Big].
\end{aligned} \tag{4.8}$$

Here, the terms parameterized by the coefficients η, ζ describe reactive spin-transfer torques, whereas the term with β describes a dissipative spin-transfer torque.

Furthermore, as discussed in section 2.2.3, the inversion symmetry breaking gives rise to another set of torques even in homogeneous systems, which do not involve gradients of the antiferromagnetic vectors. Following the same approach as above [112], we find the pumped charge currents that are lowest order in the spin-orbit coupling: $C_1/\gamma\, \hat{z} \times \dot{\mathbf{m}}$, $C_2/\gamma\, \hat{z} \times (\mathbf{n} \times \dot{\mathbf{n}})$ and $C_3/\gamma\, \hat{z} \times (\mathbf{m} \times \dot{\mathbf{m}})$, which after applying the Onsager relations lead to

$$\begin{aligned}
\tau_{\mathbf{n},\mathrm{SOT}} &= -\frac{C_1}{2}\mathbf{n} \times (\hat{z} \times \mathbf{j}) - \frac{C_2}{2}\mathbf{m} \times \Big[\mathbf{n} \times (\hat{z} \times \mathbf{j})\Big] - \frac{C_3}{2}\mathbf{n} \times \Big[\mathbf{m} \times (\hat{z} \times \mathbf{j})\Big], \\
\tau_{\mathbf{m},\mathrm{SOT}} &= -\frac{C_1}{2}\mathbf{m} \times (\hat{z} \times \mathbf{j}) - \frac{C_2}{2}\mathbf{n} \times \Big[\mathbf{n} \times (\hat{z} \times \mathbf{j})\Big] - \frac{C_3}{2}\mathbf{m} \times \Big[\mathbf{m} \times (\hat{z} \times \mathbf{j})\Big].
\end{aligned} \tag{4.9}$$

Here, the terms proportional to C_1 are field-like (reactive) spin-orbit torques and the terms proportional to C_2, C_3 are the anti-damping (dissipative) spin-orbit torques. In ferromagnetic systems similar torques have been discussed in references [73, 76] and in antiferromagnets a microscopic analysis has been performed in reference [48].

While we cannot generically exclude the existence of spin-orbit torques beyond the exchange approximation, in microscopic models such as the Rashba model such torques do not occur. In that case, with the exception of higher harmonics, equations (4.9) capture the spin-orbit torques. The study of possible spin-orbit that break the exchange approximation falls outside the scope of the present work.

We emphasize that the spin-orbit torques and the spin-transfer torques differ in their nature (see also section 2.2.3). Whereas in the latter the free electrons are polarized by the local magnetization, while moving through the texture, and interact with it after being polarized, in the spin-orbit torques the polarization is due to the spin-orbit coupling in the system and not due to the magnetization. In that sense, the spin-transfer torques are a result of a non-local interaction between the electrons and the magnetic moments, while the spin-orbit torques are local.

In the later steps of the calculation, presented below, the form of both the spin-transfer and the spin-orbit torques will be simplified by retaining only the leading order terms in B_{exch}.

Equation of motion

Next, we derive the equations of motion for the Néel order parameter for a time-independent magnetic field and electric current. The Landau-Lifshitz-Gilbert equations to leading order in B_{exch} are given by [59, 60, 113]

$$\begin{aligned} \dot{\mathbf{n}} &= \gamma\Big[\mathbf{n}\times\mathbf{B}^{\text{AFM}}_{\text{eff},\mathbf{m}}\Big] + \tau_{\mathbf{n}}, \\ \dot{\mathbf{m}} &= \gamma\Big[\mathbf{n}\times\mathbf{B}^{\text{AFM}}_{\text{eff},\mathbf{n}} + \mathbf{m}\times\mathbf{B}^{\text{AFM}}_{\text{eff},\mathbf{m}}\Big] + \alpha_G\mathbf{n}\times\dot{\mathbf{n}} + \tau_{\mathbf{m}}, \end{aligned} \tag{4.10}$$

where γ is the gyromagnetic ratio, α_G is a phenomenological Gilbert damping coefficient[5] and $\tau_{\mathbf{n},\mathbf{m}}$ represent the respective current-induced torques discussed above. The effective fields are given in equations (3.27) and read

$$\begin{aligned} \mathbf{B}^{\text{AFM}}_{\text{eff},\mathbf{n}} &= \frac{2A}{M_{\text{s}}}\nabla^2\mathbf{n} + B_{\text{an}}(\mathbf{n}\cdot\hat{z})\hat{z} + B_{\text{d}}(\mathbf{m}\times\hat{z}) + \frac{D}{M_{\text{s}}}\Big[(\nabla\cdot\mathbf{n})\hat{z} - \nabla(\mathbf{n}\cdot\hat{z})\Big], \\ \mathbf{B}^{\text{AFM}}_{\text{eff},\mathbf{m}} &= -2B_{\text{exch}}\mathbf{m} + \mathbf{B} - B_{\text{d}}(\mathbf{n}\times\hat{z}). \end{aligned} \tag{4.11}$$

Writing out the torques explicitly, the Landau-Lifshitz-Gilbert equations (4.10) become

$$\begin{aligned} \dot{\mathbf{n}} &= \gamma\Big[\mathbf{n}\times\mathbf{B}^{\text{AFM}}_{\text{eff},\mathbf{m}}\Big] + \frac{\eta}{2}(\mathbf{j}\cdot\nabla)\mathbf{n} - \frac{C_1}{2}\mathbf{n}\times(\hat{z}\times\mathbf{j}), \\ \dot{\mathbf{m}} &= \gamma\Big[\mathbf{n}\times\mathbf{B}^{\text{AFM}}_{\text{eff},\mathbf{n}} + \mathbf{m}\times\mathbf{B}^{\text{AFM}}_{\text{eff},\mathbf{m}}\Big] + \alpha_G\mathbf{n}\times\dot{\mathbf{n}} + \frac{\eta}{2}\mathbf{m}\times\Big[(\mathbf{j}\cdot\nabla)\mathbf{n}\times\mathbf{n}\Big] \\ &\quad + \frac{\beta}{2}(\mathbf{j}\cdot\nabla)\mathbf{n}\times\mathbf{n} - \frac{C_1}{2}\mathbf{m}\times(\hat{z}\times\mathbf{j}) - \frac{C_2}{2}\mathbf{n}\times\Big[\mathbf{n}\times(\hat{z}\times\mathbf{j})\Big]. \end{aligned} \tag{4.12}$$

Here, only terms to leading order in B_{exch} have been kept, apart from the η and C_1 ones in the second line, which we retained in order to keep the constraints $\mathbf{n}^2 = 1$ and $\mathbf{n}\cdot\mathbf{m} = 0$ fulfilled. The term containing the effective field $\mathbf{B}^{\text{AFM}}_{\text{eff},\mathbf{m}}$ on the second line is of subleading order in B_{exch}; however, it is of the same order as the left hand side after substituting equation (4.13) below and needs to be kept as well.

---

[5] In the notation of [60], this is the G_2 damping constant.

An expression for the total magnetization can be obtained from the equation for $\dot{\mathbf{n}}$:

$$\mathbf{m} = \frac{1}{2\gamma B_{\text{exch}}}\mathbf{n}\times\dot{\mathbf{n}} + \mathbf{m}_0 - \frac{\eta}{4\gamma B_{\text{exch}}}\mathbf{n}\times(\mathbf{j}\cdot\nabla)\mathbf{n} + \frac{C_1}{4\gamma B_{\text{exch}}}\mathbf{n}\times[\mathbf{n}\times(\hat{z}\times\mathbf{j})]\,, \tag{4.13}$$

where the static magnetization $\mathbf{m}_0$ is given in equation (3.28). As discussed in section 3.3.1, we neglect the homogeneous Dzyaloshinskii-Moriya contribution B_{d} in the following.

Next, we substitute equation (4.13) into the second line of equation (4.12) and obtain a closed equation for the Néel order parameter

$$\mathbf{n}\times\ddot{\mathbf{n}} = \mathbf{B}_{\text{shape}} + \mathbf{B}_{\text{forces}}. \tag{4.14}$$

Here, we have grouped the right hand side into terms that determine the shape of the antiferromagnetic texture and terms that induce or affect its motion. The fields are given by

$$\begin{aligned}\mathbf{B}_{\text{shape}} &= 2\gamma\dot{\mathbf{n}}(\mathbf{n}\cdot\mathbf{B}_{\text{ext,eff}}) + 2B_{\text{exch}}\gamma^2\Big(\mathbf{n}\times\mathbf{B}^{\text{AFM}}_{\text{eff},\mathbf{n}}\Big) - \gamma^2(\mathbf{n}\times\mathbf{B}_{\text{ext,eff}})(\mathbf{n}\cdot\mathbf{B}_{\text{ext,eff}}),\\ \mathbf{B}_{\text{forces}} &= -\eta\gamma B_{\text{exch}}\mathbf{n}\Big[(\mathbf{j}\cdot\nabla)\mathbf{n}\cdot\mathbf{m}\Big] + \beta\gamma B_{\text{exch}}(\mathbf{j}\cdot\nabla)\mathbf{n}\times\mathbf{n} \\ &\quad - C_2\gamma B_{\text{exch}}\mathbf{n}\times\Big[\mathbf{n}\times(\hat{z}\times\mathbf{j})\Big] + 2\alpha_G\gamma B_{\text{exch}}\mathbf{n}\times\dot{\mathbf{n}},\end{aligned} \tag{4.15}$$

where the external effective field contains both the magnetic field and the current-induced contribution $\mathbf{B}_{\text{ext,eff}} = \mathbf{B} - C_1/2\gamma(\hat{z}\times\mathbf{j})$.

In deriving the equation for the Néel order parameter only terms up to linear order in $\dot{\mathbf{n}}$ and $\mathbf{j}$ have been kept. An example of a term of higher order that has been omitted is $\mathbf{n}\times(\mathbf{j}\cdot\nabla)\dot{\mathbf{n}}$.

Equation (4.14) is an important result of this work and describes the magnetization dynamics of a uniaxial antiferromagnet, with inversion symmetry broken along the $\hat{z}$-direction, under the influence of an external time-independent magnetic field and DC electric current.

Current-driven skyrmion motion

Next, we apply the collective-coordinate approach to the translational motion of an antiferromagnetic skyrmion to analyze its current-induced dynamics (see section 2.2.2). We assume that the skyrmion profile is composed of a static, cylindrical and rigid component $\mathbf{n}_{\text{sk}}$ and motion- and current-induced corrections $\delta\mathbf{n}$ that break the cylindrical symmetry (see section 3.3.2). For the time evolution we use the ansatz $\mathbf{n}(\mathbf{r},t) = \mathbf{n}(\mathbf{r}-\mathbf{R}(t))$, where $\mathbf{n} = \mathbf{n}_{\text{sk}} + \delta\mathbf{n}$ and $\mathbf{R}(t)$ is the skyrmion position. As collective coordinates we take $\{\xi_i\} = \{R_x, R_y\}$.

Throughout this section we assume that the skyrmion velocity v_{sk} is small compared to the magnon velocity c ($v_{\text{sk}} \ll c$), which is the limiting velocity in antiferromagnets. The latter is due to the Lorentz-invariance of the antiferromagnetic magnetization dynamics [50, 109]. As a consequence, the corrections can be assumed small, $|\delta\mathbf{n}| \ll |\mathbf{n}_{\text{sk}}|$.

We multiply (4.14) by $\mathbf{n}\times\partial\mathbf{n}/\partial x_\alpha$[6] for $\alpha = x, y$ and integrate over space. We use the equilibrium profile found in section 3.3.2 for $\mathbf{n}_{\mathrm{sk}}$ so that, upon projection, the terms given by $\mathbf{B}_{\mathrm{shape}}$ do not contribute to the equation of motion (see Appendix B.3 for details). To leading order in the electric currents the equation for the skyrmion position becomes

$$m_{\mathrm{eff}}\ddot{\mathbf{R}} = -\Gamma\dot{\mathbf{R}} + \Delta\mathbf{j}. \tag{4.16}$$

The coefficients read

$$\begin{aligned} m_{\mathrm{eff}} &= \frac{M_{\mathrm{s}}}{\gamma^2}\frac{x_0}{2B_{\mathrm{exch}}}, \\ \Gamma &\simeq -\frac{M_{\mathrm{s}}}{\gamma}x_0\,\alpha_G, \\ \Delta &\simeq \frac{M_{\mathrm{s}}}{2\gamma}\left[\beta x_0 - C_2 x_0^2 I_{\mathrm{AFM}}\right], \end{aligned} \tag{4.17}$$

where Γ represents a friction term and Δ characterizes the effect of the dissipative current-induced torques. The dimensionless constant I_{AFM} is determined by the skyrmion profile and we evaluate it in Appendix B.4. The characteristic length-scale x_0 is the domain wall width of the antiferromagnet and is given in equation (3.33). The skyrmion motion described by equation (4.16) is schematically depicted in figure 4.2.

The dependence of the effective mass m_{eff} on the exchange constant B_{exch} is the main difference compared to ferromagnetic skyrmion motion and results from the different nature of the magnetization dynamics in antiferromagnets. A relation for the effective mass similar to equation (4.16) has also been obtained for domain walls in antiferromagnets [109].

In deriving equation (4.16) we have considered both homogeneous and inhomogeneous current-induced torques, as well as an external magnetic field applied in the

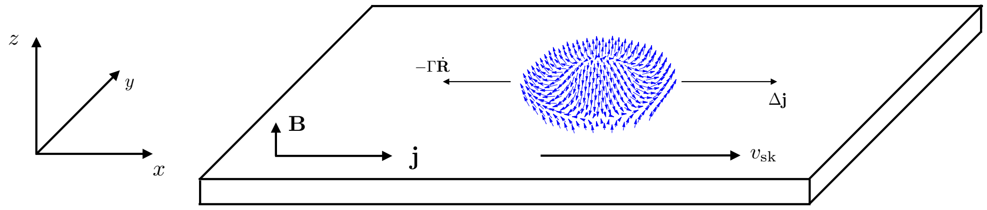

Figure 4.2: *Schematic representation of the skyrmion motion in an antiferromagnet driven by an electric current* $\mathbf{j} \parallel \hat{x}$ *and an external magnetic field* $\mathbf{B} \parallel \hat{z}$*, as described by equation (4.16). The friction force is denoted by* $\Gamma\dot{\mathbf{R}}$ *and the longitudinal current-induced force by* $\Delta\mathbf{j}$*. The combination of these forces leads to a skyrmion motion with the velocity* v_{sk}*. For simplicity, a static skyrmion shape is depicted, without taking into account the shape changes that the magnetic field and the electric current induce.*

---

[6] The choice of this factor comes from general considerations for the conserved quantities in the system. For the translational motion, the relevant quantity is the momentum [50]. Note that this also agrees with the approach taken in reference [61].

$\hat{z}$-direction. Thus, our results paint a richer picture of the current-induced antiferromagnetic skyrmion motion than discussed recently. References [52, 53] predicted longitudinal current-induced forces on the skyrmion position, as opposed to the ferromagnetic skyrmion motion, where the nonzero magnetization always leads to a transverse force. Reference [53] dealt with homogeneous torques only, whereas in reference [52] only inhomogeneous torques have been considered. In both references no magnetic field has been included. We find, that even in the presence of an applied field the skyrmion motion remains longitudinal. This is further substantiated by the findings of references [50, 114], where it is shown that gyroscopic forces (which are linear in the magnetic field) are not present in antiferromagnets for objects that exhibit the topology of skyrmions.

For an electric current applied in the $\hat{x}$-direction, an expression for the longitudinal velocity v_{sk} can be readily obtained by the steady-state solution of equation (4.16), which yields

$$v_{\mathrm{sk}} = -\left[\frac{\beta}{2\alpha_G} - \frac{C_2 x_0}{2\alpha_G} I_{\mathrm{AFM}}\right] j_x \equiv v_{\mathrm{sk},\beta} + v_{\mathrm{sk},C_2}. \tag{4.18}$$

This is the velocity corresponding to the zero-field scenario considered in references [52, 53].

Current-driven skyrmion velocity

Now, we are in a position to give an estimate for the magnitude of the longitudinal skyrmion velocity in equation (4.18). The constant $I_{\mathrm{AFM}} = 1.56$ has been evaluated in Appendix B.4. We estimate the spin-orbit torque coefficient to be $C_2 \simeq 3.4 \times 10^{-3}\,\mathrm{m^2\,A^{-1}\,s^{-1}}$ (see Appendix B.5). The Gilbert damping parameter is $\alpha_G \simeq 0.01$ [60]. The characteristic length of the system is of the order of the skyrmion size, which is typically $x_0 \simeq 10^{-8}\,\mathrm{m}$ [51, 60, 61]. Typical experimentally used current densities in ferromagnets are of the order of $j \simeq 10^{11}\,\mathrm{A\,m^{-2}}$ [73]. With this, we estimate

$$v_{\mathrm{sk},C_2} \simeq 265\,\mathrm{m\,s^{-1}}. \tag{4.19}$$

In contrast, reference [53] predicts a skyrmion velocity of $\sim 1700\,\mathrm{m\,s^{-1}}$. In that work, homogeneous torques of a similar form, but of different origin have been considered. The homogeneous torques there arise from a spin-polarized current injected vertically into the system, whereas the homogeneous torques in the present work are due to the spin-orbit coupling in the antiferromagnet. Using the values that they provide (see Table 4.2), we arrive at $v_{\mathrm{sk},C_2} \simeq 500\,\mathrm{m\,s^{-1}}$, which has the same order of magnitude as the result of reference [53].

In equation (4.12) the dissipative spin-transfer torque coefficient β has dimensions of $\mathrm{m^3\,A^{-1}\,s^{-1}}$. Its dimensionless counterpart $\tilde{\beta}$ is obtained through $\tilde{\beta} = \beta n e$, where n is the electron density and e the electron charge. Typically, in ferromagnetic systems this value is taken to be of the order of the Gilbert damping, $\tilde{\beta} \simeq \alpha_G$ [115]. Typical metallic electron densities are of the order of $n \simeq 10^{29}\,\mathrm{m^{-3}}$ so that for these parameters we find

$$v_{\mathrm{sk},\beta} \simeq 5\,\mathrm{m\,s^{-1}}. \tag{4.20}$$

Parameters	Units	This work	Zhang *et al.* [53]	Barker *et al.* [52]**
α_G	–	0.01	0.3	0.01
C_2	$\mathrm{m^2\,A^{-1}\,s^{-1}}$	0.0034	$0.2^\star$	–
β	–	0.01	–	0.1
x_0	nm	10	10	–
j	$\mathrm{A\,m^{-2}}$	10^{11}	10^{11}	$3.2 \times 10^{12\star\star\star}$
Estimated				
v_{sk,C_2}	$\mathrm{m\,s^{-1}}$	265	520	–
$v_{\mathrm{sk},\beta}$	$\mathrm{m\,s^{-1}}$	5	–	1000
Numerical results				
v_{sk}	$\mathrm{m\,s^{-1}}$	–	~ 1700	~ 2000

*This value has been calculated from the expression that the authors provide in reference [53] for their Slonczewski-like spin-transfer torque coefficient $\beta = |\hbar/(\mu_0 e)|\,P/(2dM_\mathrm{s})$, multiplied by the gyromagnetic ratio $|\gamma| = 2.211 \times 10^5\,\mathrm{m\,A^{-1}\,s^{-1}}$. Here, $\hbar$ is the reduced Planck constant, μ_0 the vacuum permeability, e the electron charge, $P = 0.4$ is the polarization rate of the spin-polarized current, $d = 0.4\,\mathrm{nm}$ the film thickness and $M_\mathrm{s} = 290\,\mathrm{kA\,m^{-1}}$ is the saturation magnetization;
**We focus only on one set of values for α_G, β and v of the range provided in reference [52];
***The authors use a value of $j = 200\,\mathrm{m\,s^{-1}}$ for the drift velocity of the electrons. We calculate the corresponding current density by taking the electron density to be $n \simeq 10^{29}\,\mathrm{m^{-3}}$.

Table 4.2: *Estimated velocities of the antiferromagnetic skyrmion using the parameters from the present work and from references [52, 53]. In all cases the velocities* v_{sk,C_2} *and* $v_{\mathrm{sk},\beta}$ *are estimated according to the expressions in equation (4.18). The numerical results for* v_sk *are taken from references [53] and [52], respectively.*

This component of the velocity corresponds to the skyrmion velocity discussed in reference [52]. Our estimate agrees with the findings of that work for the same choice of parameters (see Table 4.2).

Typical magnon velocities in antiferromagnets are of the order of $c \simeq 30\,\mathrm{km\,s^{-1}}$ (see references [109, 116]). The largest estimate of the skyrmion velocity that we obtained, using the parameters of reference [52] (Table 4.2), is still much smaller than the magnon velocity. This justifies our assumption of slow skyrmion dynamics.

4.1.3 Summary

We extended the phenomenological theory of a collinear two-sublattice antiferromagnet with uniaxial anisotropy and interfacial Dzyaloshinskii-Moriya interactions to incorporate the current-induced spin-orbit torques, together with the already studied spin-transfer torques. We used this theory to analyze the translational skyrmion motion in the presence of an out-of-plane, time-independent external magnetic field and a DC electric current. We find that the magnetic field merely modifies the shape of the antiferromagnetic skyrmion (see also section 3.3.2) and does not contribute towards the skyrmion motion. Further, our results show that the skyrmion moves in a straight line, along the direction of the applied electric current. This agrees with the numerical results of references [52, 53], which were obtained for skyrmions in the absence of a magnetic field. Depending on the choice of parameters, we find skyrmion velocities that are in the range of $1 - 1000\,\mathrm{m\,s^{-1}}$, also in agreement with numerical results [52, 53]. Finally, we find that attainable velocities are not high enough to induce sizeable deformation of the antiferromagnetic skyrmion.

In ferromagnets, the current-induced skyrmion motion has been studied extensively (e.g., see references [25, 43, 73, 79, 110, 111]). Here, we reviewed mainly the results of reference [73], where a similar phenomenological model is constructed: a uniaxial ferromagnet with interfacial Dzyaloshinskii-Moriya interactions in the presence of electric currents that induce both spin-transfer and spin-orbit torques. The effective equation of motion in terms of the collective position coordinates shows that the ferromagnetic skyrmions has both longitudinal and transversal velocity components. The estimated skyrmion velocities are of the order of $10\,\mathrm{m\,s^{-1}}$ for typical ferromagnetic parameters, in agreement with numerical results [25, 27, 110].

The analysis in this section highlights the principal difference of the magnetization dynamics in ferromagnets and antiferromagnets [45]. The ferromagnetic dynamics are intrinsically gyrotropic, as can be seen from the appearance of the Magnus force term in the effective equation of motion (4.5) for the ferromagnetic skyrmion. Further, the ferromagnetic Landau-Lifshitz-Gilbert equation is formulated in terms of the angular momentum of the system. In contrast, the antiferromagnetic dynamics are Newton-like: the corresponding Landau-Lifshitz-Gilbert equations result in an equation of forces for the Néel vector due to the presence of the second derivative with respect to time. The much higher skyrmion velocities in antiferromagnets can be traced back to the faster magnetization dynamics due to the strong exchange interactions – which is another key difference between ferromagnets and antiferromagnets [44, 117].

In conclusion, we note that current-induced ferromagnetic skyrmion motion has already been experimentally observed [29], whereas there has been no experimental observation of antiferromagnetic skyrmions yet.

4.2 Eigenmodes of confined skyrmions

In this section, we investigate numerically the confined skyrmion dynamics for both ferromagnets and antiferromagnets. Unlike the previous section, where we studied the current-driven translational motion of isolated skyrmions in a thin-film infinite plane, here we focus on the lowest-frequency eigenmodes of isolated skyrmions confined in thin-film nanodisks.

The eigenmodes of ferromagnetic skyrmions have been studied in recent literature; however, there has been no treatment of the same model and with the same finite-element method calculating the eigenfrequencies directly in frequency space, which reveals the full excitation spectrum. In antiferromagnets, there has been no investigation of the skyrmion eigenmodes yet.

Prior to the discovery of skyrmions, magnetic vortices and their excitations have been studied intensely in the context of modern information technology devices. Vortices are found in samples that are magnetized in-plane and are described by a magnetization vector curling in-plane around its core, where the magnetization is pointing out of the plane (as such, they represent "half-skyrmions"). For a given material, the vortex core can point either in the positive or negative out-of-plane direction. This is characterized by the core polarity, defined as the value of the $\hat{z}$-component of the magnetization vector at the core $p = m_z(r = 0) = \pm 1$. In finite samples gyrations of the vortex around its equilibrium position at zero external field occur in the opposite direction for both vortex polarities and have the same frequency. Recent research demonstrates that these gyrotropic modes can be used for a novel microwave frequency-controlled memory device [118]. The device exploits the frequency splitting of the clockwise and counterclockwise gyrotropic modes of the vortex (related to the core polarity $p = \pm 1$) induced by the application of an external magnetic field.

The excitations of magnetic skyrmions, similar to vortices, present another intriguing direction of modern research. As discussed in chapter 1, skyrmions are an intriguing candidate as the core element in technology applications, e.g., skyrmion racetrack memory or spin-torque oscillators [20, 43, 118, 119, 120]. The latter rely on the geometric confinement and the gyrotropic nature of the skyrmion dynamics [43]. In addition, novel methods to manipulate skyrmions (alternative to using electric currents) have been proposed, in which oscillating magnetic fields induce skyrmion motion by coupling to its excitation modes – superposed gyrotropic [121] and breathing modes [122].

Spin-wave excitations in vortices and magnetic skyrmions are generally found in the GHz range. Therefore, microwaves (frequencies ranging from few hundreds of MHz to a few hundreds of GHz) have been used to experimentally excite and observe excitation modes of skyrmion lattices [38, 39, 40, 41]. Theoretical studies predicted two gyrotropic and one breathing modes for skyrmion lattices [34], whereas the experimental works showed contradicting results[7]. Further, there is no

---

[7] A single gyrotropic and one breathing mode are observed in references [38, 39]; reference [41] reports no breathing mode and either two or one gyrotropic modes, depending on the material; both gyrotropic modes are observed in reference [40] and indirect evidence is presented for the existence of a breathing mode.

experimental evidence of the gyrotropic modes of an isolated skyrmion yet. Thus, a good understanding of the skyrmion excitations is still elusive.

In the following, we present our numerical simulations on the isolated skyrmion dynamics in confined nanodisks. First, we summarize relevant results from recent literature on the ferromagnetic skyrmion eigenmodes in section 4.2.1. We present the results of our numerical simulations for the ferromagnet in section 4.2.2, and for the antiferromagnet in section 4.2.3. The calculation of the excitation modes consists of two steps: first, we determine the groundstate texture of the magnetic nanodisk; then, we calculate the eigenmode spectrum of the relaxed equilibrium state.

4.2.1 Literature review

Ferromagnetic skyrmions have been studied extensively in recent years; the field of antiferromagnetic skyrmions is still in its infancy. Here, we summarise relevant results for stabilization of skyrmions, as well as results for skyrmion dynamics and eigenmodes.

Statics

The stability of ferromagnetic skyrmions – in lattices and as individual skyrmions, both in bulk materials and thin films – is a widely established fact, both theoretically and experimentally [10, 20]. We emphasize that a ferromagnetic confined skyrmion can be a metastable state or a groundstate, depending on the strength of the Dzyaloshinskii-Moriya interactions [26] (see also section D.3 and figure D.9). Further studies have demonstrated the stability of the skyrmion state in the presence of a static external magnetic field along the easy axis [36]. Both references [26, 36] use a micromagnetic model similar to ours. The results show that the stronger the Dzyaloshinskii-Moriya interactions, the larger the skyrmion becomes; depending on the relative orientation of the magnetic field and the skyrmion core, the skyrmion size is either reduced (antiparallel orientation) or increased[8] (parallel orientation).

In another recent study, stable confined skyrmions have been found in the absence of uniaxial anisotropy and external field [123]. There, the skyrmions are stabilized entirely due to the bulk Dzyaloshinskii-Moriya interactions and the demagnetization field. The authors consider thicker samples ($\sim 10\,\mathrm{nm}$) and allow for variation of the magnetization vector along the out-of-plane direction. It is shown that skyrmions can be found as groundstate for a large range of the external field (including zero field) and adapt their size to the size of nanodisk, similar to anisotropy-stabilized skyrmions. The model presented in reference [123] is significantly different from ours.

Antiferromagnetic skyrmions have been predicted to exist both theoretically [13, 50, 51] and numerically [52, 53, 54, 56, 57]; however, there has not been an experimental observation yet. Further, no studies exist focusing on antiferromagnetic skyrmions confined in thin film nanodisks, which is what we do in the present work.

---

[8] However, the confining potential can counteract the increase of the skyrmion size [36].

Reference	$f_{\mathrm{gyrotropic}}$(GHz)	$f_{\mathrm{breathing}}$(GHz)	R_{disk} (nm)	t (nm)
Moon *et al.* [124]	~ 1	–	80	34.0
Kim *et al.* [36]	–	$2-8^{\star}$	50	1.0
Moon *et al.* [121]	$0; 38^{\star\star}$	8	150	0.4
Mruczkiewicz *et al.* [119]	< 1	$0.7-0.9^{\star\star\star}$	125	1.4
Beg *et al.* [125]****	0.67	2	75	1.0

* These frequency values are reported in reference [36] as a function of the Dzyaloshinskii-Moriya constant and the external magnetic field strength; ** The two values correspond to two gyrotropic modes with a different sense of rotation; *** Different breathing mode frequencies are found in reference [119] as a function of the out-of-plane anisotropy; **** The model used in reference [125] is significantly different from the other references (see the discussion at the end of section 4.2.2).

Table 4.3: *List of gyrotropic and breathing mode frequencies of the isolated ferromagnetic skyrmion confined in a thin film reported in recent literature. Here,* R_{disk} *is the nanodisk radius and* t *its thickness.*

Dynamics

The excitation modes of skyrmions in ferromagnets have been studied previously on several occasions – both of skyrmion lattices and of confined isolated skyrmions – where the attention was focused primarily on gyrotropic and breathing modes. In these studies, the skyrmions were excited with time-dependent external magnetic fields. Fields that are directed out-of-plane do not affect the radial symmetry of the skyrmions and can excite skyrmion breathing modes [36, 119, 121]. In-plane magnetic fields, on the other hand, do break the radial symmetry and can excite gyrotropic modes, as well as other modes that affect the shape of the skyrmion [119, 121].

The gyrotropic modes are found at finite frequencies in the GHz range in ferromagnetic nanodisks. This is a consequence of the finite size of the sample and the resulting skyrmion confinement. In infinite samples, the skyrmion gyrotropic and translational modes (they have the same translational nature) would have zero frequency due to the translational invariance [119].

As a reference, we summarize in Table 4.3 the values of gyrotropic and breathing modes of isolated skyrmion confined in a ferromagnetic nanodisk film, calculated numerically for different models in the recent literature. We do not show results obtained for skyrmion lattices, e.g., by Mochizuki *et al.* [34], or Wang *et al.* [122]. There have been no studies yet targeting the antiferromagnetic excitation modes, prior to this work.

4.2.2 Ferromagnetic skyrmions

Here, we present our results from the numerical simulations for the ferromagnetic skyrmion dynamics. We obtain a skyrmion equilibrium state confined in a nanodisk and calculate its eigenspectrum. Finally, we compare our results to existing results from the literature.

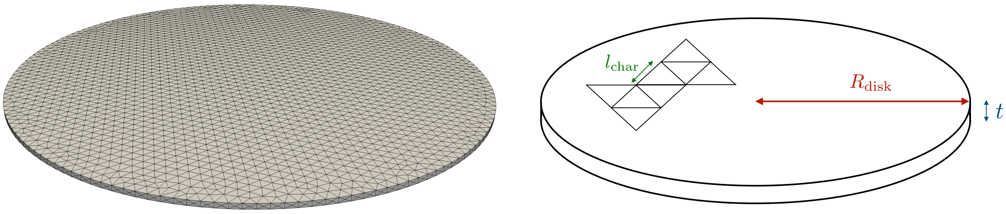

Figure 4.3: *Schematic representation of the thin film nanodisk used for the numerical simulations. The depicted lengthscales – nanodisk radius* $R_{disk} = 50\,\text{nm}$*, thickness* $t = 1\,\text{nm}$ *and characteristic length* $l_{char} = 1\,\text{nm}$ *– and line segments are not up to scale.*

The discussion in the entire chapter is based on nanodisks of radius $R_{\text{disk}} = 50\,\text{nm}$, thickness $t = 1\,\text{nm}$ and a characteristic length $l_{\text{char}} = 1\,\text{nm}$ (see figure 4.3), unless explicitly stated otherwise.

The first step towards finding the magnetization dynamics of any magnetic texture, is to find its equilibrium state. To do so, we use the model presented in section 3.2 and apply the numerical methods discussed in section 2.3.2. We make a choice for the initial state and let it relax to equilibrium.

The relaxation process is governed by the effective field of the ferromagnet (see section 2.3.2 and equation (3.8)). Within the finite element framework, we transform the effective field to its weak formulation

$$\begin{aligned}
\frac{1}{B_{\text{s}}}\int_V d^3r\Big(\mathbf{B}_{\text{eff}}\cdot\mathbf{v}\Big) = &-l_{\text{ex}}^2\int_V d^3r\Big(\nabla\mathbf{v}\cdot\nabla\mathbf{u}\Big)\\
&+\frac{B_{\text{u}}}{B_{\text{s}}}\int_V d^3r\Big(\mathbf{u}\cdot\hat{z}\Big)\Big(\mathbf{v}\cdot\hat{z}\Big)\\
&+\frac{B}{B_{\text{s}}}\int_V d^3r\Big(\mathbf{v}\cdot\hat{z}\Big)\\
&+l_{\text{DM}}\int_V d^3r\Big[\left(\nabla\cdot\mathbf{u}\right)\left(\mathbf{v}\cdot\hat{z}\right)-\mathbf{v}\cdot\nabla\left(\mathbf{u}\cdot\hat{z}\right)\Big]\\
&+\frac{l_{\text{DM}}}{2}\oint_{\partial V} d^2r\Big[\mathbf{u}\times\Big(d\hat{\mathbf{S}}\times\hat{z}\Big)\Big]\cdot\mathbf{v},
\end{aligned}\tag{4.21}$$

where $\mathbf{u}$ is the (unknown) trial function to be calculated and $\mathbf{v}$ the corresponding test function (see section 2.3.1)[9]. We solve the projected Landau-Lifshitz-Gilbert equation (2.31) numerically until the right hand side does not produce a torque on the magnetization vector anymore (zero-torque condition). During this process, we make sure that convergence is reached within the numerical precision of the simulation by tracking the change of the magnetization vector every few steps. The resulting texture $\mathbf{m}$ is the equilibrium state.

The model is parametrized by the saturation magnetization, exchange stiffness, uniaxial anisotropy constant, external magnetic field and the Dzyaloshinskii-Moriya interactions constant. We choose the parameter values to be in the range typical for ferromagnetic thin films with perpendicular anisotropy (see references

---

[9] See also section 5.1 and the corresponding code in listing 5.5.

Parameter	Value	Unit
M_s	1.0	$\mathrm{MA\,m^{-1}}$
A_ex	15.0	$\mathrm{pJ\,m^{-1}}$
K_u	371.4	$\mathrm{kJ\,m^{-3}}$
D	3.5	$\mathrm{mJ\,m^{-2}}$

Rescaled parameter	Value	Unit
B_s	1.26	T
l_ex	4.89	nm
B_u	0.74	T
l_DM	5.57	nm

Table 4.4: *List of the parameters used to obtain the ferromagnetic skyrmion groundstate and its excitations. Here,* $M_s(B_s)$ *is the saturation magnetization (field),* $A_{ex}(l_{ex})$ *the exchange stiffness parameter (exchange length),* $K_u(B_u)$ *the uniaxial anisotropy constant (field),* $D(l_{DM})$ *the Dzyaloshinskii-Moriya interactions constant (length) and* $B = 0\,\mathrm{T}$ *the external magnetic field. We show both the physical and the rescaled parameters that enter the energy functional (3.7) and the weak formulations (4.21) and (4.23), respectively. For the eigenspectrum calculation we set the Lagrange multiplier to* $\Lambda = 500\,B_s$.

[29, 36, 105]) and list them in Table 4.4. The relevant lengthscales of the model are the exchange length $l_\mathrm{ex} = 4.89\,\mathrm{nm}$, Dzyaloshinskii-Moriya length $l_\mathrm{DM} = 5.57\,\mathrm{nm}$, characteristic length (domain wall width) $x_0 = 6.36\,\mathrm{nm}$ and the cycloid length $2\pi\xi_\mathrm{FM} = 4\pi A_\mathrm{ex}/D = 53.85\,\mathrm{nm}$[10] [26] (see also the right part of Table 4.4). The cycloid length is comparable to the nanodisk radius, which already suggests that skyrmions are possible in the present setup.

Depending on the chosen initial state, different equilibrium configurations can be reached. We investigate these and compare their energies in Appendix D.2. We find that the skyrmion configuration has the lowest energy and is, therefore, the groundstate.

The initial state we use to obtain the skyrmion is defined in Appendix D.1 and shown in figure 4.4[11]. It consists of magnetization $\mathbf{m}(\mathbf{r})$ pointing in the positive $\hat{z}$-direction within a radius R_init and in the positive $\hat{z}$-direction outside of it. At

	Parameter	Value	Unit
saturation field	B_s	$\mu_0 M_\mathrm{s}$	T
exchange length	l_ex	$\sqrt{2A_\mathrm{ex}/(M_\mathrm{s}B_\mathrm{s})}$	m
anisotropy field	B_u	$2K_u/M_\mathrm{s}$	T
DM length	l_DM	$2D/(M_\mathrm{s}B_\mathrm{s})$	m

Table 4.5: *Definition of the rescaled parameters that enter the weak formulation in equation (4.21). Here,* μ_0 *is the vacuum permeability, DM stands for Dzyaloshinskii-Moriya and the corresponding physical parameters are listed in Table 4.4.*

---

[10] As a consequence, for the present set of parameters the chosen characteristic (discretization) length $l_\mathrm{char} = 1\,\mathrm{nm}$ is sufficiently small to not introduce spurious numerical effects.

[11] See also Appendix D.3 for a discussion on the stability of the skyrmion with respect to the quasi-uniform state.

(a) m_x (b) m_y (c) m_z

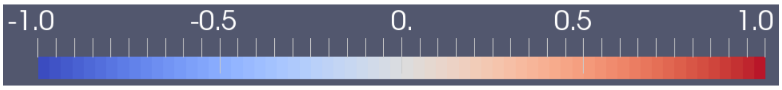

(d) Color Bar

Figure 4.4: *Visualisation of the magnetization components of the initial skyrmion state with* $R_{init} = 15\,\mathrm{nm}$.

about $r = R_{\mathrm{init}}$, the magnetization vector starts canting in the radial direction, so that a (relatively sharp) Néel domain wall occupies the transition region.

The relaxed state is shown in figure 4.5. We find that, for the chosen set of parameters, the Néel domain wall in the transition region of the skyrmion is smoothened with respect to the initial state. This increases the exchange and anisotropy energies, but lowers the Dzyaloshinskii-Moriya energy, so that the total energy is reduced. The canting of the magnetization remains in the radial direction, since this type of rotation is favored by the interfacial Dzyaloshinskii-Moriya interactions assumed in the present model. Further, we observe that the magnetization at the boundary of the nanodisk does not remain uniform and tilts radially inwards, as prescribed by the Dzyaloshinskii-Moriya-induced boundary conditions (see Appendix A.2 and reference [26]). The chirality of tilting here is determined by the sign of the Dzyaloshinskii-Moriya constant D; here it is negative.

Following the work by Rohart *et al.* [26], we calculate the confined skyrmion profile by minimizing the energy functional (3.7), while taking into account the modified boundary conditions induced by the Dzyaloshinskii-Moriya interactions. The resulting skyrmion profile equation (3.14) by fixing as initial conditions $\theta(r = 0) = 0$ and $d\theta/dr(r = 0)$ such, that the modified boundary condition (D.8) is met (see Appendix D.3). We plot the skyrmion profile solution in figure 4.6 and include for comparison the simulation results for different values of R_{init}. We find a very good agreement between the numerically relaxed and analytically predicted skyrmion profiles.

The present skyrmion is stabilized largely due to DM-induced boundary conditions and the resulting confining potential of the nanodisk edges [26]. An important consequence is that for values of $D > D_0$, the skyrmion radius depends on the size of the nanodisk (see Appendix D.3 and figure D.8). For the parameters used here this condition is fulfilled, as the threshold Dzyaloshinskii-Moriya constant

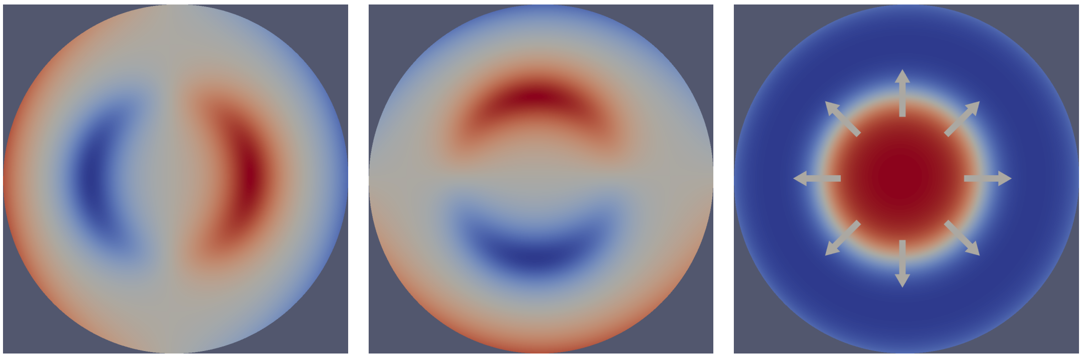

(a) m_x (b) m_y (c) m_z

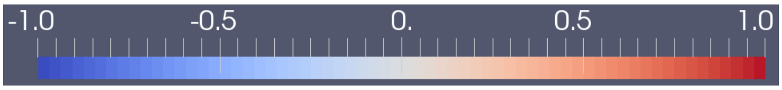

(d) Color Bar

Figure 4.5: *Visualisation of the relaxed skyrmion groundstate. Shown are the components of the magnetization vector* $\mathbf{m}$*. Note the spread out Néel domain wall between the core and the outer part of the skyrmion, as well as the canting at the nanodisk boundaries compared to the initial state in figure 4.4.*

$D_0 = 4/\pi\sqrt{A_{\mathrm{ex}}K_u} = 3\,\mathrm{mJ\,m^{-2}}$ (see section 3.2.2) is smaller than $D = 3.5\,\mathrm{mJ\,m^{-2}}$. For $D < D_0$, the skyrmion radius is fixed and independent of the nanodisk, because the skyrmion is too small to feel the effect of the edges.

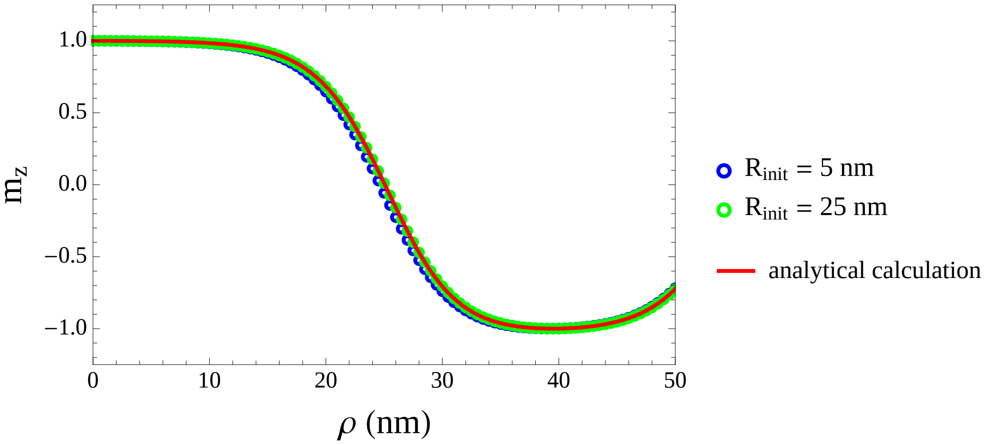

Figure 4.6: *Profile of the relaxed ferromagnetic skyrmion for the parameter set shown in Table 4.4. The solid line is the numerical integration of the profile equation (D.7) with the boundary condition (D.8). The open circles are the results of the numerical simulations for different values of the initial radius: the profiles for* $R_{init} = 5, 10, 15, 20\,\mathrm{nm}$ *and* $R_{init} = 25, 30, 35, 40\,\mathrm{nm}$ *are identical and we have plotted one from each group in blue and green color, respectively.*

Dynamics

Having obtained the equilibrium skyrmion state, we turn our attention now to finding its low-energy excitations. We consider small deviations $\delta\mathbf{m}$ from the equilibrium $\mathbf{m}_0$, plug them into the dissipationless Landau-Lifshitz-Gilbert equation (2.36) and expand to first order in $\delta\mathbf{m}$. After transforming to frequency space, we find the linearized Landau-Lifshitz-Gilbert equation (see section 2.3.2)

$$i\omega\delta\mathbf{m} = -\gamma\mathbf{m}_0 \times \mathbf{B}_{\mathrm{eff}}[\delta\mathbf{m}] - \gamma\delta\mathbf{m} \times \mathbf{B}_{\mathrm{eff}}[\mathbf{m}_0] + \Lambda\left(\mathbf{m}_0 \cdot \delta\mathbf{m}\right)\mathbf{m}_0, \tag{4.22}$$

where ω is the frequency of the eigenmode $\delta\mathbf{m}$, $\mathbf{B}_{\mathrm{eff}}$ the effective field and Λ a Lagrange multiplier that ensures that the modes we obtain are not longitudinal excitations of the magnetization vector $\mathbf{m}_0$. For the model under consideration (3.7), we transform equation (4.22) to its weak formulation

$$\begin{aligned}
-\frac{i\omega}{\gamma B_{\mathrm{s}}}\int_V d^3r\,(\mathbf{u}\cdot\mathbf{v}) = &-l_{\mathrm{ex}}^2\int_V d^3r\left[\nabla\Big(\mathbf{v}\times\mathbf{m}_0\Big)\cdot\nabla\mathbf{u} + \nabla\Big(\mathbf{v}\times\mathbf{u}\Big)\cdot\nabla\mathbf{m}_0\right]\\
&+\frac{B_{\mathrm{u}}}{B_{\mathrm{s}}}\int_V d^3r\left[(\mathbf{u}\cdot\hat{z})\,(\mathbf{m}_0\times\hat{z})\cdot\mathbf{v} + (\mathbf{m}_0\cdot\hat{z})\,(\mathbf{u}\times\hat{z})\cdot\mathbf{v}\right]\\
&+\frac{B}{B_{\mathrm{s}}}\int_V d^3r\,(\mathbf{u}\times\hat{z})\cdot\mathbf{v}\\
&+l_{\mathrm{DM}}\int_V d^3r\Bigg[(\nabla\cdot\mathbf{u})\,(\mathbf{m}_0\times\hat{z})\cdot\mathbf{v} - \mathbf{m}_0\times\nabla\,(\hat{z}\cdot\mathbf{u})\cdot\mathbf{v}\\
&\qquad\qquad + (\nabla\cdot\mathbf{m}_0)\,(\mathbf{u}\times\hat{z})\cdot\mathbf{v} - \mathbf{u}\times\nabla\,(\hat{z}\cdot\mathbf{m}_0)\cdot\mathbf{v}\Bigg]\\
&+\frac{l_{\mathrm{DM}}}{2}\oint_{\partial V} d^2r\Bigg[(\mathbf{v}\times\mathbf{m}_0)\cdot\mathbf{u}\times\left[d\hat{\mathbf{S}}\times\hat{z}\right]\\
&\qquad\qquad + (\mathbf{v}\times\mathbf{u})\cdot\mathbf{m}_0\times\left[d\hat{\mathbf{S}}\times\hat{z}\right]\Bigg]\\
&+\frac{\Lambda}{B_{\mathrm{s}}}\int_V d^3r\,(\mathbf{m}_0\cdot\mathbf{u})\,(\mathbf{m}_0\cdot\mathbf{v})\,,
\end{aligned} \tag{4.23}$$

where this time $\mathbf{u}$ represents the deviations and is the (unknown) trial function and $\mathbf{v}$ its corresponding test function. As discussed in section 2.3.2, equation (4.23) represents a generalized eigenvalue problem

$$\lambda\mathrm{M}\tilde{\mathbf{u}} = \mathrm{A}\tilde{\mathbf{u}}, \tag{4.24}$$

which we solve numerically. Here, we denoted the eigenvalue as $\lambda = -i\omega/\gamma$ and the corresponding eigenvector by $\tilde{\mathbf{u}}$. For the simulations, we use the previously relaxed skyrmion as the equilibrium state $\mathbf{m}_0$ and calculate its lowest eight modes.

Due to the formulation of the problem, we find pairs of complex eigenfrequencies and eigenmodes[12]. The physical modes are obtained from the complex eigenvectors

---

[12] Specifically, this is an artefact of using the Fourier transform $\mathbf{m}(t) \propto \mathbf{m}(\omega)e^{i\omega t}$.

through

$$\delta\mathbf{m}(t) = \mathrm{Re}\{\tilde{\mathbf{u}}\}\cos(\omega t) - \mathrm{Im}\{\tilde{\mathbf{u}}\}\sin(\omega t), \tag{4.25}$$

which also determines their time evolution.

Finally, we construct the full magnetization vector $\mathbf{m}(t)$ of the excitation modes as defined in equation (2.35). For visualization purposes[13], we scale the magnitude of $\delta\mathbf{m}(t)$ by a factor of 100

$$\tilde{\mathbf{m}}(t) = \mathbf{m}_0 + 100 \times \delta\mathbf{m}(t), \tag{4.26}$$

and, subsequently, normalize $\tilde{\mathbf{m}}(t)$.

We list the frequencies of the lowest eight eigenmodes in Table 4.6) and show their time evolution in figures 4.8 and 4.9. Among these, we find excitations of different nature - two gyrotropic modes rotating in opposite directions, a breathing mode and several rotating modes in which the skyrmion core is deformed in higher orders (twofold elongation, triangular distortion, etc.).

The numerical errors listed in Table 4.6 are due to the imprecision of the relaxation solver[14]. The profile of the relaxed ferromagnetic skyrmion as a function of the initial radius R_{init} is shown in figure 4.6. It can be seen that there is a slight deviation

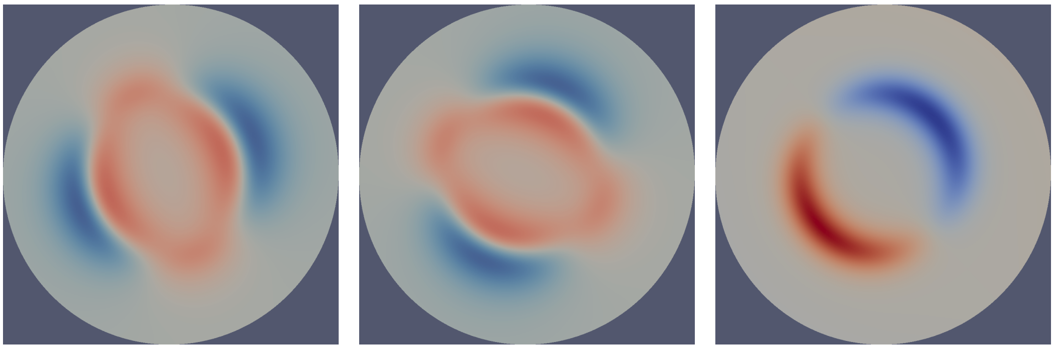

(a) δm_x (b) δm_y (c) δm_z

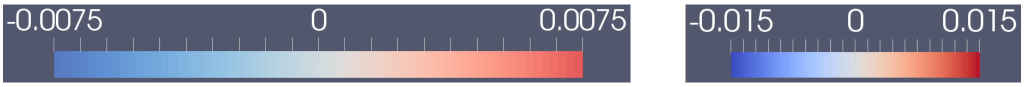

(d) Color Bar ($\delta m_{x,y}$) (e) Color Bar (δm_z)

Figure 4.7: *Visualization of the lowest excited mode of the ferromagnetic skyrmion - the clockwise gyrotropic mode (see Table 4.6 and figures 4.8a - 4.8d for reference). Shown are the components of the magnetization vector* $\delta\mathbf{m}$ *at* $t = 0$ *that represents the deviation from the groundstate* $\mathbf{m}_0$ *shown in figure 4.5. Importantly, the magnitude of* $\delta\mathbf{m}$ *is two orders of magnitude smaller than* $\mathbf{m}_0$*. The full magnetization vector* $\tilde{\mathbf{m}}(t)$*, according to equation (4.26) is shown in figure 4.8a.*

---

[13] We show the magnetization components $\delta\mathbf{m}$ of the lowest excitation mode at $t = 0$ in figure 4.7. Note, that the excitation vector is more than two orders of magnitude smaller than the groundstate magnetization vector $\mathbf{m}_0$, as shown in figure 4.5.

[14] The numerical error of the eigenvalue solver alone is found to be smaller when the relaxation solver is turned off (see the discussion in Appendix D.4).

of the relaxed profile for radii smaller or larger than the analytically predicted one. We present in this section the dynamics of a skyrmion groundstate relaxed from an initial state with $R_{\text{init}} = 15\,\text{nm}$; the numerical errors are calculated by comparing its frequencies to the ones obtained for the skyrmion shown with green symbols in figure 4.6.

The lowest excited mode is a clockwise (CW) gyrotropic mode and has a frequency of $f = 1.13\,\text{GHz}$. We visualize its time evolution in four snapshots at different times during the a full rotation around the nanodisk center in figures 4.8a - 4.8d. Higher in the spectrum we find also a counterclockwise (CCW) gyrotropic mode[15] (see figures figures 4.9e - 4.9h). Its frequency is an order of magnitude higher at $f = 13.04\,\text{GHz}$, so that it is well separated from the clockwise mode – compatible with the numerical results for skyrmion lattices [34]. The sense of rotation of both gyrotropic modes depends on the polarity of the skyrmion. In the present case we have $p = 1$ (skyrmion core pointing in the positive $\hat{z}$-direction), whereas for $p = -1$ we find that the rotation of both modes is reversed. This behaviour is consistent with recent literature results [34, 119, 121, 125, 126][16].

The second-lowest mode is at $f_{2\text{fold}} = 1.31\,\text{GHz}$ and represents an elongation of the skyrmion core along one axis in the plane. Since this mode exhibits a twofold rotational symmetry, we refer to it as the *twofold-deformed skyrmion*, see figures

Mode	Frequency (GHz)	Type	Rotation
1	1.13 ± 0.08	Gyrotropic	CW
2	1.31 ± 0.13	Twofold-deformed	CW
3	3.61 ± 0.35	Threefold-deformed	CW
4	4.95 ± 0.10	Breathing	–
5	8.47 ± 0.91	Fourfold-deformed	CW
6	13.04 ± 0.28	Gyrotropic	CCW
7	15.76 ± 1.65	Fivefold-deformed	CW
8	19.67 ± 0.12	Twofold-deformed	CCW

Table 4.6: *List of the lowest eight excited mode frequencies of the ferromagnetic skyrmion (see figure 4.5 for the equilibrium state). These are obtained for a nanodisk of radius* $R_{disk} = 50\,\text{nm}$*, thickness* $t = 1\,\text{nm}$ *and the material parameters listed in Table 4.4. The excited modes are shown in figures 4.8 and 4.9. CW and CCW stand for clockwise and counterclockwise, respectively.*

---

[15] In reference [126] the authors argue that such a mode does not fulfill all the criteria to be considered gyrotropic, as it is not the lowest-frequency mode. Since it gyrates around the nanodisk center, for simplicity we still refer to it as "gyrotropic" in the following.

[16] We note that the analytic work by Guslienko *et al.* [126] (the same convention is used in reference [119]) predicts a counterclockwise (clockwise) rotation of the gyrotropic mode for polarity $p = +1(-1)$, which is opposite of what we find. However, the authors claim that their prediction is in agreement with the results of reference [125], which match our own results. The confusion originates in the opposite definition of the polarity in the present work and in reference [126] – compare equation (B.29) for which $p = -1$, to the definition of the gyrovector in equation (3) of reference [126], where $p = +1$.

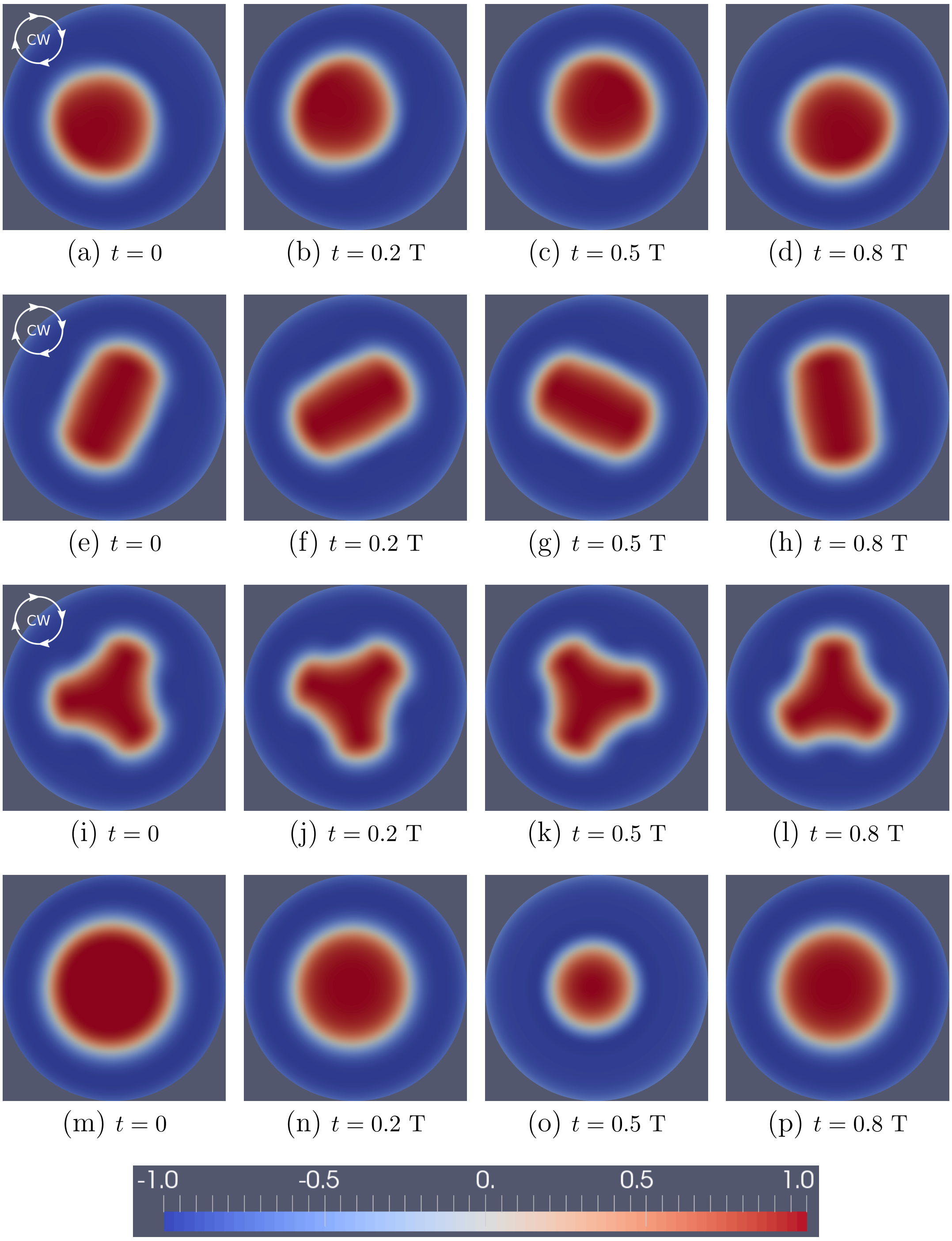

(a) $t = 0$ (b) $t = 0.2$ T (c) $t = 0.5$ T (d) $t = 0.8$ T

(e) $t = 0$ (f) $t = 0.2$ T (g) $t = 0.5$ T (h) $t = 0.8$ T

(i) $t = 0$ (j) $t = 0.2$ T (k) $t = 0.5$ T (l) $t = 0.8$ T

(m) $t = 0$ (n) $t = 0.2$ T (o) $t = 0.5$ T (p) $t = 0.8$ T

(q)

Figure 4.8: *Visualization of the ferromagnetic skyrmion excitation modes, shown in order of increasing frequency. From top to bottom - clockwise gyrotropic mode, twofold-deformed skyrmion, threefold-deformed skyrmion and breathing mode (see also Table 4.6). The arrows denote the sense of rotation of each mode, where CW stands for clockwise. Continues in figure 4.9.*

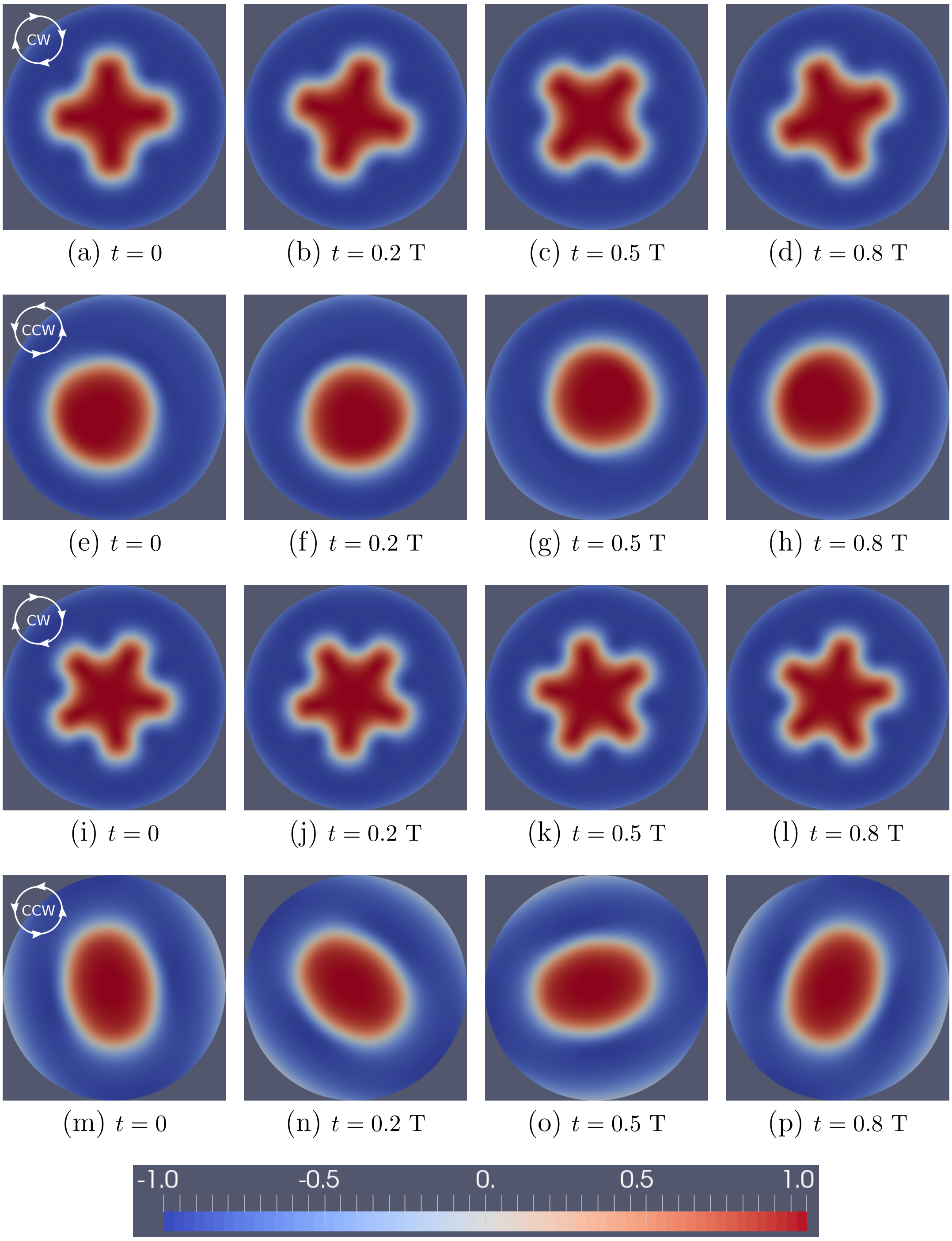

(a) $t = 0$ (b) $t = 0.2$ T (c) $t = 0.5$ T (d) $t = 0.8$ T

(e) $t = 0$ (f) $t = 0.2$ T (g) $t = 0.5$ T (h) $t = 0.8$ T

(i) $t = 0$ (j) $t = 0.2$ T (k) $t = 0.5$ T (l) $t = 0.8$ T

(m) $t = 0$ (n) $t = 0.2$ T (o) $t = 0.5$ T (p) $t = 0.8$ T

(q)

Figure 4.9: *Visualization of the ferromagnetic skyrmion excited modes, shown in order of increasing frequency (continuation from figure 4.8). From top to bottom - fourfold-deformed skyrmion, counterclockwise gyrotropic mode, five-deformed skyrmion and counterclockwise twofold-deformed skyrmion (see also Table 4.6). The arrows denote the sense of rotation of each mode, where CW and CCW stand for clockwise and counterclockwise, respectively.*

4.8e - 4.8h. This skyrmion mode rotates in the CW direction around the center of the nanodisk without being displaced from it, so that it has no gyrotropic nature. [35, 37]

The twofold-deformed skyrmion is the lowest of a series of excitation modes that exhibit a deformed shape of the skyrmion core. We find a threefold-, fourfold- and fivefold-deformed skyrmions at frequencies of $f_{\mathrm{3fold}} = 3.61\,\mathrm{GHz}$, $f_{\mathrm{4fold}} = 8.47\,\mathrm{GHz}$ and $f_{\mathrm{5fold}} = 15.76\,\mathrm{GHz}$ (figures 4.8i - 4.8l, 4.9a - 4.9d and 4.9i - 4.9l), respectively. All of these deformed modes are similar in the sense that they do not have gyrotropic nature and rotate in the CW direction. Switching the skyrmion polarity reverses the sense of rotation to CCW, as for the gyrotropic mode.

Further, we find a breathing mode at $f_{\mathrm{breathing}} = 4.95\,\mathrm{GHz}$ and show it in figures 4.8m - 4.8p. Here, the skyrmion shrinks and expands uniformly and periodically in a way that the radial symmetry is preserved, unlike the rest of the excited modes [36]. We find no discernible effect of the skyrmion polarity on the breathing mode. The order of the breathing and the lowest gyrotropic modes in the spectrum agrees well with the numerical results of references [119, 125].

The highest-frequency mode in the present range is a twofold-deformed skyrmion rotating in the CCW direction with a frequency of $f = 19.67\,\mathrm{GHz}$ (see figures 4.9m - 4.9p). Similar to the CCW gyrotropic mode, the frequency of the CCW twofold-deformed mode is an order of magnitude higher than its CW counterpart. This is a further manifestation of fact that for $p = +1$ the preferred sense of direction is counterclockwise.

The lowest few eigenmodes of the ferromagnetic skyrmion have frequencies lower than the corresponding ferromagnetic resonance (FMR) frequency of the uniform state ($f_{\mathrm{FMR}} \sim 20\,\mathrm{GHz}$, see Appendix D.4). The presence of frequencies of the order of several GHz in the ferromagnetic nanodisk excitation spectrum can be used as a characteristic feature to identify skyrmions in confined nanodisks in experiment [36].

Dependence of the frequencies on the external magnetic field

Next, we investigate the behaviour of the ferromagnetic skyrmion excitations as a function of the applied magnetic field. To do so, we sweep B in the range $0\,\mathrm{T} - 1\,\mathrm{T}$ in steps of $\Delta B = 5\,\mathrm{mT}$ and perform successive relaxation of the magnetic texture: we take the relaxed skyrmion at $B = 0\,\mathrm{T}$ (see figure 4.5) as an initial state, increase the field by ΔB, relax and repeat until we reach $B = 1\,\mathrm{T}$. We calculate the eigenfrequencies at each step of the successive relaxation and analyze the corresponding eigenmodes to take into account the effect of level crossings.

For the present setup ($p = -1$) the skyrmion core points in the opposite direction of the applied external field. As a consequence, the Zeeman energy at the core becomes too large as the field is increased and the equilibrium skyrmion shrinks until it disappears completely above $B = 0.55\,\mathrm{T}$. In the following, we focus in the range $0\,\mathrm{T} < B < 0.2\,\mathrm{T}$, as it is easily accessible in experiment and provides a good overview of the behaviour of the ferromagnetic excitation modes.

The results are plotted in figure 4.10. The clockwise and counterclockwise gyrotropic modes react differently to the magnetic field – the lowest gyrotropic mode[17]

---

[17] Note, that the lowest gyrotropic mode is CW(CCW) for the $p = +1$ ($p = -1$) skyrmion.

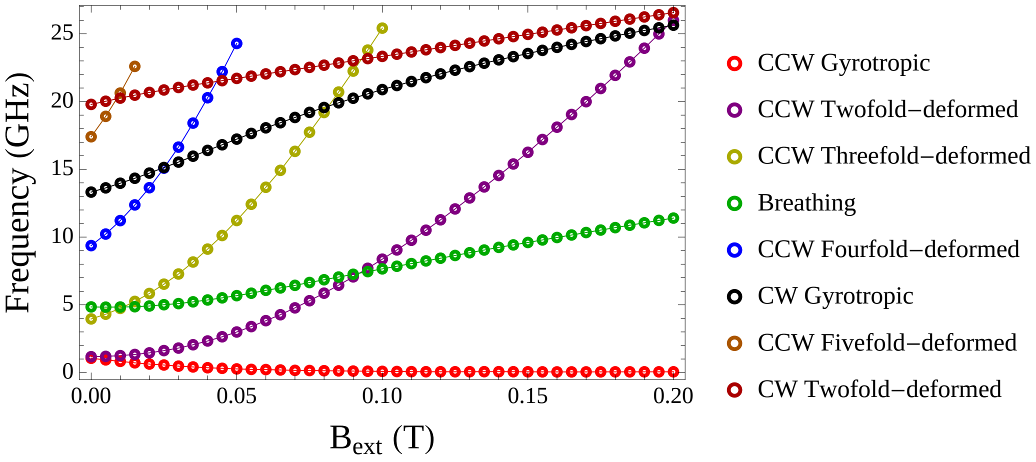

Figure 4.10: *Frequencies of the lowest eight excitation modes of the* $p = -1$ *ferromagnetic skyrmion as a function of the external magnetic field. See Tables 4.6 and 4.7 for a list of the frequencies at both ends of the range studied here.*

decreases in frequency when the field is increased, whereas the higher-frequency gyrotropic mode does the opposite. The spread of these frequencies with an applied magnetic field follows the same trend as the frequency splitting of the degenerate gyrotropic modes of magnetic vortices [118].

Four modes are found to be more sensitive to the external field than the rest, as their frequencies vary in a much larger range. This leads to several level crossings, where for particular values of B pairs of modes of different nature become degenerate (see figure 4.10). These four modes are the CCW excitations that exhibit a deformed core: the two-, three-, four- and fivefold-deformed modes. A similar behaviour of the twofold- and threefold-deformed mode as a function of the external field was found by Schütte *et al.* [37][18], as well as Lin *et al.* [35], whereas in the latter reference also

Mode	$f_{B=0\,\mathrm{T}}$ (GHz)	$f_{B=0.2\,\mathrm{T}}$ (GHz)	Rotation
Gyrotropic	1	0.06	CCW
Breathing	5	10	–
Twofold-deformed	1	16	CCW
Gyrotropic	13	24	CW
Twofold-deformed	20	25	CW

Table 4.7: *List of the five lowest-frequency excitation modes at* $B = 0.2\,\mathrm{T}$ *(middle-right column) and their respective values at* $B = 0\,\mathrm{T}$ *(middle-left column). The evolution of the modes as a function of* B *is shown in figure 4.10. The values listed here have been rounded to the leading decimal place.*

---

[18] Note, however, that the authors in reference [37] consider a purely two-dimensional ferromagnet with Dzyaloshinskii-Moriya interactions of bulk type (relevant for cubic chiral magnets), no anisotropy or dipolar fields for which a finite external magnetic field is crucial for the stability of the single skyrmion.

a similar behaviour for the fourfold- and fivefold modes is shown.

We find that the breathing mode increases in frequency with increasing external field, which agrees well with previous results [35, 36, 37]. This increase is less rapid than for the twofold- and threefold-deformed modes and as a result the order of modes changes between $B = 0\,\mathrm{T}$ and $B = 0.2\,\mathrm{T}$, consistent with references [35, 37].

Dependence of the frequencies on the sample radius

Here, we discuss the behaviour of the ferromagnetic skyrmion eigenmodes as a function of the nanodisk radius R_{disk}. For that purpose, we relax an initial skyrmion state with radius $R_{\mathrm{init}} = 15\,\mathrm{nm}$ on different nanodisks, where the radius ranges from $R_{\mathrm{disk}} = 40\,\mathrm{nm}$ to $R_{\mathrm{disk}} = 100\,\mathrm{nm}$ in steps of $\Delta R_{\mathrm{disk}} = 10\,\mathrm{nm}$. In all cases the thickness and characteristic length remain $t = 1\,\mathrm{nm}$ and $l_{\mathrm{char}} = 1\,\mathrm{nm}$, respectively. We calculate the spectrum of each configuration and track the respective eigenmodes, so that possible level crossings are taken into account.

As discussed previously, the material parameters are such that the Dzyaloshinskii-Moriya constant is larger than the threshold value, $D > D_0$ (see Appendix D.3 and figure D.8). Consequently, the skyrmion size is fixed by the confining potential of the boundaries and is different for each nanodisk.

The results are plotted in figure 4.11. We focus on the eight lowest modes discussed previously in the case of $R_{\mathrm{disk}} = 50\,\mathrm{nm}$ (see Table 4.6 and figures 4.8-4.9). We find that the frequencies of all modes follow a decreasing trend when the sample radius is increased. Similar trend is found also in references [121] and – for different setups – [43, 125][19].

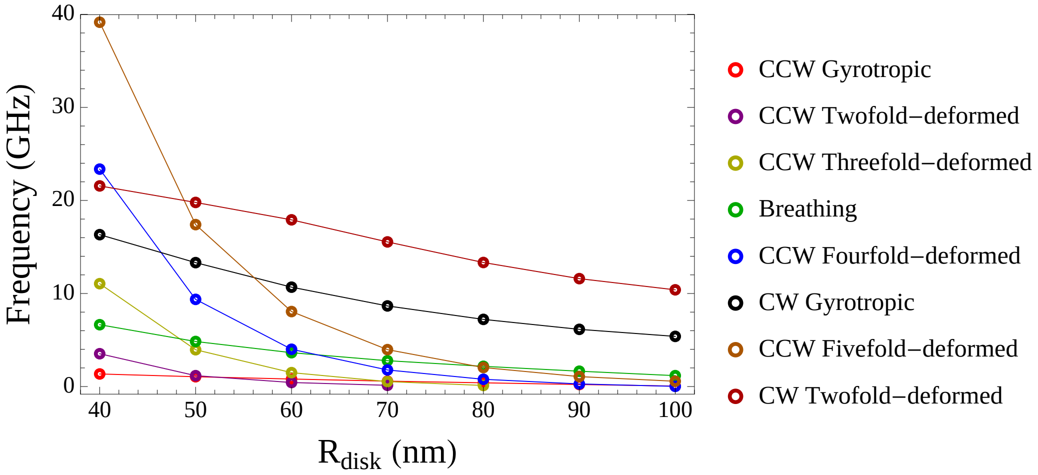

Figure 4.11: *Frequencies of the excitation modes of the* $p = -1$ *ferromagnetic skyrmion as a function of nanodisk radius. Here, we focus on eight modes listed in Table 4.6 – they are the lowest modes for the* $R_{disk} = 50\,\mathrm{nm}$ *nanodisk, but not for the nanodisk with* $R_{disk} = 40\,\mathrm{nm}$. *Note that the CCW twofold- and threefold-deformed modes disappear above* $R_{disk} = 70\,\mathrm{nm}$ *and* $R_{disk} = 80\,\mathrm{nm}$, *respectively.*

---

[19] Reference [43] deals with skyrmion gyrations excited by spin-polarized electric currents, whereas in reference [125] a different ferromagnetic model is investigated (see the summary at the end of the present section for more details).

Mode	$f_{40\,\mathrm{nm}}$ (GHz)	$f_{R_{\mathrm{disk}}=100\,\mathrm{nm}}$ (GHz)
CCW Gyrotropic	1	0.05
Breathing	7	1
CW Gyrotropic	16	5

Table 4.8: *List of the gyrotropic and breathing modes frequencies at both ends of the range shown in figure 4.11:* $R_{disk} = 40\,\mathrm{nm}$ *(middle column) and* $R_{disk} = 100\,\mathrm{nm}$ *(right column). The values are rounded to the leading decimal place and serve as a complementary qualitative guide to figure 4.11.*

We note that the counterclockwise (twofold-, threefold-, fourfold- and fivefold-) deformed modes are more sensitive to the sample radius than the remaining modes (analogous to the variation of the external magnetic field). In addition, the twofold- and threefold-deformed mode disappear above $R_{\mathrm{disk}} = 70\,\mathrm{nm}$ and $R_{\mathrm{disk}} = 80\,\mathrm{nm}$, respectively, and the lowest gyrotropic mode decreases in frequency by nearly two orders of magnitude (see Table 4.8).

Summary

We performed numerical simulations of the ferromagnetic model presented in section 3.2 on a thin nanodisk to obtain a skyrmion groundstate and calculate its low-frequency excitations. Here, the skyrmion is stabilized at zero external field through the interplay of the exchange interactions, uniaxial anisotropy and the interfacial Dzyaloshinskii-Moriya interactions. We do not take dipolar interactions into account, as they are expected to be negligible for thin films [25, 26][20]. Dipolar interactions have been included in the analysis of references [25, 36], where in the latter reference also the uniform breathing mode has been investigated. The authors find the breathing mode for zero field and $D = 3.5\,\mathrm{mJ\,m^{-2}}$ at a frequency of $f \simeq 5\,\mathrm{GHz}$, which agrees very well with our result of $f_{\mathrm{breathing}} = 4.95\,\mathrm{GHz}$ for the same material parameters. We also find a good qualitative agreement for the behaviour of the previously studied excited modes as a function of the external magnetic field – the breathing mode of the Néel skyrmion [36] and the deformed-core modes of the Bloch skyrmion references [35, 37].

An entirely different model is considered in reference [123], where only exchange, dipolar and bulk Dzyaloshinskii-Moriya interactions are taken into account. Further, the authors take into account a variation of the magnetization vector in the out-of-plane direction, use thicker nanodisks ($t = 10\,\mathrm{nm}$) and set the external field and magnetocrystalline anisotropy to zero. In such a setup a Bloch skyrmion groundstate is reported. In a follow-up study [125], the authors analyze the eigenspectrum of the zero-anisotropy Bloch skyrmion. A quantitative comparison with the present work is not possible due to the different nature of the ferromagnetic models and the corresponding skyrmion groundstates. However, there are qualitative similarities – in particular the appearance of gyrotropic, breathing and deformed-core excitation

---

[20] The setup considered in this work resembles most the one studied by Rohart *et al.* [26]

modes. There are also similarities in the declining trend of the gyrotropic and lowest breathing modes as a function of the external field and nanodisk radius. We note that the lowest breathing mode found in reference [125] exhibits a modulated contour ring rotating in the clockwise direction on top of the periodic breathing of skyrmion. We do not find such a mode in our low-frequency spectrum.

In summary, we find good agreement – qualitatively and (where possible) quantitatively – between our results for the ferromagnetic skyrmion dynamics and existing works in the literature. This establishes the validity of our approach and verifies the code that we developed to study skyrmion excitations. Next, we turn towards uncharted territory to investigate the antiferromagnetic skyrmion dynamics.

4.2.3 Antiferromagnetic skyrmions

Here, we extend the numerical analysis presented in the previous section to the confined skyrmion dynamics in antiferromagnets. We obtain an antiferromagnetic skyrmion groundstate and calculate its low-frequency spectrum.

The discussion in this section is based on the same nanodisks of radius $R_{\text{disk}} = 50\,\text{nm}$, thickness $t = 1\,\text{nm}$ and a characteristic length $l_{\text{char}} = 1\,\text{nm}$ (see figure 4.3) as for the ferromagnet in section 4.2.2, unless explicitly stated otherwise.

First, we investigate the equilibrium state of the antiferromagnet with the methods presented in section 2.3.2. The antiferromagnet is modelled according to the sublattice energy functional (3.17)[21].

The relaxation process for the antiferromagnet is governed by the sublattice effective fields shown in equation (3.20). The weak formulation of the antiferromagnetic effective fields is given by

$$\begin{aligned}
\frac{1}{B_{\text{s}}}\int_V d^3r\Big(\mathbf{B}^{\text{AFM}}_{\text{eff},i}\cdot\mathbf{v}_i\Big) =& -\frac{B_{\text{exch}}}{B_{\text{s}}}\int_V d^3r\Big(1-\delta_{ij}\Big)\Big(\mathbf{u}_i\cdot\mathbf{v}_j\Big)\\
&- l_{\text{ex}}^2\int_V d^3r\Big(\nabla\mathbf{u}_i\cdot\nabla\mathbf{v}_i\Big)\\
&+\frac{B_{\text{an}}}{B_{\text{s}}}\int_V d^3r\Big(\mathbf{u}_i\cdot\hat{z}\Big)\Big(\mathbf{v}_i\cdot\hat{z}\Big)\\
&+\frac{B}{B_{\text{s}}}\int_V d^3r\Big(\mathbf{v}_i\cdot\hat{z}\Big)\\
&-\frac{B_{\text{d}}}{B_{\text{s}}}\int_V d^3r\Big(\epsilon_{ij}\left(\mathbf{u}_i\times\hat{z}\right)\cdot\mathbf{v}_j\Big)\\
&+l_{\text{DM}}\int_V d^3r\left[\Big(\nabla\cdot\mathbf{u}_\Delta\Big)\hat{z}-\nabla\Big(\mathbf{u}_\Delta\cdot\hat{z}\Big)\right]\cdot\mathbf{v}_\Delta\\
&+\frac{l_{\text{DM}}}{2}\oint_{\partial V} d^2r\Big[\mathbf{u}_\Delta\times\Big(d\hat{\mathbf{S}}\times\hat{z}\Big)\Big]\cdot\mathbf{v}_\Delta,
\end{aligned}\tag{4.27}$$

---

[21] The formulation in terms of the individual sublattices is more general than the one in terms of the Néel vector and total magnetization (in the latter, certain terms are neglected due to the assumption $\mathbf{n}^2 \gg \mathbf{m}^2$). In addition, the sublattice formulation lends itself better to the normalization of the magnetization vectors at every iteration step, due to the nature of the projection method that we use (see section 2.3.2).

where δ_{ij} is the Kronecker delta, ϵ_{ij} the Levi-Civita symbol and summation over repeated indices $i, j = 1, 2$ (denoting the two sublattices) is implied. Here, $\mathbf{u}_i$ denotes the (unknown) trial function and $\mathbf{v}_i$ the corresponding test function for the sublattice i and we have defined $\mathbf{u}_\Delta = \mathbf{u}_1 - \mathbf{u}_2$ and $\mathbf{v}_\Delta = \mathbf{v}_1 - \mathbf{v}_2$[22]. The antiferromagnetic projected Landau-Lifshitz-Gilbert equation is solved numerically until the right hand side does not produce a torque on the magnetization vector (zero-torque condition). We make sure that convergence is reached within the numerical precision of the simulation by tracking the change of the magnetization vector every few steps. The resulting texture for $\mathbf{m}_1$ and $\mathbf{m}_2$ is the equilibrium state.

The antiferromagnetic model is parameterized by the saturation magnetization, homogeneous and inhomogeneous exchange constant, uniaxial anisotropy constant, external magnetic field and the homogeneous and inhomogeneous Dzyaloshinskii-Moriya constant. For a better comparison between the ferromagnet and antiferromagnet (see also section 3.3.2), we use the same material parameters for the exchange stiffness, anisotropy and Dzyaloshinskii-Moriya interactions as for the ferromagnet (see Table 4.4). We choose the homogeneous exchange constant to be sufficiently larger than the remaining energy scales and such that it is the same order of magnitude as typical antiferromagnets [127][23]. The parameters are listed in Table 4.9[24]. The corresponding lengthscales of the problem are $l_{\mathrm{ex}} = 4.89\,\mathrm{nm}$, $l_{\mathrm{DM}} = 5.57\,\mathrm{nm}$, $x_0 = 6.36\,\mathrm{nm}$ and the cycloid length $2\pi\xi_{\mathrm{AFM}} = 8\pi A/D = 53.85\,\mathrm{nm}$ (see section 3.3.2). The cycloid length is comparable to the nanodisk radius, so that skyrmions are expected to appear in this setup (as for the ferromagnet).

Parameter	Value	Unit
M_{s}	1	$\mathrm{MA\,m^{-1}}$
J_{ex}	91	$\mathrm{MJ\,m^{-3}}$
A_{ex}	15	$\mathrm{pJ\,m^{-1}}$
J_{ani}	743	$\mathrm{kJ\,m^{-3}}$
D	7	$\mathrm{mJ\,m^{-2}}$

Rescaled parameter	Value	Unit
B_{s}	1.26	T
B_{exch}	90.90	T
l_{ex}	4.89	nm
B_{an}	0.74	T
l_{DM}	5.57	nm

Table 4.9: *List of the parameters used to obtain the antiferromagnetic skyrmion groundstate and its excitations. Here,* $M_s(B_s)$ *is the saturation magnetization (field),* $J_{ex}(B_{\mathrm{exch}})$ *the homogeneous exchange constant (field),* $A(l_{ex})$ *the exchange stiffness parameter (exchange length),* $J_{ani}(B_{\mathrm{an}})$ *the uniaxial anisotropy constant (field),* $D(l_{DM})$ *the inhomogeneous Dzyaloshinskii-Moriya interactions constant (length),* $B_d = 0\,\mathrm{T}$ *the homogeneous Dzyaloshinskii-Moriya field and* $B = 0\,\mathrm{T}$ *the external magnetic field. We show both the physical and the rescaled parameters that enter the energy functional (3.17) and the weak formulations (4.27) and (5.15-4.31), respectively. For the spectrum calculation we set the Lagrange multiplier to* $\Lambda = 500\,B_s$.

---

[22] See also section 5.2 and the corresponding code in listing 5.10.

[23] Note that there is no reference set of parameters, since antiferromagnetic skyrmions are yet to be observed experimentally.

[24] For completeness, we introduced the energy densities J_{ex} and J_{ani}, which correspond to the exchange field B_{exch} and the anisotropy field B_{an}, respectively (see Table 4.10).

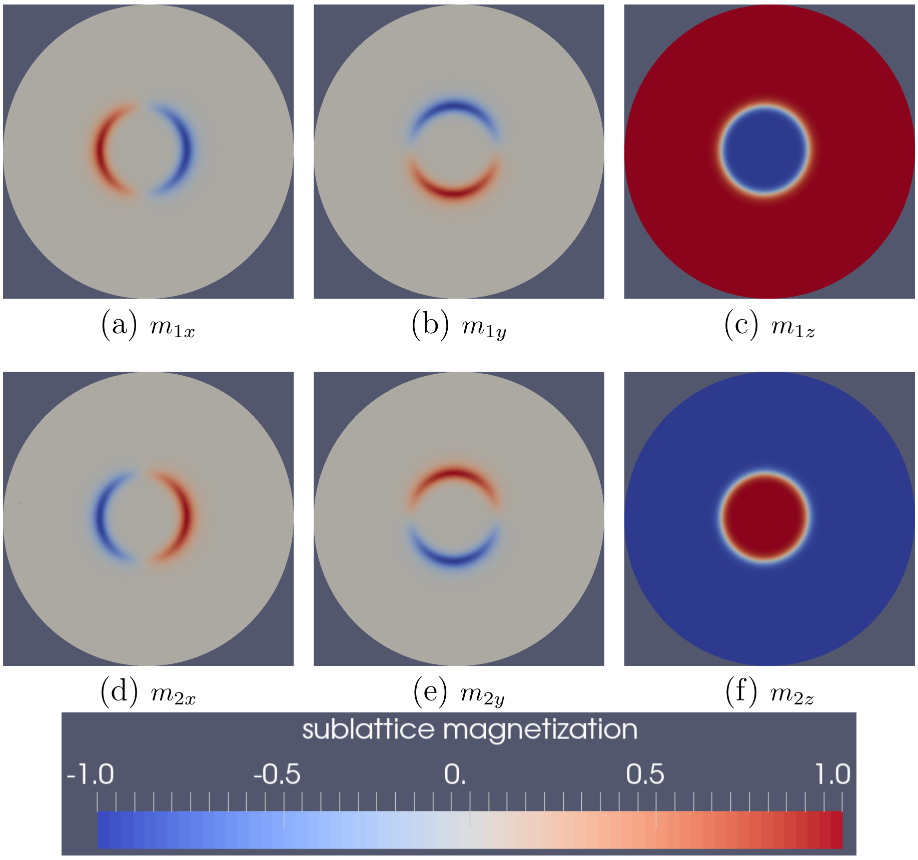
(a) m_{1x} (b) m_{1y} (c) m_{1z}

(d) m_{2x} (e) m_{2y} (f) m_{2z}

Figure 4.12: *Visualisation of the initial antiferromagnetic skyrmion-like state (radius* 15 nm*) - shown are the vector components of both sublattice magnetizations.*

We investigate the relaxation of different initial states and compare the energies of the obtained equilibrium states (see Appendix D.2). We find that, for the present set of parameters, the skyrmion configuration has the lowest energy and, therefore, represents the groundstate, as for the ferromagnet.

The antiferromagnetic skyrmion is obtained by starting from a skyrmion-like initial state (see Appendix D.1), which is extended to cover two mirrored sublattices

	Parameter	Value	Unit
saturation field	B_s	$\mu_0 M_\mathrm{s}$	T
exchange field	B_exch	$J_\mathrm{ex}/M_\mathrm{s}$	T
exchange length	l_ex	$\sqrt{2A/(M_\mathrm{s}B_\mathrm{s})}$	m
anisotropy field	B_an	$J_\mathrm{ani}/M_\mathrm{s}$	T
DM length	l_DM	$D/(M_\mathrm{s}B_\mathrm{s})$	m

Table 4.10: *Definition of the rescaled parameters that enter the weak formulation in equation (4.27). Here,* μ_0 *is the vacuum permeability, DM stands for Dzyaloshinskii-Moriya and the corresponding physical parameters are listed in Table 4.9.*

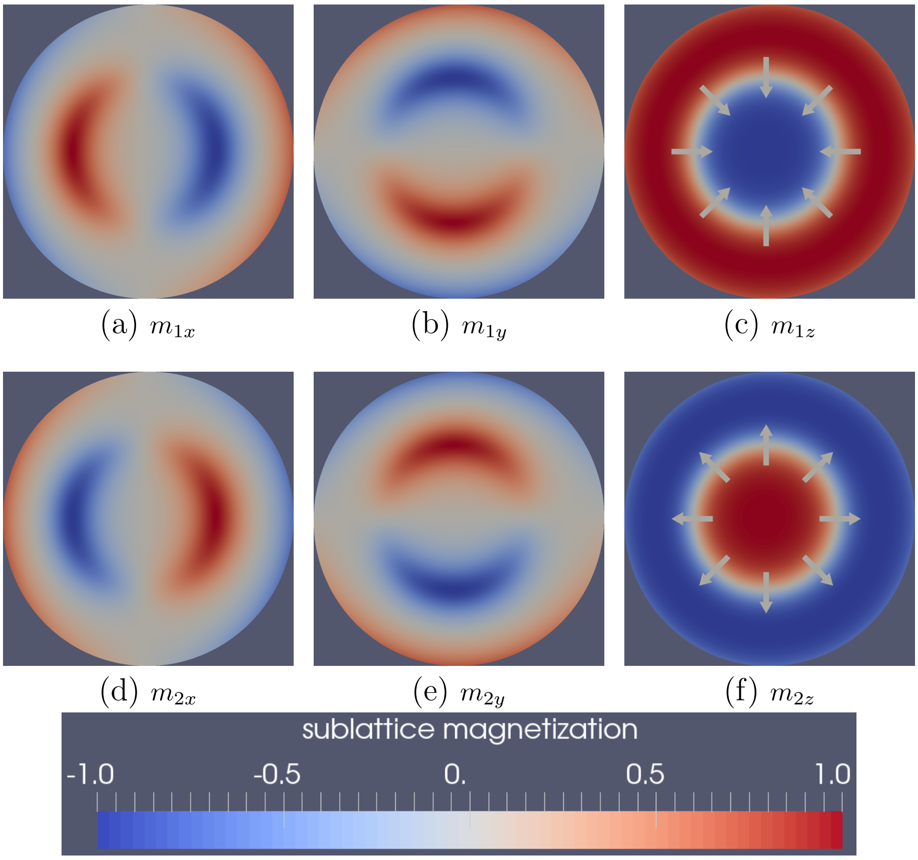
(a) m_{1x} (b) m_{1y} (c) m_{1z}

(d) m_{2x} (e) m_{2y} (f) m_{2z}

Figure 4.13: *Visualisation of the relaxed antiferromagnetic skyrmion state - shown are the magnetization components of both sublattice vectors* $\mathbf{m}_1$ *and* $\mathbf{m}_2$*.*

(with $\mathbf{m}_1 = -\mathbf{m}_2$). The two sublattices of the initial state are shown in figure 4.12.

We show the relaxed antiferromagnetic skyrmion in figure 4.13. Similar to the ferromagnet, for the chosen set of parameters, the equilibrium skyrmion exhibits a smoother transition region – where the Néel vector rotates in the radial direction – compared to the initial state (see figure 4.12). During the relaxation process the anisotropy and inhomogeneous energies are increased (compared to the initial state), whereas the Dzyaloshinskii-Moriya energy is lowered. The homogeneous exchange remains largely unchanged[25] and does not affect the skyrmion profile at zero external field[26]. As for the ferromagnet, there is an additional canting of the magnetization vectors at the nanodisk edges, which is induced by the Dzyaloshinskii-Moriya interactions. It is clearly visible that the canting is chiral – $\mathbf{m}_1$ is canting radially outward and $\mathbf{m}_2$ radially inward (compare the in-plane components of $\mathbf{m}_1$ and $\mathbf{m}_2$ at the edges of the nanodisk in figure 4.13)[27].

In chapter 3, we emphasized that the profile equation for the ferromagnet and antiferromagnetic skyrmion are identical at zero external field. This allows us to

---

[25] For the relaxed skyrmion we find $\mathbf{m}_1 \cdot \mathbf{m}_2 = -0.999$ (that is, a deviation from the perfect alignment between of the order of 10^{-3}).

[26] As can be seen in equations (3.34), the exchange field enters the profile equation only in combination with the external field.

[27] The chirality depends on the sign of D, as discussed in chapter 3.

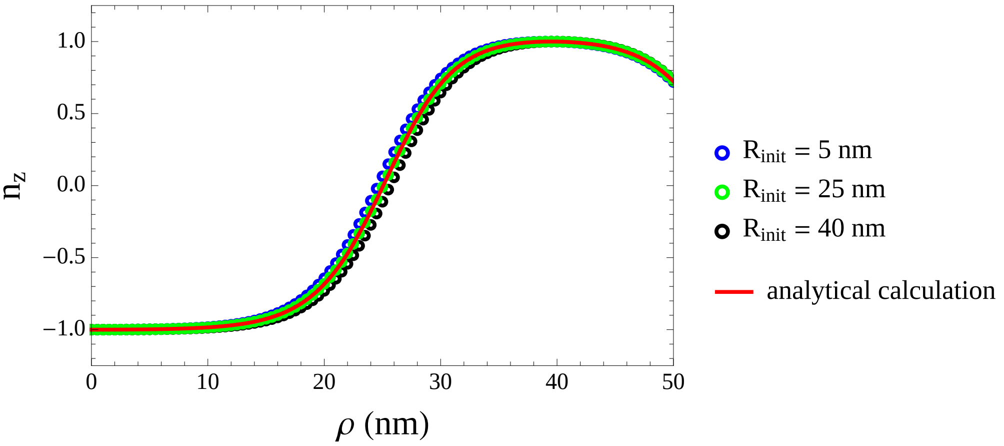

Figure 4.14: *Profile of the relaxed antiferromagnetic skyrmion for the parameter set shown in Table 4.9. The solid red line is the numerical solution of the profile equation (3.34) with the boundary condition (3.35). The open circles are the numerical simulation results for different values of the initial radius: the profiles for* $R_{init} = 5, 10, 15, 20\,\mathrm{nm}$ *and* $R_{init} = 30, 35, 40\,\mathrm{nm}$ *are identical and we have plotted one from each group in blue and black color, respectively.*

obtain analytically the expected profile for the confined antiferromagnetic skyrmion (see section 3.3.2). We solve the profile equation (3.34) with initial condition $\theta(\rho = 0) = \pi$ and apply the shooting method to find $d\theta/d\rho(\rho = 0)$ such, that the boundary condition (3.35) is fulfilled. The antiferromagnetic skyrmion is a texture of the Néel vector; therefore, we transform the sublattice magnetization vectors to the Néel vector according to equation (3.22) and plot both the analytical and numerical results in figure (4.14)

All the results for the confined ferromagnetic skyrmion hold in the present case as well. The antiferromagnet skyrmion is stabilized largely due to modified boundary conditions and the resulting confining potential of the nanodisk edges, analogous to the ferromagnetic skyrmion [26]. An important consequence is that for values of $D > D_0$, the skyrmion radius depends on the size of the nanodisk (see Appendix D.3 and figure D.8). For the parameters used here this condition is fulfilled, as $D = 7\,\mathrm{mJ\,m^{-2}}$ is larger than the threshold Dzyaloshinskii-Moriya constant $D_0 = 4/\pi\sqrt{2AB_{\mathrm{an}}M_{\mathrm{s}}} = 6\,\mathrm{mJ\,m^{-2}}$ (see equation (3.33) and section 3.3.2). For $D < D_0$, the skyrmion radius is fixed and independent of the nanodisk, because the skyrmion is too small to feel the effect of the edges (see figure D.8).

Dynamics

Next, we investigate the low-frequency excitations of the antiferromagnetic skyrmion groundstate. We extend the formalism presented in section 2.3.2 to a collinear antiferromagnet with two sublattices, by considering small deviations $\delta\mathbf{m}_1$ and $\delta\mathbf{m}_2$ to the equilibrium magnetizations $\mathbf{m}_{0_1}$ and $\mathbf{m}_{0_2}$. This leads to the linearized Landau-Lifshitz-Gilbert equation for each sublattice

$$i\omega\delta\mathbf{m}_i = -\gamma\mathbf{m}_{0_i} \times \mathbf{B}_{\mathrm{eff}}[\delta\mathbf{m}_i, \delta\mathbf{m}_i] - \gamma\delta\mathbf{m}_i \times \mathbf{B}_{\mathrm{eff}}[\mathbf{m}_{0_i}, \mathbf{m}_{0_i}] + \Lambda\left(\mathbf{m}_{0_i} \cdot \delta\mathbf{m}_i\right)\mathbf{m}_{0_i}, \tag{4.28}$$

where $i = 1, 2$ denotes the sublattice, ω is the frequency of the corresponding eigenmode, $\mathbf{B}_{\mathrm{eff}}$ the effective field (see equations (3.20)) and Λ a Lagrange multiplier that ensures that the modes we obtain are not longitudinal excitations of the magnetization vector $\mathbf{m}_0$. Equation (4.28) is the direct extension of equation (2.39) to two-sublattice collinear antiferromagnets.

We transform equations (4.28) to their weak formulation, by multiplying each equation with the corresponding test functions $\mathbf{v}_1$ and $\mathbf{v}_2$, integrate over space and renormalize the prefactors by the saturation field B_{s} to make the equations dimensionless. Added together, they lead to the eigenvalue equation for the six-dimensional vector $\tilde{\mathbf{u}}$

$$\lambda \mathrm{M} \tilde{\mathbf{u}} = \mathrm{A} \tilde{\mathbf{u}}, \tag{4.29}$$

with the eigenvalues $\lambda = -i\omega/\gamma$,

$$\mathrm{M} \tilde{\mathbf{u}} = \frac{1}{B_{\mathrm{s}}} \int_V d^3 r \Big(\mathbf{u}_i \cdot \mathbf{v}_i \Big) \tag{4.30}$$

and the right hand side given by

$$\begin{aligned}
\mathrm{A} \tilde{\mathbf{u}} = & - \frac{B_{\mathrm{exch}}}{B_{\mathrm{s}}} \int_V d^3 r \Big(1 - \delta_{ij} \Big) \Bigg[\Big(\mathbf{m}_{0_i} \times \mathbf{u}_j \Big) \cdot \mathbf{v}_i + \Big(\mathbf{u}_i \times \mathbf{m}_{0_j} \Big) \cdot \mathbf{v}_i \Bigg] \\
& - l_{\mathrm{ex}}^2 \int_V d^3 r \Bigg[\nabla \Big(\mathbf{v}_i \times \mathbf{m}_{0_i} \Big) \cdot \nabla \mathbf{u}_i + \nabla \Big(\mathbf{v}_i \times \mathbf{u}_i \Big) \cdot \nabla \mathbf{m}_{0_i} \Bigg] \\
& + \frac{B_{\mathrm{an}}}{B_{\mathrm{s}}} \int_V d^3 r \Bigg[(\mathbf{u}_i \cdot \hat{z}) (\mathbf{m}_{0_i} \times \hat{z}) \cdot \mathbf{v}_i + (\mathbf{m}_{0_i} \cdot \hat{z}) (\mathbf{u}_i \times \hat{z}) \cdot \mathbf{v}_i \Bigg] \\
& + \frac{B}{B_{\mathrm{s}}} \int_V d^3 r \, (\mathbf{u}_i \times \hat{z}) \cdot \mathbf{v}_i \\
& + \frac{B_{\mathrm{d}}}{B_{\mathrm{s}}} \int_V d^3 r \, \epsilon_{ij} \Bigg[\mathbf{m}_{0_i} \times \Big(\mathbf{u}_j \times \hat{z} \Big) \cdot \mathbf{v}_i + \mathbf{u}_i \times \Big(\mathbf{m}_{0_j} \times \hat{z} \Big) \cdot \mathbf{v}_i \Bigg] \\
& + l_{\mathrm{DM}} \int_V d^3 r \, \epsilon_{ij} \Bigg[\Big(\nabla \cdot \mathbf{u}_\Delta \Big) (\mathbf{m}_{0_i} \times \hat{z}) \cdot \mathbf{v}_i - \mathbf{m}_{0_i} \times \nabla \Big(\hat{z} \cdot \mathbf{u}_\Delta \Big) \cdot \mathbf{v}_i \\
& \qquad + \Big(\nabla \cdot \mathbf{m}_{0_\Delta} \Big) (\mathbf{u}_i \times \hat{z}) \cdot \mathbf{v}_i - \mathbf{u}_i \times \nabla \Big(\hat{z} \cdot \mathbf{m}_{0_\Delta} \Big) \cdot \mathbf{v}_i \Bigg] \left| \mathbf{m}_{0_j} \right| \\
& + \frac{l_{\mathrm{DM}}}{2} \oint_{\partial V} d^2 r \, \epsilon_{ij} \Bigg[(\mathbf{v}_i \times \mathbf{m}_{0_i}) \cdot \mathbf{u}_\Delta \times \Big[d\hat{\mathbf{S}} \times \hat{z} \Big] \\
& \qquad + (\mathbf{v}_i \times \mathbf{u}_i) \cdot \mathbf{m}_{0_\Delta} \times \Big[d\hat{\mathbf{S}} \times \hat{z} \Big] \Bigg] \left| \mathbf{m}_{0_j} \right| \\
& + \frac{\Lambda}{B_{\mathrm{s}}} \int_V d^3 r \, (\mathbf{m}_{0_i} \cdot \mathbf{u}_i) (\mathbf{m}_{0_i} \cdot \mathbf{v}_i) \, .
\end{aligned} \tag{4.31}$$

Here, δ_{ij} is the Kronecker delta, ϵ_{ij} the Levi-Civita symbol and summation over repeated indices $i, j = 1, 2$ (denoting the two sublattices) is implied[28]. Again, $\mathbf{u}_i$ denotes the (unknown) trial function and $\mathbf{v}_i$ the corresponding test function for the sublattice i and we have defined $\mathbf{u}_\Delta = \mathbf{u}_1 - \mathbf{u}_2$, $\mathbf{v}_\Delta = \mathbf{v}_1 - \mathbf{v}_2$ and $\mathbf{m}_{0_\Delta} = \mathbf{m}_{0_1} - \mathbf{m}_{0_2}$[29].

The excitations of the antiferromagnetic skyrmion are obtained by solving equation (5.15) numerically (see section 2.3.2). We plug in the relaxed skyrmion in the equilibrium sublattice magnetization vectors $\mathbf{m}_{0_1}$ and $\mathbf{m}_{0_2}$ and calculate the lowest nine eigenmodes.

The physical eigenvectors for the individual sublattices are obtained from the complex eigenvectors through (see footnote [12])

$$\delta\mathbf{m}_i(t) = \mathrm{Re}\{\tilde{\mathbf{u}}_i\}\cos(\omega t) - \mathrm{Im}\{\tilde{\mathbf{u}}_i\}\sin(\omega t), \tag{4.32}$$

and transformed into the language of the order parameters as

$$\begin{aligned} \delta\mathbf{n}(t) &= \frac{1}{2}\Bigg[\delta\mathbf{m}_1(t) - \delta\mathbf{m}_2(t)\Bigg], \\ \delta\mathbf{m}_{\mathrm{AFM}}(t) &= \frac{1}{2}\Bigg[\delta\mathbf{m}_1(t) + \delta\mathbf{m}_2(t)\Bigg]. \end{aligned} \tag{4.33}$$

The full sublattice magnetization vectors $\mathbf{m}_i(t)$ of the excitation modes are constructed according to equation (2.35). For visualization purposes[30], we scale the magnitude of each $\delta\mathbf{m}_i(t)$ by a factor of 100

$$\tilde{\mathbf{m}}_i(t) = \mathbf{m}_{0_i} + 100 \times \delta\mathbf{m}_i(t), \tag{4.34}$$

normalize $\tilde{\mathbf{m}}_i(t)$ and transform to the Neel vector $\delta\mathbf{n}(t)$ in equation (4.33).

We list the frequencies of the lowest nine eigenmodes in Table 4.11 and show their time evolution in figures 4.16-4.18. Similar to the ferromagnet, we obtain modes of different nature – displaced, breathing and deformed-core modes. However, since at zero magnetic field there is no preferred sense of rotation, the modes do not rotate, but rather oscillate between different configurations. Another important difference is that we find two modes for each type in the antiferromagnet; this can be traced back to the doubled number of degrees of freedom due to the presence of two sublattices.

The numerical errors listed in Table 4.11 originate from the imprecision of the relaxation solver[31]. We have shown the profile of the relaxed antiferromagnetic skyrmion as a function of the initial radius R_{init} in figure 4.14. It can be seen that there is a slight deviation of the relaxed profile for initial radii smaller or larger

---

[28] For a more compact representation we have included the magnitude of the unit vector $|\mathbf{m}_{0_j}|$ in the volume terms proportional to l_{DM}.

[29] See also section 5.2 and the corresponding code in listing 5.18.

[30] We show the Néel excitation vector components $\delta\mathbf{n}$ of the lowest two excitation modes at $t = 0$ in figure 4.15. Note, that the excitation vector is more than two orders of magnitude smaller than the groundstate Néel vector $\mathbf{n}_0$ (see figure 4.13 for the magnitude of the corresponding sublattice magnetization vectors $\mathbf{m}_{0_1}$ and $\mathbf{m}_{0_2}$).

[31] We have determined the numerical error of the eigenvalue solver alone to be of the order of kHz. The error of the resonance frequencies of the uniform state increases by three orders of magnitude when numerical errors from the relaxation solver are included (see the discussion in Appendix D.4).

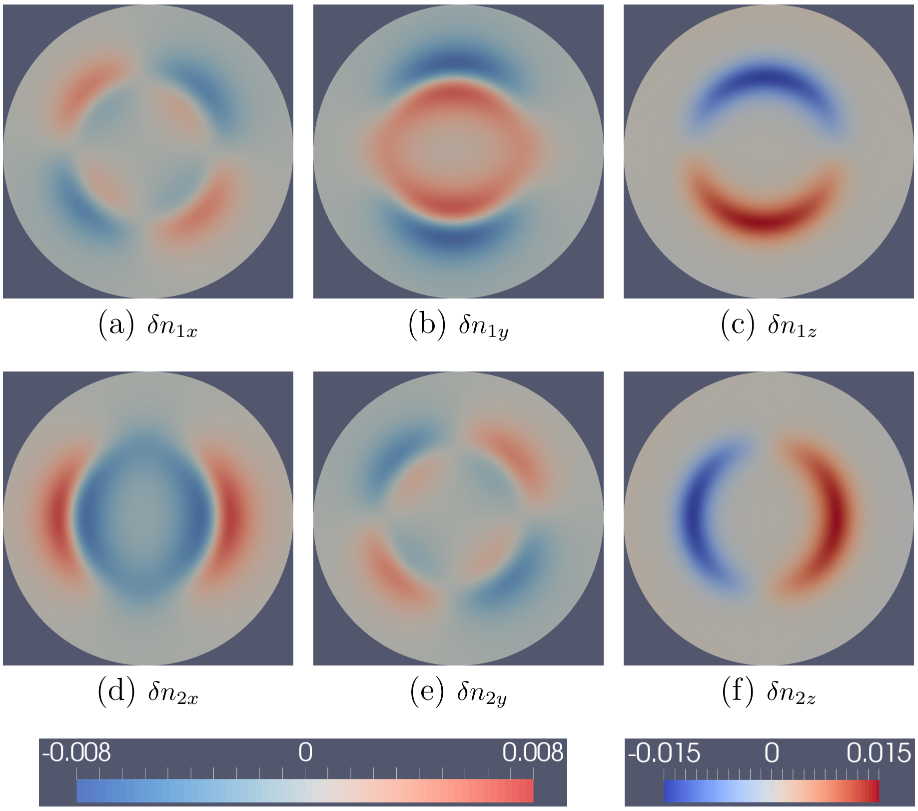

(a) δn_{1x} (b) δn_{1y} (c) δn_{1z}

(d) δn_{2x} (e) δn_{2y} (f) δn_{2z}

(g) Color Bar ($\delta n_{x,y}$) (h) Color Bar (δn_z)

Figure 4.15: *Top view visualization of the lowest two excited modes of the antiferromagnetic skyrmion (the linear displacement modes) at* $t = 0$ *(see Table 4.11, and figures 4.16a - 4.16d and 4.16e - 4.16h for reference). Shown are the components of the Néel excitation vector* $\delta\mathbf{n}_{1,2}(t = 0)$*, corresponding to the equilibrium skyrmion state in figure 4.13. The corresponding total magnetization of both modes is found numerically to be negligible –* $|\delta\mathbf{m}_{AFM,1,2}| \simeq 10^{-7} - 10^{-11}$.

than the analytically predicted equilibrium radius; however, for the chosen material parameters, there is one case that matches the analytical profile very well[32] (shown with green symbols in figure 4.14). To avoid the effects of coincidence, we present in this section the dynamics of the $R_{\text{init}} = 15\,\text{nm}$ skyrmion and then calculate the numerical error by comparing its frequencies to the ones obtained for the skyrmion shown with green symbols in figure 4.14.

The lowest two modes in the current setup exhibit a skyrmion core displaced from its equilibrium position. Thus, they correspond to the lowest gyrotropic mode observed for the ferromagnetic skyrmion. However, the two modes here do not rotate, but rather oscillate back and forth in orthogonal directions, as shown in figures 4.16a-4.16h, at frequencies of $f_1 = 59.63\,\text{GHz}$ and $f_2 = 59.66\,\text{GHz}$. Within the numerical errors these are identical, as is expected from the point of view of symmetry:

---

[32] This is due to the initial radius being almost identical with the target radius. For material parameters different from the ones listed in Table 4.9, the target equilibrium radius will be different (see chapter 3) and the resulting numerical profile will not match it perfectly.

Mode	Frequency (GHz)	Type
1	59.63 ± 0.38	Linear displacement
2	59.66 ± 0.35	Linear displacement
3	66.65 ± 0.25	Twofold-deformed
4	66.67 ± 0.26	Twofold-deformed
5	72.59 ± 0.01	Breathing
6	119.74 ± 1.48	Threefold-deformed
7	119.74 ± 1.48	Threefold-deformed
8	189.14 ± 2.42	Fourfold-deformed
9	189.14 ± 2.42	Fourfold-deformed

Table 4.11: *List of the lowest nine excited mode frequencies of the antiferromagnetic skyrmion (see figure 4.13 for the equilibrium state). These are obtained for a nanodisk of radius* $R_{disk} = 50\,\mathrm{nm}$*, thickness* $t = 1\,\mathrm{nm}$ *and the material parameters listed in Table 4.9. We show the excited modes in figures 4.16-4.18.*

there is nothing within our model that distinguishes one in-plane direction from the other.

The second-lowest pair of modes is found at $f_3 = 66.65\,\mathrm{GHz}$ and $f_4 = 66.67\,\mathrm{GHz}$ and represents a skyrmion with an elongated core with a two-fold rotational symmetry (see figures 4.16i-4.16p). Due to the same consideration as above, the modes are degenerate and oscillate between two elongated configurations each – one along the $\hat{x}$- and $\hat{y}$-direction (figures 4.16i-4.16l) and the other diagonally (4.16m-4.16p). In complete analogy to the ferromagnet, the skyrmion core is not displaced from its equilibrium position so that the modes cannot be regarded as gyrotropic.

Higher in the low-frequency spectrum we find further modes that are characterized by a deformed skyrmion core – a pair of threefold-deformed skyrmion modes at $f_{6,7} = 119.74\,\mathrm{GHz}$ (figures 4.17a-4.17h) and a fourfold-deformed skyrmion at $f_{8,9} = 189.14\,\mathrm{GHz}$ (figures 4.17i-4.17p).

We find a breathing mode at $f_{\text{breathing}} = 72.59\,\mathrm{GHz}$ and depict it in figures 4.18a-4.18e. As for the ferromagnet, the skyrmion expands and shrinks uniformly in such a way that the radial symmetry is preserved.

Compared to the ferromagnetic skyrmion, the lowest modes here appear at frequencies higher by at least an order of magnitude. This is a consequence of the faster magnetization dynamics of antiferromagnets, due to the large value of the exchange field B_{exch} [44]. In addition, the modes are spread out more in the spectrum – for the ferromagnetic skyrmion we find eight different modes in a range of $\sim 20\,\mathrm{GHz}$, whereas here there are five different modes in a range of $\sim 130\,\mathrm{GHz}$. The antiferromagnetic resonance frequency of the uniform state for the present set of parameters is $\sim 330\,\mathrm{GHz}$ (see Appendix D.4), which is considerably higher than the lowest-frequency excitation of the antiferromagnetic skyrmion ($\sim 60\,\mathrm{GHz}$). These results indicate that the low-frequency excitation spectrum of the confined antiferromagnetic skyrmion exhibits features distinct from the spectrum of the uniform state, and could provide a guide towards the experimental observation of an antiferromagnetic

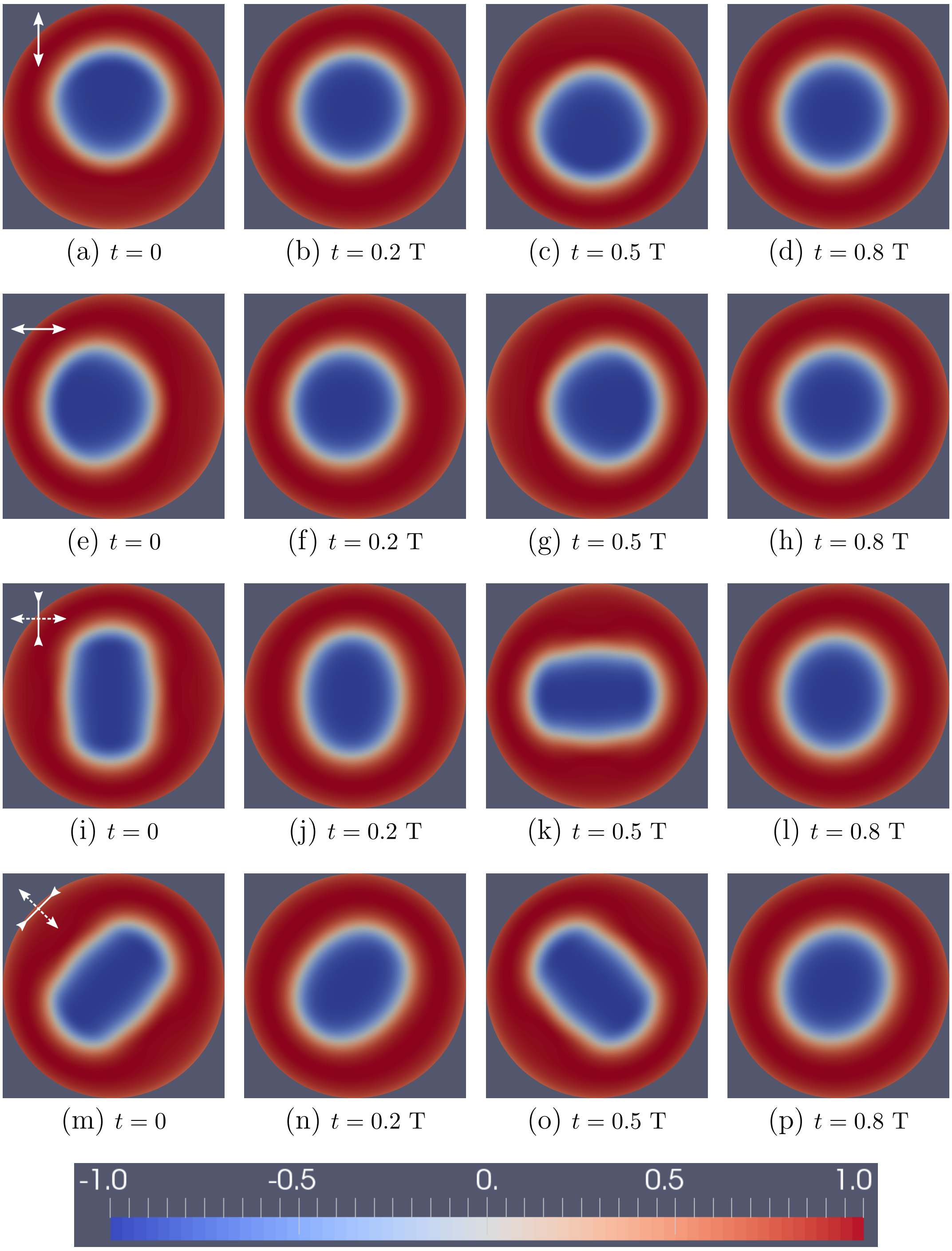

(a) $t = 0$ (b) $t = 0.2$ T (c) $t = 0.5$ T (d) $t = 0.8$ T

(e) $t = 0$ (f) $t = 0.2$ T (g) $t = 0.5$ T (h) $t = 0.8$ T

(i) $t = 0$ (j) $t = 0.2$ T (k) $t = 0.5$ T (l) $t = 0.8$ T

(m) $t = 0$ (n) $t = 0.2$ T (o) $t = 0.5$ T (p) $t = 0.8$ T

(q)

Figure 4.16: *Visualization of the antiferromagnetic skyrmion excitation modes, shown in order of increasing frequency - the two linear displacement modes and both twofold-deformed skyrmion modes (see also Table 4.11). The arrows denote the direction of motion; the deformed-modes oscillate first in the direction of the solid arrow and then continue along the dashed arrow. Continues in figures 4.17 and 4.18.*

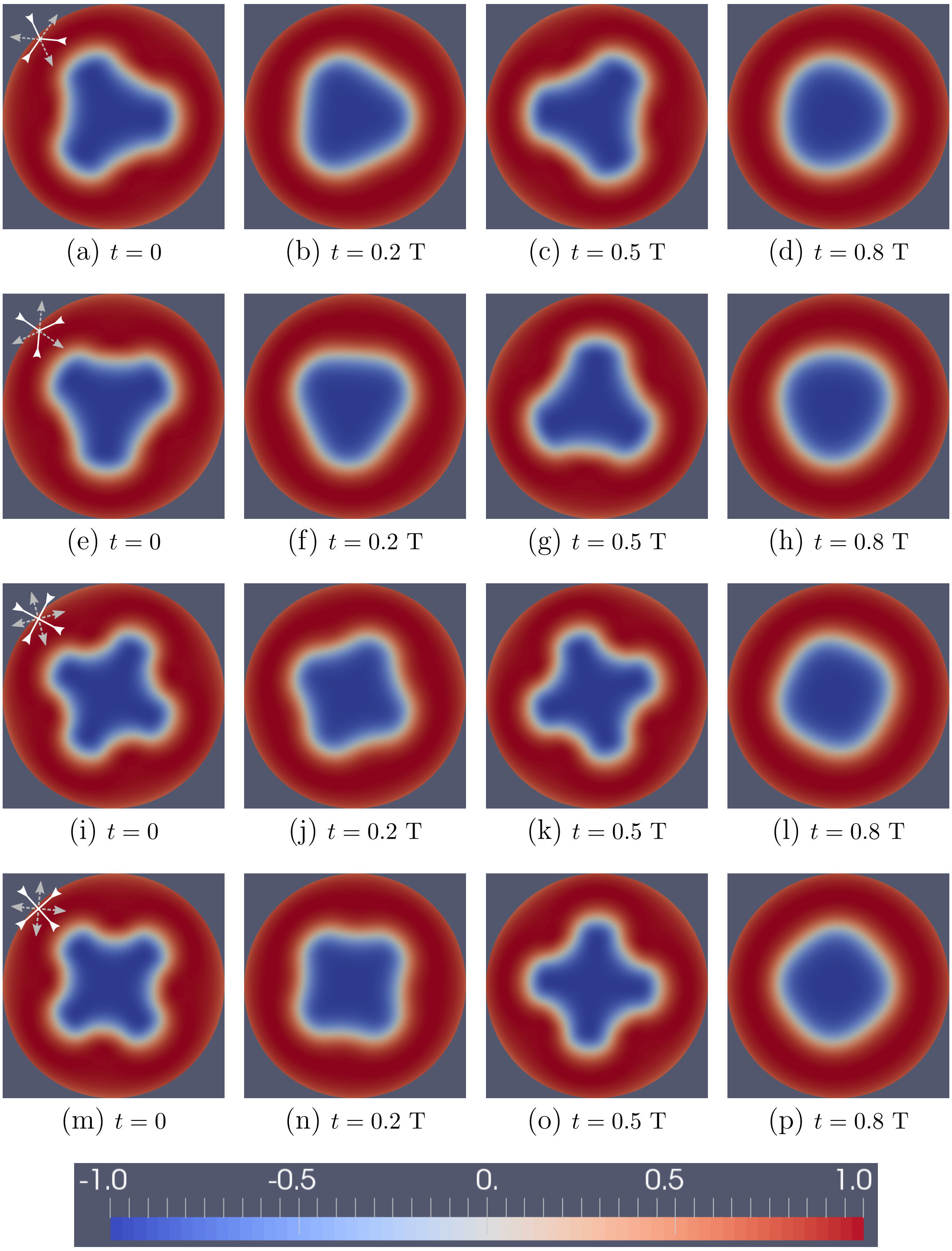

(a) $t = 0$ (b) $t = 0.2$ T (c) $t = 0.5$ T (d) $t = 0.8$ T

(e) $t = 0$ (f) $t = 0.2$ T (g) $t = 0.5$ T (h) $t = 0.8$ T

(i) $t = 0$ (j) $t = 0.2$ T (k) $t = 0.5$ T (l) $t = 0.8$ T

(m) $t = 0$ (n) $t = 0.2$ T (o) $t = 0.5$ T (p) $t = 0.8$ T

(q)

Figure 4.17: *(Continuation from figure 4.16) Antiferromagnetic skyrmion excitation modes 6 to 9 (see Table 4.11) shown in order of increasing frequency. From top to bottom - threefold-deformed skyrmion and fourfold-deformed skyrmion. The modes are deformed first in the direction of the solid arrow and subsequently, the dashed arrow. See also figure 4.18.*

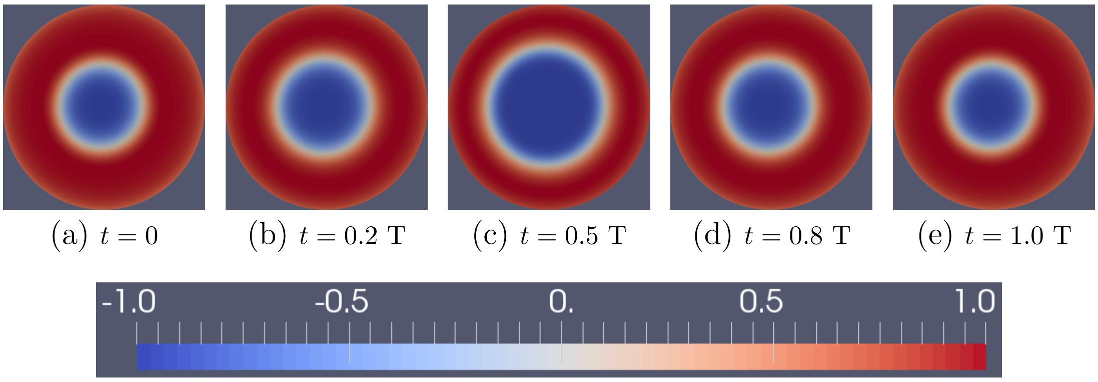

(a) $t = 0$ (b) $t = 0.2$ T (c) $t = 0.5$ T (d) $t = 0.8$ T (e) $t = 1.0$ T

(f)

Figure 4.18: *Visualization of the antiferromagnetic skyrmion breathing mode (see Table 4.11). Continuation from figures 4.16 and 4.17.*

skyrmion, similar to ferromagnets [36].

Dependence of the frequencies on the external magnetic field

Next, we investigate the behaviour of the antiferromagnetic skyrmion excitations as a function of the applied magnetic field. To do so, we sweep B in the range $0\,\mathrm{T} - 2\,\mathrm{T}$[33] in steps of $\Delta B = 50\,\mathrm{mT}$ and perform successive relaxation of the magnetic texture: we take the relaxed skyrmion at $B = 0\,\mathrm{T}$ (see figure 4.13) as an initial state, increase the field by ΔB, relax and repeat until we reach $B = 2\,\mathrm{T}$. We calculate the eigenfrequencies at each step of the successive relaxation and analyze the corresponding eigenmodes to take into account the effect of possible level crossings.

We plot the resulting frequencies in figure 4.19. There are two features that are different from the ferromagnetic skyrmion. First, the antiferromagnetic skyrmion is significantly more robust to the external field, in agreement with the analytical calculations shown in section 3.3.2: whereas its ferromagnetic counterpart vanishes at values higher than $0.6\,\mathrm{T}$, the antiferromagnetic skyrmion persists in the range studied here. This is not surprising, since antiferromagnets are known to be insensitive to magnetic fields [44]. Second, due to the large spread of the modes within the spectrum, we do not observe any level crossings.

As the magnetic field is applied to the system, the in-plane symmetry is lifted and the eigenmodes' time evolution changes – apart from the breathing mode – from oscillations between different configurations to in-plane rotations. This happens in such a way that the lower-frequency mode of the two (of the same type) rotates counterclockwise and the higher, clockwise. Contrary to the ferromagnetic skyrmion, the sense of rotation does not depend on the polarity of the skyrmion and the lower-frequency mode is counterclockwise for both $p = \pm 1$. The sense of rotation is determined by the direction of the applied magnetic field – reversing the field to point in the negative $\hat{z}$-direction reverses the direction of all the modes in Table 4.12.

---

[33] We choose the range $0\,\mathrm{T} < B < 2\,\mathrm{T}$ to highlight the differences between the ferromagnet and the antiferromagnet. The latter skyrmion remains stable also for stronger magnetic fields.

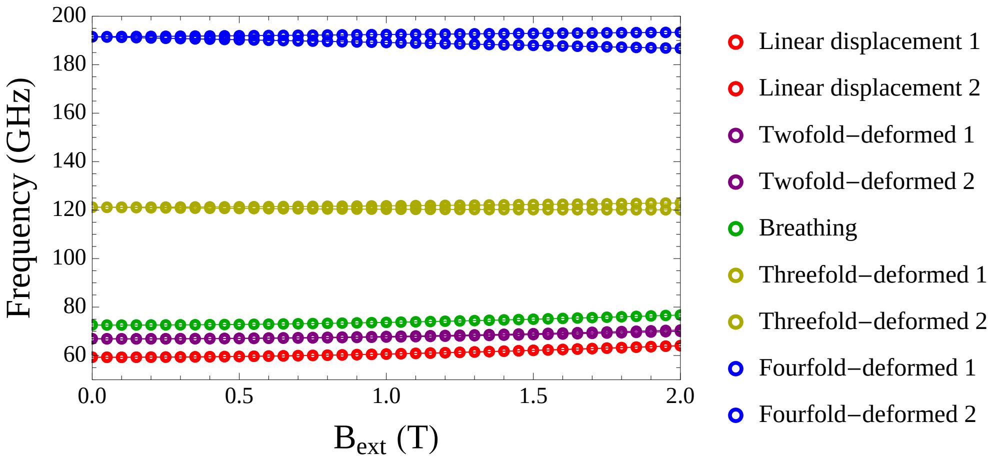

Figure 4.19: *Frequencies of the lowest nine excitation modes of the* $p = -1$ *antiferromagnetic skyrmion as a function of the external magnetic field. See Tables 4.11 and 4.12 for a list of the frequencies at both ends of the range studied here.*

Further, we find that increasing the magnetic field increases also the magnitude of the total magnetization excitation vector $\delta\mathbf{m}_{\mathrm{AFM}}$, consistent with the trend predicted by equation (3.28). At zero magnetic field we found that $|\delta\mathbf{m}_{\mathrm{AFM}}| \simeq 10^{-7} - 10^{-11}$ for the lowest excitation mode (see figure 4.15), whereas at $B = 2\,\mathrm{T}$ the magnitude increases by at least three orders of magnitude (see figure 4.20). We show this effect only for the lowest mode, but the trend is valid for all nine modes.

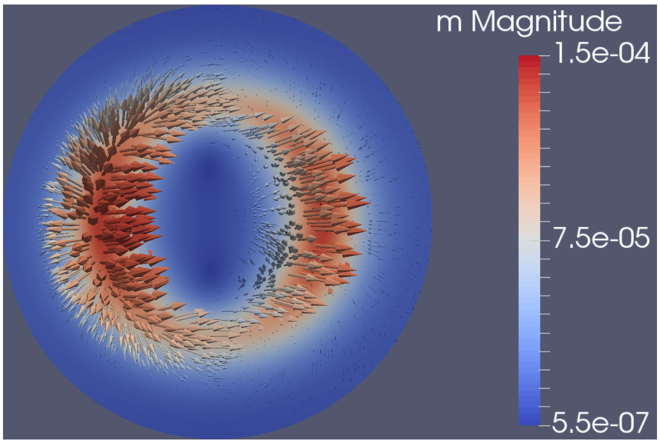

(a) (b)

Figure 4.20: *Total magnetization vector* $\delta\mathbf{m}_{AFM}$ *of the lowest-frequency excitation mode of the antiferromagnetic skyrmion at* $B = 2\,\mathrm{T}$ *(snapshot at* $t = 0$*). The arrows represent the direction of the vector* $\delta\mathbf{m}_{AFM}$ *and the color code, its magnitude. Here, we find* $|\delta\mathbf{m}_{AFM}| \simeq 10^{-4} - 10^{-7}$*, which is three orders of magnitude higher than in the zero-field state (see figure 4.15). See also equation (4.33) for the definition of the total magnetization vector.*

Mode	$f_{B=0\,\mathrm{T}}$(GHz)	$f_{B=2\,\mathrm{T}}$(GHz)	Rotation
Linear displacement	60	64	CCW
Linear displacement	60	64	CW
Twofold-deformed	67	70	CCW
Twofold-deformed	67	71	CW
Breathing	73	77	-
Threefold-deformed	120	120	CCW
Threefold-deformed	120	123	CW
Fourfold-deformed	189	187	CCW
Fourfold-deformed	189	193	CW

Table 4.12: *List of the antiferromagnetic skyrmion excitation frequencies as a function of the external field. Shown are the nine modes from Table 4.9 for two values of the magnetic field – at* $B = 0\,\mathrm{T}$ *and* $B = 2\,\mathrm{T}$*. The evolution of the modes as a function of B is shown in figure 4.19. The values listed here have been rounded to the nearest integer; the numerical errors shown in Table 4.9 apply here as well.*

Dependence of the frequencies on the sample radius

We create an initial skyrmion state of $R_{\mathrm{init}} = 15\,\mathrm{nm}$ on a sample with $R_{\mathrm{disk}} = 40\,\mathrm{nm}$ and relax until an equilibrium state is reached. We calculate the corresponding eigenfrequencies and eigenmodes, increase the nanodisk radius by $\Delta R_{\mathrm{disk}} = 10\,\mathrm{nm}$ and repeat the procedure until we reach $R_{\mathrm{disk}} = 100\,\mathrm{nm}$. We keep $B = 0\,\mathrm{T}$ and use the material parameters listed in Table 4.9. In that case, we have $D > D_0$, so that the skyrmion size is fixed by the nanodisk dimensions due to the confining potential of the boundaries. As a consequence, for each R_{disk} the skyrmion has a different size.

The results are plotted in figure 4.21. Similar to the ferromagnet, all investigated

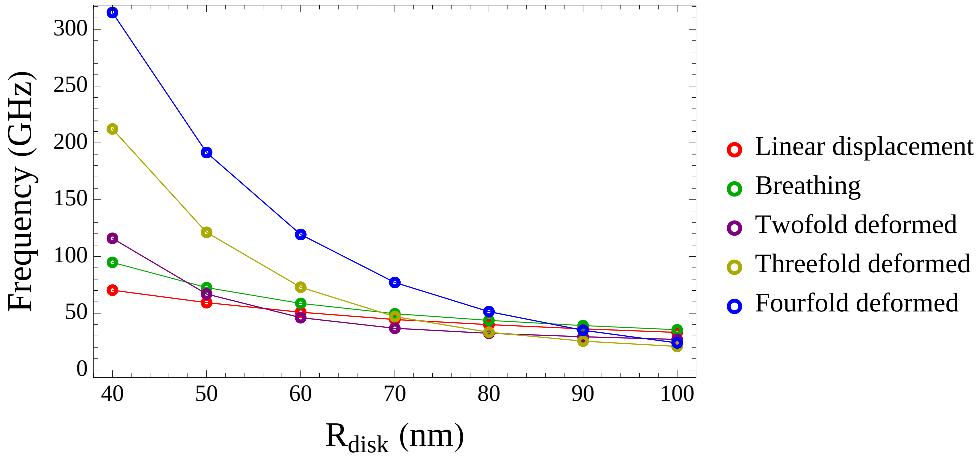

Figure 4.21: *Frequencies of the excitation modes of the* $p = -1$ *antiferromagnetic skyrmion as a function of the nanodisk radius. We show the modes listed in Table 4.11. See Table 4.13 for the frequencies at both ends of the range considered here.*

Mode	$f_{40\,\mathrm{nm}}$ (GHz)	$f_{100\,\mathrm{nm}}$ (GHz)
Linear displacement	70	33
Breathing	95	35
Twofold-deformed	116	27
Threefold-deformed	212	21
Fourfold-deformed	315	24

Table 4.13: *List of the antiferromagnetic skyrmion excitations as a function of* R_{disk}*: shown are the five types of modes from Table 4.11 at both ends of the range considered in this chapter:* $R_{disk} = 40\,\mathrm{nm}$ *(middle column) and* $R_{disk} = 100\,\mathrm{nm}$ *(right column). The values are rounded to the nearest integer and serve as a complementary qualitative guide to figure 4.21.*

excitation modes of the antiferromagnetic skyrmion decrease in frequency as the nanodisk radius R_{disk} is increased. As a further similarity, we find that the deformed-core modes (twofold-, threefold- and fourfold-deformed ones) are more sensitive to changes in the nanodisk radius than the other modes. However, the displaced modes decrease in frequency roughly by a factor of two, whereas the lowest gyrotropic mode of the ferromagnet decreases by two orders of magnitude.

4.2.4 Summary

In this section, we studied numerically the lowest-frequency excitation modes of both ferromagnetic and antiferromagnetic skyrmions confined in nanodisk samples, based on the phenomenological models developed in chapter 3.

In the ferromagnet, we obtained a skyrmion groundstate at zero external field that agrees with the analytical predictions. The low-frequency spectrum of the skyrmion groundstate exhibits gyrotropic, deformed-core and breathing modes, consistent with previous theoretical [34, 35, 36, 119, 125] and experimental results [38, 39, 40, 41][34]. The rotation sense of the lowest modes of each type depend on the skyrmion polarity[35]: clockwise for $p = +1$, and counterclockwise for $p = -1$. This is also in agreement with recent literature results [34, 119, 121, 125, 126]. In conclusion, we find a good agreement with literature and take this as a verification of our micromagnetic code.

Next, we presented the numerical calculations of the confined skyrmion eigenmodes in a two-sublattice antiferromagnet. First, we obtained a skyrmion groundstate consistent with the analytical predictions [13]. The material parameters of the antiferromagnet were chosen in such a way that the effective parameters (e.g., characteristic domain wall width x_0 and cycloid lengths $\xi_{\mathrm{FM,AFM}}$; see also chapter 3) are identical to the ferromagnet. We find that the resulting skyrmion profiles

---

[34] We note that there is no consensus yet on the gyrotropic modes, as these experiments report different results; see the discussion in the introduction of section 4.2

[35] This does not include the breathing mode, as the mode does not represent a rotation of the skyrmion.

are also identical, in agreement with the analytical treatment (see the discussion in section 3.3.2).

We investigated the nine lowest-frequency excitation modes of the antiferromagnetic skyrmion. We found that the modes come in pairs, which is a consequence of the doubled amount of degrees of freedom in the antiferromagnet due to the existence of two sublattices. There is one exception to this observation, which is the breathing mode: the lowest-frequency spectrum shows only one such mode.

The types of excitations modes are the same as for the ferromagnet: "translation," deformed-core and breathing modes. Importantly, at zero magnetic field the modes do not rotate, but rather oscillate between two configurations. This reflects the fact that there is no preferred sense of rotation in the antiferromagnet at zero field. When the field is applied in the out-of-plane direction, the modes transform from oscillations to rotations. In particular, the "translation" modes transform to rotation in a way that the skyrmion core is displaced from the center of the nanodisk. Therefore, we identify the antiferromagnetic linear-displacement modes as the counterpart of the ferromagnetic gyrotropic mode. Here, the sense of rotation depends on the relative orientation of the magnetic field and the skyrmion core: for opposite orientations the lowest mode of each pair is counterclockwise and the highest, clockwise; for parallel orientations the rotations are reversed. This is found to be true also for the deformed-core modes.

There is a numerical indication that the two modes in each pair split in frequency as a function of the external field; this will be a direction to pursue in future work.

Further, we find that the antiferromagnetic skyrmion modes have frequencies larger by at least an order of magnitude than the corresponding ferromagnetic modes. This is simply a manifestation of the faster magnetization dynamics in antiferromagnets, as was discussed in chapter 1.

Similar to the ferromagnet, the lowest antiferromagnetic skyrmion excitation frequencies are lower than the antiferromagnetic resonance frequency of the uniform state. Therefore, the presence of such low-frequency features in the spectrum could be used as a signature to identify antiferromagnetic skyrmions experimentally.

Finally, we found a similar declining trend of the excitation frequencies of both ferromagnetic and antiferromagnetic skyrmions as a function of the nanodisk radius. The skyrmions considered in this work are in the regime $D > D_0$, so that the skyrmion size is fixed by the sample dimensions. Further studies of skyrmions independent of the sample size (that is, in the opposite regime $D < D_0$) will shed more light onto the influence of the sample on the skyrmion dynamics, which is important for any device applications.

We emphasize that the finite-element eigenvalue method was used in this work to calculate the low-frequency spectrum of both ferromagnetic and antiferromagnetic skyrmions confined in a nanodisk. With this method, we are able to go beyond the modes that have been observed experimentally [38, 39, 40, 41], and calculate the full spectrum of confined skyrmions. A possible approach to determine how the modes are likely to be excited in experiment is to perturb the equilibrium state by introducing an external excitation into the model (e.g., a time-dependent magnetic field) and subsequently calculate the power spectral density of the skyrmion excitations [36, 125]. Previous studies for ferromagnets have suggested that

- oscillating magnetic fields applied in the out-of-plane direction [36, 37, 121, 125][36], as well as both oscillating magnetic and electric fields applied in-plane can be used to excite the breathing mode [37];
- to excite the gyrotropic mode, external magnetic field need to be applied within the plane [121, 125];
- the deformed-core skyrmion modes can be excited by a local probe, such as the spin-polarized scanning tunneling microscope [35].

The situation in antiferromagnets is more complicated, as the observation of antiferromagnetic order is notoriously difficult [44]. Due to the vanishingly small static magnetization, external magnetic fields are not expected to be able to excite the skyrmion excitation modes. Possible alternative approaches are to employ the dynamic magnetization that arises due to skyrmion motion, which can be coupled to time-dependent external magnetic fields[37], or use the recently observed Néel spin-orbit torques [49] that can electrically manipulate the Néel order parameter.

---

[36] The breathing mode is radially symmetric, so that external perturbations that preserve the radial symmetry are expected to be able to excite it.

[37] See the dynamic term in equation (4.13), which describes the total magnetization of an antiferromagnet.

Chapter 5

Reference and numerical code

This chapter serves as a reference for the numerically relevant characteristics of the phenomenological model, both for a ferromagnet and an antiferromagnet. We list the energy functionals, effective fields, projected and linearized Landau-Lifshitz-Gilbert equations, as well as their weak formulations.

5.1 Ferromagnetic model

The ferromagnetic micromagnetic model consists of the exchange interactions (A_{ex}), out-of-plane uniaxial anisotropy (K_u), Dzyaloshinskii-Moriya interactions (D) and external field (B). The order parameter of the model is the unit vector of the magnetization $\mathbf{m}$

$$F_{\mathrm{FM}} = \int d^3r \bigg\{ A_{\mathrm{ex}}(\nabla\mathbf{m})^2 - K_u(\mathbf{m}\cdot\hat{z})^2 - BM_{\mathrm{s}}(\mathbf{m}\cdot\hat{z}) \\ - D\Big[(\mathbf{m}\cdot\hat{z})(\nabla\cdot\mathbf{m}) - (\mathbf{m}\cdot\nabla)(\mathbf{m}\cdot\hat{z})\Big]\bigg\}. \tag{5.1}$$

This energy functional is coded as shown in listing 5.3.

Parameter	Unit
A_{ex}	$\mathrm{J\,m^{-1}}$
K_u	$\mathrm{J\,m^{-3}}$
B	T
D	$\mathrm{J\,m^{-2}}$
M_{s}	$\mathrm{A\,m^{-1}}$

Table 5.1: *Overview of the parameter units in equation (5.1).*

Parameter	Unit
$2A_{\text{ex}}/M_{\text{s}}$	$\text{T}\,\text{m}^2$
$2K_u/M_{\text{s}}$	T
B	T
$2D/M_{\text{s}}$	T m
M_{s}	$\text{A}\,\text{m}^{-1}$

Table 5.2: *Overview of the parameter units in equation (5.2).*

Effective field

The effective field of the ferromagnetic model is (see section 3.2.1)

$$\mathbf{B}_{\text{eff,FM}} = \frac{2A_{\text{ex}}}{M_{\text{s}}}\nabla^2\mathbf{m} + \frac{2K_u}{M_{\text{s}}}(\mathbf{m}\cdot\hat{z})\hat{z} + B\hat{z} + \frac{2D}{M_{\text{s}}}\Big[\hat{z}(\nabla\cdot\mathbf{m}) - \nabla(\mathbf{m}\cdot\hat{z})\Big]. \tag{5.2}$$

As discussed in section 2.3.1, we divide equation (5.2) by a reference saturation field $B_{\text{s}} = \mu_0 M_{\text{s}}$ to obtain the dimensionless effective field

$$\hat{\mathbf{B}}_{\text{eff,FM}} = l_{\text{ex}}^2\left(\nabla^2\mathbf{m}\right) + \frac{B_{\text{u}}}{B_{\text{s}}}(\mathbf{m}\cdot\hat{z})\hat{z} + \frac{B}{B_{\text{s}}}\hat{z} + l_{\text{DM}}\Big[\hat{z}(\nabla\cdot\mathbf{m}) - \nabla(\mathbf{m}\cdot\hat{z})\Big], \tag{5.3}$$

where the rescaled parameters are listed in Table 5.3.

Projected Landau-Lifshitz-Gilbert equation

The projection method leads to the following equation (see section 2.3.2)

$$\begin{aligned}\frac{1}{B_{\text{s}}}\int_V d^3r\Big(\mathbf{B}_{\text{eff}}\cdot\mathbf{v}\Big) =& -l_{\text{ex}}^2\int_V d^3r\Big(\nabla\mathbf{v}\cdot\nabla\mathbf{u}\Big)\\ &+\frac{B_{\text{u}}}{B_{\text{s}}}\int_V d^3r\Big(\mathbf{u}\cdot\hat{z}\Big)\Big(\mathbf{v}\cdot\hat{z}\Big)\\ &+\frac{B}{B_{\text{s}}}\int_V d^3r\Big(\mathbf{v}\cdot\hat{z}\Big)\\ &+l_{\text{DM}}\int_V d^3r\Big[\,(\nabla\cdot\mathbf{u})\,(\mathbf{v}\cdot\hat{z}) - \mathbf{v}\cdot\nabla\,(\mathbf{u}\cdot\hat{z})\Big]\\ &+\frac{l_{\text{DM}}}{2}\oint_{\partial V} d^2r\Big[\mathbf{u}\times\Big(d\hat{\mathbf{S}}\times\hat{z}\Big)\Big]\cdot\mathbf{v},\end{aligned} \tag{5.4}$$

	Parameter	Expression	Unit
exchange length	l_{ex}^2	$2A_{\text{ex}}/M_{\text{s}}B_{\text{s}}$	m
anisotropy field	B_{u}	$2K_u/M_{\text{s}}$	T
DM length	l_{DM}	$2D/M_{\text{s}}B_{\text{s}}$	m

Table 5.3: *Overview of the parameter units in equation (5.4).*

where $d\hat{\mathbf{S}}$ is a unit vector normal to the surface of the sample and $\mathbf{u}$ is the trial function to be calculated within the finite-element method (see listing 5.5).

Linearized Landau-Lifshitz-Gilbert equation

The eigenmodes of a magnetization structure is calculated from the linearized Landau-Lifshitz-Gilbert equation (see section 2.3.2) in frequency space

$$i\omega\delta\mathbf{m} = -\gamma\mathbf{m}_0 \times \mathbf{B}_{\text{eff}}[\delta\mathbf{m}] - \gamma\delta\mathbf{m} \times \mathbf{B}_{\text{eff}}[\mathbf{m}_0] + \Lambda\left(\mathbf{m}_0 \cdot \delta\mathbf{m}\right)\mathbf{m}_0, \tag{5.5}$$

where ω is the frequency of the corresponding eigenmode, $\mathbf{B}_{\text{eff}}$ the effective field given in equation (5.2), $\mathbf{m}_0$ the equilibrium magnetization configuration and $\delta\mathbf{m}$ the linear deviations transverse to $\mathbf{m}_0$, as described by equation (2.35). The weak formulation of the above equation becomes

$$\begin{aligned}
-\frac{i\omega}{\gamma B_{\text{s}}}\int_V d^3r\left(\mathbf{u}\cdot\mathbf{v}\right) = &-l_{\text{ex}}^2\int_V d^3r\left[\nabla\Big(\mathbf{v}\times\mathbf{m}_0\Big)\cdot\nabla\mathbf{u} + \nabla\Big(\mathbf{v}\times\mathbf{u}\Big)\cdot\nabla\mathbf{m}_0\right] \\
&+\frac{B_{\text{u}}}{B_{\text{s}}}\int_V d^3r\left[\left(\mathbf{u}\cdot\hat{z}\right)\left(\mathbf{m}_0\times\hat{z}\right)\cdot\mathbf{v} + \left(\mathbf{m}_0\cdot\hat{z}\right)\left(\mathbf{u}\times\hat{z}\right)\cdot\mathbf{v}\right] \\
&+\frac{B}{B_{\text{s}}}\int_V d^3r\left(\mathbf{u}\times\hat{z}\right)\cdot\mathbf{v} \\
&+l_{\text{DM}}\int_V d^3r\Big[\left(\nabla\cdot\mathbf{u}\right)\left(\mathbf{m}_0\times\hat{z}\right)\cdot\mathbf{v} - \mathbf{m}_0\times\nabla\left(\hat{z}\cdot\mathbf{u}\right)\cdot\mathbf{v} \\
&\qquad + \left(\nabla\cdot\mathbf{m}_0\right)\left(\mathbf{u}\times\hat{z}\right)\cdot\mathbf{v} - \mathbf{u}\times\nabla\left(\hat{z}\cdot\mathbf{m}_0\right)\cdot\mathbf{v}\Big] \\
&+\frac{l_{\text{DM}}}{2}\oint_{\partial V} d^2r\Big[\left(\mathbf{v}\times\mathbf{m}_0\right)\cdot\mathbf{u}\times\left[d\hat{\mathbf{S}}\times\hat{z}\right] \\
&\qquad + \left(\mathbf{v}\times\mathbf{u}\right)\cdot\mathbf{m}_0\times\left[d\hat{\mathbf{S}}\times\hat{z}\right]\Big] \\
&+\frac{\Lambda}{B_{\text{s}}}\int_V d^3r\left(\mathbf{m}_0\cdot\mathbf{u}\right)\left(\mathbf{m}_0\cdot\mathbf{v}\right),
\end{aligned} \tag{5.6}$$

where the deviations are now denoted by $\mathbf{u}$. Here, it was explicitly assumed, that both anisotropy and external field point in the $\hat{z}$-direction. The corresponding code script is given in listing 5.16.

5.2 Antiferromagnetic model

Here, we are considering a collinear two-sublattice antiferromagnet that is described by the magnetic moments $\mathbf{M}_1 = M_\mathrm{s}\mathbf{m}_1$ and $\mathbf{M}_2 = M_\mathrm{s}\mathbf{m}_2$. Here, M_s is the saturation magnetization of the antiferromagnet and $\mathbf{m}_1$, $\mathbf{m}_2$ are the sublattice unit magnetization vectors.

The antiferromagnetic micromagnetic model includes the homogeneous (B_exch) and inhomogeneous exchange interaction (A), out-of-plane uniaxial anisotropy (B_an), Dzyaloshinskii-Moriya interactions (D) and external field (B). The order parameter of the model is the unit Néel vector of the magnetization $\mathbf{n} = (\mathbf{m}_1 - \mathbf{m}_2)/2$, complemented by the unit antiferromagnetic magnetization $\mathbf{m} = (\mathbf{m}_1 + \mathbf{m}_2)/2$ [55]

$$\begin{aligned} F_\mathrm{AFM} = \int d\mathbf{r}\Bigg\{ & 2A\left(\nabla\mathbf{n}\right)^2 + 2B_\mathrm{exch}M_\mathrm{s}\mathbf{m}^2 - B_\mathrm{an}M_\mathrm{s}(\mathbf{n}\cdot\hat{z})^2 - 2BM_\mathrm{s}(\mathbf{m}\cdot\hat{z}) \\ & + 2B_\mathrm{d}M_\mathrm{s}(\mathbf{m}\times\mathbf{n})\cdot\hat{z} - D\Big[(\hat{z}\cdot\mathbf{n})(\nabla\cdot\mathbf{n}) - (\mathbf{n}\cdot\nabla)(\hat{z}\cdot\mathbf{n})\Big]\Bigg\}. \end{aligned} \tag{5.7}$$

However, for the numerical simulations it is more convenient to rewrite the energy functional (5.7) in terms of the sublattice magnetization vectors:

$$\begin{aligned} F_\mathrm{AFM} = \int d^3r\Bigg\{ & A\Big[(\nabla\mathbf{m}_1)^2 + (\nabla\mathbf{m}_2)^2\Big] + B_\mathrm{exch}M_\mathrm{s}\left(\mathbf{m}_1\cdot\mathbf{m}_2\right) \\ & - \frac{B_\mathrm{an}M_\mathrm{s}}{2}\Big[(\mathbf{m}_1\cdot\hat{z})^2 + (\mathbf{m}_2\cdot\hat{z})^2\Big] - BM_\mathrm{s}\Big[(\mathbf{m}_1\cdot\hat{z}) + (\mathbf{m}_2\cdot\hat{z})\Big] \\ & - B_\mathrm{d}M_\mathrm{s}\Big[\mathbf{m}_1\times\mathbf{m}_2\Big]\cdot\hat{z} + f_\mathrm{DM,surface}\Bigg\}, \end{aligned} \tag{5.8}$$

where the Dzyaloshinskii-Moriya functional is given by

$$f_\mathrm{DM} = -\frac{D}{4}\Bigg\{\Big[(\mathbf{m}_1 - \mathbf{m}_2)\cdot\hat{z}\Big]\Big[\nabla\cdot(\mathbf{m}_1 - \mathbf{m}_2)\Big] - (\mathbf{m}_1 - \mathbf{m}_2)\cdot\nabla\Big[(\mathbf{m}_1 - \mathbf{m}_2)\cdot\hat{z}\Big]\Bigg\}. \tag{5.9}$$

The corresponding code script is shown in listing 5.8.

Parameter	Unit
B_exch	T
A	$\mathrm{J\,m^{-1}}$
B_an	T
B	T
B_d	T
D	$\mathrm{J\,m^{-2}}$
M_s	$\mathrm{A\,m^{-1}}$

Table 5.4: *Overview of the parameter units in equation (5.7).*

Effective fields

The effective field of the antiferromagnetic model is derived from the energy functional (5.8). The sublattice form of the effective field is defined by

$$\mathbf{B}_{\text{eff},1}^{\text{AFM}} = -\frac{1}{M_\text{s}}\frac{\delta F_\text{AFM}}{\delta \mathbf{m}_1}, \qquad \text{and} \qquad \mathbf{B}_{\text{eff},2}^{\text{AFM}} = -\frac{1}{M_\text{s}}\frac{\delta F_\text{AFM}}{\delta \mathbf{m}_2}. \tag{5.10}$$

The effective fields become

$$\begin{aligned}\mathbf{B}_{\text{eff},1}^{\text{AFM}} &= \frac{2A}{M_\text{s}}\nabla^2\mathbf{m}_1 - B_\text{exch}\mathbf{m}_2 + B_\text{an}(\mathbf{m}_1\cdot\hat{z})\hat{z} + B\hat{z} + B_\text{d}(\mathbf{m}_2\times\hat{z}) + \mathbf{B}_\text{DM}^\text{AFM},\\ \mathbf{B}_{\text{eff},2}^{\text{AFM}} &= \frac{2A}{M_\text{s}}\nabla^2\mathbf{m}_2 - B_\text{exch}\mathbf{m}_1 + B_\text{an}(\mathbf{m}_2\cdot\hat{z})\hat{z} + B\hat{z} - B_\text{d}(\mathbf{m}_1\times\hat{z}) - \mathbf{B}_\text{DM}^\text{AFM},\end{aligned} \tag{5.11}$$

where the Dzyaloshinskii-Moriya field is

$$\mathbf{B}_\text{DM}^\text{AFM} = \frac{D}{2M_\text{s}}\left[\hat{z}\Big(\nabla\cdot(\mathbf{m}_1-\mathbf{m}_2)\Big) - \nabla\Big((\mathbf{m}_1-\mathbf{m}_2)\cdot\hat{z}\Big)\right]. \tag{5.12}$$

Projected Landau-Lifshitz-Gilbert equations

To proceed, we cast the effective fields dimensionless, by dividing equations (5.11) by the reference saturation field $B_\text{s} = \mu_0 M_\text{s}$. The corresponding weak formulation for both sublattices can be combined in a six-vector expression (see section 2.3.2)

$$\begin{aligned}\frac{1}{B_\text{s}}\int_V d^3r\Big(\mathbf{B}_{\text{eff},i}^{\text{AFM}}\cdot\mathbf{v}_i\Big) =& -\frac{B_\text{exch}}{B_\text{s}}\int_V d^3r\Big(1-\delta_{ij}\Big)\Big(\mathbf{u}_i\cdot\mathbf{v}_j\Big)\\ &- l_\text{ex}^2\int_V d^3r\Big(\nabla\mathbf{u}_i\cdot\nabla\mathbf{v}_i\Big) + \frac{B_\text{an}}{B_\text{s}}\int_V d^3r\Big(\mathbf{u}_i\cdot\hat{z}\Big)\Big(\mathbf{v}_i\cdot\hat{z}\Big)\\ &+ \frac{B}{B_\text{s}}\int_V d^3r\Big(\mathbf{v}_i\cdot\hat{z}\Big) - \frac{B_\text{d}}{B_\text{s}}\int_V d^3r\Big(\epsilon_{ij}\,(\mathbf{u}_i\times\hat{z})\cdot\mathbf{v}_j\Big)\\ &+ l_\text{DM}\int_V d^3r\left[\Big(\nabla\cdot\mathbf{u}_\Delta\Big)\hat{z} - \nabla\Big(\mathbf{u}_\Delta\cdot\hat{z}\Big)\right]\cdot\mathbf{v}_\Delta\\ &+ \frac{l_\text{DM}}{2}\oint_{\partial V} d^2r\Big[\mathbf{u}_\Delta\times\Big(d\hat{\mathbf{S}}\times\hat{z}\Big)\Big]\cdot\mathbf{v}_\Delta,\end{aligned} \tag{5.13}$$

where δ_{ij} is the Kronecker delta, ϵ_{ij} the Levi-Civita symbol and summation over repeated indices $i, j = 1, 2$ (denoting the two sublattices) is implied. Here, $d\hat{\mathbf{S}}$ is the unit vector normal to the surface of the sample, $\mathbf{u}_i$ denotes the (unknown) trial function and $\mathbf{v}_i$ the corresponding test function for the sublattice i, and we have defined $\mathbf{u}_\Delta = \mathbf{u}_1 - \mathbf{u}_2$ and $\mathbf{v}_\Delta = \mathbf{v}_1 - \mathbf{v}_2$. The code script is shown in listing 5.10.

	Parameter	Expression	Unit
exchange length	l_ex^2	$2A/M_\text{s}B_\text{s}$	m
DM length	l_DM	$D/M_\text{s}B_\text{s}$	m

Table 5.5: *Overview of the parameter units in (5.13).*

Linearized Landau-Lifshitz-Gilbert equations

In the antiferromagnet, the linearized Landau-Lifshitz-Gilbert equations (see section 2.3.2) read

$$i\omega\delta\mathbf{m}_i = -\gamma\mathbf{m}_{0_i}\times\mathbf{B}_{\text{eff}}[\delta\mathbf{m}_i,\delta\mathbf{m}_i] - \gamma\delta\mathbf{m}_i\times\mathbf{B}_{\text{eff}}[\mathbf{m}_{0_i},\mathbf{m}_{0_i}] + \Lambda\left(\mathbf{m}_{0_i}\cdot\delta\mathbf{m}_i\right)\mathbf{m}_{0_i}, \tag{5.14}$$

where $i = 1, 2$ denotes the sublattice, ω the frequency of the corresponding eigenmode, $\mathbf{B}_{\text{eff}}$ the effective field given in equations (5.11) and Λ the Lagrange multiplier. The weak formulation of equations (5.14) leads to the eigenvalue equation for the six-dimensional vector $\tilde{\mathbf{u}}$

$$-\frac{i\omega}{\gamma}\mathrm{M}\tilde{\mathbf{u}} = \mathrm{A}\tilde{\mathbf{u}}, \tag{5.15}$$

where

$$\mathrm{M}\tilde{\mathbf{u}} = \frac{1}{B_{\text{s}}}\int_V d^3r\Big(\mathbf{u}_i\cdot\mathbf{v}_i\Big) \tag{5.16}$$

and the right hand side given by

$$\begin{aligned}
\mathrm{A}\tilde{\mathbf{u}} = &-\frac{B_{\text{exch}}}{B_{\text{s}}}\int_V d^3r\Big(1-\delta_{ij}\Big)\bigg[\Big(\mathbf{m}_{0_i}\times\mathbf{u}_j\Big)\cdot\mathbf{v}_i + \Big(\mathbf{u}_i\times\mathbf{m}_{0_j}\Big)\cdot\mathbf{v}_i\bigg]\\
&- l_{\text{ex}}^2\int_V d^3r\bigg[\nabla\Big(\mathbf{v}_i\times\mathbf{m}_{0_i}\Big)\cdot\nabla\mathbf{u}_i + \nabla\Big(\mathbf{v}_i\times\mathbf{u}_i\Big)\cdot\nabla\mathbf{m}_{0_i}\bigg]\\
&+\frac{B_{\text{an}}}{B_{\text{s}}}\int_V d^3r\bigg[\left(\mathbf{u}_i\cdot\hat{z}\right)\left(\mathbf{m}_{0_i}\times\hat{z}\right)\cdot\mathbf{v}_i + \left(\mathbf{m}_{0_i}\cdot\hat{z}\right)\left(\mathbf{u}_i\times\hat{z}\right)\cdot\mathbf{v}_i\bigg]\\
&+\frac{B}{B_{\text{s}}}\int_V d^3r\left(\mathbf{u}_i\times\hat{z}\right)\cdot\mathbf{v}_i\\
&+\frac{B_{\text{d}}}{B_{\text{s}}}\int_V d^3r\,\epsilon_{ij}\bigg[\mathbf{m}_{0_i}\times\Big(\mathbf{u}_j\times\hat{z}\Big)\cdot\mathbf{v}_i + \mathbf{u}_i\times\Big(\mathbf{m}_{0_j}\times\hat{z}\Big)\cdot\mathbf{v}_i\bigg]\\
&+ l_{\text{DM}}\int_V d^3r\,\epsilon_{ij}\bigg[\Big(\nabla\cdot\mathbf{u}_\Delta\Big)\left(\mathbf{m}_{0_i}\times\hat{z}\right)\cdot\mathbf{v}_i - \mathbf{m}_{0_i}\times\nabla\Big(\hat{z}\cdot\mathbf{u}_\Delta\Big)\cdot\mathbf{v}_i\\
&\qquad\qquad + \Big(\nabla\cdot\mathbf{m}_{0_\Delta}\Big)\left(\mathbf{u}_i\times\hat{z}\right)\cdot\mathbf{v}_i - \mathbf{u}_i\times\nabla\Big(\hat{z}\cdot\mathbf{m}_{0_\Delta}\Big)\cdot\mathbf{v}_i\bigg]\left|\mathbf{m}_{0_j}\right|\\
&+\frac{l_{\text{DM}}}{2}\oint_{\partial V} d^2r\,\epsilon_{ij}\bigg[\left(\mathbf{v}_i\times\mathbf{m}_{0_i}\right)\cdot\mathbf{u}_\Delta\times\Big[d\hat{\mathbf{S}}\times\hat{z}\Big]\\
&\qquad\qquad + \left(\mathbf{v}_i\times\mathbf{u}_i\right)\cdot\mathbf{m}_{0_\Delta}\times\Big[d\hat{\mathbf{S}}\times\hat{z}\Big]\bigg]\left|\mathbf{m}_{0_j}\right|\\
&+\frac{\Lambda}{B_{\text{s}}}\int_V d^3r\left(\mathbf{m}_{0_i}\cdot\mathbf{u}_i\right)\left(\mathbf{m}_{0_i}\cdot\mathbf{v}_i\right).
\end{aligned} \tag{5.17}$$

Here, δ_{ij} is the Kronecker delta, ϵ_{ij} the Levi-Civita symbol and summation over repeated indices $i, j = 1, 2$ (denoting the two sublattices) is implied[1]. Again, $\mathbf{u}_i$ denotes the (unknown) trial function and $\mathbf{v}_i$ the corresponding test function for the sublattice i and we have defined $\mathbf{u}_\Delta = \mathbf{u}_1 - \mathbf{u}_2$, $\mathbf{v}_\Delta = \mathbf{v}_1 - \mathbf{v}_2$ and $\mathbf{m}_{0_\Delta} = \mathbf{m}_{0_1} - \mathbf{m}_{0_2}$. The corresponding code script is shown in listing 5.18.

5.3 Relaxation solver

Here, we list the Python script that describes the relaxation solver. We divide the representation into two parts: for the ferromagnet and for the antiferromagnet. The energy contributions are coded in unified form language (UFL).

Ferromagnet

Energy

Here, we list the code used to calculate the energy functional in (5.1).

```
# Create vector function space and test/trial functions.
  V = VectorFunctionSpace(mesh, 'CG', 1)
  u = TrialFunction(V)
  v = TestFunction(V)
  m0 = Function(V)
  m1 = Function(V)
  tmp = Function(V)
  m0_backup = Function(V)

# Manually cast `GenericVector` objects into `PETScVector` objects.
  m0_vec = m0.vector()
  m0_vec = as_backend_type(m0_vec)
  m1_vec = m1.vector()
  m1_vec = as_backend_type(m1_vec)
  tmp_vec = tmp.vector()
  tmp_vec = as_backend_type(tmp_vec)

# Measures
dx = Measure('cell', mesh)            # volume element
ds = Measure('exterior_facet', mesh)  # surface surrounding the volume
dP = Measure('vertex', mesh)          # point-wise
```

Listing 5.1: *Definition of functions for the ferromagnet.*

```
# Input parameters
  params['M_sat']         # saturation magnetization
  params['A_ex']          # exchange stiffness
  params['K_u1']          # uniaxial anisotropy constant
  params['B_ext']         # external magnetic field strength
  params['D']             # Dzyaloshinskii-Moriya interactions constant
  params['K_uni_vec']     # uniaxial anisotropy direction
  params['B_ext_vec']     # external magnetic field direction
```

---

[1] For a more compact representation we have included the magnitude of the unit vector $|\mathbf{m}_{0_j}|$ in the volume terms proportional to l_{DM}.

```

# Internal conversion of parameters
  k_vec = Constant(params['K_uni_vec'])
  B_vec = Constant(params['B_ext_vec'])

# Rescaling of the mesh
  mesh_scale = 1.0e-9
```

Listing 5.2: *Input variables for the ferromagnet.*

```
# Define the ferromagnetic energy functional
    exch_ufl = Constant(params['A_ex']/(mesh_scale**2)) *
                 inner(nabla_grad(m1), nabla_grad(m1))

    ani_ufl = - Constant(params['K_u1']) * inner(k_vec, m1)**2

    dmi_ufl = - Constant(params['D']/mesh_scale) *
                (inner(m1, zhat) * div(m1) -
                 inner(m1, nabla_grad(inner(zhat, m1))))

    ext_ufl = - Constant(params['B_ext']*params['M_sat']) *
                 inner(B_vec, m1)

# Add up all contributions
    total_energy_ufl =  exch_ufl + ani_ufl + dmi_ufl + ext_ufl

# Assemble all terms
    assemble(exch_ufl * dx)
    assemble(ani_ufl * dx)
    assemble(dmi_ufl * dx)
    assemble(ext_ufl * dx)
    assemble(total_energy_ufl * dx)
```

Listing 5.3: *Calculation of the ferromagnetic energy; see equation (5.1).*

Weak formulation

Here, we list the code used to define the effective field terms in equation (5.4).

```
# Internal conversion of parameters
  B_sat    = mu0 * params['M_sat']
  l_ex_sqr = 2. * params['A_ex'] / (mu0 * params['M_sat']**2)
  B_u      = 2. * params['K_u1'] / params['M_sat']
  l_DM     = 2. * params['D'] / params['M_sat'] / B_sat
  k_vec    = Constant(params['K_uni_vec'])
  B_vec    = Constant(params['B_ext_vec'])

# Rescaling of the mesh
  mesh_scale = 1.0e-9
  l_ex_sqr  /= (mesh_scale**2)
  l_DM      /= mesh_scale
```

Listing 5.4: *Rescaled variables for the ferromagnetic effective field.*

```
  fm_exch_ufl = Constant(-l_ex_sqr) *
                  inner(nabla_grad(u), nabla_grad(v)) * dx

  fm_ani_ufl = Constant(B_u / B_sat) *
                  inner(k_vec, u) * inner(k_vec, v) * dx

  fm_ext_ufl = Constant(params['B_ext'] / B_sat) *
                  inner(B_vec, v) * dx

  fm_dmi_ufl = Constant(l_DM) *
                 (inner(v, zhat) * div(u) -
                  inner(v, nabla_grad(inner(u, zhat)))) * dx
            +
               Constant(0.5 * l_DM) *
                  inner(v, cross(cross(zhat, nhat), u)) * ds
```

Listing 5.5: *Weak formulation of the ferromagnetic effective field; see equation (5.4).*

Antiferromagnet

Energy

Here, we list the code used to calculate the energy functional in equation (5.8).

```
# Create vector function space and test/trial functions.
  Q = VectorElement('CG', mesh.ufl_cell(), 1, 3)
  V = FunctionSpace(mesh, MixedElement([Q, Q]))
  u = TrialFunctions(V)
  v = TestFunctions(V)
  m0_full = Function(V)
  m0_backup = Function(V)
  m1_full = Function(V)
  tmp_full = Function(V)

# Manually cast `GenericVector` objects into `PETScVector` objects.
  m0_vec = m0_full.vector()
  m0_vec = as_backend_type(m0_vec)
  m1_vec = m1_full.vector()
  m1_vec = as_backend_type(m1_vec)
  tmp_vec = tmp_full.vector()
  tmp_vec = as_backend_type(tmp_vec)

# Split the "full" tensorial vectors into two three-component vectors.
  m0 = m0_full.split()
  m1 = m1_full.split()
  tmp = tmp_full.split()

# Measures
dx = Measure('cell', mesh)              # volume element
ds = Measure('exterior_facet', mesh)    # surface surrounding the volume
dP = Measure('vertex', mesh)            # point-wise
```

Listing 5.6: *Definition of functions for the antiferromagnet.*

```
# Input parameters
  params['Bs']            # saturation field
```

```
 params['B_ex_hom']     # homogeneous exchange field
 params['l_ex_inh']     # exchange length
 params['B_ani']        # uniaxial anisotropy field
 params['B_ext']        # external magnetic field strength
 params['B_DM_hom']     # homogeneous DM interactions field
 params['l_DM_inh']     # Dzyaloshinskii−Moriya interactions length
 params['B_ani_vec']    # uniaxial anisotropy direction
 params['B_ext_vec']    # external magnetic field direction

# Internal conversion of parameters
 Ms = params['Bs']/mu0
 Aex = ((params['l_ex_inh']*mesh_scale)**2) * params['Bs'] * Ms / 2
 DMI = (params['l_DM_inh']*mesh_scale) * params['Bs'] * Ms

# Rescaling of the mesh
 mesh_scale = 1.0
```

Listing 5.7: *Input variables for the antiferromagnet.*

```
# Define the AFM energy functional
   exch_inh_ufl = Constant(Aex) *
                  (inner(nabla_grad(m1[0]), nabla_grad(m1[0])) +
                   inner(nabla_grad(m1[1]), nabla_grad(m1[1])))

   exch_hom_ufl = Constant(params['B_ex_hom']*Ms) *
                  inner(m1[0], m1[1])

   ani_ufl = − Constant(params['B_ani']*Ms/2) *
                  (inner(Constant(params['B_ani_vec']), m1[0])**2 +
                   inner(Constant(params['B_ani_vec']), m1[1])**2)

   dmi_hom_ufl = − Constant(params['B_DM_hom']*Ms) *
                      inner(cross(m1[0], m1[1]), zhat)

   dmi_inh_ufl = − Constant(DMI/4) *
       (inner(m1[0] − m1[1], zhat) * div(m1[0] − m1[1]) −
        inner(m1[0] − m1[1], nabla_grad(inner(zhat, m1[0] − m1[1]))))

   ext_ufl = − Constant(params['B_ext']*Ms) *
                  (inner(Constant(params['B_ext_vec']), m1[0]) +
                   inner(Constant(params['B_ext_vec']), m1[1]))

# Add up all contributions
   total_energy_ufl =  exch_hom_ufl + exch_inh_ufl + ani_ufl +
                       dmi_hom_ufl + dmi_inh_ufl + ext_ufl

# Assemble all terms
   assemble(exch_inh_ufl * dx)
   assemble(exch_hom_ufl * dx)
   assemble(ani_ufl * dx)
   assemble(dmi_hom_ufl * dx)
   assemble(dmi_inh_ufl * dx)
   assemble(ext_ufl * dx)
   assemble(total_energy_ufl * dx)
```

Listing 5.8: *Calculation of the antiferromagnetic energy; see equation (5.8).*

Weak formulation

Here, we list the code used to define the effective field terms in equations (5.13).

```
# Define additional vectors.
  zhat = Constant((0., 0., 1.))
  nhat = FacetNormal(mesh)

# Rescaling of the mesh
  mesh_scale = 1.0e-9
  l_ex_inh /= mesh_scale
  l_DM_inh /= mesh_scale
```

Listing 5.9: *Variables for the antiferromagnetic effective field.*

```
    afm_exch_inh_ufl = Constant(-params['l_ex_inh']**2) *
                      (inner(nabla_grad(u[0]), nabla_grad(v[0])) +
                       inner(nabla_grad(u[1]), nabla_grad(v[1]))) * dx

    afm_exch_hom_ufl = Constant(-params['B_ex_hom']/params['Bs']) *
                      (inner(u[0], v[1]) + inner(u[1], v[0])) * dx

    afm_ani_ufl = Constant(params['B_ani']/params['Bs']) *
                      (inner(k_vec, u[0]) * inner(k_vec, v[0]) +
                       inner(k_vec, u[1]) * inner(k_vec, v[1])) * dx

    afm_dmi_hom_ufl = Constant(-params['B_DM_hom']/params['Bs']) *
                      (inner(v[0], cross(zhat, u[1])) -
                       inner(v[1], cross(zhat, u[0]))) * dx

    afm_ext_ufl = Constant(params['B_ext']/params['Bs']) *
                      (inner(Constant(params['B_ext_vec']), v[0]) +
                       inner(Constant(params['B_ext_vec']), v[1])) * dx

    afm_dmi_inh_ufl = Constant(params['l_DM_inh']) *
                  (inner(v[0] - v[1], zhat * div(0.5 * (u[0] - u[1]))) -
                   inner(v[0] - v[1],
                     nabla_grad(inner(zhat, 0.5 * (u[0] - u[1]))))) * dx
                       +
                         Constant(0.5 * params['l_DM_inh']) *
                   inner(v[0] - v[1],
                     cross(cross(zhat, nhat), 0.5 * (u[0] - u[1]))) * ds
```

Listing 5.10: *Weak formulation of the antiferromagnetic effective fields; see equations (5.13)*

Solver Object

Here, we list the code that shows how the weak formulations are assembled into matrices for the ferromagnet:

```
# Define the workspace PETSc vector/matrix pair.
    A = PETScMatrix()
    b = PETScVector()

```

```
# Combine the weak forms depending on the (time)step size ‘h0‘.
    a_ufl = Constant(1/B_sat_ref) * inner(u, v) * dx
          - Constant(h0) * (fm_exch_ufl + fm_ani_ufl + fm_dmi_ufl)

    L_ufl = Constant(1/B_sat_ref) * inner(m0, v) * dx
          + Constant(h0) * fm_ext_ufl

    assemble(a_ufl, tensor=A, keep_diagonal=True)
    assemble(L_ufl, tensor=b)
```

Listing 5.11: *Assembling the weak formulations into matrices for the ferromagnet.*

and for the antiferromagnet:

```
# Define the workspace PETSc vector/matrix pair.
    A = PETScMatrix()
    b = PETScVector()

# Combine the weak forms depending on the (time)step size ‘h0‘.
    a_ufl = Constant(1/params['Bs']) *
            (inner(u[0], v[0]) + inner(u[1], v[1])) * dx
          - Constant(h0) *
            (afm_exch_hom_ufl - afm_exch_inh_ufl - afm_ani_ufl
                              - afm_dmi_hom_ufl - afm_dmi_inh_ufl)

    L_ufl = Constant(1/params['Bs']) *
            (inner(m0[0], v[0]) + inner(m0[1], v[1])) * dx
          + Constant(h0) * afm_ext_ufl


    assemble(a_ufl, tensor=A, keep_diagonal=True)
    assemble(L_ufl, tensor=b)
```

Listing 5.12: *Assembling the weak formulations into matrices for the antiferromagnet.*

The following script describes the solution of the resulting linear algebra problem by standard Krylov methods (see section 2.3.1)

```
# Create a new PETSc Krylov-space linear solver.
    solver = PETSc.KSP()
    solver.create()
    solver.setNormType(solver.NormType.DEFAULT)
    solver.setTolerances(rtol=1.0e-10,
                         atol=1.0e-50,
                         divtol=1.0e5,
                         max_it=100000)
    solver.setType(solver.Type.GCR)
    solver.setOperators(A.mat(), A.mat())
    solver.setInitialGuessNonzero(True)
    solver.setUseFischerGuess(1, 50)

# Get and modify the "preconditioner" ('PC') object
    pc = solver.getPC()
    pc.setType(pc.Type.HYPRE)

# Finally, apply any user-defined options.
    solver.setFromOptions()
```

```
# Solve the linear system for the unknown magnetic field.  Store the
    result in `tmp` because it's not normalized yet.
 solver.solve(b.vec(), tmp_vec.vec())
```

Listing 5.13: *Relaxation solver object.*

The final step within the projection method is the normalization of the magnetization vector at iteration step

```
# Perform a pointwise renormalization of the ferromagnetic `tmp` into
    the unit vector field `m1`
expr = conditional(eq(inner(tmp, tmp), 0.0),
                   Constant((0.0, 0.0, 0.0)),
                   tmp / sqrt(inner(tmp, tmp)))

assemble(inner(expr, v) * dP, tensor=m1_vec)

# Perform a pointwise renormalization of the antiferromagnetic `tmp`
    into the unit vector field `m1`
expr1 = conditional(eq(inner(tmp[0], tmp[0]), 0.0),
      Constant((0., 0., 0.)), tmp[0] / sqrt(inner(tmp[0], tmp[0])))
expr2 = conditional(eq(inner(tmp[1], tmp[1]), 0.0),
      Constant((0., 0., 0.)), tmp[1] / sqrt(inner(tmp[1], tmp[1])))

assemble((inner(expr1, v[0]) + inner(expr2, v[1])) * dP,
         tensor=m1_vec)
```

Listing 5.14: *Renormalization of the magnetization vectors.*

5.4 Eigenspectrum solver

Ferromagnet

The following scripts implement equation (5.6).

```
# Create vector function space and test/trial functions.
V = VectorFunctionSpace(mesh, 'CG', 1)
u = TrialFunction(V)
v = TestFunction(V)
m0 = Function(V)

# Define additional vectors.
zhat = Constant((0., 0., 1.))
nhat = FacetNormal(mesh)

# Set up the weak formulation of the relaxation problem.
dx = Measure('cell', mesh)
ds = Measure('exterior_facet', mesh)
dP = Measure('vertex', mesh)
```

Listing 5.15: *Definition of functions for the ferromagnetic spectrum solver.*

```
# Weak formulation of the linearized Landau-Lifshitz-Gilbert equation
fm_exch_ufl = Constant(-l_ex_sqr) *
      (inner(nabla_grad(u), nabla_grad(cross(v, m0))) +
       inner(nabla_grad(m0), nabla_grad(cross(v, u)))) * dx
```

```
 fm_ani_ufl = Constant(B_u1 / B_sat_ref) *
       (inner(k_vec, u) * inner(v, cross(m0, k_vec)) +
        inner(k_vec, m0) * inner(v, cross(u, k_vec))) * dx

 fm_ext_ufl = Constant(params['B_ext'] / B_sat_ref) *
        inner(v, cross(u, B_vec)) * dx

 fm_dmi_ufl = Constant(-l_DM) *
       (div(u) * inner(v, cross(m0, zhat)) -
        inner(v, cross(m0, nabla_grad(inner(u, zhat)))) +
        div(m0) * inner(v, cross(u, zhat)) -
        inner(v, cross(u, nabla_grad(inner(m0, zhat))))) * dx
            +
              Constant(-0.5 * l_DM) *
       (inner(v, cross(m0, cross(cross(zhat, nhat), u))) +

 lagrange_ufl = Constant(params['lambda']) *
        inner(v, m0) * inner(m0, u) * dx
```

Listing 5.16: *Weak formulation of the linearized Landau-Lifshitz-Gilbert equation for the ferromagnet; see equation (5.6)*

Antiferromagnet

The following scripts implement equations (5.17).

```
# Create vector function space and test/trial functions.
 Q = VectorElement('CG', mesh.ufl_cell(), 1, 3)
 V = FunctionSpace(mesh, MixedElement([Q, Q]))
 u = TrialFunctions(V)
 v = TestFunctions(V)
 m0_full = Function(V)

# Define additional vectors.
 zhat = Constant((0., 0., 1.))
 nhat = FacetNormal(mesh)
 K_vec = Constant(params['B_ani_vec'])
 B_vec = Constant(params['B_ext_vec'])

# Split the "full" tensorial vectors into two three-component
# vectors.
 m0 = m0_full.split()

# Set up the weak formulation of the relaxation problem.
 dx = Measure('cell', mesh)
 ds = Measure('exterior_facet', mesh)
 dP = Measure('vertex', mesh)
```

Listing 5.17: *Definition of functions for the antiferromagnetic spectrum solver.*

```
# Weak formulation of the linearized Landau-Lifshitz-Gilbert equation
 afm_exch_hom_ufl = Constant(params['B_ex_hom']/params['Bs']) * \
       (inner(v[0], cross(u[0], m0[1])) + \
        inner(v[0], cross(m0[0], u[1])) + \
        inner(v[1], cross(u[1], m0[0])) + \
        inner(v[1], cross(m0[1], u[0]))) * dx
```

```
    afm_exch_inh_ufl = Constant(params['l_ex_inh']**2) * \
          (inner(nabla_grad(u[0]), nabla_grad(cross(v[0], m0[0]))) + \
           inner(nabla_grad(m0[0]), nabla_grad(cross(v[0], u[0]))) + \
           inner(nabla_grad(u[1]), nabla_grad(cross(v[1], m0[1]))) + \
           inner(nabla_grad(m0[1]), nabla_grad(cross(v[1], u[1])))) * dx

    afm_ani_ufl = Constant(-params['B_ani']/params['Bs']) * \
          (inner(K_vec, u[0]) * inner(v[0], cross(m0[0], K_vec)) + \
           inner(K_vec, m0[0]) * inner(v[0], cross(u[0], K_vec)) + \
           inner(K_vec, u[1]) * inner(v[1], cross(m0[1], K_vec)) + \
           inner(K_vec, m0[1]) * inner(v[1], cross(u[1], K_vec))) * dx

    afm_ext_ufl = Constant(-params['B_ext']/params['Bs']) * \
          (inner(v[0], cross(u[0], B_vec)) + \
           inner(v[1], cross(u[1], B_vec))) * dx

    afm_dmi_hom_ufl = Constant(-params['B_DM_hom']/params['Bs']) * \
          (inner(v[0], cross(u[0], cross(m0[1], zhat))) + \
           inner(v[0], cross(m0[0], cross(u[1], zhat))) - \
           inner(v[1], cross(u[1], cross(m0[0], zhat))) - \
           inner(v[1], cross(m0[1], cross(u[0], zhat)))) * dx


    afm_dmi_inh_ufl = Constant(-params['l_DM_inh']) * \
          (inner(v[0], cross(u[0], zhat)) * div(n_0) -
           inner(v[0], cross(u[0], nabla_grad(inner(n_0, zhat)))) + \
           inner(v[0], cross(m0[0], zhat)) * div(n_1) -
           inner(v[0], cross(m0[0], nabla_grad(inner(n_1), zhat)))) - \
           inner(v[1], cross(u[1], zhat)) * div(n_0) +
           inner(v[1], cross(u[1], nabla_grad(inner(n_0, zhat)))) -
           inner(v[1], cross(m0[1], zhat)) * div(n_1) +
           inner(v[1], cross(m0[1], nabla_grad(inner(n_1, zhat))))) * dx
                    +
          Constant(-0.5 * params['l_DM_inh']) *
          (inner(v[0], cross(m0[0], cross(cross(zhat, nhat), n_1))) +
           inner(v[0], cross(u[0], cross(cross(zhat, nhat), n_0))) -
           inner(v[1], cross(m0[1], cross(cross(zhat, nhat), n_1))) -
           inner(v[1], cross(u[1], cross(cross(zhat, nhat), n_0)))) * ds

    afm_lagrange_ufl = Constant(params['lambda']) *
          (inner(v[0], inner(m0[0], u[0]) * m0[0]) +
           inner(v[1], inner(m0[1], u[1]) * m0[1])) * dx

# Introduce for better readability
    n_0 = 0.5 * (m0[0] - m0[1])
    n_1 = 0.5 * (u[0] - u[1])
```

Listing 5.18: *Weak formulation of the linearized Landau-Lifshitz-Gilbert equations for the antiferromagnet; see eqs. (5.17).*

Eigenspectrum Solver Object

```
# Assemble the LHS bilinear form a(u,v) into a PETSc matrix.
    A = PETScMatrix()
    assemble(a_ufl, tensor=A, keep_diagonal=True)
```

```
# Assemble the mass matrix.
  M = PETScMatrix()
  assemble(Constant(1.0 / B_sat_ref) * inner(u, v) * dx, tensor=M,
    keep_diagonal=True)
```

Listing 5.19: *Assemble the matrices for the ferromagnet.*

```
# Assemble the LHS bilinear form a(u,v) into a PETSc matrix.
  A = PETScMatrix()
  assemble(a_ufl, tensor=A, keep_diagonal=True)

# Assemble the mass matrix.
  M = PETScMatrix()
  assemble(Constant(1.0/params['Bs']) *
           (inner(u[0], v[0]) + inner(u[1], v[1])) * dx,
           tensor=M, keep_diagonal=True)
```

Listing 5.20: *Assemble the matrices for the antiferromagnet.*

```
# Create a SLEPc ”Eigenvalue Problem Solver” (‘EPS‘) object and
# adjust its parameters.
  eps = SLEPc.EPS()
  eps.create()
  eps.setFromOptions()
  eps.setType(eps.Type.KRYLOVSCHUR)
  eps.setProblemType(eps.ProblemType.GNHEP)
  eps.setWhichEigenpairs(eps.Which.TARGET_MAGNITUDE)
  eps.setTarget(0.1)
  eps.setTolerances(tol=1.0e-8, max_it=500)
  eps.setDimensions(nev=10)
  eps.setOperators(A.mat(), M.mat())

# Get and modify the ”basis vector” (‘BV‘) object associated to the
# eigensolver object.
  bv = eps.getBV()
  bv.setOrthogonalization(refine=bv.OrthogRefineType.ALWAYS)

# Get and modify the ”spectral transformation” (‘ST‘) object
# associated to the eigensolver object.
  st = eps.getST()
  st.setType(st.Type.SINVERT)

# Get and modify the ”Krylov subspace problem” (‘KSP‘) object
# associated with the spectral transformation.
  ksp = st.getKSP()
  ksp.setType(ksp.Type.GCR
  ksp.setTolerances(rtol=1.0e-8)

# Get and modify the ”preconditioner” (‘PC‘) object associated with
# the KSP object.
  pc = ksp.getPC()
  pc.setType(pc.Type.LU)
  pc.setFactorSolverPackage('mumps')
  pc.setFactorOrdering(ord_type='rcm')
  pc.setFactorLevels(1)

```

```
# Run the EPS solver.
  eps.solve()
```

Listing 5.21: *Eigenspectrum solver object.*

5.5 Mesh

Here, we list the code used to generate the mesh of a nanodisk with radius $R_{\text{disk}} = 50\,\text{nm}$, thickness $t = 1.0\,\text{nm}$ and a characteristic length $l_{\text{char}} = 1.0\,\text{nm}$ with Gmsh [91]. We define four points (p1-p4) around the origin (p0) of a circle and connect them via circular segments (l0-l3). Finally, we extrude the obtained circular surface in the $\hat{z}$-direction to obtain the nanodisk of the desired thickness:

```
General.ExpertMode = 1;
Mesh.Algorithm = 6;
Mesh.Algorithm3D = 4;
Mesh.Format = 1;

height = 1.0;
radius = 50.0;
lchar = 1.0;

p0 = newp; Point(p0) = {{ 0., 0., -0.5 * height, lchar }};
p1 = newp; Point(p1) = {{ 0., radius, -0.5 * height, lchar }};
p2 = newp; Point(p2) = {{ -radius, 0., -0.5 * height, lchar }};
p3 = newp; Point(p3) = {{ 0., -radius, -0.5 * height, lchar }};
p4 = newp; Point(p4) = {{ radius, 0., -0.5 * height, lchar }};

l0 = newl; Circle(l0) = {{ p1, p0, p2 }};
l1 = newl; Circle(l1) = {{ p2, p0, p3 }};
l2 = newl; Circle(l2) = {{ p3, p0, p4 }};
l3 = newl; Circle(l3) = {{ p4, p0, p1 }};

ll0 = newll; Line Loop(ll0) = {{ l0, l1, l2, l3 }};
s0 = news; Plane Surface(s0) = {{ ll0 }};

out[] = Extrude {{ 0, 0, height }} {{ Surface{{s0}}; }};
s1 = out[0];
v0 = out[1];

Physical Surface(2001) = {{ s0 }};
Physical Surface(2002) = {{ s1 }};
Physical Volume(3001) = {{ v0 }};
```

Listing 5.22: *Mesh generation with the open-source software Gmsh.*

Chapter 6

Conclusions

In this work, we investigated the static and dynamic properties of ferromagnetic and antiferromagnetic skyrmions stabilized by interfacial Dzyaloshinskii-Moriya interactions in thin films. We performed both analytical and numerical calculations based on the phenomenological models presented in chapter 3.

The static properties of ferromagnetic skyrmions have been widely studied, both theoretically and experimentally [10, 12, 13, 20, 24]. In contrast, antiferromagnetic skyrmions have not been experimentally observed yet and there are still many open questions. Given the importance of thin films for technological applications, we discussed the effect that finite-size samples have on antiferromagnetic skyrmions in chapter 3, following the approach in reference [26]. Importantly, we derived the boundary condition, induced by the Dzyaloshinskii-Moriya interactions, that determines the profile of an antiferromagnetic skyrmion confined in a circular nanodisk.

We extended the phenomenological theory describing uniaxial antiferromagnets with interfacial Dzyaloshinskii-Moriya interactions to incorporate the current-induced spin-orbit torques, together with the already studied spin-transfer torques. We used this theory to analyze the translational skyrmion motion in the presence of a time-independent external magnetic field and a DC electric current analytically in section 4.1. We find that the magnetic field merely modifies the shape of the antiferromagnetic skyrmion and does not contribute towards the skyrmion motion. Further, our results show that the skyrmion moves in a straight line, along the direction of the applied electric current. This agrees with the numerical results reported in references [52, 53], which were obtained for skyrmions in the absence of a magnetic field. Depending on the choice of parameters, we find skyrmion velocities that are in the range of $1 - 1000\,\mathrm{m\,s^{-1}}$, in agreement with the numerical results of references [52, 53].

Given the importance of the skyrmion excitation modes in ferromagnets [20], we developed a micromagnetic code to calculate the eigenspectrum of a confined antiferromagnetic skyrmion. We verified the code in section 4.2 on the ferromagnetic skyrmion: we observe gyrotropic, breathing and deformed-core modes in the low-frequency excitation spectrum, in good qualitative agreement with existing results [34, 35, 36, 119]. Importantly, we also find a good quantitative agreement for the frequency of the ferromagnetic skyrmion breathing mode obtained in reference [36], for the same model as ours, but with a different numerical method.

We applied the micromagnetic code to a two-sublattice antiferromagnetic thin film and obtained numerically a skyrmion groundstate that is consistent with the theoretical predictions, as described in chapter 3 and in reference [13].

The excitation modes of the antiferromagnetic skyrmions are found to be of the same type as for the ferromagnet: "translational," breathing and deformed-core modes. The differences can be traced back to the unique properties of antiferromagnets:

(i) due to the exchange enhancement [44, 109], the frequencies of the skyrmion modes in antiferromagnets are at least an order of magnitude higher than in ferromagnets;

(ii) we find two pairs of each type of mode in the low-frequency spectrum in the antiferromagnet, which is a consequence of the doubled amount of degrees of freedom due to the presence of two magnetic sublattices;

(iii) the antiferromagnetic modes do not have a rotational nature at zero magnetic field, in contrast to the ferromagnet. There is no preferred sense of rotation in the antiferromagnet at zero field; however, this symmetry is lifted when the magnetic field is turned on and the skyrmion excitations begin to rotate.

Importantly, the low-frequency spectrum of the antiferromagnetic skyrmion shows characteristic features that are absent in the uniform antiferromagnetic state, which could prove useful in the attempts to identify antiferromagnetic skyrmions experimentally.

Finally, our method to calculate the skyrmion excitation modes numerically gives us access to the full eigenmode spectrum. A direction for future research is to identify a way to experimentally excite the obtained eigenmodes. Numerically, this could be achieved by introducing an external excitation into the model (such as a time-dependent magnetic field) and calculating the power spectral density of the excitations, as proposed in references [36, 125] for ferromagnets. This approach will be coupled with on-going research into the possible ways to experimentally identify antiferromagnetic textures: e.g., employing the dynamical magnetization that an antiferromagnetic texture develops when it is set in motion, or the recently discovered Néel spin-orbit torques [48, 49] that can electrically manipulate the Néel order parameter.

Appendix A

Details of the numerical formulation

A.1 Weak formulation of the eigenvalue equation

Here, we construct the weak formulation of linearized Landau-Lifshitz-Gilbert equation (2.39) of the ferromagnet. Equation (2.39) reads

$$i\omega\delta\mathbf{m} = -\gamma\mathbf{m}_0 \times \mathbf{B}_{\text{eff}}[\delta\mathbf{m}] - \gamma\delta\mathbf{m} \times \mathbf{B}_{\text{eff}}[\mathbf{m}_0] + \Lambda\left(\mathbf{m}_0 \cdot \delta\mathbf{m}\right)\mathbf{m}_0, \tag{A.1}$$

where the ferromagnetic effective field is specified in equation (3.8)

$$\mathbf{B}_{\text{eff}}[\mathbf{m}] = \frac{2A_{\text{ex}}}{M_{\text{s}}}\nabla^2\mathbf{m} + 2K_u(\mathbf{m}\cdot\hat{z})\hat{z} + 2B\hat{z} + \frac{2D}{M_{\text{s}}}\Big[\hat{z}(\nabla\cdot\mathbf{m}) - \nabla(\hat{z}\cdot\mathbf{m})\Big]. \tag{A.2}$$

Following the finite-element method nomenclature (see section 2.3.1), we denote the excitation vector $\delta\mathbf{m}$ as the trial function $\mathbf{u}$. To construct the weak formulation of equation (A.1), we multiply it by a test function $\mathbf{v}$ and integrate over the entire volume V. The left hand side of equation (A.1) becomes

$$i\omega\int_V d^3r\left(\mathbf{u}\cdot\mathbf{v}\right), \tag{A.3}$$

the first term of the right hand side

$$\begin{aligned}-\gamma\int_V d^3r\Bigg\{&\frac{2A_{\text{ex}}}{M_{\text{s}}}\left(\mathbf{m}_0\times\nabla^2\mathbf{u}\right)\cdot\mathbf{v} + 2K_u\left(\mathbf{u}\cdot\hat{z}\right)\left(\mathbf{m}_0\times\hat{z}\right)\cdot\mathbf{v}\\ &+\frac{2D}{M_{\text{s}}}\Bigg[\left(\nabla\cdot\mathbf{u}\right)\left(\mathbf{m}_0\times\hat{z}\right)\cdot\mathbf{v} - \mathbf{m}_0\times\nabla\left(\hat{z}\cdot\mathbf{u}\right)\cdot\mathbf{v}\Bigg]\Bigg\},\end{aligned} \tag{A.4}$$

the second term on the right hand side

$$\begin{aligned}-\gamma\int_V d^3r\Bigg\{&\frac{2A_{\text{ex}}}{M_{\text{s}}}\left(\mathbf{u}\times\nabla^2\mathbf{m}_0\right)\cdot\mathbf{v} + 2K_u\left(\mathbf{m}_0\cdot\hat{z}\right)\left(\mathbf{u}\times\hat{z}\right)\cdot\mathbf{v} + 2B\left(\mathbf{u}\times\hat{z}\right)\cdot\mathbf{v}\\ &+\frac{2D}{M_{\text{s}}}\Bigg[\left(\nabla\cdot\mathbf{m}_0\right)\left(\mathbf{u}\times\hat{z}\right)\cdot\mathbf{v} - \mathbf{u}\times\nabla\left(\hat{z}\cdot\mathbf{m}_0\right)\cdot\mathbf{v}\Bigg]\Bigg\},\end{aligned} \tag{A.5}$$

and the Lagrange multiplier term

$$\Lambda \int_V d^3r \left(\mathbf{m}_0 \cdot \mathbf{u}\right)\left(\mathbf{m}_0 \cdot \mathbf{v}\right). \tag{A.6}$$

Next, we integrate by parts the exchange interaction terms in equations (A.4 -A.5)

$$\begin{aligned} \int_V d^3r \left(\mathbf{v} \times \mathbf{m}_0\right) \cdot \nabla^2 \mathbf{u} &= \oint_{\partial V} d^2r \left(\mathbf{v} \times \mathbf{m}_0\right) \cdot \frac{\partial \mathbf{u}}{\partial S} - \int_V d^3r \nabla\Big(\mathbf{v} \times \mathbf{m}_0\Big) \cdot \nabla \mathbf{u}, \\ \int_V d^3r \left(\mathbf{v} \times \mathbf{u}\right) \cdot \nabla^2 \mathbf{m}_0 &= \oint_{\partial V} d^2r \left(\mathbf{v} \times \mathbf{u}\right) \cdot \frac{\partial \mathbf{m}_0}{\partial S} - \int_V d^3r \nabla\Big(\mathbf{v} \times \mathbf{u}\Big) \cdot \nabla \mathbf{m}_0. \end{aligned} \tag{A.7}$$

Here, through the surface terms, the boundary conditions for $\partial\mathbf{u}/\partial S$ and $\partial\mathbf{m}_0/\partial S$ naturally enter the variational problem. Equation (A.27) describes the modified boundary conditions for the ferromagnetic magnetization vector $\mathbf{m}$ in the presence of Dzyaloshinskii-Moriya interactions (see Appendix A.2 for details). To obtain the expressions for the deviation $\mathbf{u}$ ($\delta\mathbf{m}$) we plug equation (2.35) in equation (A.27)

$$\frac{\partial \mathbf{m}_0}{\partial S} + \frac{\partial \mathbf{u}}{\partial S} = \frac{D}{2A_{\text{ex}}}\Bigg\{\mathbf{m}_0 \times \Big[d\hat{\mathbf{S}} \times \hat{z}\Big] + \mathbf{u} \times \Big[d\hat{\mathbf{S}} \times \hat{z}\Big]\Bigg\}. \tag{A.8}$$

We know already that the equilibrium magnetization $\mathbf{m}_0$ satisfies equation (A.27); it follows that

$$\frac{\partial \mathbf{u}}{\partial S} = \frac{D}{2A_{\text{ex}}}\mathbf{u} \times \Big[d\hat{\mathbf{S}} \times \hat{z}\Big]. \tag{A.9}$$

Consequently, the surface terms in equations (A.4 -A.5) and (A.7) become

$$\begin{aligned} &\frac{2A_{\text{ex}}}{M_{\text{s}}} \oint_{\partial V} d^2r \Bigg[\left(\mathbf{v} \times \mathbf{m}_0\right) \cdot \frac{\partial \mathbf{u}}{\partial S} + \left(\mathbf{v} \times \mathbf{u}\right) \cdot \frac{\partial \mathbf{m}_0}{\partial S}\Bigg] \\ &= \frac{D}{M_{\text{s}}} \oint_{\partial V} d^2r \Bigg[\left(\mathbf{v} \times \mathbf{m}_0\right) \cdot \mathbf{u} \times \Big[d\hat{\mathbf{S}} \times \hat{z}\Big] + \left(\mathbf{v} \times \mathbf{u}\right) \cdot \mathbf{m}_0 \times \Big[d\hat{\mathbf{S}} \times \hat{z}\Big]\Bigg]. \end{aligned} \tag{A.10}$$

Next, we bring together all contributions in equations (A.3 -A.6) and divide the resulting equation by the saturation field $B_{\text{s}} = \mu_0 M_{\text{s}}$, to obtain a dimensionless differential equation (continues on the next page)

$$\begin{aligned} -\frac{i\omega}{\gamma B_{\text{s}}} \int_V d^3r \left(\mathbf{u} \cdot \mathbf{v}\right) = &- \frac{2A_{\text{ex}}}{M_{\text{s}} B_{\text{s}}} \int_V d^3r \Bigg[\nabla\Big(\mathbf{v} \times \mathbf{m}_0\Big) \cdot \nabla \mathbf{u} + \nabla\Big(\mathbf{v} \times \mathbf{u}\Big) \cdot \nabla \mathbf{m}_0\Bigg] \\ &+ \frac{2K_u}{B_{\text{s}}} \int_V d^3r \Bigg[\left(\mathbf{u} \cdot \hat{z}\right)\left(\mathbf{m}_0 \times \hat{z}\right) \cdot \mathbf{v} + \left(\mathbf{m}_0 \cdot \hat{z}\right)\left(\mathbf{u} \times \hat{z}\right) \cdot \mathbf{v}\Bigg] \\ &+ \frac{2B}{B_{\text{s}}} \int_V d^3r \left(\mathbf{u} \times \hat{z}\right) \cdot \mathbf{v} \\ &+ \frac{2D}{M_{\text{s}} B_{\text{s}}} \int_V d^3r \Bigg[\left(\nabla \cdot \mathbf{u}\right)\left(\mathbf{m}_0 \times \hat{z}\right) \cdot \mathbf{v} - \mathbf{m}_0 \times \nabla\left(\hat{z} \cdot \mathbf{u}\right) \cdot \mathbf{v} \end{aligned}$$

$$+ \left(\nabla \cdot \mathbf{m}_0\right)\left(\mathbf{u} \times \hat{z}\right) \cdot \mathbf{v} - \mathbf{u} \times \nabla\left(\hat{z} \cdot \mathbf{m}_0\right) \cdot \mathbf{v}\Bigg]$$

$$+ \frac{D}{M_\mathrm{s} B_\mathrm{s}} \oint_{\partial V} d^2 r \Bigg[\left(\mathbf{v} \times \mathbf{m}_0\right) \cdot \mathbf{u} \times \left[d\hat{\mathbf{S}} \times \hat{z}\right] + \left(\mathbf{v} \times \mathbf{u}\right) \cdot \mathbf{m}_0 \times \left[d\hat{\mathbf{S}} \times \hat{z}\right]\Bigg]$$

$$+ \frac{\Lambda}{B_\mathrm{s}} \int_V d^3 r \left(\mathbf{m}_0 \cdot \mathbf{u}\right)\left(\mathbf{m}_0 \cdot \mathbf{v}\right). \tag{A.11}$$

We can write equation (A.11) in matrix form as

$$-\frac{i\omega}{\gamma} \mathrm{M}\tilde{\mathbf{u}} = \mathrm{A}\tilde{\mathbf{u}}, \tag{A.12}$$

and treat it as a generalized eigenvalue problem. Here, $\mathrm{A}\tilde{\mathbf{u}}$ represent the entire right hand side of equation (A.11) and $\mathrm{M}\tilde{\mathbf{u}} = (1/B_\mathrm{s}) \int_V d^3 r (\mathbf{u} \cdot \mathbf{v})$.

A.2 Boundary conditions in the presence of Dzyaloshinskii-Moriya interactions

Rohart *et al.* [26] showed that when Dzyaloshinskii-Moriya interactions are present in ferromagnetic nanodisks nontrivial natural boundary conditions arise and have to be taken into account for a correct description of the magnetic texture. Here, using a variational principle, we rederive the boundary condition for ferromagnets and extend the approach to derive the corresponding boundary condition in antiferromagnets.

A.2.1 Ferromagnets

The ferromagnetic energy functional (3.7) considered in this work incorporates exchange interactions, uniaxial anisotropy, external magnetic field and the interfacial Dzyaloshinskii-Moriya interactions

$$F_\mathrm{FM}[\mathbf{m}] = F_\mathrm{exch}[\mathbf{m}] + F_\mathrm{ani}[\mathbf{m}] + F_\mathrm{ext}[\mathbf{m}] + F_\mathrm{DM}[\mathbf{m}], \tag{A.13}$$

where $\mathbf{m}$ is the unit magnetization vector. Within the variational principle, the equilibrium magnetization structure is found from the condition

$$\frac{\delta F_\mathrm{FM}}{\delta \mathbf{m}} = 0, \tag{A.14}$$

where δ denotes functional differentiation [128]. Due to the constraint $|\mathbf{m}| = 1$, the possible variations $\delta\mathbf{m}$ of the magnetization vector need always be orthogonal to $\mathbf{m}$, so that $\delta\mathbf{m} \cdot \mathbf{m} = 0$. This can be incorporated by introducing arbitrary infinitesimal rotation vector $\delta\omega$ such that

$$\delta\mathbf{m} = \delta\omega \times \mathbf{m}. \tag{A.15}$$

Next, we calculate the functional derivative in equation (A.14) using the definition [128]

$$\frac{\delta F_{\mathrm{FM}}}{\delta \mathbf{m}} = F_{\mathrm{FM}}[\mathbf{m}+\delta\mathbf{m}] - F_{\mathrm{FM}}[\mathbf{m}], \tag{A.16}$$

for each term in equation (A.13) separately. Up to leading order in $\delta\mathbf{m}$ we get for the exchange term

$$\begin{aligned}\frac{\delta F_{\mathrm{exch}}}{\delta \mathbf{m}} &= F_{\mathrm{exch}}[\mathbf{m}+\delta\mathbf{m}] - F_{\mathrm{exch}}[\mathbf{m}] \\ &= 2A_{\mathrm{ex}}\int_V d^3r\,(\nabla\mathbf{m})\cdot(\nabla\delta\mathbf{m}) \\ &= -2A_{\mathrm{ex}}\int_V d^3r\,\left(\nabla^2\mathbf{m}\right)\cdot\delta\mathbf{m} + 2A_{\mathrm{ex}}\oint_{\partial V} d^2r\frac{\partial\mathbf{m}}{\partial S}\cdot\delta\mathbf{m},\end{aligned} \tag{A.17}$$

where we have integrated by parts and made use of the divergence theorem. Here, $\partial\mathbf{m}/\partial S$ represents the derivative in the direction normal to the surrounding surface ∂V. We plug in the definition of $\delta\mathbf{m}$ from equation (A.15) to obtain

$$\frac{\delta F_{\mathrm{exch}}}{\delta \mathbf{m}} = -2A_{\mathrm{ex}}\int_V d^3r\,\left(\mathbf{m}\times\nabla^2\mathbf{m}\right)\cdot\delta\omega + 2A_{\mathrm{ex}}\oint_{\partial V} d^2r\left(\mathbf{m}\times\frac{\partial\mathbf{m}}{\partial S}\right)\cdot\delta\omega. \tag{A.18}$$

Similarly, we find for the anisotropy and external field components

$$\begin{aligned}\frac{\delta F_{\mathrm{ani}}}{\delta \mathbf{m}} &= -2K_u M_{\mathrm{s}}\int_V d^3r(\mathbf{m}\cdot\hat{z})(\mathbf{m}\times\hat{z})\cdot\delta\omega, \\ \frac{\delta F_{\mathrm{ext}}}{\delta \mathbf{m}} &= -BM_{\mathrm{s}}\int_V d^3r(\mathbf{m}\times\hat{z})\cdot\delta\omega.\end{aligned} \tag{A.19}$$

For the Dzyaloshinskii-Moriya term $\delta F_{\mathrm{DM}}/\delta\mathbf{m}$ we need to integrate by parts again

$$\begin{aligned}\frac{\delta F_{\mathrm{DM}}}{\delta \mathbf{m}} = -D\int_V d^3r\Big[&(\delta\mathbf{m}\cdot\hat{z})(\nabla\cdot\mathbf{m}) - \delta\mathbf{m}\cdot\nabla(\mathbf{m}\cdot\hat{z}) \\ &+ (\mathbf{m}\cdot\hat{z})(\nabla\cdot\delta\mathbf{m}) - \mathbf{m}\cdot\nabla(\delta\mathbf{m}\cdot\hat{z})\Big] \\ = -2D\int_V d^3r\Big[&(\delta\mathbf{m}\cdot\hat{z})(\nabla\cdot\mathbf{m}) - \delta\mathbf{m}\cdot\nabla(\mathbf{m}\cdot\hat{z})\Big] \\ &- D\oint_{\partial V} d^2r\Big[(\mathbf{m}\cdot\hat{z})(d\hat{\mathbf{S}}\cdot\delta\mathbf{m}) - (\mathbf{m}\cdot d\hat{\mathbf{S}})(\delta\mathbf{m}\cdot\hat{z})\Big],\end{aligned} \tag{A.20}$$

to obtain

$$\begin{aligned}\frac{\delta F_{\mathrm{DM}}}{\delta \mathbf{m}} = -2D\int_V d^3r&\Big[(\nabla\cdot\mathbf{m})(\mathbf{m}\times\hat{z}) - \mathbf{m}\times\nabla(\mathbf{m}\cdot\hat{z})\Big]\cdot\delta\omega \\ - D\oint_{\partial V} d^2r&\Big[(\mathbf{m}\cdot\hat{z})(\mathbf{m}\times d\hat{\mathbf{S}}) - (\mathbf{m}\cdot d\hat{\mathbf{S}})(\mathbf{m}\times\hat{z})\Big]\cdot\delta\omega.\end{aligned} \tag{A.21}$$

With this, we have found all the terms that constitute the functional derivative $\delta F_{\mathrm{FM}}/\delta\mathbf{m}$. The equilibrium condition (A.14) can be split into a volume part

$$\int_V d^3r\Big\{-2A_{\mathrm{ex}}\left(\mathbf{m}\times\nabla^2\mathbf{m}\right)-2K_uM_{\mathrm{s}}(\mathbf{m}\cdot\hat{z})(\mathbf{m}\times\hat{z}) \\ -BM_{\mathrm{s}}(\mathbf{m}\times\hat{z})-2D\Big[(\nabla\cdot\mathbf{m})(\mathbf{m}\times\hat{z})-\mathbf{m}\times\nabla(\mathbf{m}\cdot\hat{z})\Big]\Big\}\cdot\delta\omega=0, \tag{A.22}$$

and a surface part

$$\oint_{\partial V} d^2r\left\{2A_{\mathrm{ex}}\left(\mathbf{m}\times\frac{\partial\mathbf{m}}{\partial S}\right)-D\Big[(\mathbf{m}\cdot\hat{z})(\mathbf{m}\times d\hat{\mathbf{S}})-(\mathbf{m}\cdot d\hat{\mathbf{S}})(\mathbf{m}\times\hat{z})\Big]\right\}\cdot\delta\omega=0, \tag{A.23}$$

both of which have to hold for arbitrary $\delta\omega$. We rewrite equation (A.22) as

$$\mathbf{m}\times\tilde{\mathbf{B}}_{\mathrm{eff}}=0, \tag{A.24}$$

where the effective "energy density" is given by

$$\tilde{\mathbf{B}}_{\mathrm{eff}}=2A_{\mathrm{ex}}\nabla^2\mathbf{m}+2K_uM_{\mathrm{s}}(\mathbf{m}\cdot\hat{z})\hat{z}+BM_{\mathrm{s}}\hat{z}+2D\Big[(\nabla\cdot\mathbf{m})\hat{z}-\nabla(\mathbf{m}\cdot\hat{z})\Big]. \tag{A.25}$$

With $\tilde{\mathbf{B}}_{\mathrm{eff}}=M_{\mathrm{s}}\mathbf{B}_{\mathrm{eff,FM}}$ we reproduce the effective field in equation (3.8).

The surface equation provides a condition on the normal derivative of $\mathbf{m}$

$$2A_{\mathrm{ex}}\frac{\partial\mathbf{m}}{\partial S}-D\Big[(\mathbf{m}\cdot\hat{z})d\hat{\mathbf{S}}-(\mathbf{m}\cdot d\hat{\mathbf{S}})\hat{z}\Big]=0, \tag{A.26}$$

where $d\hat{\mathbf{S}}$ is the unit vector normal to the surface and, using the vector product identity $\mathbf{a}\times(\mathbf{b}\times\mathbf{c})=\mathbf{b}(\mathbf{a}\cdot\mathbf{c})-\mathbf{c}(\mathbf{a}\cdot\mathbf{b})$, we find

$$\frac{\partial\mathbf{m}}{\partial S}=\frac{1}{\xi_{\mathrm{FM}}}\mathbf{m}\times\Big[d\hat{\mathbf{S}}\times\hat{z}\Big], \tag{A.27}$$

where $\xi_{\mathrm{FM}}=2A_{\mathrm{ex}}/D$. This equation has first been obtained by Rohart *et al.* [26]. As the authors pointed out, equation (A.27) originates entirely from the volume energies considered in present model and is, consequently, a "natural" boundary condition. The model contains no specific micromagnetic energies at the sample edges. In the absence of Dzyaloshinskii-Moriya interactions the boundary condition reduces to the trivial condition $\partial\mathbf{m}/\partial S=0$. In Appendix B.1 we express equation (A.27) in spherical coordinates.

In the context of the finite element method equation (A.24) represents a bulk partial differential equation and equation (A.27), its corresponding "natural" (Neumann) boundary condition (see section 2.3.1). Together, both equations define a variational problem that can be tackled with the techniques presented in section 2.3.

A.2.2 Antiferromagnets

We investigate the model described in terms of the antiferromagnetic sublattices, as this is the description we use in the numerical simulations. The antiferromagnetic energy functional (3.17) contains homogeneous and inhomogeneous exchange interactions, uniaxial anisotropy, external magnetic field and homogeneous and inhomogeneous interfacial Dzyaloshinskii-Moriya interactions

$$F_{\mathrm{AFM}} = F_{\mathrm{hom.exch}} + F_{\mathrm{inh.exch}} + F_{\mathrm{ani}} + F_{\mathrm{ext}} + F_{\mathrm{hom.DM}} + F_{\mathrm{inh.DM}}, \tag{A.28}$$

where all terms are functionals of both $\mathbf{m}_1$ and $\mathbf{m}_2$.

The equilibrium condition in this case involves the functional derivatives with respect to both magnetization vectors

$$\frac{\delta F_{\mathrm{AFM}}}{\delta \mathbf{m}_i} = 0, \tag{A.29}$$

where $i = 1, 2$. As in the ferromagnetic case, we introduce variations $\delta\mathbf{m}_i$ that do not change the magnitude of $\mathbf{m}_i$

$$\delta\mathbf{m}_i = \delta\omega_i \times \mathbf{m}_i, \tag{A.30}$$

for arbitrary vectors $\delta\omega_i$. We calculate the functional derivatives according to the definition

$$\begin{aligned} \frac{\delta F_{\mathrm{AFM}}}{\delta \mathbf{m}_1} &= F_{\mathrm{AFM}}[\mathbf{m}_1 + \delta\mathbf{m}_1, \mathbf{m}_2] - F_{\mathrm{AFM}}[\mathbf{m}_1, \mathbf{m}_2], \\ \frac{\delta F_{\mathrm{AFM}}}{\delta \mathbf{m}_2} &= F_{\mathrm{AFM}}[\mathbf{m}_1, \mathbf{m}_2 + \delta\mathbf{m}_2] - F_{\mathrm{AFM}}[\mathbf{m}_1, \mathbf{m}_2]. \end{aligned} \tag{A.31}$$

In the following, we list the expressions for the functional derivatives of each term in equation (A.28) separately. We do not show the intermediate steps, since they are equivalent to the ferromagnetic calculation in section A.2.1. Up to leading order in $\delta\mathbf{m}_i$ we get for the homogeneous exchange term

$$\frac{\delta F_{\mathrm{hom.exch}}}{\delta \mathbf{m}_i} = B_{\mathrm{exch}} M_{\mathrm{s}} \left(1 - \delta_{ij}\right) \int_V d^3r \Big(\mathbf{m}_i \times \mathbf{m}_j\Big) \cdot \delta\omega_i, \tag{A.32}$$

where δ_{ij} is the Kronecker delta and no summation over repeated indices is implied. For the anisotropy, external field and homogeneous Dzyaloshinskii-Moriya terms we find, respectively,

$$\begin{aligned} \frac{\delta F_{\mathrm{ani}}}{\delta \mathbf{m}_i} &= -B_{\mathrm{an}} M_{\mathrm{s}} \int_V d^3r \left(\mathbf{m}_i \cdot \hat{z}\right)\left(\mathbf{m}_i \times \hat{z}\right) \cdot \delta\omega_i, \\ \frac{\delta F_{\mathrm{ext}}}{\delta \mathbf{m}_i} &= -B M_{\mathrm{s}} \int_V d^3r \left(\mathbf{m}_i \times \hat{z}\right) \cdot \delta\omega_i, \\ \frac{\delta F_{\mathrm{hom.DM}}}{\delta \mathbf{m}_i} &= -B_{\mathrm{d}} M_{\mathrm{s}}\, \epsilon_{ij} \int_V d^3r \Big[\mathbf{m}_i \times \Big(\mathbf{m}_j \times \hat{z}\Big)\Big] \cdot \delta\omega_i, \end{aligned} \tag{A.33}$$

where ϵ_{ij} is the two-dimensional Levi-Civita symbol. The inhomogeneous contributions to the energy functional need to be integrated by parts, as shown first on the example of the exchange interactions

$$\frac{\delta F_{\text{inh.exch}}}{\delta \mathbf{m}_i} = -2A\left[\int_V d^3r\Big(\mathbf{m}_i \times \nabla^2\mathbf{m}_i\Big) + \oint_{\partial V} d^2r\left(\mathbf{m}_i \times \frac{\partial \mathbf{m}_i}{\partial S}\right)\right]\cdot \delta\omega_i. \tag{A.34}$$

The inhomogeneous Dzyaloshinskii-Moriya terms become

$$\begin{aligned}\frac{\delta F_{\text{inh.DM}}}{\delta \mathbf{m}_i} &= \mp D\int_V d^3r\Big[\left(\nabla\cdot\mathbf{n}\right)\left(\mathbf{m}_i\times\hat{z}\right) - \mathbf{m}_i\times\nabla\left(\mathbf{n}\cdot\hat{z}\right)\Big]\cdot\delta\omega_i \\ &\mp \frac{D}{2}\oint_{\partial V} d^2r\Big[\left(\mathbf{n}\cdot\hat{z}\right)\Big(\mathbf{m}_i\times d\hat{\mathbf{S}}\Big) - \Big(\mathbf{n}\cdot d\hat{\mathbf{S}}\Big)\Big(\mathbf{m}_i\times\hat{z}\Big)\Big]\cdot\delta\omega_i,\end{aligned} \tag{A.35}$$

where the negative (positive) sign applies to sublattice 1 (2) and, for a better overview, we used the definition of the Néel vector $2\mathbf{n} = \mathbf{m}_1 - \mathbf{m}_2$.

Plugging all of the above contributions into the equilibrium conditions (A.29) leads to equations involving integrals both over the whole volume V and over the surrounding surface ∂V. These equations have to hold for all $\delta\omega_i$. First, we list the volume terms for both sublattices

$$\begin{aligned}\int_V d^3r\Bigg\{ &-2A\left(\mathbf{m}_i\times\nabla^2\mathbf{m}_i\right) + B_{\text{exch}}M_{\text{s}}\left(1-\delta_{ij}\right)\left(\mathbf{m}_i\times\mathbf{m}_j\right) - BM_{\text{s}}\left(\mathbf{m}_i\times\hat{z}\right) \\ &- B_{\text{an}}M_{\text{s}}\left(\mathbf{m}_i\cdot\hat{z}\right)\left(\mathbf{m}_i\times\hat{z}\right) - B_{\text{d}}M_{\text{s}}\epsilon_{ij}\Big[\mathbf{m}_i\times\left(\mathbf{m}_j\times\hat{z}\right)\Big] \\ &- D\epsilon_{ij}\Big[\left(\nabla\cdot\mathbf{n}\right)\left(\mathbf{m}_i\times\hat{z}\right) - \mathbf{m}_i\times\nabla\left(\mathbf{n}\cdot\hat{z}\right)\Big]\Bigg\}\cdot\delta\omega_i = 0,\end{aligned} \tag{A.36}$$

and rewrite them as the Landau-Lifshitz-Gilbert equations in equilibrium

$$\mathbf{m}_i \times \mathbf{B}^{\text{AFM}}_{\text{eff},i} = 0. \tag{A.37}$$

Up to a factor of M_{s} we recover the effective fields in equations (3.20-3.21).

The surface terms that complement equations (A.36) are

$$\oint_{\partial V} d^2r\,\mathbf{m}_i\times\left\{2A\frac{\partial\mathbf{m}_i}{\partial S} - \frac{D}{2}\epsilon_{ij}\left[\Big(\mathbf{n}\cdot\hat{z}\Big)d\hat{\mathbf{S}} - \Big(\mathbf{n}\cdot d\hat{\mathbf{S}}\Big)\hat{z}\right]\right\}\cdot\delta\omega_i = 0, \tag{A.38}$$

and define the boundary conditions at the sample boundaries for both magnetization vectors

$$\begin{aligned}\frac{\partial\mathbf{m}_1}{\partial S} &= \frac{1}{2\xi_{\text{AFM}}}(\mathbf{m}_1-\mathbf{m}_2)\times\Big[d\hat{\mathbf{S}}\times\hat{z}\Big], \\ \frac{\partial\mathbf{m}_2}{\partial S} &= -\frac{1}{2\xi_{\text{AFM}}}(\mathbf{m}_1-\mathbf{m}_2)\times\Big[d\hat{\mathbf{S}}\times\hat{z}\Big],\end{aligned} \tag{A.39}$$

where $\xi_{\text{AFM}} = 4A/D$. Equation (A.39) is the extension of the result in reference [26] to collinear two-sublattice antiferromagnets. No specific micromagnetic energies are considered at the sample boundaries in this case, so that equations (A.39) represent a “natural” boundary condition. We show its expression in spherical coordinates in Appendix B.1.

Appendix B

Skyrmion algebra

B.1 Skyrmion profile equation

Here, we derive the one-dimensional profile equation for both ferromagnetic and antiferromagnetic skyrmions. We consider a steady state of the Landau-Lifshitz-Gilbert equation for each of the systems and parameterize the corresponding magnetization vectors (**m** for ferromagnets and **n** for antiferromagnets) in spherical coordinates and the position vector **r** in cylindrical coordinates. Two forms of each profile equation are presented – one suitable for skyrmions in infinite planes (with a rescaled dimensionless radial coordinate) and the other, for confined skyrmions. Finally, we rewrite the boundary conditions relevant for finite samples with Dzyaloshinskii-Moriya interactions (see Appendix A.2) in spherical coordinates.

B.1.1 Ferromagnetic skyrmions

The dissipationess Landau-Lifshitz-Gilbert equation (3.10) for a steady state in ferromagnets is

$$\mathbf{m}(\mathbf{r}) \times \mathbf{B}_{\text{eff,FM}}(\mathbf{r}) = 0, \tag{B.1}$$

with the effective field in equation (3.8)

$$\mathbf{B}_{\text{eff,FM}} = \frac{2A_{\text{ex}}}{M_{\text{s}}}\nabla^2\mathbf{m} + 2K_u(\mathbf{m}\cdot\hat{z})\hat{z} + B\hat{z} + \frac{2D}{M_{\text{s}}}\Big[\hat{z}(\nabla\cdot\mathbf{m}) - \nabla(\hat{z}\cdot\mathbf{m})\Big]. \tag{B.2}$$

We parametrize the magnetization vector **m** in spherical coordinates as

$$\mathbf{m}(\mathbf{r}) = \begin{pmatrix} \sin\theta(\rho)\cos\psi(\phi) \\ \sin\theta(\rho)\sin\psi(\phi) \\ \cos\theta(\rho) \end{pmatrix}, \tag{B.3}$$

the position vector in cylindrical coordinates

$$\mathbf{r} = \rho\begin{pmatrix} \cos\phi \\ \sin\phi \\ 0 \end{pmatrix}. \tag{B.4}$$

Using the identities in Appendix C) we rewrite each term in equation (B.1) in spherical coordinates

$$\begin{aligned}
\mathbf{m}\times\nabla^2\mathbf{m} &= \left[\frac{1}{\rho}\frac{d\theta}{d\rho}+\frac{d^2\theta}{d\rho^2}-\frac{1}{\rho^2}\sin\theta\cos\theta\right]\hat{e}_\psi,\\
(\mathbf{m}\cdot\hat{z})(\mathbf{m}\times\hat{z}) &= \Big[-\sin\theta\cos\theta\Big]\hat{e}_\psi,\\
(\mathbf{m}\times\hat{z}) &= \Big[-\sin\theta\Big]\hat{e}_\psi,\\
\mathbf{m}\times\Big[\hat{z}(\nabla\cdot\mathbf{m})-\nabla(\hat{z}\cdot\mathbf{m})\Big] &= \Big[-\frac{1}{\rho}\sin^2\theta\Big]\hat{e}_\psi,
\end{aligned} \tag{B.5}$$

where $\hat{e}_\psi$ is the azimuthal unit vector defined in equation (C.1). Since all terms are pointing in the direction of $\hat{e}_\psi$, we obtain the scalar equation

$$\frac{2A_{\rm ex}}{M_{\rm s}}\left[\frac{1}{\rho}\frac{d\theta}{d\rho}+\frac{d^2\theta}{d\rho^2}-\frac{\sin\theta\cos\theta}{\rho^2}\right]-2K_u\sin\theta\cos\theta-B\sin\theta-\frac{2D}{M_{\rm s}}\frac{\sin^2\theta}{\rho}=0. \tag{B.6}$$

There are different representations of equation (B.6) that are more suitable for analysis, depending on the problem at hand.

Infinite-plane skyrmions

For the infinite-plane skyrmion it is instructive to rescale the radial coordinate according to $\tilde{\rho}=\rho/x_0$, where x_0 is the characteristic domain wall width in ferromagnets

$$x_0=\sqrt{\frac{A_{\rm ex}}{K_uM_{\rm s}}}. \tag{B.7}$$

We rewrite the left hand side of equation (B.6) in terms of $\tilde{\rho}$

$$\begin{aligned}
&\frac{2A_{\rm ex}}{M_{\rm s}}\frac{1}{x_0^2}\left[\frac{1}{\tilde{\rho}}\frac{d\theta}{d\tilde{\rho}}+\frac{d^2\theta}{d\tilde{\rho}^2}-\frac{\sin\theta\cos\theta}{\tilde{\rho}^2}\right]-2K_u\sin\theta\cos\theta-B\sin\theta-\frac{2D}{M_{\rm s}}\frac{1}{x_0}\frac{\sin^2\theta}{\tilde{\rho}}\\
&\qquad\frac{d^2\theta}{d\tilde{\rho}^2}+\frac{1}{\tilde{\rho}}\frac{d\theta}{d\tilde{\rho}}-\frac{\sin\theta\cos\theta}{\tilde{\rho}^2}-\sin\theta\cos\theta-\frac{B}{2K_u}\sin\theta-\frac{D}{\sqrt{A_{\rm ex}K_uM_{\rm s}}}\frac{\sin^2\theta}{\tilde{\rho}},
\end{aligned}$$

and, finally, obtain the dimensionless profile equation

$$\frac{d^2\theta}{d\tilde{\rho}^2}+\frac{1}{\tilde{\rho}}\frac{d\theta}{d\tilde{\rho}}-\frac{\sin\theta\cos\theta}{\tilde{\rho}^2}-\sin\theta\cos\theta-\frac{B}{2K_u}\sin\theta-\frac{4D}{\pi D_0}\frac{\sin^2\theta}{\tilde{\rho}}=0. \tag{B.8}$$

Here, we introduced the threshold value for the Dzyaloshinskii-Moriya constant, as in equation (3.13)

$$D_0=\frac{4}{\pi}\sqrt{A_{\rm ex}K_uM_{\rm s}}. \tag{B.9}$$

Confined skyrmions

In this case there is no translational invariance and it is better not to rescale the radial coordinate. We divide equation (B.6) by $2A_{\mathrm{ex}}/M_{\mathrm{s}}$ and use the definition of the characteristic length x_0 to rewrite

$$\frac{d^2\theta}{d\rho^2}+\frac{1}{\rho}\frac{d\theta}{d\rho}-\frac{\sin\theta\cos\theta}{\rho^2}-\frac{\sin\theta\cos\theta}{x_0^2}-\frac{B}{\frac{2A_{\mathrm{ex}}}{M_{\mathrm{s}}}}\sin\theta-\frac{D}{A_{\mathrm{ex}}}\frac{\sin^2\theta}{\rho}=0$$
$$\frac{d^2\theta}{d\rho^2}+\frac{1}{\rho}\frac{d\theta}{d\rho}-\sin\theta\cos\theta\left(\frac{1}{\rho^2}+\frac{1}{x_0^2}\right)-\frac{B}{2K_u}\frac{\sin\theta}{x_0^2}-2\frac{\sin^2\theta}{\xi_{\mathrm{FM}}\rho}=0. \tag{B.10}$$

Here, we introduced the lengthscale

$$\xi_{\mathrm{FM}}=\frac{2A_{\mathrm{ex}}}{D}. \tag{B.11}$$

In finite samples with Dzyaloshinskii-Moriya interactions equation (B.10) needs to be complemented by the boundary condition (A.27). Without loss of generality, we consider here a magnetization variation along the $\hat{x}$-axis and rewrite the boundary condition in spherical coordinates. Uniform states or skyrmions in perpendicularly magnetized samples experience in this case a canting of the magnetization vector in the xz-plane as a result of the modified boundary condition (A.27). For a nanodisk sample the normal vector at both edges of the disk points along $d\hat{\mathbf{S}}=\pm\hat{x}$. Then, using the identities in Appendix C and setting $\phi=0$, we obtain

$$\frac{d\theta}{dx}=\frac{1}{\xi_{\mathrm{FM}}}. \tag{B.12}$$

Equation (B.12) has first been presented in reference [26].

B.1.2 Antiferromagnetic skyrmions

For the antiferromagnet, we parameterize the Néel vector in spherical coordinates

$$\mathbf{n}_{\mathrm{sk}}=\begin{pmatrix}\sin\theta(\rho)\cos\psi(\phi)\\ \sin\theta(\rho)\sin\psi(\phi)\\ \cos\theta(\rho)\end{pmatrix}, \tag{B.13}$$

and the position vector as in equation (B.4). The dissipationless Landau-Lifshitz-Gilbert equation (3.31) for the antiferromagnetic Néel vector simplifies for a steady state to[1]

$$\mathbf{n}\times\mathbf{B}^{\mathrm{AFM}}_{\mathrm{eff},\mathbf{n}}-\frac{B^2}{2B_{\mathrm{exch}}}(\mathbf{n}\times\hat{z})(\mathbf{n}\cdot\hat{z})=0, \tag{B.14}$$

where the effective field is shown in equation (3.20) and reads

$$\mathbf{B}^{\mathrm{AFM}}_{\mathrm{eff},\mathbf{n}}=\frac{2A}{M_{\mathrm{s}}}\nabla^2\mathbf{n}+B_{\mathrm{an}}(\mathbf{n}\cdot\hat{z})\hat{z}+\frac{D}{M_{\mathrm{s}}}\Big[(\nabla\cdot\mathbf{n})\hat{z}-\nabla(\mathbf{n}\cdot\hat{z})\Big]. \tag{B.15}$$

---

[1] Here, we consider a static antiferromagnetic texture in the absence of electric currents.

Analogous to the ferromagnet, we use the identities in Appendix C and express each term in equation (B.14) in spherical coordinates

$$\begin{aligned}\mathbf{n}\times\nabla^2\mathbf{n} &= \left[\frac{1}{\rho}\frac{d\theta}{d\rho}+\frac{d^2\theta}{d\rho^2}-\frac{1}{\rho^2}\sin\theta\cos\theta\right]\hat{e}_\psi,\\ (\mathbf{n}\cdot\hat{z})(\mathbf{n}\times\hat{z}) &= \Big[-\sin\theta\cos\theta\Big]\hat{e}_\psi,\\ \mathbf{n}\times\Big[\hat{z}(\nabla\cdot\mathbf{n})-\nabla(\hat{z}\cdot\mathbf{n})\Big] &= \Big[-\frac{1}{\rho}\sin^2\theta\Big]\hat{e}_\psi. \end{aligned}\tag{B.16}$$

All terms are proportional to the azimuthal unit vector $\hat{e}_\psi$, which allows us to write

$$\frac{2A}{M_\mathrm{s}}\left[\frac{1}{\rho}\frac{d\theta}{d\rho}+\frac{d^2\theta}{d\rho^2}-\frac{\sin\theta\cos\theta}{\rho^2}\right]-B_\mathrm{an}\sin\theta\cos\theta-\frac{D}{M_\mathrm{s}}\frac{\sin^2\theta}{\rho}+\frac{B^2}{2B_\mathrm{exch}}\sin\theta\cos\theta=0.\tag{B.17}$$

Infinite-plane skyrmions

We rescale the radial coordinate in equation (B.17) according to $\tilde{\rho}=\rho/x_0$, where the antiferromagnetic domain wall width is given by

$$x_0=\sqrt{\frac{2A}{B_\mathrm{an}M_\mathrm{s}}}.\tag{B.18}$$

The left hand side of equation (B.17) is expressed in terms of $\tilde{\rho}$

$$\begin{aligned}&\frac{2A}{M_\mathrm{s}}\frac{1}{x_0^2}\left[\frac{1}{\tilde{\rho}}\frac{d\theta}{d\tilde{\rho}}+\frac{d^2\theta}{d\tilde{\rho}^2}-\frac{\sin\theta\cos\theta}{\tilde{\rho}^2}\right]-B_\mathrm{an}\sin\theta\cos\theta-\frac{D}{M_\mathrm{s}}\frac{1}{x_0}\frac{\sin^2\theta}{\tilde{\rho}}+\frac{B^2}{2B_\mathrm{exch}}\sin\theta\cos\theta\\ &\quad\frac{d^2\theta}{d\tilde{\rho}^2}+\frac{1}{\tilde{\rho}}\frac{d\theta}{d\tilde{\rho}}-\frac{\sin\theta\cos\theta}{\tilde{\rho}^2}-\sin\theta\cos\theta-\frac{D}{\sqrt{2AB_\mathrm{an}M_\mathrm{s}}}\frac{\sin^2\theta}{\tilde{\rho}}+\frac{B^2}{2B_\mathrm{exch}B_\mathrm{an}}\sin\theta\cos\theta,\end{aligned}$$

and defines the dimensionless profile equation

$$\frac{d^2\theta}{d\tilde{\rho}^2}+\frac{1}{\tilde{\rho}}\frac{d\theta}{d\tilde{\rho}}-\frac{\sin\theta\cos\theta}{\tilde{\rho}^2}-\frac{4D}{\pi D_0}\frac{\sin^2\theta}{\tilde{\rho}}-\left(1-\frac{B^2}{B_0^2}\right)\sin\theta\cos\theta=0.\tag{B.19}$$

Here, we introduced the threshold value of the Dzyaloshinskii-Moriya constant and the spin-flop field

$$\begin{aligned}D_0&=\frac{4}{\pi}\sqrt{2AB_\mathrm{an}M_\mathrm{s}},\\ B_0&=\sqrt{2B_\mathrm{exch}B_\mathrm{an}}.\end{aligned}\tag{B.20}$$

Confined skyrmions

In the case of confined skyrmions there is no translational invariance and there is no benefit in casting the radial coordinate dimensionless. We divide equation (B.17) by $2A/M_\mathrm{s}$ and simplify the coefficients

$$\begin{aligned}\frac{d^2\theta}{d\rho^2}+\frac{1}{\rho}\frac{d\theta}{d\rho}+\frac{\sin\theta\cos\theta}{\rho^2}-\frac{\sin\theta\cos\theta}{\frac{2A}{B_\mathrm{an}M_\mathrm{s}}}-\frac{D}{2A}\frac{\sin^2\theta}{\rho}+\frac{B^2}{2B_\mathrm{exch}\frac{2A}{M_\mathrm{s}}}\sin\theta\cos\theta=0\\ \frac{d^2\theta}{d\rho^2}+\frac{1}{\rho}\frac{d\theta}{d\rho}-\frac{\sin\theta\cos\theta}{\rho^2}-\frac{\sin\theta\cos\theta}{x_0^2}-2\frac{\sin^2\theta}{\xi_\mathrm{AFM}\rho}+\frac{B^2}{2B_\mathrm{exch}B_\mathrm{an}x_0^2}\sin\theta\cos\theta=0,\end{aligned}$$

to obtain the profile equation

$$\frac{d^2\theta}{d\rho^2}+\frac{1}{\rho}\frac{d\theta}{d\rho}-\sin\theta\cos\theta\left[\frac{1}{\rho^2}+\frac{1}{x_0^2}\left(1-\frac{B^2}{B_0^2}\right)\right]-2\frac{\sin^2\theta}{\xi_\mathrm{AFM}\rho}=0. \tag{B.21}$$

Here, the characteristic domain wall width x_0 is shown in equation (B.18), the spin-flop field B_0, in equation (B.20) and we introduced the characteristic cycloid length in antiferromagnets

$$\xi_\mathrm{AFM}=\frac{4A}{D}. \tag{B.22}$$

Analogous to ferromagnets, in finite antiferromagnetic samples equation (B.21) needs to be complemented by a boundary condition at the sample edges when Dzyaloshinskii-Moriya interactions are present. In Appendix A.2.2, we derive the corresponding boundary condition for the individual sublattices $\mathbf{m}_1$ and $\mathbf{m}_2$ and show it in equation (A.39). We translate this condition in terms of the Néel vector by using the definition in equation (3.22)

$$\frac{\partial\mathbf{n}}{\partial S}=\frac{1}{\xi_\mathrm{AFM}}\mathbf{n}\times\left(d\hat{\mathbf{S}}\times\hat{z}\right), \tag{B.23}$$

where $d\hat{\mathbf{S}}$ is the unit vector normal to the sample surface. Without loss of generality, we consider the magnetization variation along the $\hat{x}$-axis and rewrite the boundary condition in spherical coordinates. Uniform states or skyrmions in perpendicularly magnetized samples will experience a canting of the Néel vector in the xz-plane as a result of the modified boundary condition (B.23). For a nanodisk sample the normal vector at both edges of the disk in the $\hat{x}$-direction becomes $d\hat{\mathbf{S}}=\pm\hat{x}$. Then, using the identities in Appendix C and setting $\phi=0$, we obtain

$$\frac{d\theta}{dx}=\frac{1}{\xi_\mathrm{AFM}}. \tag{B.24}$$

B.2 Collective coordinates in ferromagnets

Here, we elaborate on the collective coordinate description of the equation of motion for the ferromagnetic skyrmion. To arrive from equation (4.4) to equation (4.5) we use the ansatz [72, 73, 74]

$$\dot{\mathbf{m}} = \sum_i \frac{\partial \mathbf{m}}{\partial \xi_i} \dot{\xi}_i, \tag{B.25}$$

where ξ_i are the collective coordinates and are chosen to be the center of mass coordinates of the skyrmion $\{\xi_i\} = \{R_x, R_y\}$. The time dependence of the magnetization vector is implicitly given by the collective coordinates with $\mathbf{m}(\mathbf{r}, t) = \mathbf{m}(\mathbf{r} - \mathbf{R}(t))$, so that one needs to use the following identity when calculating its derivatives

$$\frac{\partial \mathbf{m}}{\partial \xi_i} = -\frac{\partial \mathbf{m}}{\partial x_i}, \tag{B.26}$$

where $i = x, y$. To obtain the equation of motion for the skyrmion texture, we multiply the Landau-Lifshitz-Gilbert equation (4.4) by $\mathbf{m} \times \partial \mathbf{m}/\partial x_\beta$ for $\beta = x, y$ and integrate over space (for the infinite plane that we consider here, this amounts to a two-dimensional integral). We represent the magnetization vector $\mathbf{m}$ in spherical coordinates and the position vector $\mathbf{r}$ in cylindrical coordinates (see Appendix B.1). We consider a Néel skyrmion with $p = -1$ so that $\psi = \phi$ and $\theta(\rho = 0) = \pi$ (see figure 3.2b).

We illustrate the procedure explicitly for the term on the left hand side of equation (4.4):

$$\begin{aligned}
&\int d^2 r \, \dot{\mathbf{m}} \cdot \left(\mathbf{m} \times \frac{\partial \mathbf{m}}{\partial x_\beta} \right) \\
&= -\sum_\alpha \int d^2 r \, \frac{\partial \mathbf{m}}{\partial x_\alpha} \cdot \left(\mathbf{m} \times \frac{\partial \mathbf{m}}{\partial x_\beta} \right) \dot{\xi}_\alpha \\
&= -\sum_\alpha \int d^2 r \, \mathbf{m} \cdot \left(\frac{\partial \mathbf{m}}{\partial x_\beta} \times \frac{\partial \mathbf{m}}{\partial x_\alpha} \right) \dot{\xi}_\alpha .
\end{aligned} \tag{B.27}$$

Using the identities listed in section C.3 we simplify further to

$$-\sum_\alpha \int d^2 r \left[\sin\theta \frac{d\theta}{d\rho} \frac{\sin^2\phi}{\rho} + \sin\theta \frac{d\theta}{d\rho} \frac{\cos^2\phi}{\rho} \right] \epsilon_{\beta\alpha} \dot{\xi}_\alpha . \tag{B.28}$$

We evaluate the integral[2] (continues on the next page)

$$\begin{aligned}
\int d^2 r \, \mathbf{m} \cdot \left(\frac{\partial \mathbf{m}}{\partial x_\beta} \times \frac{\partial \mathbf{m}}{\partial x_\alpha} \right) &= \int_0^\infty d\rho \, \rho \int_0^{2\pi} d\phi \left[\sin\theta \frac{d\theta}{d\rho} \frac{\sin^2\phi}{\rho} + \sin\theta \frac{d\theta}{d\rho} \frac{\cos^2\phi}{\rho} \right] \epsilon_{\beta\alpha} \\
&= \pi \epsilon_{\beta\alpha} \int_0^\infty d\rho \rho \left[\frac{d\theta}{d\rho} \frac{\sin\theta}{\rho} + \frac{d\theta}{d\rho} \frac{\sin\theta}{\rho} \right]
\end{aligned}$$

---

[2] This integral is connected to the value of the topological charge, as shown in equation (3.5).

$$\begin{aligned} &= 2\pi\epsilon_{\beta\alpha}\int_0^\infty d\rho \frac{d\theta}{d\rho}\sin\theta \\ &= 2\pi\epsilon_{\beta\alpha}\int_\pi^0 d\theta\sin\theta \\ &= -4\pi\epsilon_{\beta\alpha}, \end{aligned} \tag{B.29}$$

where $\epsilon_{\beta\alpha}$ is the two-dimensional Levi-Civita symbol (see section C.4). Finally, we obtain

$$\int d^2r\, \dot{\mathbf{m}}\cdot\left(\mathbf{m}\times\frac{\partial\mathbf{m}}{\partial x_\beta}\right) = -4\pi\epsilon_{\beta\alpha}. \tag{B.30}$$

The remaining terms in equation (4.4) are transformed in the same fashion using the identities listed in Appendix C. There are three more distinct integrals that appear during the calculation:

$$\begin{aligned} \int d^2r\left(\frac{\partial\mathbf{m}}{\partial x_\alpha}\cdot\frac{\partial\mathbf{m}}{\partial x_\beta}\right) &= \pi\delta_{\alpha\beta}\int_0^\infty d\rho\left[\left(\frac{d\theta}{d\rho}\right)^2\rho+\frac{\sin^2\theta}{\rho}\right], \\ \int d^2r\left(\frac{\partial\mathbf{m}}{\partial x_\beta}\right)_i &= \pi\delta_{\beta,i}\int_0^\infty d\rho\left[\frac{d\theta}{d\rho}\cos\theta\rho+\sin\theta\right], \\ \int d^2r\left(\frac{\partial\mathbf{m}}{\partial x_\beta}\times\mathbf{m}\right)_i &= -\pi\epsilon_{\beta i}\int_0^\infty d\rho\left[\frac{d\theta}{d\rho}\rho+\sin\theta\cos\theta\right]. \end{aligned} \tag{B.31}$$

We rescale the radial coordinate ρ by the characteristic length of the system x_0, defined in equation (3.13),

$$\tilde{\rho} = \frac{\rho}{x_0}. \tag{B.32}$$

This has the advantage that all the integrals over the skyrmion profile in equations (B.32) can be casted dimensionless. We define

$$\begin{aligned} 4D &= \int_0^\infty d\tilde{\rho}\left[\left(\frac{d\theta}{d\tilde{\rho}}\right)^2\tilde{\rho}+\frac{\sin^2\theta}{\tilde{\rho}}\right], \\ 4x_0I' &= x_0\int_0^\infty d\tilde{\rho}\left[\frac{d\theta}{d\tilde{\rho}}\tilde{\rho}+\sin\theta\cos\theta\right], \\ 4x_0I &= x_0\int_0^\infty d\tilde{\rho}\left[\frac{d\theta}{d\tilde{\rho}}\cos\theta\tilde{\rho}+\sin\theta\right], \end{aligned} \tag{B.33}$$

and list the expressions for all the terms in equation (4.4)

$$\begin{aligned} \int d^2r\, \dot{\mathbf{m}}\cdot\left(\mathbf{m}\times\frac{\partial\mathbf{m}}{\partial x_\beta}\right) &= 4\pi\sum_\alpha\epsilon_{\beta\alpha}\dot{\xi}_\alpha, \\ \gamma\int d^2r\Big(\mathbf{m}\times\mathbf{B}_{\text{eff,FM}}\Big)\cdot\left(\mathbf{m}\times\frac{\partial\mathbf{m}}{\partial x_\beta}\right) &= 0, \\ \alpha_{\text{G,FM}}\int d^2r\Big(\mathbf{m}\times\dot{\mathbf{m}}\Big)\cdot\left(\mathbf{m}\times\frac{\partial\mathbf{m}}{\partial x_\beta}\right) &= -4\pi\alpha_{\text{G,FM}}D\sum_\alpha\delta_{\alpha\beta}\dot{\xi}_\alpha, \end{aligned}$$

$$\begin{aligned}
\alpha_{\mathrm{FM}} \int d^2r \, (\mathbf{j}\cdot\nabla)\,\mathbf{m}\cdot\left(\mathbf{m}\times\frac{\partial\mathbf{m}}{\partial x_\beta}\right) &= -4\pi\alpha_{\mathrm{FM}}\sum_\alpha \epsilon_{\beta\alpha}\, j_\alpha, \\
a_{\mathrm{FM}} \int d^2r \left(\mathbf{m}\times(\mathbf{j}\times\hat{z})\right)\cdot\left(\mathbf{m}\times\frac{\partial\mathbf{m}}{\partial x_\beta}\right) &= 4\pi a_{\mathrm{FM}} x_0 I \sum_\alpha \epsilon_{\beta\alpha} j_\alpha, \\
\beta_{\mathrm{FM}} \int d^2r \Big(\mathbf{m}\times(\mathbf{j}\cdot\nabla)\,\mathbf{m}\Big)\cdot\left(\mathbf{m}\times\frac{\partial\mathbf{m}}{\partial x_\beta}\right) &= 4\pi\beta_{\mathrm{FM}} D \sum_\alpha \delta_{\alpha\beta} j_\alpha, \\
b_{\mathrm{FM}} \int d^2r \Big(\mathbf{m}\times\Big[\mathbf{m}\times(\mathbf{j}\times\hat{z})\Big]\Big)\cdot\left(\mathbf{m}\times\frac{\partial\mathbf{m}}{\partial x_\beta}\right) &= 4\pi b_{\mathrm{FM}} x_0 I' \sum_\alpha \delta_{\beta\alpha} j_\beta. \qquad \text{(B.34)}
\end{aligned}$$

After plugging these expressions into equation (4.4), dividing by 4π and observing that every terms contains a sum over $\alpha = x, y$, we obtain the equation of motion for the center of mass coordinates of the ferromagnetic skyrmion

$$\epsilon_{\beta\alpha}\left(\dot{\xi}_\alpha + \alpha_{\mathrm{FM}} j_\alpha\right) = D\delta_{\alpha\beta}\left(-\alpha_{\mathrm{G,FM}}\dot{\xi}_\alpha + \beta_{\mathrm{FM}} j_\alpha\right) + a_{\mathrm{FM}} x_0 I \epsilon_{\beta\alpha} j_\alpha + b_{\mathrm{FM}} x_0 I' \delta_{\beta\alpha} j_\beta, \tag{B.35}$$

or, in vector form,

$$\tilde{\mathbf{G}}\times\Big(\dot{\mathbf{R}} + \alpha_{\mathrm{FM}}\mathbf{j}\Big) = -D\Big(\alpha_{\mathrm{G,FM}}\dot{\mathbf{R}} - \beta_{\mathrm{FM}}\mathbf{j}\Big) + a_{\mathrm{FM}} x_0 I\Big(\hat{z}\times\mathbf{j}\Big) + b_{\mathrm{FM}} x_0 I'\mathbf{j}, \tag{B.36}$$

where $\tilde{\mathbf{G}} = -Q\hat{z}$ with the topological charge $Q = -1$. Finally, we multiply equation (B.36) by a factor of $M_{\mathrm{s}} x_0/\gamma$ and arrive at the force equation (4.5).

B.3 Collective coordinates in antiferromagnets

In complete analogy to section B.2, here we elaborate on the collective coordinate calculation of the antiferromagnetic skyrmion. The ansatz (B.37) is generalized to [61, 74]

$$\begin{aligned}
\dot{\mathbf{n}} &= \sum_i \frac{\partial\mathbf{n}}{\partial\xi_i}\dot{\xi}_i, \\
\ddot{\mathbf{n}} &= \sum_i \frac{\partial\mathbf{n}}{\partial\xi_i}\ddot{\xi}_i + \mathcal{O}(\dot{\xi}_i^2),
\end{aligned} \tag{B.37}$$

where ξ_i are the collective coordinates and the second term in the last equation can be neglected because it is quadratic in the velocities, which are assumed to be small. The time dependence of the antiferromagnetic skyrmion texture is given by $\mathbf{n}(\mathbf{r}, t) = \mathbf{n}(\mathbf{r} - \mathbf{R}(t))$, where the Néel vector is composed of a static, cylindrical and rigid component $\mathbf{n}_{\mathrm{sk}}$ and motion- and current-induced corrections $\delta\mathbf{n}$ that break the cylindrical symmetry (see section 3.3.2), so that $\mathbf{n} = \mathbf{n}_{\mathrm{sk}} + \delta\mathbf{n}$. As collective coordinates, we take again $\{\xi_i\} = \{R_x, R_y\}$. The relation (B.26) holds for the Néel vector as well.

We apply the same procedure as in section B.2 to equation (4.14) to arrive at the final equation of motion for the antiferromagnetic skyrmion (4.16): multiply by

$\mathbf{n} \times \partial \mathbf{n}/\partial x_\alpha$ and integrate over space. Since the Néel vector is a unit vector, the same integrals appear here as in section (B.2). We have

$$\begin{aligned} \int d^2r \left(\frac{\partial \mathbf{n}}{\partial x_\alpha} \cdot \frac{\partial \mathbf{n}}{\partial x_\beta} \right) &= 4\pi D \delta_{\alpha\beta}, \\ \int d^2r \left(\frac{\partial \mathbf{n}}{\partial x_\beta} \times \mathbf{n} \right)_i &= -4\pi I' x_0 \epsilon_{\beta i}, \end{aligned} \tag{B.38}$$

where the numbers D and I' are defined in equation (B.33).

Next, we list the collective coordinate expressions for all the terms in equation (4.14) that give a finite contribution

$$\begin{aligned} \int d^2r\, (\mathbf{n} \times \ddot{\mathbf{n}}) \cdot \left(\mathbf{n} \times \frac{\partial \mathbf{n}}{\partial x_\beta} \right) &= -4\pi D \sum_\alpha \delta_{\alpha\beta} \ddot{\xi}_\alpha, \\ -\beta\gamma B_{\text{exch}} \int d^2r \Big(\mathbf{n} \times (\mathbf{j} \cdot \nabla)\, \mathbf{n} \Big) \cdot \left(\mathbf{n} \times \frac{\partial \mathbf{n}}{\partial x_\beta} \right) &= -4\pi D \beta\gamma B_{\text{exch}} \sum_\alpha \delta_{\alpha\beta} j_\alpha, \\ C_2\gamma B_{\text{exch}} \int d^2r \Big(\mathbf{n} \times \Big[\mathbf{n} \times (\mathbf{j} \times \hat{z}) \Big] \Big) \cdot \left(\mathbf{n} \times \frac{\partial \mathbf{n}}{\partial x_\beta} \right) &= 4\pi I' x_0 C_2 \gamma B_{\text{exch}} \sum_\alpha \delta_{\beta\alpha} j_\beta, \\ 2\alpha_G \gamma B_{\text{exch}} \int d^2r \Big(\mathbf{n} \times \dot{\mathbf{n}} \Big) \cdot \left(\mathbf{n} \times \frac{\partial \mathbf{n}}{\partial x_\beta} \right) &= -8\pi D \alpha_G \gamma B_{\text{exch}} \sum_\alpha \delta_{\alpha\beta} \dot{\xi}_\alpha. \end{aligned} \tag{B.39}$$

The terms contained in the field $\mathbf{B}_{\text{shape}}$ in equation (4.14) define the skyrmion profile $\mathbf{n}(\mathbf{r})$, which we use to evaluate the integrals within the current procedure (see equation (3.31) and the discussion in section 3.3.2). As a consequence, within the approximations we consider in this work, the terms in $\mathbf{B}_{\text{shape}}$ cancel each other out and do not contribute to the equation of motion. The current-induced torque term proportional to η in $\mathbf{B}_{\text{forces}}$ is proportional to $\mathbf{n}$ and also vanishes after the multiplication by $\mathbf{n} \times \partial \mathbf{n}/\partial x_\beta$.

The equation of motion for the antiferromagnetic skyrmion becomes

$$\delta_{\alpha\beta} \ddot{\xi}_\alpha = \gamma B_{\text{exch}} \left[\beta \delta_{\alpha\beta} j_\alpha - C_2 x_0 \frac{I'}{D} \delta_{\beta\alpha} j_\beta \right] + 2\alpha_G \gamma B_{\text{exch}} \delta_{\alpha\beta} \dot{\xi}_\alpha, \tag{B.40}$$

or, in vector form

$$\ddot{\mathbf{R}} = \gamma B_{\text{exch}} \left[\beta - C_2 x_0 \frac{I'}{D} \right] \mathbf{j} + 2\alpha_G \gamma B_{\text{exch}} \dot{\mathbf{R}}. \tag{B.41}$$

Finally, multiplying by the factor $M_s x_0/(2\gamma^2 B_{\text{exch}})$ and setting $I_{\text{AFM}} = I'/D$ leads to the end result in equation (4.16).

B.4 Integral evaluation

Using the profiles obtained in sections 3.2 and 3.3 for the ferromagnet and antiferromagnet, respectively, we can evaluate the integrals in equations (B.33)

$$\begin{aligned} D &= \frac{1}{4}\int_0^\infty d\tilde{\rho}\left[\left(\frac{d\theta}{d\tilde{\rho}}\right)^2\tilde{\rho} + \frac{\sin^2\theta}{\tilde{\rho}}\right], \\ I' &= \frac{1}{4}\int_0^\infty d\tilde{\rho}\left[\frac{d\theta}{d\tilde{\rho}}\tilde{\rho} + \sin\theta\cos\theta\right], \\ I &= \frac{1}{4}\int_0^\infty d\tilde{\rho}\left[\frac{d\theta}{d\tilde{\rho}}\cos\theta\tilde{\rho} + \sin\theta\right]. \end{aligned} \tag{B.42}$$

In addition, we evaluate the value of the topological charge

$$Q = \frac{1}{2}\int_0^\infty d\tilde{\rho}\frac{d\theta}{d\tilde{\rho}}\sin\theta. \tag{B.43}$$

As discussed in section 3.3, at zero external field the profiles of the ferromagnetic and the antiferromagnetic skyrmions are identical. Then, for $D/D_0 = 0.9$ we find $Q = -1$ and

$$\begin{aligned} D &= 1.578, \\ I' &= 1.931, \\ I &= -0.001, \end{aligned} \tag{B.44}$$

so that the constant in equation (4.17) becomes $I_{\mathrm{AFM}} = I'/D = 1.223$.

For the antiferromagnetic skyrmion with $D/D_0 = 0.99$ and $B = 2\,\mathrm{T}$ (see figure 3.11 and Table 3.3) we find $Q_{\mathrm{AFM}} = -1$ and

$$\begin{aligned} D &= 5.246, \\ I' &= 8.194, \end{aligned} \tag{B.45}$$

and $I_{\mathrm{AFM}} = 1.561$.

B.5 Estimates

Here, we estimate the antidamping spin-orbit torque coefficient C_2 in equation (4.14). In reference [48] the authors consider a torque of the form

$$\tau_{\mathbf{M}_1} \propto \mathbf{M}_1 \times [\mathbf{M}_1 \times (\hat{z} \times \mathbf{j})], \tag{B.46}$$

and give a numerical value of the field $\mathbf{B}_1 \propto \mathbf{M}_1 \times (\hat{z} \times \mathbf{j})$ for interband processes. The value of that field for magnetization vectors pointing along the $\hat{z}$-direction is found to be $|\mathbf{B}_1| \simeq 0.2\,\mathrm{mT}$ per $0.1\,\mathrm{A\,cm^{-1}}$ so that

$$|\mathbf{B}_1| \simeq 2 \times 10^{-5}\,\mathrm{T\,m\,A^{-1}}. \tag{B.47}$$

From equation (4.9) it follows that in the torque term $(C_2/2)\mathbf{m} \times [\mathbf{n} \times (\hat{z} \times \mathbf{j})]$ the coefficient has units of

$$[C_2] = \left[\mathrm{m}^2\mathrm{A}^{-1}\mathrm{s}^{-1}\right]. \tag{B.48}$$

Note the difference in dimensionality of $[\mathbf{M}_1] = [\mathrm{A\,s}^{-1}]$ in reference [48] and $[\mathbf{m}] = [1]$ in the present work. The correct correspondence is

$$\frac{C_2}{2} \simeq \frac{\mu_B}{\hbar} |\mathbf{B}_1|\, t = 1.7 \times 10^{-3}\,\mathrm{m}^2\,\mathrm{A}^{-1}\,\mathrm{s}^{-1}. \tag{B.49}$$

Here, $t = 1\,\mathrm{nm}$ is a typical value for the thickness of a thin film. It has to be included i the calculation, because in reference [48] the authors consider a strictly two-dimensional film.

Appendix C

Identities

Here, we list identities that are used throughout this thesis.

C.1 Unit vectors in spherical and cylindrical coordinates

We label the unit vectors in spherical coordinates as

$$\hat{e}_\rho = \begin{pmatrix} \sin\theta(\rho)\cos\psi(\phi) \\ \sin\theta(\rho)\sin\psi(\phi) \\ \cos\theta(\rho) \end{pmatrix}, \qquad \hat{e}_\theta = \begin{pmatrix} \cos\theta(\rho)\cos\psi(\phi) \\ \cos\theta(\rho)\sin\psi(\phi) \\ -\sin\theta(\rho) \end{pmatrix}, \qquad \hat{e}_\psi = \begin{pmatrix} -\sin\psi(\phi) \\ \cos\psi(\phi) \\ 0 \end{pmatrix}, \tag{C.1}$$

where we explicitly show that the polar angle θ is function only of the (cylindrical) radial coordinate ρ and the azimuthal angle ψ, of the (cylindrical) azimuthal angle ϕ. The position vector becomes in cylindrical coordinates

$$\mathbf{r} = \begin{pmatrix} \rho\cos\phi \\ \rho\sin\phi \\ 0 \end{pmatrix}, \qquad \text{with} \qquad \begin{cases} \rho = \sqrt{x^2+y^2}, \\ \phi = \arctan\left(y/x\right), \end{cases} \tag{C.2}$$

and the corresponding unit vectors read

$$\hat{e}_\rho^{\text{cyl}} = \begin{pmatrix} \cos\phi \\ \sin\phi \\ 0 \end{pmatrix}, \qquad \hat{e}_\phi^{\text{cyl}} = \begin{pmatrix} -\sin\phi \\ \cos\phi \\ 0 \end{pmatrix}, \qquad \hat{z} = \begin{pmatrix} 0 \\ 0 \\ 1 \end{pmatrix}. \tag{C.3}$$

In this work, we are studying Néel skyrmions. Therefore, in the following, we restrict our attention to the case $\psi = \phi$. The following relations hold

$$\begin{aligned} &\hat{e}_\rho \times \hat{e}_\theta = \hat{e}_\psi, \\ &\hat{e}_\theta \times \hat{e}_\psi = \hat{e}_\rho, \\ &\hat{e}_\rho \times \hat{e}_\psi = -\hat{e}_\theta, \\ &\hat{e}_\rho \times \begin{pmatrix} \cos\psi \\ \sin\psi \\ 0 \end{pmatrix} = \begin{pmatrix} -\cos\theta\sin\psi, \\ \cos\theta\cos\psi, \\ 0 \end{pmatrix} = \cos\theta\hat{e}_\psi. \end{aligned} \tag{C.4}$$

Derivatives

Cylindrical coordinates:

$$\begin{aligned} \frac{\partial \rho}{\partial x} &= \cos\phi, & \frac{\partial \phi}{\partial x} &= -\frac{\sin\phi}{\rho}, \\ \frac{\partial \rho}{\partial y} &= \sin\phi, & \frac{\partial \phi}{\partial y} &= \frac{\cos\phi}{\rho}. \end{aligned} \tag{C.5}$$

Spherical coordinates:

$$\begin{aligned} \frac{\partial \mathbf{m}}{\partial x} &= \frac{d\theta}{d\rho}\cos\phi\,\hat{e}_\theta - \frac{\sin\theta}{\rho}\sin\phi\,\hat{e}_\phi, \\ \frac{\partial \mathbf{m}}{\partial y} &= \frac{d\theta}{d\rho}\sin\phi\,\hat{e}_\theta + \frac{\sin\theta}{\rho}\cos\phi\,\hat{e}_\phi, \end{aligned} \tag{C.6}$$

where we have used that $\partial_i\theta = \partial_i\rho\,\partial_\rho\theta$, for $i = x, y$.

C.2 Skyrmion profile

The identities in this section are used in Appendix B.1. The parameters in spherical coordinates are $\theta(\rho)$ and $\psi(\phi)$. We focus on Néel skyrmions, so that $\psi(\phi) = \phi$:

$$\begin{aligned} \frac{\partial \mathbf{m}}{\partial \rho} &= \frac{d\theta}{d\rho}\hat{e}_\theta, \\ \frac{\partial^2 \mathbf{m}}{\partial \rho^2} &= -\left(\frac{d\theta}{d\rho}\right)^2 \hat{e}_\rho + \frac{d^2\theta}{d\rho^2}\hat{e}_\theta, \\ \frac{\partial \mathbf{m}}{\partial \phi} &= \sin\theta\hat{e}_\psi, \\ \frac{\partial^2 \mathbf{m}}{\partial \phi^2} &= 0. \end{aligned} \tag{C.7}$$

We rewrite the unit vector $\mathbf{m} = \hat{e}_\rho$ in cylindrical coordinates

$$\mathbf{m} = \mathbf{m}_\rho \hat{e}_\rho^{\mathrm{cyl}} + \mathbf{m}_\phi \hat{e}_\phi^{\mathrm{cyl}} + \mathbf{m}_z \hat{z}, \qquad \text{with} \qquad \begin{cases} \mathbf{m}_\rho = \sin\theta, \\ \mathbf{m}_\phi = 0, \\ \mathbf{m}_z = \cos\theta. \end{cases} \tag{C.8}$$

The following identities hold for $\mathbf{m}$ with $\mathbf{r}$ in cylindrical coordinates

$$\begin{aligned} \nabla f &= \frac{\partial f}{\partial \rho}\hat{e}_\rho^{\mathrm{cyl}} + \frac{1}{\rho}\frac{\partial f}{\partial \phi}\hat{e}_\phi^{\mathrm{cyl}} + \frac{\partial f}{\partial z}\hat{z}, \\ \nabla\cdot\mathbf{m} &= \frac{1}{\rho}\frac{\partial\left(\rho\mathbf{m}_\rho\right)}{\partial \rho} + \frac{1}{\rho}\frac{\partial \mathbf{m}_\phi}{\partial \phi} + \frac{\partial \mathbf{m}_z}{\partial z}, \\ \nabla^2\mathbf{m} &= \frac{1}{\rho}\frac{\partial \mathbf{m}}{\partial \rho} + \frac{\partial^2 \mathbf{m}}{\partial \rho^2} + \frac{1}{\rho^2}\frac{\partial^2 \mathbf{m}}{\partial \phi^2}. \end{aligned} \tag{C.9}$$

Using the identities in equation (C.7) we get

$$\begin{aligned}\nabla\cdot\mathbf{m} &= \frac{1}{\rho}\sin\theta+\cos\theta\frac{\partial\theta}{\partial\rho},\\ \nabla^2\mathbf{m} &= \left[\frac{1}{\rho}\frac{d\theta}{d\rho}+\frac{d^2\theta}{d\rho^2}\right]\hat{e}_\theta-\left(\frac{d\theta}{d\rho}\right)^2\hat{e}_\rho.\end{aligned}\tag{C.10}$$

C.3 Collective coordinates

$$\begin{aligned}\frac{\partial\mathbf{m}}{\partial x}\times\frac{\partial\mathbf{m}}{\partial y} &= \left(\sin\theta\frac{d\theta}{d\rho}\frac{\sin^2\phi}{\rho}+\sin\theta\frac{d\theta}{d\rho}\frac{\cos^2\phi}{\rho}\right)\hat{e}_\rho,\\ \mathbf{m}\cdot\left(\frac{\partial\mathbf{m}}{\partial x}\times\frac{\partial\mathbf{m}}{\partial y}\right) &= \sin\theta\frac{d\theta}{d\rho}\frac{\sin^2\phi}{\rho}+\sin\theta\frac{d\theta}{d\rho}\frac{\cos^2\phi}{\rho},\\ \frac{\partial\mathbf{m}}{\partial x}\cdot\frac{\partial\mathbf{m}}{\partial x} &= \left(\frac{d\theta}{d\rho}\right)^2\cos^2\phi+\frac{\sin^2\theta}{\rho^2}\sin^2\phi,\\ \frac{\partial\mathbf{m}}{\partial y}\cdot\frac{\partial\mathbf{m}}{\partial y} &= \left(\frac{d\theta}{d\rho}\right)^2\sin^2\phi+\frac{\sin^2\theta}{\rho^2}\cos^2\phi,\\ \frac{\partial\mathbf{m}}{\partial x}\times\mathbf{m} &= -\frac{d\theta}{d\rho}\cos\phi\begin{pmatrix}-\sin\phi\\ \cos\phi\\ 0\end{pmatrix}-\frac{\sin\theta}{\rho}\sin\phi\begin{pmatrix}\cos\theta\cos\phi\\ \cos\theta\sin\phi\\ -\sin\theta\end{pmatrix},\\ \frac{\partial\mathbf{m}}{\partial y}\times\mathbf{m} &= -\frac{d\theta}{d\rho}\sin\phi\begin{pmatrix}-\sin\phi\\ \cos\phi\\ 0\end{pmatrix}+\frac{\sin\theta}{\rho}\cos\phi\begin{pmatrix}\cos\theta\cos\phi\\ \cos\theta\sin\phi\\ -\sin\theta\end{pmatrix}.\end{aligned}\tag{C.11}$$

C.4 Levi-Civita symbol identities

In two dimensions we have

$$\epsilon_{\alpha\beta}=\begin{cases}+1, & \text{for } \alpha\beta=xy;\\ -1, & \text{for } \alpha\beta=yx;\\ 0, & \text{otherwise.}\end{cases}\tag{C.12}$$

We need also the following identity

$$\sum_\alpha \epsilon_{\alpha\beta}\epsilon_{\alpha\gamma}=\delta_{\beta\gamma},\tag{C.13}$$

where $\delta_{\beta\gamma}$ is the Kronecker-Delta. Further,

$$\begin{aligned}\sum_\alpha(\mathbf{j}\times\hat{z})_\alpha\delta_{\beta\alpha} &= \begin{pmatrix}j_y\\ -j_x\\ 0\end{pmatrix}_\beta &&= \sum_\gamma\epsilon_{\beta\gamma}j_\gamma,\\ \sum_\alpha(\mathbf{j}\times\hat{z})_\alpha\epsilon_{\beta\alpha} &= \sum_\alpha\epsilon_{\beta\alpha}\begin{pmatrix}j_y\\ -j_x\\ 0\end{pmatrix}_\alpha &&= -\sum_\gamma\delta_{\beta\gamma}j_\beta.\end{aligned}\tag{C.14}$$

C.5 List of constants

Symbol	Value	Units	Constant
γ	1.7608596×10^{11}	$\mathrm{rad\,s^{-1}\,T^{-1}}$	electron gyromagnetic ratio
$\hbar$	1.0545718×10^{34}	$\mathrm{J\,s}$	reduced Planck constant
e	$1.6021766 \times 10^{-19}$	C	electron charge
μ_0	1.2566371×10^{-6}	$\mathrm{N\,A^{-2}}$	vacuum permeability

Appendix D

Numerical Simulations

D.1 Skyrmion initial state

Here, we present the ansatz for the initial skyrmion-like state used in the numerical simulations. The relaxation procedure of the simulations finds the equilibrium state, on which the effective field does not exert any torque (see section 2.3.2), which corresponds to the closest energy minimum of the model. As a consequence, the equilibrium state depends on the initial state (see also Appendix D.2) and it is important to choose it carefully.

In this work, we focus our attention on skyrmions of the Néel type (see figure 3.1). A state with the same winding of the magnetization vector $\mathbf{m}$ as the Néel skyrmion can be modelled by the following ansatz for the polar angle θ_{sk}

$$\cos\theta_{\mathrm{sk}}(x,y) = \frac{2}{\left[\left(\frac{x-x_0}{R_{\mathrm{init}}}\right)^2 + \left(\frac{y-y_0}{R_{\mathrm{init}}}\right)^2\right]^n + 1} - 1, \tag{D.1}$$

where x_0, y_0 are the coordinates of the center of the skyrmion, R_{init} is the skyrmion radius and n is a parameter controlling the smoothness of the winding (see figure D.1a). The resulting skyrmion magnetization vector can be constructed as

$$\mathbf{m}_{\mathrm{sk}} = \cos\theta_{\mathrm{sk}}(x,y)\begin{pmatrix}0\\0\\1\end{pmatrix} + \frac{\sin\theta_{\mathrm{sk}}(x,y)}{\sqrt{(x-x_0)^2+(y-y_0)^2}}\begin{pmatrix}x-x_0\\y-y_0\\0\end{pmatrix}. \tag{D.2}$$

This ansatz is chosen in such a way, that it produces a magnetization pointing in the positive $\hat{z}$-direction at the skyrmion core ($\theta_{\mathrm{sk}} = 0$, which corresponds to polarity $p = +1$) and in the negative $\hat{z}$-direction outside the skyrmion ($\theta_{\mathrm{sk}} = \pi$)[1]. The magnetization vector $\mathbf{m}_{\mathrm{sk}}$ is depicted in figure D.1b. A state with the opposite polarity ($p = -1$) is obtained by taking $-\mathbf{m}_{\mathrm{sk}}$.

---

[1] An alternative ansatz for the polar angle is provided in reference [24].

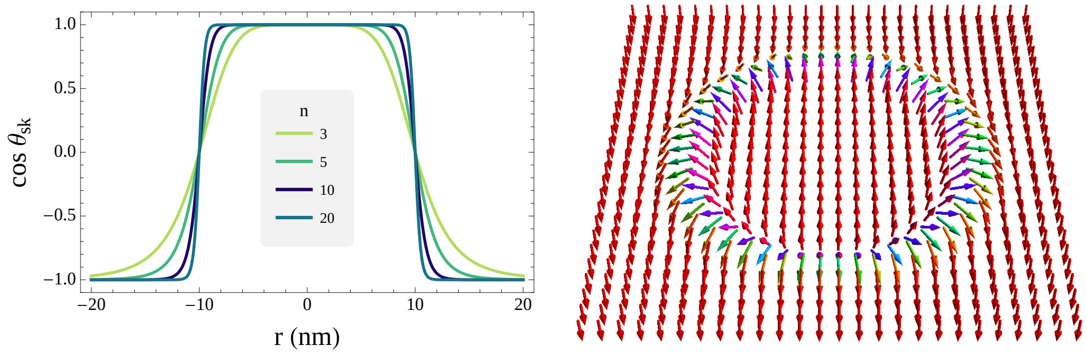

(a) Polar angle (b) Magnetization vector

Figure D.1: *Visualization of the skyrmion-like state defined in equations (D.1-D.2): (a) z-component of the magnetization vector* $\mathbf{m}_{sk}$ *for different values of the smoothness parameter n and (b) full magnetization vector* $\mathbf{m}_{sk}$ *for* $n = 10$. *Both figures show a state for* $x_0 = y_0 = 0$ *and* $R_{init} = 10\,\mathrm{nm}$.

D.2 Equilibrium states

For the simulations in this work we use a nanodisk of radius $R = 50\,\mathrm{nm}$, thickness $t = 1\,\mathrm{nm}$ and characteristic length of $l_{\mathrm{char}} = 1\,\mathrm{nm}$.

D.2.1 Ferromagnets

Here, we present more details on the skyrmion groundstate discussed in section 4.2.2. An equilibrium state is found according to the zero-torque criterion: the Landau-Lifshitz-Gilbert equation (2.31) is solved iteratively until the torque acting on the magnetization vector $\mathbf{m}$ due to the effective field is minimal (in other words, the difference between the magnetization vector in two successive steps of the algorithm is smaller than a specified threshold). Here, we investigate the equilibrium states

Initial state	Final state	F_{FM} (aJ)
(i)	Néel DW	−3.44
(ii)	Néel DW	−3.44
(iii)	Quasi-uniform state	−3.36
(iv)	Skyrmion	−3.47
(v)	Mixed state	−3.42

Table D.1: *Comparison of the different initial states, the corresponding equilibrium states and energies in a ferromagnet. The last column shows the energy of the equilibrium state calculated according to equation (D.3) and is given in units of* 10^{-18} J. *Legend: Uniform state in the (i)*$\hat{x}$*-, (ii)*$\hat{y}$*-, (iii)*$\hat{z}$*-direction, (iv) skyrmion-like and (v) random initial state. DW stands for domain wall. The equilibrium states are shown in figures D.2 and D.3.*

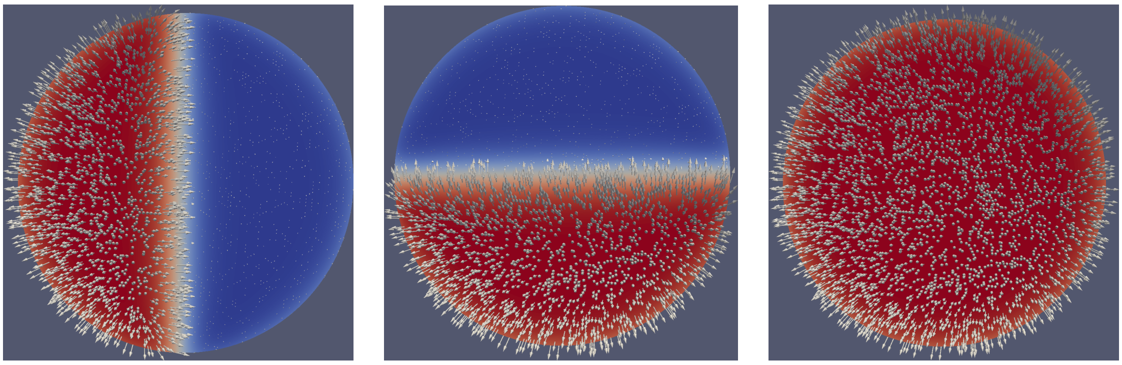

(a) Néel DW (b) Néel DW (c) Quasi-uniform state

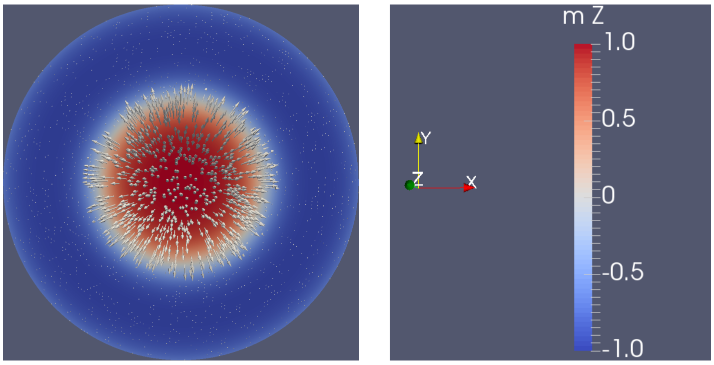

(d) Skyrmion (e) Legend

Figure D.2: *Equilibrium states of the ferromagnet, obtained for four different initial states: (a) uniform state in the* $\hat{x}$*-direction (i),(b) uniform state in the* $\hat{y}$*-direction (ii), (c) uniform state in the* $\hat{z}$*-direction (iii) and (d) skyrmion-like state (iv). DW stands for domain wall. The color code in all images represents the* m_z*-component of the magnetization vector and is shown together with the coordinate axes in (e).*

obtained during the relaxation process from the following initial states: (i-iii) uniform states in the $\hat{x}, \hat{y}$ and $\hat{z}$-direction, a (iv) skyrmion-like initial state and (v) a random initial state. We calculate the energies of the different states according to the energy functional (3.7)[2]

$$F_{\mathrm{FM}} = F_{\mathrm{exch}} + F_{\mathrm{ani}} + F_{\mathrm{ext}} + F_{\mathrm{DM}} \tag{D.3}$$

and list them in Table D.1. We use as simulation parameters $M_{\mathrm{s}} \simeq 1\,\mathrm{MA\,m^{-1}}$, $A_{\mathrm{ex}} \simeq 15\,\mathrm{pJ\,m^{-1}}$, $K_u \simeq 371\,\mathrm{kJ\,m^{-3}}$ (in the $\hat{z}$-direction), $B = 0\,\mathrm{T}$ and $D \simeq 3.5\,\mathrm{mJ\,m^{-2}}$ (see Table 4.4).

We find that the in-plane uniform initial states (i) and (ii) relax to a Néel domain wall, whereas the out-of-plane uniform state (iii) remains uniform in most of the sample, up to the Dzyaloshinskii-Moriya-interactions-induced canting at the edges (see figures D.2a, D.2b and D.2c) [26]. The two domain wall states have identical energy. This is to be expected, since there is nothing to distinguish between the $\hat{x}$- and $\hat{y}$-direction in our model. Further, the domain walls are of Néel type due to the

---

[2] The corresponding numerical code is shown in listing 5.3.

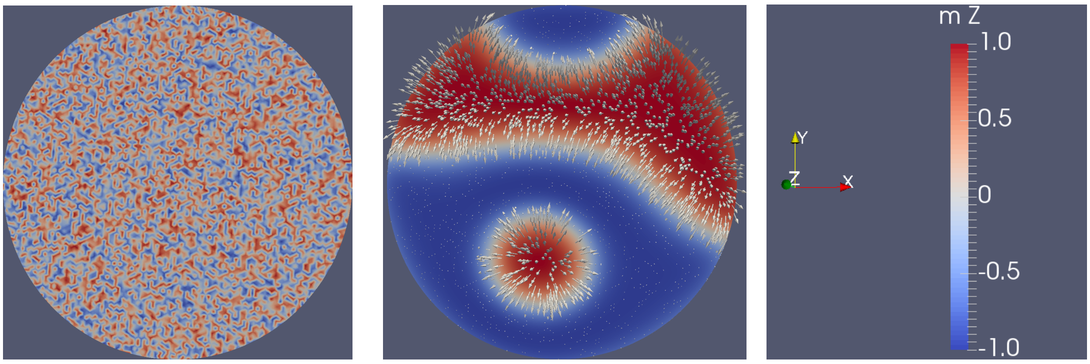

(a) Initial (b) Equilibrium (c) Legend

Figure D.3: *Randomly selected initial state and its corresponding equilibrium state.*

form of the Dzyaloshinskii-Moriya interactions that we have chosen for the model[3]. Both domain wall states have lower energy than the equilibrium state of (iii).

The skyrmion-like initial state (iv) relaxes to a skyrmion state (figure D.2d). The radius of the relaxed skyrmion depends on the nanodisk radius, as was also discussed in recent works [25, 123]. Initial state (iv) leads to equilibrium state with the lowest energy out of all that we studied here. We show all components of the magnetization vector of the skyrmion equilibrium state in figure 4.5 in the main text.

A randomly generated state (figure D.3a) takes considerable longer to relax than initial state (i-iv). The relaxed state is shown in figure D.3b and has a higher energy than the skyrmion state. We have tested other random initial states as well: some take even longer to converge and still have lower energy than the skyrmion.

D.2.2 Antiferromagnets

Next, we relax the initial states (i)-(v), as labelled in Appendix D.2.1, in an antiferromagnetic sample. The equilibrium states are found by applying the same zero-torque criterion on the antiferromagnetic Landau-Lifshitz-Gilbert equations (3.19). We calculate the energies of the equilibrium antiferromagnetic states according to the energy functional (3.17)[4]

$$F_{\mathrm{AFM}} = F_{\mathrm{hom.exch}} + F_{\mathrm{inh.exch}} + F_{\mathrm{ani}} + F_{\mathrm{ext}} + F_{\mathrm{hom.DM}} + F_{\mathrm{inh.DM}}, \tag{D.4}$$

and show them in Table D.2.

In antiferromagnets, the largest energy scale is the homogeneous exchange interaction (in the antiferromagnet NiO, for example, it takes the value of $B_{\mathrm{exch}} \simeq 100\,\mathrm{T}$ [129, 130]). To obtain a good comparison between ferromagnets and antiferromagnets, the remaining parameters are chosen to be similar to that of a typical ferromagnet, while respecting the dominance of the scale set by B_{exch}. Therefore, we choose

---

[3] In this work, we use interfacial Dzyaloshinskii-Moriya interactions. Bulk Dzyaloshinskii-Moriya interactions will produce different results.

[4] The corresponding numerical code is shown in listing 5.8.

as simulation parameters $B_\mathrm{s} = 1.26\,\mathrm{T}$, $B_\mathrm{exch} = 90.90\,\mathrm{T}$, $l_\mathrm{ex} = 4.89\,\mathrm{nm}$, $B_\mathrm{an} = 0.74\,\mathrm{T}$, $B = 0\,\mathrm{T}$, $B_\mathrm{d} = 0\,\mathrm{T}$ and $l_\mathrm{DM} = 5.57\,\mathrm{nm}$ (see Table 4.9)

We note, that at zero external and Dzyaloshinskii-Moriya fields the antiferromagnetic magnetization vector is zero (see equation (3.28) and the discussion in section 3.3.2). In that case, the homogeneous exchange energy does not contribute to the profile of the equilibrium texture, as can be seen from equations (3.32) and (3.34). However, we find that the numerically calculated homogeneous energy is different for each equilibrium state considered in Table D.2 and, consequently, changes the energy balance between the different equilibrium states[5]. Further, all equilibrium states exhibit a total magnetization that is at least four orders of magnitude smaller than the Néel vector. This shows that we obtained realistic antiferromagnetic states, for which the exchange approximation is justified and $|\mathbf{n}| \gg |\mathbf{m}|$ (see section 3.3.1 [51]). This motivates us to disregard the homogeneous energy contribution for the energy balance and consider instead $F_\mathrm{AFM} - F_\mathrm{hom.exch}$, which we also list in Table D.2.

Comparing the results in Tables D.3 and D.4, we find that the hierarchy of equilibrium states corresponding to (i)-(v) in both ferromagnets and antiferromagnets are identical. This is a direct consequence of the equivalence between the profile equations in both systems at zero external field, as discussed in section 3.3.2. The difference of a factor of two between the ferromagnetic and antiferromagnetic energies is due to the different definition of the interaction constants – compare equations (3.7) and (3.24) – and the chosen material parameters (see Tables 4.4 and 4.9).

The conclusions drawn in Appendix D.2.1 apply here as well. Both in-plane uniform states (i) and (ii) relax to Néel domain walls, which have a lower energy than the quasi-uniform equilibrium state, originating from the out-of-plane uniform state (iii) (see figures D.4a-D.4c). The randomly generated state (iv) relaxes to a mixed state, which here has a lower energy than all the uniform initial state (figure D.5).

Initial state	Final state	F_AFM (pJ)	$F_\mathrm{AFM} - F_\mathrm{hom.exch}$ (aJ)
(i)	Néel DW	−72.03	−6.88
(ii)	Néel DW	−72.03	−6.88
(iii)	Quasi-uniform state	−72.05	−6.72
(iv)	Skyrmion	−72.01	−6.96
(v)	Mixed state	−72.00	−6.93

Table D.2: *Comparison of the different initial states, their corresponding equilibrium states and energies in an antiferromagnet. The full energy of the antiferromagnetic equilibrium state is given in units of* 10^{-15} J *and the energy without the homogeneous exchange contribution (last column), in* 10^{-18} J*. For the labelling of the initial states see Table D.1. The equilibrium states are shown in figures D.4 and D.5.*

---

[5] For a perfect antiferromagnetic alignment the two sublattices are antiparallel, so that $\mathbf{m}_1 \cdot \mathbf{m}_2 = -1$. Here, we find that this scalar product differs for each equilibrium state from the perfect alignment by a factor of $10^{-3} - 10^{-4}$ and, therefore, changes the energy in equation (3.17).

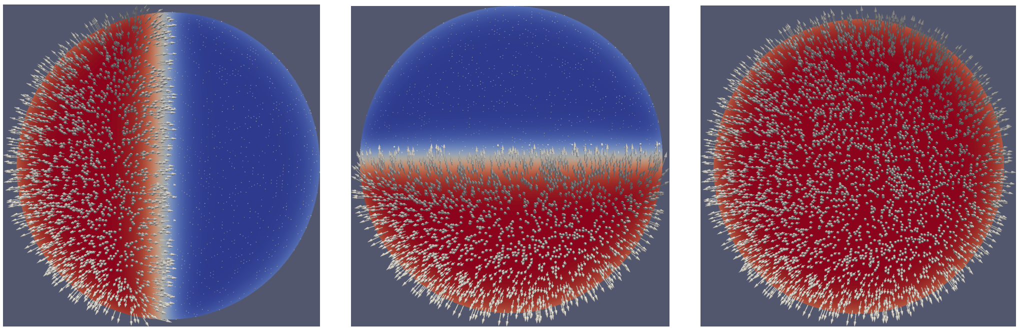

(a) Néel DW (b) Néel DW (c) Quasi-uniform state

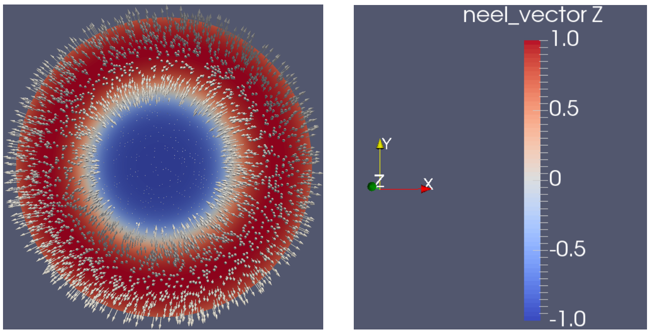

(d) Skyrmion (e) Legend

Figure D.4: *Equilibrium states of the antiferromagnet, obtained for four different initial states; labeling as in figure D.2. In all figures what is depicted is the Néel vector and its z-component is encoded into the color legend. DW stands for domain wall.*

Finally, we find the skyrmion to be the groundstate. We have depicted its $\hat{z}$-component here in figure D.4d; the other components are shown in the main text in figure 4.13.

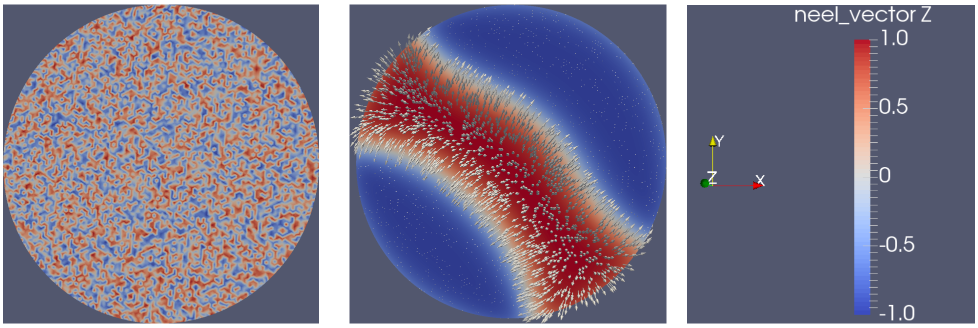

(a) Initial (b) Equilibrium (c) Legend

Figure D.5: *Randomly generated initial state of the antiferromagnetic Néel vector and its corresponding equilibrium state.*

D.3 Magnetization canting at the boundaries

Recently, Rohart *et al.* [26] showed that to properly model a magnetization texture on a finite sample (as opposed to infinite samples) in the presence of Dzyaloshinskii-Moriya interactions, one has to take into account the induced magnetization canting at the edges. We have derived the corresponding "proper" boundary conditions in section 3.2.2 (see the discussion under "confined skyrmions") and Appendix A.2. Here, we reproduce the analytical and numerical results of reference [26] for ferromagnets with our code and use this a further validation of it.

The model we use in the present work contains exchange interactions, uniaxial anisotropy, interfacial Dzyaloshinskii-Moriya interactions and we neglect external fields and dipole-dipole interactions, as described in section 3.2.1[6].

In all simulations in this section we use a nanodisk of radius $R_{\text{disk}} = 50\,\text{nm}$, thickness $t = 1\,\text{nm}$ and characteristic length of $l_{\text{char}} = 1\,\text{nm}$, and the material parameters $M_{\text{s}} = 1\,\text{MA}\,\text{m}^{-1}$, $A_{\text{ex}} = 16\,\text{pJ}\,\text{m}^{-1}$, $K_u = 510\,\text{kJ}\,\text{m}^{-3}$ and $D = 3\,\text{mJ}\,\text{m}^{-2}$, unless stated otherwise. To find equilibrium skyrmion states we use the skyrmion-like initial states discussed in Appendix D.1 with radius $R_{\text{init}} = 10\,\text{nm}$.

Uniform states (one dimension)

First, we reproduce the magnetization canting that occurs in ferromagnetic uniform states when Dzyaloshinskii-Moriya interactions are present.

The profile of the magnetization texture along the $\hat{x}$-axis (in an effectively one-dimensional problem) can be analytically described by the polar angle $\theta(x)$ and is defined by the equation [26, 70]

$$\frac{d^2\theta}{dx^2} = \frac{\sin\theta\cos\theta}{x_0}, \tag{D.5}$$

$$\frac{d\theta}{dx} = \frac{1}{\xi_{\text{FM}}}, \tag{D.6}$$

where equation (D.5) is valid within the sample (that is, for $R_{\text{disk}} < x < R_{\text{disk}}$) and equation (D.6) – at the nanodisk boundary ($x = -R_{\text{disk}}$ or $x = R_{\text{disk}}$). Here, $x_0 = \sqrt{A_{\text{ex}}/K_u}$ is the characteristic length of the ferromagnet (domain wall width) and $\xi_{\text{FM}} = 2A_{\text{ex}}/D$, the characteristic cycloid length in the ferromagnet[7].

Equation (D.5) is obtained by variational methods from the ferromagnetic energy functional (3.7) and is a well-known result for ferromagnetic infinite films. Equation (D.6) is directly obtained from equation (A.27), where the surface normal $d\hat{\mathbf{S}}$ is in the positive (negative) $\hat{x}$-direction at $x = R_{\text{disk}}$ ($x = -R_{\text{disk}}$) and is essential for finite samples in the presence of the Dzyaloshinskii-Moriya interactions. As noted by Rohart *et al.*, equation (D.6) arises from volume terms (see Appendix A.2) and is, therefore, a "natural" boundary condition. Due to its presence the uniform state is not a solution of the profile equation (D.5) in finite-dimensional samples with Dzyaloshinskii-Moriya interactions.

---

[6] The same model is considered in reference [26]. By reproducing their results, we verify that our code is working properly and can be used to study the problems in the present work.

[7] The corresponding cycloid period is given by $L_0 = 2\pi\xi_{\text{FM}}$ in a zero-anisotropy sample [26].

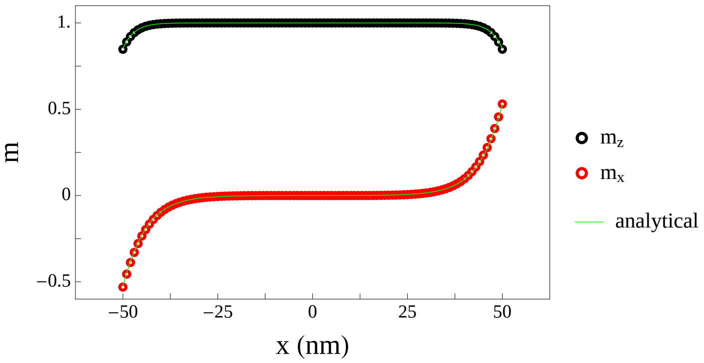

Figure D.6: *Magnetization canting at the edges of a finite ferromagnetic sample induced by the Dzyaloshinskii-Moriya interactions. Plotted are the results of analytical calculations (green solid lines) and numerical simulations (red and black open circles) for the material parameters* $M_s = 1\,\mathrm{MA\,m^{-1}}$, $A_{ex} = 16\,\mathrm{pJ\,m^{-1}}$, $K_u = 510\,\mathrm{kJ\,m^{-3}}$ *and* $D = 3\,\mathrm{mJ\,m^{-2}}$. *We use a nanodisk of radius* $R_{disk} = 50\,\mathrm{nm}$ *and thickness* $t = 1\,\mathrm{nm}$, *and analyze the radially-symmetric magnetization texture along the entire diameter in the* $\hat{x}$*-direction.*

We integrate equation (D.5) numerically with boundary conditions $\theta(x = 0) = 0$ and $\theta'(x = R_{\text{disk}}) = 1/\xi_{\text{FM}}$, and plot the results in figure D.6 with a solid line. For the numerical simulations, we initialize a uniform state (in which the magnetization points along the easy axis) on the nanodisk, apply the relaxation solver (see section 2.3.2) and investigate the change of the magnetization vector only in the $\hat{x}$-direction[8]. The simulation results are plotted in figure D.6 with thick open symbols.

We find a very good agreement between the numerical and analytical calculations[9], as reported in reference [26]. Quantitatively, the numerical result for m_x at the edge deviates from the analytical result by less than 1 %. The value for m_x can be expressed through the characteristic values x_0 and ξ_{FM} when the anisotropy is sufficiently large to avoid cycloid configurations $m_x = \pm x_0/\xi_{\text{FM}}$ [26]. For the parameters we use here this amounts to $x_0 = 5.60\,\text{nm}$, $\xi_{\text{FM}} = 10.67\,\text{nm}$ and $m_x = 0.525$.

Skyrmions

Next, to find the skyrmion solution, we consider a two-dimensional problem described by the same model. As shown in section 3.2.2, the skyrmion profile equation can be obtained from the energy functional [26] (continues on the next page)

$$\frac{d^2\theta}{d\rho^2} = -\frac{1}{\rho}\frac{d\theta}{d\rho} + \frac{\sin 2\theta}{2}\left(\frac{1}{\rho^2} + \frac{1}{x_0^2}\right) + \frac{2}{\xi_{\text{FM}}}\frac{\sin^2\theta}{\rho}, \tag{D.7}$$

---

[8] In reference [26] the authors consider a stripe that is infinite in the $\hat{y}$-direction and has a width of 100 nm in the $\hat{x}$-direction. Here, we investigate the change of the magnetization along the diameter in the $\hat{x}$-direction of the nanodisk. Since the model is radially-symmetric, the two situations are equivalent.

[9] Note, that we refer to the solutions of equations (D.5) and (D.7) as analytical, even though we use numerical integration to obtain them. In that way, we emphasize the difference with the full numerical simulations based on the solution of the Landau-Lifshitz-Gilbert equation with the finite-element method (see section 2.3.2).

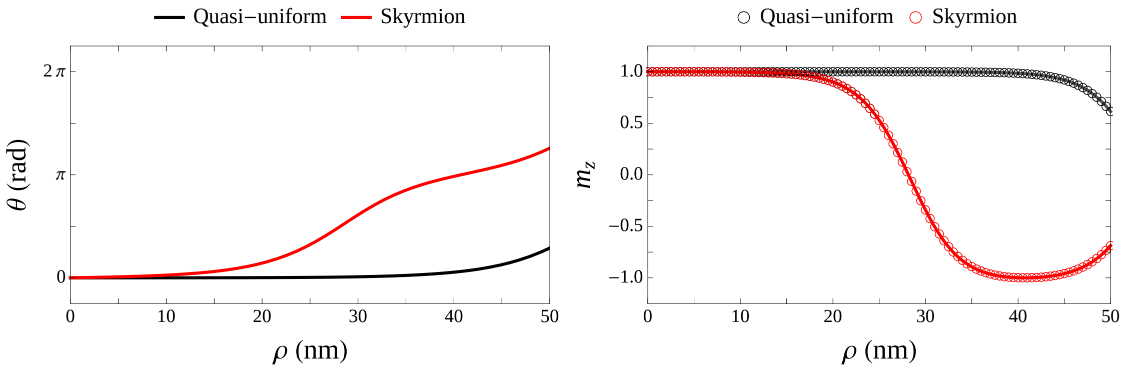

(a) (b)

Figure D.7: *(a) Polar angle $\theta(\rho)$ and (b) z-component of the magnetization vector* $\mathbf{m}$ *of the quasi-uniform and skyrmion states in a nanodisk with radius $R_{disk} = 50\,\mathrm{nm}$ and $t = 1\,\mathrm{nm}$. Shown are the results of analytical calculations (solid lines) and numerical simulations (red and black open circles) for $D = 4.5\,\mathrm{mJ\,m^{-2}}$ and the rest of the parameters as in figure D.6. We do not show here higher-order states.*

$$\frac{d\theta}{d\rho} = \frac{1}{\xi_{\mathrm{FM}}}, \tag{D.8}$$

where, as before, equation (D.7) is valid within the sample (here the entire nanodisk) and equation (D.8), at the sample edge.

We integrate the profile equation (D.7) numerically with boundary conditions $\theta(\rho = 0) = 0$ and $d\theta/d\rho(\rho = 0)$ such, that the boundary condition (D.8) is matched (see sections 3.1 and 3.2.2 for details). We show the results in figure D.7 (solid lines). For the numerical simulations we use $D = 4.5\,\mathrm{mJ\,m^{-2}}$ and the rest of the parameters are as before.

We find a very good agreement between the simulations and the numerical integration of equations (D.7-D.8) – as reported in reference [26] – when the relaxation is started from the skyrmion-like discussed in Appendix D.1. For both methods we show two solutions[10] – the quasi-uniform state and the skyrmions state. Both solutions exhibit a canting at the edges that is induced by the boundary conditions. We also note that the boundary condition (D.8) is chiral - the direction of canting (inwards or outwards) depends on the sign of D[11] (see also the derivation in Appendix A.2).

Size of the confined skyrmion

Next, we show that the confined-skyrmion radius depends both on the value of the Dzyaloshinskii-Moriya constant D and the nanodisk radius R_{disk}.

---

[10] There are two more magnetization configurations that exists for the current setup, namely 2π and 3π rotation of the magnetization [26]. They are not relevant for the present work and we do not discuss them further.

[11] The sign of D is negative, as in section 3.2.2. The only difference is the initial condition $\theta(\rho = 0) = 0$: compare to figure 3.5, where we have chosen $\theta(\rho = 0) = \pi$.

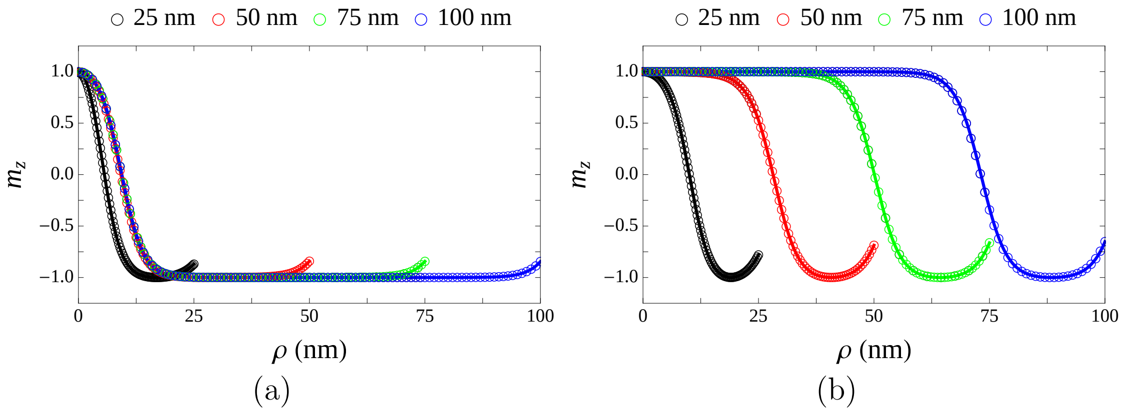

Figure D.8: *Confined-skyrmion radius as a function of the nanodisk radius R_{disk} for two different values of the Dzyaloshinskii-Moriya constant: (a) $D = 3\,\mathrm{mJ\,m^{-2}}$ and (b) $D = 4.5\,\mathrm{mJ\,m^{-2}}$. Solid lines represent the results of analytical calculations and open circles, the corresponding numerical simulations.*

Depending on the ratio D/D_0 (see equation 3.13 for the definition of D_0) the skyrmion behaves qualitatively different [26]. For $D < D_0$ the skyrmion radius is independent of the size of the nanodisk and matches the radius of the infinite-plane skyrmion (see section 3.2.2). The resulting skyrmion is too small to feel the effects of the edge (see figure D.8a[12]). For $D > D_0$ the skyrmion size is fixed by the nanodisk and expands until it feels the edge (see figure D.8b). A single skyrmion can be stabilized in the nanodisk if the disk radius is not too large compared to the cycloid length $L_0 = 2\pi\xi_{\mathrm{FM}}$ (which is determined by D). Otherwise only configurations with larger rotation of the magnetization vectors (that is, higher topological charge) are possible (2π, 3π, etc.; see also reference [26]). Further, the magnetization vector of the skyrmion does not rotate continuously along the entire radius, but does so on a lengthscale of x_0. In that sense, the confined skyrmion resembles a magnetic bubble[13].

Energy

We proceed by plotting the energy of the quasi-uniform and skyrmion state as a function of the Dzyaloshinskii-Moriya constant. We perform numerical simulations on the $R_{\mathrm{disk}} = 50\,\mathrm{nm}$ nanodisk with the same material parameters as before, where D is swept in steps of $\Delta D = 0.5\,\mathrm{mJ\,m^{-2}}$. To capture also the metastable equilibrium states, we investigate separately the relaxation of both a uniform state polarized in the $\hat{z}$-direction and an initial skyrmion state with radius $R_{\mathrm{init}} = 10\,\mathrm{nm}$.

The results are plotted in figure D.9. We find that the quasi-uniform state exists for values of $D \leq 6\,\mathrm{mJ\,m^{-2}}$ and the skyrmion for $2.5\,\mathrm{mJ\,m^{-2}} \leq D \leq 7\,\mathrm{mJ\,m^{-2}}$. These results reproduce well the ones by Rohart *et al.* [26][14].

---

[12] However, for the smallest nanodisk the skyrmion does feel the edge and shrinks as a result.

[13] A major difference being the stabilization due to Dzyaloshinskii-Moriya interactions, whereas bubbles are stabilized by external fields and/or dipole-dipole interactions [26].

[14] We do not find a skyrmion for $D = 2\,\mathrm{mJ\,m^{-2}}$; this is attributed to the inaccuracies of the

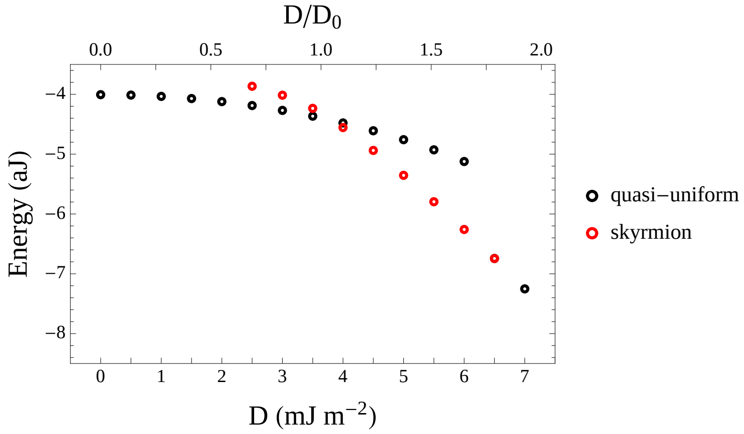

Figure D.9: *Energy of the quasi-uniform and skyrmion states as a function of D. Shown are the results of numerical simulations on a nanodisk with radius* $R_{disk} = 50\,\mathrm{nm}$ *in the range where equilibrium quasi-uniform and skyrmion states have been found. The energy is depicted in units of* $10^{-18}\,\mathrm{J}$.

D.4 Resonance calculations of uniformly-magnetized nanodisks

Here, we apply the eigenspectrum solver (see section 2.3.2) to homogeneous magnetic systems, for which the resonance frequencies can be derived analytically. We use sample with the parameters specified in Appendix D.2.

D.4.1 Ferromagnets

In ferromagnetic thin films the resonance frequency can be obtained by investigating the Landau-Lifshitz-Gilbert equation with the precession terms only. For simplicity, here we consider a ferromagnetic model containing only uniaxial anisotropy and external fields, both pointing in the $\hat{z}$-direction. In such a system, the resonance frequency is given by [68]

$$f_{\mathrm{FM,analytical}} = \frac{\gamma}{2\pi}\left(B + \frac{2K_u}{M_\mathrm{s}}\right), \tag{D.9}$$

where B is the external field, K_u the uniaxial anisotropy constant and M_s the saturation magnetization.

To calculate the frequencies numerically, we initialize a uniform state pointing in the $\hat{z}$-direction and calculate its spectrum with the eigenspectrum solver. In that way, we avoid any extra errors that might come from the relaxation solver (see Appendix D.5). We turn off the exchange and Dzyaloshinskii-Moriya interactions ($A_\mathrm{ex} = D = 0$), and retain only the uniform fields. We use $K_u = 371\,\mathrm{kJ\,m^{-3}}$, $B = 0\,\mathrm{T}$, $M_\mathrm{s} = 1\,\mathrm{MA\,m^{-1}}$ and $\Lambda = 500$ as base values, and subsequently vary K_u and B.

---

relaxation solver (see Appendix D.5).

B(T)	$f_{\text{analytical}}$(GHz)	$f_{\text{numerical}}$(GHz)	Δf(kHz)	δf
0	20.83	20.83	4.21	2.02×10^{-7}
5	160.96	160.96	32.54	2.02×10^{-7}
10	301.08	301.08	60.87	2.02×10^{-7}
K_u/K_u^{ref}	$f_{\text{analytical}}$(GHz)	$f_{\text{numerical}}$(GHz)	Δf(kHz)	δf
2	41.67	41.67	8.42	2.02×10^{-7}
5	104.16	104.16	21.06	2.02×10^{-7}
10	208.33	208.33	42.12	2.02×10^{-7}

Table D.3: *Comparison of the numerical and analytical results for the resonance frequencies of a thin film ferromagnet, modelled by uniaxial anisotropy and external magnetic fields only. The analytical frequency is calculated according to equation (D.9), where the anisotropy constant is set to* $K_u^{ref} = 371\,\mathrm{kJ\,m^{-3}}$ *and the saturation magnetization to* $M_s = 1\,\mathrm{MA\,m^{-1}}$. *In the lower table we have set the external field to zero. The last two columns show the absolute (given in* kHz*) and the relative error of the numerical result with respect to the analytical result.*

We show the numerically calculated frequencies and the corresponding deviations from the analytical results in Table D.3, where we defined the absolute error $\Delta f = f_{\text{analytical}} - f_{\text{numerical}}$ and the relative error $\delta f = \Delta f / f_{\text{analytical}}$. The results show that the numerically calculated frequencies reproduce the analytical frequencies very well, with a relative error of the order of $\mathcal{O}(10^{-7})$. In all cases we find a relative error of

$$\left(\frac{f_{\text{analytical}} - f_{\text{numerical}}}{f_{\text{analytical}}}\right)_{\text{FM}} = 2.02 \times 10^{-7}. \tag{D.10}$$

This serves as a validation of the eigenspectrum solver for ferromagnets.

D.4.2 Antiferromagnets

Similar to ferromagnets, the resonance frequency in antiferromagnets can be found by studying the Landau-Lifshitz-Gilbert equations with the precession terms only. We consider a model containing only homogeneous exchange interactions, uniaxial anisotropy and external fields (both pointing in the $\hat{z}$-direction). In such a system, the resonance frequency is given by [68, 127, 129, 130]

$$f_{\text{AFM,analytical}} = \frac{\gamma}{2\pi}\left(B \pm \sqrt{B_{\text{an}}\left(2B_{\text{exch}} + B_{\text{an}}\right)}\right), \tag{D.11}$$

where B is the external magnetic field, B_{an} the anisotropy field and B_{exch} the homogeneous exchange interactions field. As opposed to the ferromagnet, for fixed exchange and anisotropy fields, the antiferromagnet exhibits two resonance frequencies for large enough external fields. Here, we focus only on the lowest frequency of the two, which decreases with increasing external field.

$B(\mathrm{T})$	$f_{\mathrm{analytical}}(\mathrm{GHz})$	$f_{\mathrm{numerical}}(\mathrm{GHz})$	$\Delta f(\mathrm{kHz})$	δf
0	326.46	326.46	66.00	2.02×10^{-7}
5	186.33	186.33	37.67	2.02×10^{-7}
10	46.21	46.21	9.34	2.02×10^{-7}
$B_{\mathrm{an}}/B_{\mathrm{an}}^{\mathrm{ref}}$	$f_{\mathrm{analytical}}(\mathrm{GHz})$	$f_{\mathrm{numerical}}(\mathrm{GHz})$	$\Delta f(\mathrm{kHz})$	δf
2	462.62	462.62	93.53	2.02×10^{-7}
5	735.91	735.91	148.78	2.02×10^{-7}
10	1051.10	1051.10	212.51	2.02×10^{-7}

Table D.4: *Comparison of the numerical and analytical antiferromagnetic resonance frequencies in the presence of homogeneous exchange, uniaxial anisotropy and external magnetic field only. The analytical frequency is calculated according to equation (D.11), where we use an exchange field of* $B_{\mathrm{exch}} = 90.90\,\mathrm{T}$ *and saturation field of* $B_s = 1.26\,\mathrm{T}$*. For the upper Table we have used an anisotropy field of* $B_{\mathrm{an}}^{ref} = 0.74\,\mathrm{T}$ *and for the lower Table, an external field of* $B = 0\,\mathrm{T}$*. The last two columns show the absolute (given in* kHz*) and the relative error of the numerical result with respect to the analytical result.*

Again, we initialize a uniform state pointing in the $\hat{z}$-direction and calculate its spectrum with the eigenspectrum solver. We turn off the all inhomogeneous fields, as well as the homogeneous Dzyaloshinskii-Moriya interactions ($A = D = B_{\mathrm{d}} = 0$). We use $B_{\mathrm{exch}} = 90.90$, T, $B_{\mathrm{an}} = 0.74\,\mathrm{T}$, $B = 0\,\mathrm{T}$, $B_{\mathrm{s}} = 1.26\,\mathrm{T}$ and $\Lambda = 500$ as base values, and subsequently vary B_{an} and B.

The numerically calculated frequencies, together with the corresponding errors are shown in Table D.4 (see Appendix D.4.1 for the definition of the errors). Comparing the present results with the ones in Appendix D.4.1 shows that with similar choice of parameters the antiferromagnetic resonance frequencies are at least an order of magnitude larger than the ferromagnetic ones. Depending on the parameters of the antiferromagnet under consideration, the frequencies can be even higher (typical values are of the order of $10^2 - 10^3\,\mathrm{GHz}$ [127]).

The results show that the numerically calculated antiferromagnetic frequencies reproduce the analytical frequencies very well, with the same relative error as for the ferromagnets:

$$\left(\frac{f_{\mathrm{analytical}} - f_{\mathrm{numerical}}}{f_{\mathrm{analytical}}}\right)_{\mathrm{AFM}} = 2.02 \times 10^{-7}. \tag{D.12}$$

This serves as a validation of the eigenspectrum solver for antiferromagnets.

D.5 Relaxation-solver effects on the resonance frequencies

In Appendix D.4 we performed eigenspectrum calculations on magnetic states that are perfectly aligned in the $\hat{z}$-direction. By doing this, we could obtain an estimate

$B(\mathrm{T})$	$f_{\mathrm{analytical}}(\mathrm{GHz})$	$f_{\mathrm{numerical}}(\mathrm{GHz})$	$\Delta f(\mathrm{kHz})$	δf
0	20.83	20.83	5.02×10^{3}	2.41×10^{-4}
5	160.96	160.96	1.61×10^{2}	1.00×10^{-6}
10	301.08	301.08	1.21×10^{2}	4.02×10^{-7}
K_u/K_u^{ref}	$f_{\mathrm{analytical}}(\mathrm{GHz})$	$f_{\mathrm{numerical}}(\mathrm{GHz})$	$\Delta f(\mathrm{kHz})$	δf
2	41.67	41.67	1.79×10^{3}	4.31×10^{-5}
5	104.16	104.16	6.16×10^{2}	5.91×10^{-6}
10	208.33	208.33	3.59×10^{2}	1.72×10^{-6}

Table D.5: *Comparison of numerical and analytical results for the ferromagnetic resonance frequencies for a state that has been relaxed from the* 111*-direction to the* $\hat{z}$*-direction. The simulation parameters are the same as shown in Table D.3. Note the difference in the absolute error* Δf *compared to the ideal case.*

of the numerical error of $\mathcal{O}(10^{-7})$ that comes from the eigenspectrum solver alone. This value represents the accuracy of the eigenspectrum solver.

Here, we investigate the additional numerical errors that appear due to the relaxation solver. Instead of initializing a state that is perfectly aligned in the $\hat{z}$-direction, we choose an initial state that points in the 111-direction[15] and let it relax according to the corresponding energy functional. As in Appendix D.4, we model the magnetic system only by uniaxial anisotropy and external magnetic field (and homogeneous exchange interactions for the antiferromagnet). During the relaxation process the anisotropy and external fields will relax the 111-state to point in the $\hat{z}$-direction. Finally, we apply the spectrum solver to the relaxed state. The mesh and simulation parameters are the same as in Appendix D.4.

D.5.1 Ferromagnets

We show the numerically calculated frequencies of the ferromagnetic relaxed state in Table D.5. The relaxation process has a sizeable effect on in the absolute error - it is higher by at least two orders of magnitude for all parameter sets considerer here. The relative error is affected less strongly. The largest error is found for zero external field and anisotropy of $K_u = 371\,\mathrm{kJ\,m^{-3}}$

$$\begin{aligned} \Big(\Delta f\Big)_{\mathrm{FM}} &= 5.02\,\mathrm{MHz}, \\ \Big(\delta f\Big)_{\mathrm{FM}} &= 2.41 \times 10^{-4}. \end{aligned} \tag{D.13}$$

Further, we find that the relaxation-induced error diminishes with both increasing external field and anisotropy. For large values of either of these parameters the absolute error is still higher than in the ideal case (by two orders of magnitude), whereas the relative error becomes comparable to the ideal case – of the order of $\mathcal{O}(10^{-6}) - \mathcal{O}(10^{-7})$.

---

[15] That is, a state in which the magnetization vector $\mathbf{m}$ has equal components $m_x = m_y = m_z$.

B(T)	$f_{\text{analytical}}$(GHz)	$f_{\text{numerical}}$(GHz)	Δf(kHz)	δf
0	326.46	326.44	1.54×10^4	4.70×10^{-5}
5	186.33	186.33	8.86×10^3	4.76×10^{-5}
10	46.21	46.21	2.55×10^3	5.52×10^{-5}
$B_{\text{an}}/B_{\text{an}}^{\text{ref}}$	$f_{\text{analytical}}$(GHz)	$f_{\text{numerical}}$(GHz)	Δf(kHz)	δf
2	462.62	462.62	5.76×10^3	1.25×10^{-5}
5	735.91	735.90	1.31×10^3	1.78×10^{-6}
10	1051.10	1051.10	5.62×10^2	5.35×10^{-7}

Table D.6: *Comparison of numerical and analytical results for the antiferromagnetic resonance frequencies for a state that has been relaxed from the* 111*-direction to the* $\hat{z}$*-direction. We use the same parameters described in Table D.4. Note the difference in the absolute error* Δf *compared to the ideal case.*

D.5.2 Antiferromagnets

The antiferromagnetic resonance frequencies calculated numerically for the antiferromagnetic relaxed state are listed in Table D.6. As for the ferromagnet, the relaxation process affects considerably the calculated frequencies. The absolute error increases by two to four orders of magnitude. The relative error is affected less strongly, but still increases by up to two orders of magnitude. We find that the external field has a weaker effect on the antiferromagnet than in the ferromagnet – in the present case, the relative error is largely unchanged at $\mathcal{O}(10^{-5})$ for the range of values tested here, whereas in the ferromagnet the relative error decreases from $\mathcal{O}(10^{-4})$ to $\mathcal{O}(10^{-7})$. This is a manifestation of the insensitivity of the antiferromagnets to external magnetic fields [44]. We find the largest absolute error[16] for zero external field and anisotropy of $B_{\text{an}} = 0.74\,\text{T}$

$$\begin{aligned} \Big(\Delta f\Big)_{\text{AFM}} &= 15.35\,\text{MHz}, \\ \Big(\delta f\Big)_{\text{AFM}} &= 4.70 \times 10^{-5}. \end{aligned} \tag{D.14}$$

Further, we find that both the absolute and relative error decrease with increasing anisotropy. When increasing the magnetic field, the absolute error is diminished, but the relative error is (slightly) increased. The latter is due to the fact that we consider the lowest resonance frequency, which for the antiferromagnet decreases with increasing magnetic field.

---

[16] We emphasize this set of errors instead of the ones at $B = 10\,\text{T}$ (which show the largest relative error), because we do not consider such high values of the external field within the numerical simulations in the main part of this work.

Bibliography

[1] I. Zutic, J. Fabian, and S. D. Sarma, “Spintronics: Fundamentals and applications,” *Reviews of Modern Physics*, vol. 76, no. 2, pp. 323–410, 2004.

[2] A. Hirohata and K. Takanashi, “Future perspectives for spintronic devices,” *Journal of Physics D: Applied Physics*, vol. 47, no. 19, p. 193001, 2014.

[3] S. A. Wolf, A. Y. Chtchelkanova, and D. M. Treger, “Spintronics – A retrospective and perspective,” *IBM Journal of Research and Development*, vol. 50, no. 1, pp. 101–110, 2006.

[4] J. Sinova, “Spin Seebeck effect: Thinks globally but acts locally,” *Nature Materials*, vol. 9, no. 11, pp. 880–1, 2010.

[5] D. Ralph and M. D. Stiles, “Spin transfer torques,” *Journal of Magnetism and Magnetic Materials*, vol. 320, no. 7, pp. 1190–1216, 2008.

[6] J. Sinova and I. Zutic, “New moves of the spintronics tango,” *Nature Materials*, vol. 11, no. 5, pp. 368–71, 2012.

[7] S. S. P. Parkin, M. Hayashi, and L. Thomas, “Magnetic Domain-Wall Racetrack Memory,” *Science*, vol. 320, no. 5873, pp. 190–194, 2008.

[8] A. Fert, V. Cros, and J. Sampaio, “Skyrmions on the track,” *Nature Nanotechnology*, vol. 8, no. 3, pp. 152–156, 2013.

[9] T. Skyrme, “A unified field theory of mesons and baryons,” *Nuclear Physics*, vol. 31, pp. 556–569, 1962.

[10] N. Nagaosa and Y. Tokura, “Topological properties and dynamics of magnetic skyrmions.” *Nature Nanotechnology*, vol. 8, no. 12, pp. 899–911, 2013.

[11] A. N. Bogdanov and D. Yablonskii, “Thermodynamically stable ‘vortices’ in magnetically ordered crystals. The mixed state of magnets,” *Zh. Eksp. Teor. Fiz.*, vol. 95, no. 1, p. 178, 1989.

[12] A. N. Bogdanov and A. Hubert, “Thermodynamically stable magnetic vortex states in magnetic crystals,” *Journal of Magnetism and Magnetic Materials*, vol. 138, no. 3, pp. 255–269, 1994.

[13] U. K. Rößler, A. N. Bogdanov, and C. Pfleiderer, “Spontaneous skyrmion ground states in magnetic metals,” *Nature*, vol. 442, no. 7104, pp. 797–801, 2006.

[14] S. Muhlbauer, B. Binz, F. Jonietz, C. Pfleiderer, A. Rosch, A. Neubauer, R. Georgii, and P. Boni, “Skyrmion Lattice in a Chiral Magnet,” *Science*, vol. 323, no. 5916, pp. 915–919, 2009.

[15] A. Neubauer, C. Pfleiderer, B. Binz, A. Rosch, R. Ritz, P. G. Niklowitz, and P. Böni, “Topological Hall Effect in the *A* Phase of MnSi,” *Physical Review Letters*, vol. 102, no. 18, p. 186602, 2009.

[16] X. Z. Yu, Y. Onose, N. Kanazawa, J. H. Park, J. H. Han, Y. Matsui, N. Nagaosa, and Y. Tokura, “Real-space observation of a two-dimensional skyrmion crystal,” *Nature*, vol. 465, no. 7300, pp. 901–904, 2010.

[17] F. Jonietz, S. Mühlbauer, C. Pfleiderer, A. Neubauer, W. Münzer, A. Bauer, T. Adams, R. Georgii, P. Böni, R. A. Duine, K. Everschor, M. Garst, and A. Rosch, “Spin transfer torques in MnSi at ultralow current densities.” *Science*, vol. 330, no. 6011, pp. 1648–1651, 2010.

[18] I. E. Dzyaloshinsky, “A thermodynamic theory of “weak” ferromagnetism of antiferromagnetics,” *Journal of Physics and Chemistry of Solids*, vol. 4, no. 4, pp. 241–255, 1958.

[19] T. Moriya, “Anisotropic Superexchange Interaction and Weak Ferromagnetism,” *Physical Review*, vol. 120, no. 1, pp. 91–98, 1960.

[20] G. Finocchio, F. Büttner, R. Tomasello, M. Carpentieri, and M. Kläui, “Magnetic skyrmions: from fundamental to applications,” *Journal of Physics D: Applied Physics*, vol. 49, no. 42, p. 423001, 2016.

[21] S. Heinze, K. von Bergmann, M. Menzel, J. Brede, A. Kubetzka, R. Wiesendanger, G. Bihlmayer, and S. Blügel, “Spontaneous atomic-scale magnetic skyrmion lattice in two dimensions,” *Nature Physics*, vol. 7, no. 9, pp. 713–718, 2011.

[22] T. Schulz, R. Ritz, A. Bauer, M. Halder, M. Wagner, C. Franz, C. Pfleiderer, K. Everschor, M. Garst, and A. Rosch, “Emergent electrodynamics of skyrmions in a chiral magnet,” *Nature Physics*, vol. 8, no. 4, pp. 301–304, 2012.

[23] K. Everschor, M. Garst, B. Binz, F. Jonietz, S. Mühlbauer, C. Pfleiderer, and A. Rosch, “Rotating skyrmion lattices by spin torques and field or temperature gradients,” *Physical Review B*, vol. 86, no. 5, p. 054432, 2012.

[24] N. S. Kiselev, a. N. Bogdanov, R. Schäfer, and U. K. Rößler, “Chiral skyrmions in thin magnetic films: new objects for magnetic storage technologies?” *Journal of Physics D: Applied Physics*, vol. 44, p. 392001, 2011.

[25] J. Sampaio, V. Cros, S. Rohart, A. Thiaville, and A. Fert, “Nucleation, stability and current-induced motion of isolated magnetic skyrmions in nanostructures.” *Nature Nanotechnology*, vol. 8, no. 11, pp. 839–44, 2013.

[26] S. Rohart and A. Thiaville, “Skyrmion confinement in ultrathin film nanostructures in the presence of Dzyaloshinskii-Moriya interaction,” *Physical Review B*, vol. 88, no. 18, p. 184422, 2013.

[27] R. Tomasello, E. Martinez, R. Zivieri, L. Torres, M. Carpentieri, and G. Finocchio, “A strategy for the design of skyrmion racetrack memories,” *Scientific Reports*, vol. 4, no. 1, p. 6784, 2015.

[28] N. Romming, C. Hanneken, M. Menzel, J. E. Bickel, B. Wolter, K. von Bergmann, A. Kubetzka, and R. Wiesendanger, “Writing and Deleting Single Magnetic Skyrmions,” *Science*, vol. 341, no. 6146, pp. 636–639, 2013.

[29] S. Woo, K. Litzius, B. Krüger, M.-Y. Im, L. Caretta, K. Richter, M. Mann, A. Krone, R. M. Reeve, M. Weigand, P. Agrawal, I. Lemesh, M.-A. Mawass, P. Fischer, M. Kläui, and G. S. D. Beach, “Observation of room-temperature magnetic skyrmions and their current-driven dynamics in ultrathin metallic ferromagnets,” *Nature Materials*, vol. 15, no. 5, pp. 501–506, 2016.

[30] X. Zhang, M. Ezawa, and Y. Zhou, “Magnetic skyrmion logic gates: conversion, duplication and merging of skyrmions,” *Scientific Reports*, vol. 5, no. 1, p. 9400, 2015.

[31] O. Boulle, J. Vogel, H. Yang, S. Pizzini, D. de Souza Chaves, A. Locatelli, T. O. Menteş, A. Sala, L. D. Buda-Prejbeanu, O. Klein, M. Belmeguenai, Y. Roussigné, A. Stashkevich, S. M. Chérif, L. Aballe, M. Foerster, M. Chshiev, S. Auffret, I. M. Miron, and G. Gaudin, “Room-temperature chiral magnetic skyrmions in ultrathin magnetic nanostructures,” *Nature Nanotechnology*, vol. 11, no. 5, pp. 449–454, 2016.

[32] S. Krause and R. Wiesendanger, “Spintronics: Skyrmionics gets hot,” *Nature Materials*, vol. 15, no. 5, pp. 493–494, 2016.

[33] K. Litzius, I. Lemesh, B. Krüger, P. Bassirian, L. Caretta, K. Richter, F. Büttner, K. Sato, O. A. Tretiakov, J. Förster, R. M. Reeve, M. Weigand, I. Bykova, H. Stoll, G. Schütz, G. S. D. Beach, and M. Kläui, “Skyrmion Hall effect revealed by direct time-resolved X-ray microscopy,” *Nature Physics*, vol. 13, no. 2, pp. 170–175, 2016.

[34] M. Mochizuki, “Spin-Wave Modes and Their Intense Excitation Effects in Skyrmion Crystals,” *Physical Review Letters*, vol. 108, no. 1, p. 017601, 2012.

[35] S. Z. Lin, C. D. Batista, and A. Saxena, “Internal modes of a skyrmion in the ferromagnetic state of chiral magnets,” *Physical Review B - Condensed Matter and Materials Physics*, vol. 89, no. 2, p. 024415, 2014.

[36] J.-V. Kim, F. Garcia-Sanchez, J. Sampaio, C. Moreau-Luchaire, V. Cros, and A. Fert, “Breathing modes of confined skyrmions in ultrathin magnetic dots,” *Physical Review B*, vol. 90, p. 064410, 2014.

[37] C. Schütte and M. Garst, "Magnon-skyrmion scattering in chiral magnets," *Physical Review B*, vol. 90, no. 9, p. 094423, 2014.

[38] Y. Onose, Y. Okamura, S. Seki, S. Ishiwata, and Y. Tokura, "Observation of Magnetic Excitations of Skyrmion Crystal in a Helimagnetic Insulator Cu_2OSeO_3," *Physical Review Letters*, vol. 109, no. 3, p. 037603, 2012.

[39] Y. Okamura, F. Kagawa, M. Mochizuki, M. Kubota, S. Seki, S. Ishiwata, M. Kawasaki, Y. Onose, and Y. Tokura, "Microwave magnetoelectric effect via skyrmion resonance modes in a helimagnetic multiferroic." *Nature Communications*, vol. 4, p. 2391, 2013.

[40] F. Büttner, C. Moutafis, M. Schneider, B. Krüger, C. M. Günther, J. Geilhufe, C. v. K. Schmising, J. Mohanty, B. Pfau, S. Schaffert, A. Bisig, M. Foerster, T. Schulz, C. A. F. Vaz, J. H. Franken, H. J. M. Swagten, M. Kläui, and S. Eisebitt, "Dynamics and inertia of skyrmionic spin structures," *Nature Physics*, vol. 11, no. 3, pp. 225–228, 2015.

[41] T. Schwarze, J. Waizner, M. Garst, A. Bauer, I. Stasinopoulos, H. Berger, C. Pfleiderer, and D. Grundler, "Universal helimagnon and skyrmion excitations in metallic, semiconducting and insulating chiral magnets," *Nature Materials*, vol. 14, no. 5, pp. 478–483, 2015.

[42] G. Finocchio, M. Ricci, R. Tomasello, A. Giordano, M. Lanuzza, V. Puliafito, P. Burrascano, B. Azzerboni, and M. Carpentieri, "Skyrmion based microwave detectors and harvesting," *Applied Physics Letters*, vol. 107, no. 26, p. 262401, 2015.

[43] F. Garcia-Sanchez, J. Sampaio, N. Reyren, V. Cros, and J.-V. Kim, "A skyrmion-based spin-torque nano-oscillator," *New Journal of Physics*, vol. 18, no. 7, p. 075011, 2016.

[44] T. Jungwirth, X. Marti, P. Wadley, and J. Wunderlich, "Antiferromagnetic spintronics," *Nature Nanotechnology*, vol. 11, no. 3, pp. 231–241, 2016.

[45] E. V. Gomonay and V. Loktev, "Spintronics of antiferromagnetic systems (Review Article)," *Low Temp. Phys.*, vol. 40, no. 1, pp. 17–35, 2014.

[46] A. B. Shick, S. Khmelevskyi, O. N. Mryasov, J. Wunderlich, and T. Jungwirth, "Spin-orbit coupling induced anisotropy effects in bimetallic antiferromagnets: A route towards antiferromagnetic spintronics," *Physical Review B*, vol. 81, p. 212409, 2010.

[47] X. Marti, I. Fina, C. Frontera, J. Liu, P. Wadley, Q. He, R. J. Paull, J. D. Clarkson, J. Kudrnovský, I. Turek, J. Kuneš, D. Yi, J.-H. Chu, C. T. Nelson, L. You, E. Arenholz, S. Salahuddin, J. Fontcuberta, T. Jungwirth, and R. Ramesh, "Room-temperature antiferromagnetic memory resistor." *Nature Materials*, vol. 13, no. 4, pp. 367–374, 2014.

[48] J. Železný, H. Gao, K. Výborný, J. Zemen, J. Mašek, A. Manchon, J. Wunderlich, J. Sinova, and T. Jungwirth, "Relativistic Néel-Order Fields Induced by Electrical Current in Antiferromagnets," *Physical Review Letters*, vol. 113, no. 15, p. 157201, 2014.

[49] P. Wadley, B. Howells, J. Zelezny, C. Andrews, V. Hills, R. P. Campion, V. Novak, K. Olejník, F. Maccherozzi, S. S. Dhesi, S. Y. Martin, T. Wagner, J. Wunderlich, F. Freimuth, Y. Mokrousov, J. Kunes, J. S. Chauhan, M. J. Grzybowski, A. W. Rushforth, K. W. Edmonds, B. L. Gallagher, and T. Jungwirth, "Electrical switching of an antiferromagnet," *Science*, vol. 351, pp. 587–590, 2016.

[50] B. A. Ivanov and A. K. Kolezhuk, "Solitons in low-dimensional antiferromagnets," *Low Temp. Phys.*, vol. 21, pp. 275–301, 1995.

[51] A. N. Bogdanov, U. K. Roessler, M. Wolf, and K. H. Muller, "Magnetic structures and reorientation transitions in noncentrosymmetric uniaxial antiferromagnets," *Physical Review B*, vol. 66, p. 214410, 2002.

[52] J. Barker and O. A. Tretiakov, "Static and Dynamical Properties of Antiferromagnetic Skyrmions in the Presence of Applied Current and Temperature," *Physical Review Letters*, vol. 116, no. 14, p. 147203, 2016.

[53] X. Zhang, Y. Zhou, and M. Ezawa, "Antiferromagnetic Skyrmion: Stability, Creation and Manipulation," *Scientific Reports*, vol. 6, p. 24795, 2016.

[54] C. Jin, C. Song, J. Wang, and Q. Liu, "Dynamics of antiferromagnetic skyrmion driven by the spin Hall effect," *Applied Physics Letters*, vol. 109, no. 18, p. 182404, 2016.

[55] H. Velkov, O. Gomonay, M. Beens, G. Schwiete, A. Brataas, J. Sinova, and R. A. Duine, "Phenomenology of current-induced skyrmion motion in antiferromagnets," *New Journal of Physics*, vol. 18, no. 7, p. 075016, 2016.

[56] R. Keesman, M. Raaijmakers, A. E. Baerends, G. T. Barkema, and R. A. Duine, "Skyrmions in square-lattice antiferromagnets," *Physical Review B*, vol. 94, no. 5, p. 054402, 2016.

[57] B. Göbel, A. Mook, J. Henk, and I. Mertig, "Antiferromagnetic skyrmion crystals: Generation, topological Hall, and topological spin Hall effect," *Physical Review B*, vol. 96, no. 6, p. 060406, 2017.

[58] P. M. Buhl, F. Freimuth, S. Blügel, and Y. Mokrousov, "Topological spin Hall effect in antiferromagnetic skyrmions," *Physica Status Solidi (RRL) - Rapid Research Letters*, vol. 11, no. 4, p. 1700007, 2017.

[59] H. V. Gomonay and V. M. Loktev, "Spin transfer and current-induced switching in antiferromagnets," *Physical Review B*, vol. 81, no. 14, p. 144427, 2010.

[60] K. M. D. Hals, Y. Tserkovnyak, and A. Brataas, “Phenomenology of Current-Induced Dynamics in Antiferromagnets,” *Physical Review Letters*, vol. 106, p. 107206, 2011.

[61] E. G. Tveten, A. Qaiumzadeh, O. Tretiakov, and A. Brataas, “Staggered Dynamics in Antiferromagnets by Collective Coordinates,” *Physical Review Letters*, vol. 110, p. 127208, 2013.

[62] R. Cheng, J. Xiao, Q. Niu, and A. Brataas, “Spin pumping and spin-transfer torques in antiferromagnets,” *Physical Review Letters*, vol. 113, p. 057601, 2014.

[63] A. Kosevich, B. Ivanov, and A. Kovalev, “Magnetic Solitons,” *Physics Reports*, vol. 194, no. 3-4, pp. 117–238, 1990.

[64] L. D. Landau and E. M. Lifshitz, “On the Theory of the Dispersion of Magnetic Permeability in Ferromagnetic Bodies,” *Phys. Zeitsch. der Sow.*, vol. 8, pp. 153–169, 1935.

[65] ——, *Statistical Physics, Part 2*, ser. Course of Theoretical Physics. Oxford: Pergamon Press, 1980, vol. 9.

[66] ——, *Electrodynamics of Continuous Media*, ser. Course of Theoretical Physics. Oxford: Pergamon Press, 1960, vol. 8.

[67] T. Gilbert, “Classics in Magnetics A Phenomenological Theory of Damping in Ferromagnetic Materials,” *IEEE Transactions on Magnetics*, vol. 40, no. 6, pp. 3443–3449, 2004.

[68] J. M. D. Coey, *Magnetism and Magnetic Materials.* Cambridge: Cambridge University Press, 2009.

[69] L. D. Landau and E. M. Lifshitz, *Statistical Physics, Part 1*, ser. Course of Theoretical Physics. Oxford: Pergamon Press, 1980, vol. 5.

[70] I. E. Dzyaloshinskii, “Theory of Helicoidal Structures in Antiferromagnets. I. Nonmetals,” *Sov. Phys. JETP*, vol. 19, no. 4, pp. 960–971, 1964.

[71] A. Leonov, “Twisted, localized, and modulated states described in the phenomenological theory of chiral and nanoscale ferromagnets,” Ph.D. dissertation, 2011.

[72] A. A. Thiele, “Steady-State Motion of Magnetic Domains,” *Physical Review Letters*, vol. 30, no. 6, p. 230, 1973.

[73] M. E. Knoester, J. Sinova, and R. A. Duine, “Phenomenology of current-skyrmion interactions in thin films with perpendicular magnetic anisotropy,” *Physical Review B*, vol. 89, no. 6, p. 064425, 2014.

[74] O. Tretiakov, D. Clarke, G.-W. Chern, Y. B. Bazaliy, and O. Tchernyshyov, “Dynamics of Domain Walls in Magnetic Nanostrips,” *Physical Review Letters*, vol. 100, no. 12, p. 127204, 2008.

[75] D. Clarke, O. Tretiakov, G.-W. Chern, Y. B. Bazaliy, and O. Tchernyshyov, "Dynamics of a vortex domain wall in a magnetic nanostrip: Application of the collective-coordinate approach," *Physical Review B*, vol. 78, no. 13, p. 134412, 2008.

[76] K. M. D. Hals and A. Brataas, "Spin-orbit torques and anisotropic magnetization damping in skyrmion crystals," *Physical Review B*, vol. 89, p. 064426, 2014.

[77] C. Chappert, A. Fert, and F. N. Van Dau, "The emergence of spin electronics in data storage." *Nature Materials*, vol. 6, no. 11, pp. 813–23, 2007.

[78] J. Slonczewski, "Current-driven excitation of magnetic multilayers," *Journal of Magnetism and Magnetic Materials*, vol. 159, no. 1-2, pp. L1–L7, 1996.

[79] A. Thiaville, Y. Nakatani, J. Miltat, and Y. Suzuki, "Micromagnetic understanding of current-driven domain wall motion in patterned nanowires," *Europhysics Letters (EPL)*, vol. 69, no. 6, pp. 990–996, 2004.

[80] A. Brataas and K. M. D. Hals, "Spin-orbit torques in action." *Nature Nanotechnology*, vol. 9, no. 2, pp. 86–88, 2014.

[81] M. J. Donahue and D. G. Porter, *OOMMF User's Guide, Version 1.0*, 1999, vol. NISTIR 6376.

[82] MicroMagnum, *http://micromagnum.informatik.uni-hamburg.de.*

[83] A. Vansteenkiste, J. Leliaert, M. Dvornik, M. Helsen, F. Garcia-Sanchez, and B. Van Waeyenberge, "The design and verification of MuMax3," *AIP Advances*, vol. 4, no. 10, pp. 0–22, 2014.

[84] C. Abert, L. Exl, F. Bruckner, A. Drews, and D. Suess, "magnum.fe : A micromagnetic finite-element simulation code based on FEniCS," *Journal of Magnetism and Magnetic Materials*, vol. 345, pp. 29–35, 2013.

[85] C. W. Abert, *Discrete Mathematical Concepts in Micromagnetic Computations.* PhD Thesis, 2013.

[86] A. Logg, K.-A. Mardal, and G. Wells, *Automated Solution of Differential Equations by the Finite Element Method*, ser. Lecture Notes in Computational Science and Engineering, A. Logg, K.-A. Mardal, and G. Wells, Eds. Berlin, Heidelberg: Springer Berlin Heidelberg, 2012, vol. 84.

[87] J. Fidler and T. Schrefl, "Micromagnetic modelling — the current state of the art," *Journal of Physics D: Applied Physics*, vol. 33, no. 15, pp. R135 – R156, 2000.

[88] M. S. Alnaes, J. Blechta, J. Hake, A. Johansson, B. Kehlet, A. Logg, C. Richardson, J. Ring, M. E. Rognes, and G. N. Wells, "The FEniCS project version 1.5," *Archive of Numerical Software*, vol. 3, no. 100, pp. 9–23, 2015.

[89] M. S. Alnæs, A. Logg, K. B. Ølgaard, M. E. Rognes, and G. N. Wells, "Unified form language," *ACM Transactions on Mathematical Software*, vol. 40, no. 2, pp. 1–37, 2014.

[90] A. Logg and G. N. Wells, "DOLFIN," *ACM Transactions on Mathematical Software*, vol. 37, no. 2, pp. 1–28, 2010.

[91] C. Geuzaine and J.-F. Remacle, "Gmsh: A 3-D finite element mesh generator with built-in pre- and post-processing facilities," *International Journal for Numerical Methods in Engineering*, vol. 79, no. 11, pp. 1309–1331, 2009.

[92] V. Simoncini and D. B. Szyld, "Recent computational developments in Krylov subspace methods for linear systems," *Numerical Linear Algebra with Applications*, vol. 14, no. 1, pp. 1–59, 2007.

[93] Y. Saad and M. H. Schultz, "GMRES: a generalized minimal residual algorithm for solving nonsymmetric linear," *SIAM J. Sci. Stat. Comput.*, vol. 7, no. 3, pp. 856–869, 1986.

[94] S. C. Eisenstat, M. H. Schultz, and H. C. Elman, "Variational iterative methods for nonsymmetric systems of linear equations," *SIAM J. Numer. Anal*, vol. 20, no. 2, pp. 345–357, 1983.

[95] S. Balay, S. Abhyankar, M. F. Adams, J. Brown, P. Brune, K. Buschelman, L. Dalcin, V. Eijkhout, D. Kaushik, M. G. Knepley, L. C. McInnes, W. D. Gropp, K. Rupp, B. F. Smith, S. Zampini, H. Zhang, and H. Z, "PETSc Users Manual," Argonne National Laboratory, Tech. Rep. ANL-95/11 - Revision 3.7, 2016.

[96] Ahrens, James, Geveci, Berk, Law, and Charles, *ParaView: An End-User Tool for Large Data Visualization.* Visualization Handbook, Elsevier, 2005.

[97] W. Schroeder, K. Martin, and B. Lorensen, *The Visualization Toolkit.* (4th ed.), Kitware, 2005.

[98] C. Garcia-Cervera and Weinan E, "Improved gauss-seidel projection method for micromagnetics simulations," *IEEE Transactions on Magnetics*, vol. 39, no. 3, pp. 1766–1770, 2003.

[99] X.-P. Wang, C. J. García-Cervera, and W. E, "A Gauss–Seidel Projection Method for Micromagnetics Simulations," *Journal of Computational Physics*, vol. 171, no. 1, pp. 357–372, 2001.

[100] E. Weinan and X.-P. Wang, "Numerical Methods for the Landau–Lifshitz Equation," *SIAM Journal on Numerical Analysis*, vol. 38, no. 5, pp. 1647–1665, 2000.

[101] M. D'Aquino, C. Serpico, G. Miano, and C. Forestiere, "A novel formulation for the numerical computation of magnetization modes in complex micromagnetic systems," *Journal of Computational Physics*, vol. 228, no. 17, pp. 6130–6149, 2009.

[102] V. Hernández, J. E. Román, A. Tomas, and V. Vidal, "A survey of software for sparse eigenvalue problems," Universitat Politècnica de València, Tech. Rep. STR-6, 2009, available at http://slepc.upv.es.

[103] V. Hernández, J. E. Román, and V. Vidal, "Slepc: A scalable and flexible toolkit for the solution of eigenvalue problems," *ACM Trans. Math. Softw.*, vol. 31, no. 3, pp. 351–362, 2005.

[104] ——, *SLEPc: Scalable Library for Eigenvalue Problem Computations.* Berlin, Heidelberg: Springer Berlin Heidelberg, 2003, pp. 377–391.

[105] S. Emori, U. Bauer, S.-M. Ahn, E. Martinez, and G. S. D. Beach, "Current-driven dynamics of chiral ferromagnetic domain walls." *Nature Materials*, vol. 12, no. 7, pp. 611–6, 2013.

[106] A. N. Bogdanov, A. V. Zhuravlev, and U. K. Rößler, "Spin-flop transition in uniaxial antiferromagnets: Magnetic phases, reorientation effects, and multidomain states," *Physical Review B*, vol. 75, no. 9, p. 094425, 2007.

[107] A. B. Butenko, A. A. Leonov, U. K. Rößler, and A. N. Bogdanov, "Stabilization of skyrmion textures by uniaxial distortions in noncentrosymmetric cubic helimagnets," *Physical Review B*, vol. 82, no. 5, pp. 1–4, 2010.

[108] E. V. Gomonai, B. A. Ivanov, and V. A. L'vov, "Symmetry and dynamics of domain walls," *Sov. Phys. JETP*, vol. 70, no. January, p. 174, 1990.

[109] O. Gomonay, T. Jungwirth, and J. Sinova, "High Antiferromagnetic Domain Wall Velocity Induced by Néel Spin-Orbit Torques," *Physical Review Letters*, vol. 117, no. 1, p. 017202, 2016.

[110] J. Iwasaki, M. Mochizuki, and N. Nagaosa, "Universal current-velocity relation of skyrmion motion in chiral magnets." *Nature Communications*, vol. 4, p. 1463, 2013.

[111] A. Hrabec, J. Sampaio, M. Belmeguenai, I. Gross, R. Weil, S. M. Chérif, A. Stashkevich, V. Jacques, A. Thiaville, and S. Rohart, "Current-induced skyrmion generation and dynamics in symmetric bilayers," *Nature Communications*, vol. 8, p. 15765, 2017.

[112] R. A. Duine, M. Beens, H. Velkov, O. Gomonay, J. Sinova, and A. Brataas, *To be published.*

[113] I. V. Baryakhtar and B. A. Ivanov, "Nonlinear magnetization waves of an antiferromagnet," *Sov. J. Low Temp. Phys.*, vol. 5, p. 361, 1979.

[114] B. A. Ivanov and D. D. Sheka, "Dynamics of Vortices and Their Contribution to the Response Functions of Classical Quasi-Two-Dimensional Easy-Plane Antiferromagnet," *Physical Review Letters*, vol. 72, no. 3, p. 404, 1994.

[115] S. Zhang and Z. Li, "Roles of Nonequilibrium Conduction Electrons on the Magnetization Dynamics of Ferromagnets," *Physical Review Letters*, vol. 93, no. 12, p. 127204, 2004.

[116] M. T. Hutchings and E. J. Samuelsen, "Measurement of Spin-Wave Dispersion in NiO by Inelastic Neutron Scattering and Its Relation to Magnetic Properties," *Physical Review B*, vol. 6, no. 9, p. 3447, 1972.

[117] O. Gomonay, T. Jungwirth, and J. Sinova, "Concepts of antiferromagnetic spintronics," *Physica Status Solidi (RRL) - Rapid Research Letters*, vol. 11, no. 4, p. 1700022, 2017.

[118] B. Pigeau, G. de Loubens, O. Klein, A. Riegler, F. Lochner, G. Schmidt, L. W. Molenkamp, V. S. Tiberkevich, and A. N. Slavin, "A frequency-controlled magnetic vortex memory," *Applied Physics Letters*, vol. 96, no. 13, p. 132506, 2010.

[119] M. Mruczkiewicz, M. Krawczyk, and K. Y. Guslienko, "Spin excitation spectrum in a magnetic nanodot with continuous transitions between the vortex, Bloch-type skyrmion, and Néel-type skyrmion states," *Physical Review B*, vol. 95, no. 9, p. 094414, 2017.

[120] K. Y. Guslienko and Z. V. Gareeva, "Gyrotropic Skyrmion Modes in Ultrathin Magnetic Circular Dots," *IEEE Magnetics Letters*, vol. 8, pp. 1–5, 2017.

[121] K.-W. Moon, D.-H. Kim, S.-G. Je, B. S. Chun, W. Kim, Z. Qiu, S.-B. Choe, and C. Hwang, "Skyrmion motion driven by oscillating magnetic field," *Scientific Reports*, vol. 6, no. 1, p. 20360, 2016.

[122] W. Wang, M. Beg, B. Zhang, W. Kuch, and H. Fangohr, "Driving magnetic skyrmions with microwave fields," *Physical Review B*, vol. 92, no. 2, p. 020403, 2015.

[123] M. Beg, R. Carey, W. Wang, D. Cortés-Ortuño, M. Vousden, M.-A. Bisotti, M. Albert, D. Chernyshenko, O. Hovorka, R. L. Stamps, and H. Fangohr, "Ground state search, hysteretic behaviour, and reversal mechanism of skyrmionic textures in confined helimagnetic nanostructures," *Scientific Reports*, vol. 5, p. 17137, 2015.

[124] K.-W. Moon, B. S. Chun, W. Kim, Z. Q. Qiu, and C. Hwang, "Control of skyrmion magnetic bubble gyration," *Physical Review B*, vol. 89, no. 6, p. 064413, 2014.

[125] M. Beg, M. Albert, M.-A. Bisotti, D. Cortés-Ortuño, W. Wang, R. Carey, M. Vousden, O. Hovorka, C. Ciccarelli, C. S. Spencer, C. H. Marrows, and H. Fangohr, "Dynamics of skyrmionic states in confined helimagnetic nanostructures," *Physical Review B*, vol. 95, no. 1, pp. 1–16, 2017.

[126] K. Guslienko and Z. Gareeva, "Magnetic skyrmion low frequency dynamics in thin circular dots," *Journal of Magnetism and Magnetic Materials*, vol. 442, pp. 176–182, 2017.

[127] C. Kittel, *Introduction to Solid State Physics*, 8th ed. Wiley, 2004.

[128] A. Altland and B. D. Simons, *Condensed Matter Field Theory*, 2nd ed. Cambridge: Cambridge University Press, 2010.

[129] C. Kittel, "Theory of Antiferromagnetic Resonance," *Physical Review*, vol. 82, no. 4, pp. 565–565, 1951.

[130] F. Keffer and C. Kittel, "Theory of Antiferromagnetic Resonance," *Physical Review*, vol. 85, no. 2, pp. 329–337, 1952.

List of publications

H. Velkov, O. Gomonay, M. Beens, G. Schwiete, A. Brataas, J. Sinova and R. A. Duine, “Phenomenology of current-induced skyrmion motion in antiferromagnets,” *New Journal of Physics*, vol. 18, no. 7, p. 075016, 2016.

Y. Yamane, O. Gomonay, H. Velkov, and J. Sinova, “Combined effect of magnetic field and charge current on antiferromagnetic domain-wall dynamics,” *Physical Review B*, vol. 96, p. 064408, 2017.

Versicherung

Hiermit versichere ich, dass ich diese Dissertation selbstständig verfasst habe. Ich habe ausschließlich die angegebenen Quellen und Hilfsmittel verwendet und habe von der Ordnung zur Sicherung guter wissenschaftlicher Praxis in Forschung und Lehre und zum Verfahren zum Umgang mit wissenschaftlichem Fehlverhalten Kenntnis genommen.

Ich habe oder hatte die jetzt als Dissertation vorgelegte Arbeit nicht schon als Prüfungsarbeit für eine andere Prüfung eingereicht.

Ich habe die gleiche Abhandlung oder Teile davon noch nicht als Dissertation bei einer anderen Fakultät oder einem anderen Fachbereich eingereicht.

Hristo Velkov